DOCTOR OF PHILOSOPHY

Efficient numerical approaches for ab-initio linear and nonlinear optics

Alliati, Ignacio Martin

Award date:
2023

Awarding institution:
Queen's University Belfast

Efficient numerical approaches for ab-initio linear and nonlinear optics

A thesis presented upon application for
admission to the degree of

Doctor of Philosophy

in the Faculty of Engineering and Physical Sciences
by

Ignacio Martin Alliati

School of Mathematics and Physics
Queen's University Belfast
Northern Ireland

October 2023

Abstract

Progress in the field of computational materials science is largely driven by the **methods** available for simulating materials and predicting their properties. For optical excitations in particular, successful *ab-initio* formalisms exist but their computational implementation often faces challenges in terms of performance and numerical efficiency. Overcoming these barriers by proposing and developing alternative methods for the calculation of linear and nonlinear optical properties is therefore the overarching objective of this thesis.

The state of the art for the description of linear optical excitations in extended systems is given by the Bethe-Salpeter equation (BSE) framework, in which the number of **k**-points required usually leads to computational limitations. We then propose an efficient double grid approach to **k**-sampling, involving a coarse **k**-grid that drives the computational cost and a fine **k**-grid that is responsible for approximately capturing excitonic effects while requiring minimal extra computation. Our approach is compatible with Haydock's iterative solution of the BSE and produces satisfactory results for systems with spatially-delocalised, loosely-bound excitons. The validity of the approximations involved and the limitations of the approach are also discussed.

The nonlinear optical regime is typically addressed with non-perturbative methods based on explicit time propagation, which makes them computationally costly. We tackle this issue by proposing a reformulation of the so-called real-time approach [Phys. Rev. B **88**, 235113, (2013)] based on Floquet theory, which leads to a self-consistent time-independent eigenvalue problem. The method presented here applies to periodically-driven quantum systems with weak electric fields and remains valid for extended systems as it uses the

dynamical Berry-phase polarisation.

The implementation of this Floquet scheme at the independent particle level reproduces the results of the real-time approach for 2^{nd} and 3^{rd} order susceptibilities of a number of bulk and two-dimensional materials, while reducing the associated computational cost by one or two orders of magnitude. The inclusion of local fields and many-body effects introduced instabilities in the Floquet self-consistent cycle that could not be yet mitigated, leading to only a handful of converged results at the time-dependent Hartree level. These divergencies are linked to high population inversions, according to insights gained following the development of a Floquet analysis tool capable of extracting Floquet states from a time-dependent solution produced by, e.g., the real-time approach.

After critically evaluating the contributions of this thesis to the field of computational materials science, it was concluded that the methods proposed and developed here have the potential to accelerate the *ab-initio* calculation of linear and nonlinear optical properties. Avenues for future exploration on these topics are also identified in light of the findings reported in this work.

Acknowledgements

I would like to start by expressing my deepest gratitude to my supervisor Myrta Grüning, this work was only possible thanks to her expert advice, detailed guidance and unconditional support. Her motivating ideas and insightful contributions are at the core of what has been an immensely enjoyable learning experience for me. I am forever indebted to Myrta for having introduced me to the world of methods development, which has transformed my understanding of electronic structure and resonated with my conception of science.

I am extremely thankful to my former secondary supervisor, Jorge Kohanoff, to whom I owe so much, both professionally and personally. Jorge repeatedly showed me the right path when I could not see it, helping me at every step of the way. He played a big role in my decision to take this PhD position. I would like to extend my sincere thanks to my former supervisor, Elton Santos, and my current secondary supervisor, Piotr Chudzinski, for their guidance and support, and the interesting discussions we have had.

I would also like to express my profound gratitude to Davide Sangalli for his involvement into this project and for hosting me in Milan during a highly enriching learning opportunity. I gratefully acknowledge his physical insights, code-related support and mentorship. I sincerely thank Claudio Attaccalite for his detailed feedback on my work and the insightful discussions we have had. I extend my gratitude to Daniele Varsano for guiding me in my tutoring endeavours and Andrea Marini for his thought-provoking comments on my work.

I am also thankful to Malachy Montgomery, for his regular support and unlimited patience, and Conrad Johnston, whose invaluable assistance got me through the beginning of my PhD. I gratefully acknowledge Alejandro Molina-Sánchez, Fulvio Paleari, Alberto

Guandalini and Miki Bonacci for their help and the interesting discussions we held. I am as well thankful for the support I received from Declan Scullion, Mathias Augustin, Dina Abdul-Wahab and Sam Shepherd. A special thanks goes to all members of the ASC and the Yambo community, who made me feel welcome and valued since day one.

At a personal level, I would like to warmly thank my family and friends for always being there for me, you all are a huge part of this process. I am thankful to Nico, Pato, Fede and Santi for turning every trip to Argentina into the most memorable of times; to Flor, Seba, Lucas, Keke and Barby for their eternal friendship; to Juan for still taking care of me as his little brother; to my father for ingraining a sense of self-confidence in me; and to my mother for teaching me to value happiness and education above all else. Finally, I could not have undertaken this journey without the love and companionship of my wife, Naza. I am forever grateful for her support, encouragement and unimaginable patience.

Financial support from the Engineering and Physical Sciences Research Council (EPSRC) is gratefully acknowledged.

"Langsam. Schleppend. *Wie ein Naturlaut.*"

Gustav Mahler, 1888.

Contents

Chapter 1

Introduction

We introduce two overlapping research fields that provide the context for the present thesis. First, we describe the optical phenomena to be studied in this work and present a short account of their relevance for current and potential applications. Next, we assess our ability to make quantitative ab-initio predictions of materials properties and discuss the implications this has for computational materials science as a research area. We then focus on currently available methods for the calculation of optical properties and the challenges they face in terms of performance and numerical efficiency. These computational barriers motivate the alternative formulations proposed and developed in this work, and help us establish a number of key questions to be addressed throughout this thesis.

Quantum mechanics represents one of the great revolutions in twentieth-century physics [1], and arguably, in all of science. More than a hundred years have passed since this radical shift in our understanding of the world around us, yet it continues to puzzle even the brightest minds with counter-intuitive phenomena like entanglement and its deep philosophical implications. This has warranted a characterisation of quantum mechanics as a *strange* theory that became ubiquitous in science communication circles. While there may be an element of truth in that depiction, an utilitarian (and somewhat contrasting) perspective should have far greater prominence on the general perception of this theory, i.e., quantum mechanics is a very powerful 'engineering tool' we have at our disposal. There is a great deal we *do* understand about quantum mechanics, which has enabled or assisted the development of remarkable technologies such as computers, electronics and lasers. It is in this

context that the present thesis is conceived, as it relies on or relates to said technologies, and it stands on the firm theoretical foundations of quantum mechanics. Moreover, it follows a similar mindset of improving theoretical frameworks in pursue of further technological developments.

The modelling and simulation of materials at the microscopic scale is often cited as another *technology* derived from quantum mechanics [2] and the developments that followed, e.g., the availability of computers. It implies the formulation of mathematical frameworks for the quantitative prediction of certain properties, their computational implementation and execution. This set of tasks form what is known as computational materials science, or simply, computational materials. This field is at a momentous stage, establishing itself as a central discipline within physics and reaching a growing variety of scientific areas as an increasingly standard tool. At its core, the present thesis seeks to improve the capabilities of this *technology* by means of devising and implementing alternative and more efficient algorithms to overcome the limitations faced by currently available methods (See Section 1.2). As an overarching solution to these challenges is unlikely, progress is rather made by addressing these issues with a particular problem in mind [3]. In this thesis, the motivating question is given by optical phenomena, a subject that combines considerable theoretical and computational complexity with significant relevance in terms of current and prospective technological applications (See Section 1.1).

1.1 Optical phenomena

Light is arguably the most useful probe we have of the physical reality around us. Whether it is coming at the James Webb Space Telescope from a distant galaxy, or probing the inner structure of matter, electromagnetic radiation always reveals something about the media it propagates through. Naturally, this is only possible thanks to the interactions between light and matter, which are collectively referred to as optical phenomena. A deep understanding and control of light-matter interactions has huge potential for applications, not only using

light as a probe, i.e., designing ever more capable optical instruments, but also as a means to achieve some goal, e.g., photovoltaic cells.

The present thesis will focus on optical phenomena between infrared to near-ultraviolet radiation and the electrons in crystalline solids. In detriment of reflection and transmission, we are interested in the propagation of light through a material, which can involve processes such as optical absorption. This interaction implies the transfer of energy from the incoming radiation to the electrons, thus promoting them from their ground state to a higher-energy state in what we call an optical excitation. The latter is a central concept in this thesis, which we intend to study from a theoretical standpoint. This will require a quantum-mechanical description of the energy levels accessible to the electrons within a crystal (i.e., the electronic structure) as well as some account of the changes induced by the excitations. Moreover, *ab-initio* formalisms will be used throughout the thesis, which implies dispensing with any empirical parameters in favour of just the periodic table and the principles of quantum mechanics. A critical assessment of existing theoretical frameworks (see Chapter 2) together with the development and implementation of new methods (see Chapters 3-6) constitutes much of this thesis.

1.1.1 Linear optics

The effects of an electric field, $\mathcal{E}$, in a material can be understood in terms of the polarisation they induce, P, i.e., the dipole moment per unit volume resulting from the charge displacements generated by the electric field. These processes are mathematically confined to a so-called response function or susceptibility, $\chi(\mathcal{E})$, a magnitude representing an input-output relationship between $\mathcal{E}$ and P. While this response function is, in general, a function of the intensity of the electric field, neglecting this dependency is usually a very good approximation,

$$\mathrm{P} = \chi(\mathcal{E})\,\mathcal{E} \;\rightarrow\; \mathrm{P} = \chi\,\mathcal{E}, \tag{1.1}$$

where the tensorial nature of these variables is ignored for simplicity, as well as their time and space dependencies. Eq. 1.1 embodies the physics of the linear regime, which captures the predominant effects of optical excitations and successfully describes a wide variety of optical phenomena, e.g., absorption.

The vast majority of optical phenomena that can be observed experimentally and exploited in practical applications can be well described within the linear regime. A deep understanding of the processes involved in linear optics is therefore of utmost importance, and the progress made so far has led to innumerable applications. We restrict this discussion to the field of optoelectronics since this thesis focuses on electronic excitations in *gapped* materials, i.e., the applications for which this thesis could be relevant would probably fall within that area. Optoelectronic devices are nowadays ubiquitous, permeating several aspects of our daily life. For instance, light-emitting diodes (LEDs) find numerous applications in low-cost illumination (which warranted the 2014 Nobel Prize in physics [4]), signals and digital displays, among others [5]. Together with optical fibres, they have revolutionised telecommunications, playing a major role in the rise of information technology. Optoelectronic devices also find applications in photovoltaic (solar) cells for sustainable energy generation [6]. Photodetectors are also essential for optical instruments, enabling a wide range of spectroscopies that allow us to further characterise materials. Moreover, recent advances in optoelectronics relate to the role low-dimensional materials can play in this area, in terms of new or tuneable physical effects and better device integration [7–9].

1.1.2 Nonlinear optics

The linearity proposed in Eq. 1.1 can be seen as the leading term of an expansion in powers of the electric field,

$$\mathrm{P} = \chi^{(1)}\,\mathcal{E} + \chi^{(2)}\,\mathcal{E}^2 + \chi^{(3)}\,\mathcal{E}^3 + \mathcal{O}(\mathcal{E}^4), \tag{1.2}$$

where $\chi^{(n)}$ is the nth-order susceptibility [10]. The fact that higher-order response functions are several orders of magnitude smaller than $\chi^{(1)}$ explains why the linear regime is such a

good approximation and nonlinear effects can only be observed with high-intensity electric fields. The latter became available only after the discovery of the laser (1960), which provided a highly-coherent high-intensity monochromatic light beam. This allowed for the observation of second optical harmonics ($\chi^{(2)}$) in crystalline quartz [11], in what constituted the first nonlinear optics experiment of the laser era. This milestone marks the beginning of a new chapter in the field of nonlinear optics, which has been flourishing ever since.

Nonlinear optics has developed into a vast and very rich subject, encompassing a wide variety of optical phenomena and holding promise of potential applications in several areas of photonics, e.g., all-optical switching [12,13]. An important distinction within this field is determined by the intensity of the light beam required to observe a given nonlinear process, resulting in the so-called 'traditional' and extreme nonlinear regimes. The transition to the extreme regime occurs whenever the energy associated with said intensity becomes comparable or surpasses the characteristic energy of the material under study [14], at which point the power expansion in Eq. 1.2 is no longer a good approximation. The extreme regime requires field intensities beyond 1×10^{12} W cm^{-2}, which could only be achieved several decades after the discovery of the laser. At variance, the seminal experiments by Franken *et al.* [11] were conducted with intensities around 1×10^{7} W cm^{-2}, which is high enough to generate measurable optical harmonics without affecting the validity of Eq. 1.2. The use of these so-called 'weak' electric fields, i.e., weak in comparison with the extreme nonlinear regime, limits the extent to which electrons are expected to populate excited states, a concept we will revisit in Chapter 6. The present thesis will focus on this 'traditional' regime and refer to it simply as nonlinear optics.

Progress in this field has resulted in several applications, among which we can distinguish nonlinear optical spectroscopies as an invaluable tool for investigating materials properties. This is largely due to second harmonic generation (SHG) and its symmetry dependence, i.e., it is a forbidden process in systems with inversion symmetry. For this reason, it has been traditionally used on surfaces and interfaces [15–17], and more recently for the characterisation and imaging of two-dimensional flakes [18–21]. This nonlinear optical

phenomenon can also act as a highly sensitive probe of magnetic ordering in atomically-thin materials [22–24] and multiferroics [25,26]. In particular, SHG presents itself as a useful probe for two-dimensional antiferromagnets provided the phase transition breaks inversion symmetry, thus filling a gap between traditional magnetometric techniques and magneto-optical Kerr effect (MOKE) microscopies. While the former require large sample volumes, the latter can detect two-dimensional magnetism only if the net magnetisation is non-zero, which typically applies to ferromagnets [27]. Finally, due to the sensitivity to changes in the electric polarisation, SHG can also probe the dynamics of excited systems, tracking, for instance, the formation of excitons, exciton-phonon coupling and demagnetisation of antiferromagnets [28, 29].

1.2 Computational materials science

The field of computational materials has been growing fast over the past decades, primarily due to the tremendous success of density functional theory [30] (DFT) and the ingenious formulation of Kohn and Sham [31] (KS). Despite the fact that the underlying ideas of DFT were present in the late 1920's and were put on firm ground by 1964, the widespread application of this framework only started in the 1990's (which, in part, relates to the computational resources available at the time). An almost exponential growth in the number of DFT-related publications was registered since then, surpassing ten thousand yearly contributions by the late 2000's [32]. In terms of impact, a 2014 list of the most cited 100 papers included twelve publications relating to DFT, two of which made it to the top 10 [33]. A more recent scientometric study tracks citations of the 31 most used electronic structure *ab-initio* packages based on DFT, also revealing an almost exponential growth of the yearly number of publications citing said codes [34].

The other pillar of this rapid expansion is computational, i.e., the widespread availability of high-performance computing (HPC) resources. Electronic structure methods benefited from a steep and sustained increase in the computational power available to perform *ab-*

initio calculations, first growing according to Moore's law [1] and, more recently, boosted by the advent of GPU cards for highly intensive computing tasks. The rise to prominence of *ab-initio* methods, particularly DFT, was also possible thanks to the development of a vast number of commercial and freely-available codes implementing the KS scheme and other approaches. The apparent threat this poses for the reproducibility of DFT results has been recently addressed in a community-wide effort [35]. Crucially, it was concluded that most of the codes and methods used nowadays predict essentially identical results, putting past and future research efforts on a firmer footing.

All this remarkable progress in electronic structure theory and computation has greatly contributed to many areas of research, in particular, as DFT codes became standard tools in disciplines well beyond the communities that developed them. Numerous properties are routinely calculated with relative ease and quick turnarounds, specially ground state properties *via* DFT, like atomic structures, elastic constants, magnetic orderings, etc. In essence, we have a *technology* capable of computing several properties in quantitative agreement with experiments, thus providing physical insights into various phenomena and complementing experimental efforts. Crucially, the predictive power of *ab-initio* electronic structure methods has the potential to unlock the field of computational material exploration. This stems from the fact that simulating materials can be more straightforward and cost-effective than conducting the analogous experiments in the laboratory. Hence, one can use this *technology* to perform a high-throughput screening of tens of thousands of materials in the quest for a desired property, which has been facilitated since the advent of automation tools for electronic structure calculations [36, 37]. High-throughput studies can then contribute to a more educated selection of materials for experimental trials, considerably reducing the cost and time scales associated with materials discovery and functionalisation.

The rapid growth of computational materials science as a research field has been primarily driven by DFT, which has a very high ratio of predictive power to computational complexity. However, its most widely used formulation turns it into a ground-state method [31],

[1] Whether the limits of Moore's law have been nowadays reached or not is currently debated.

which has its obvious limitations, i.e., arguably more interesting physics comes from electronic excitations, like optical properties. Many-body perturbation theory (MBPT) offers a suitable and very successful framework for tackling these problems, at the expense of being much more computationally demanding than DFT [38–41]. Having benefited from a sustained increase in the computational power available, MBPT methods came to represent a growing contribution to the success story of electronic structure methods. Nonetheless, the computational demands of MBPT methods are still their main shortcoming. Overcoming these computational barriers can assist MBPT in following a similar trajectory as DFT in terms of research impact and is therefore a key motivation in the present thesis.

1.2.1 Limitations and challenges

While MBPT presents an advantage respect to DFT regarding the physics it can successfully describe, it usually involves more cumbersome calculations [38–41]. DFT considers one-particle equations for non-interacting electrons and approximates (non-local) electron-electron interactions *via* a local mean-field scattering potential. At variance, MBPT theory treats non-locality explicitly through the self-energy operator, which inevitably translates into heavier computations. Another important factor determining the computational cost of both frameworks lies in the need for *convergence studies*. This refers to the truncation of parameters that should in principle be infinite, as required for any numerical implementation, and implies finding the minimum value of any such parameter that nonetheless captures all the relevant physics. Examples of these parameters are the number of basis states in a basis expansion or the density of sampling points in a numerical integral. In comparison with DFT, MBPT requires more convergence studies and usually presents a slower convergence, i.e., it requires larger values of the same parameters.

Among these parameters we can distinguish the so-called **k**-points. This relates to the discrete sampling applied to a group of numerical integrals that play a crucial role in periodic systems and will be discussed in Sections 2.1 and 2.2. As a general obser-

vation on *gapped* materials, suffices to say that DFT presents a faster *convergence* with respect to **k**-sampling than MBPT, i.e., it requires fewer **k**-points overall. Depending on the system under study, this can render MBPT calculations prohibitively costly, particularly when computing optical properties *via* the Bethe-Salpeter Equation (BSE). In fact, more often than not, the BSE scheme runs into computational limitations while seeking **k**-points convergence and, as a result, the calculation of optical spectra is not as straightforward or *streamlined* as that of DFT-based ground state properties. **Overcoming these computational challenges will boost our ability to calculate optical spectra efficiently with currently available supercomputers, thus furthering the capabilities of computational materials as a research field**. This is therefore a key motivation of the present thesis, which is addressed in Chapter 3.

The calculation of nonlinear optical properties represents another area of computational materials science where successful theories exist but their implementation faces considerable barriers in terms of the computational resources required. Most successful approaches for the calculation of nonlinear susceptibilities in extended systems, certainly beyond the second order in Eq. 1.2, involve explicit time evolution governed by a given Hamiltonian, e.g., the so-called real-time approach [42, 43]. This method allows for a relatively straightforward inclusion of excitonic effects within the MBPT framework, as it *only* entails adding the corresponding self-energy operator to the Hamiltonian. Another crucial advantage of the real-time approach lies on the capability of computing susceptibilities to many orders simultaneously, since it is not perturbative in the electric field. However, these benefits are sometimes overshadowed by the computational cost it entails, which is very high even by MBPT standards. **It is therefore a central incentive of the present thesis to reduce this barrier and bring the simulation of nonlinear optical processes into the *mainstream* of computational materials science**. The use of Floquet theory (introduced in Section 2.4) holds promise in circumventing the elevated computational cost of the real-time approach while retaining its main advantages, as will be explored in Chapters 4-6.

1.3 Structure of this thesis

As we tried to convey in the previous sections, the overlap between the research fields of optics and computational materials science results both in remarkable opportunities and sizeable challenges. The former refer to the idea of accelerating the discovery of functional materials for applications in optoelectronics and nonlinear optical devices. The latter are represented by the computational limitations faced by currently available methods in the calculation linear and nonlinear optical properties. The present thesis contributes to tackling these shortcomings and aims at enhancing the capabilities of computational materials science.

The reminder of the thesis will be structured as follows. Chapter 2 describes the theoretical background regarding the currently available frameworks for the calculation of linear and nonlinear optical properties, leading to a discussion on their shortcomings and previous attempts to overcome them. The basics of Floquet theory are also presented here. The methods in Chapter 2 represent a benchmark upon which improvements will be proposed and tested in subsequent chapters. Chapter 3 is devoted to linear optics and proposes an efficient approach to **k**-sampling in the BSE scheme. We seek to investigate whether this approximation can still capture excitonic effects correctly and evaluate the computational gains achieved by this method.

Chapters 4-6 focus on nonlinear optical properties. The key question to address here relates to whether Floquet theory can be used to reformulate the time-dependent problem of the real-time approach as a time-independent eigenproblem, and what conditions are required of the Hamiltonian to achieve that. As equally important is to verify that the above-mentioned advantages of the real-time approach are retained in the reformulated eigenproblem. Moreover, it is also essential to quantify the speed-up attained by this Floquet approach. We attempt this in two stages depending on the level of theory considered, i.e., we reformulate the real-time approach at the independent-particle level in Chapter 4 and we defer the inclusion of excitonic effects to Chapter 5.

Chapter 6 explores how the eigenstates of the Floquet eigenproblem can be obtained from the solution of the real-time approach, and proposes a method to achieve that. This attempts to reveal what kind of so-called Floquet states should be expected in each situation, and how they depend on the inclusion of excitonic effects.

Finally, Chapter 7 revisits the key questions set out here in light of the advances presented in Chapters 3-6, thus providing the conclusions of this thesis alongside an outlook to future endeavours.

Chapter 2

Theoretical background

We review the current theoretical frameworks for the ab-initio description of linear and nonlinear optical processes, starting with a discussion on Density Functional Theory as the method of choice for ground-state calculations. We then consider the linear regime, covering from the Independent Particle Approximation (IPA) to the inclusion of many-body effects for the description of excitons via the Bethe-Salpeter equation (BSE). Next, we review the tools available for predicting nonlinear optical properties with particular focus in time-dependent approaches. We highlight the challenges and bottlenecks affecting the efficiency of these methods as a motivation for our own implementations. In addition, we set out the basics of Floquet theory and its application to periodically driven quantum systems. [1]

The present thesis is broadly concerned with *ab-initio* optical excitations of electrons in solids. In particular, we focus on neutral excitations, i.e., electron-hole pairs, as those involved in spectroscopic measurements of optical absorption or second harmonic generation (SHG). This is intrinsically a time-dependent problem, as we perturb a system with an external field, $\mathcal{E}(t)$, and analyse its response in real time. Indeed, this logic motivates one of the frameworks used to describe these phenomena from a theoretical standpoint, i.e., the so-called real-time approach. The latter implies solving the time evolution of the system with the perturbing field in order to access its dynamical properties. Among these, one can

[1] Chapter 2 includes content that first appeared in two published articles reporting work carried out as part of this PhD, with some emendations and changes of phrase to better elaborate the work. In particular, the last subsections of Section 2.2.2 were adapted from Alliati, Sangalli & Grüning, Frontiers in Chemistry, 9, 763946 (2022), and Section 2.3.1 first appeared in Alliati & Grüning, Electronic Structure, 5, 017001 (2023).

obtain the dynamical polarisation, $\mathrm{P}(t)$, induced by the external field, which is a central quantity in the study of light-matter interaction. This polarisation is usually expanded in powers of the electric field (see Eq. 1.2), thus defining n-th order response functions or susceptibilities, $\chi^{(n)}$. Ultimately, these functions relate to the observables measured in the experiments we intend to reproduce and can be easily obtained once the dynamical polarisation is known as a function of time.

An alternative framework for describing optical excitations implies finding individual expressions for the various susceptibilities based on transition probabilities between occupied and unoccupied states, e.g., calculating correlation functions *via* response theory. This can be achieved considering partial derivatives respect to the external field or the induced charge density (rather than time derivatives), which results in a time-independent formalism. The choice between the real-time or perturbative approaches usually depends on the regime of optical excitation under consideration. The perturbative approach is preferred in the linear regime, i.e., calculating $\chi^{(1)}$ to obtain absorption spectra, and will be described in Section 2.2. With the exception of some perturbative expressions available for $\chi^{(2)}$, nonlinear optical excitations in solids are normally addressed with real-time approaches, as explained in Section 2.3. In any case, either as the unperturbed system or as a starting point for the time-dependent problem, an *ab-initio* description of the electronic ground state is required (see Section 2.1). Finally, Section 2.4 presents Floquet theory as an alternative for reformulating the time-dependent formalism into a time-independent non-perturbative eigenproblem, provided time periodicity is present in the system.

2.1 Ground state electronic structure

In the atomic scale, matter can be represented as a collection of atomic nuclei and their corresponding electrons interacting with one another and among themselves via Coulomb forces. Adding the kinetic energy of each particle to these electrostatic contributions, one can obtain the Hamiltonian operator for a system of P nuclei and N electrons,

$$\begin{aligned}\hat{\mathcal{H}} = &-\sum_{I=1}^{P}\frac{\hbar^2}{2M_I}\nabla_I^2 - \sum_{i=1}^{N}\frac{\hbar^2}{2m}\nabla_i^2 + \frac{e^2}{2}\sum_{I=1}^{P}\sum_{J\neq I}^{P}\frac{Z_I Z_J}{|\mathbf{R}_I - \mathbf{R}_J|} \\ &+ \frac{e^2}{2}\sum_{i=1}^{N}\sum_{j\neq i}^{N}\frac{1}{|\mathbf{r}_i - \mathbf{r}_j|} - e^2\sum_{I=1}^{P}\sum_{i=1}^{N}\frac{Z_I}{|\mathbf{R}_I - \mathbf{r}_i|},\end{aligned} \tag{2.1}$$

where m, e and $\mathbf{r}_i$ are the mass, charge and position of the electrons while M_I, Z_I and $\mathbf{R}_I$ represent the nuclear mass, charge and coordinates. In principle, all the information included in Eq. 2.1 is known and one should be able to find the energy eigenstates of this Hamiltonian, $\Psi(\mathbf{R}_1, \mathbf{R}_2 ... \mathbf{R}_P, \mathbf{r}_1, \mathbf{r}_2 ... \mathbf{r}_N)$. The latter would provide the ground state many-body wavefunction and a general solution to the time-dependent Schrödinger equation, $\Psi(\mathbf{R}_1, \mathbf{R}_2 ... \mathbf{R}_P, \mathbf{r}_1, \mathbf{r}_2 ... \mathbf{r}_N, t)$, from which any property of the system can be derived. In practice, this is impossible to solve with the exception of very few simple systems. The main issue with this Hamiltonian is the two-body nature of the Coulomb interaction, which makes the Schrödinger equation non separable. Mathematically, it means that the 3(P+N) degrees of freedom in the equation are coupled. Physically, that the position of, e.g., one electron depends on that of the nuclei and all the remaining electrons.

For almost every system of interest, solving the Schrödinger equation will require us to decouple some of these degrees of freedom, turning the solution into an inevitably approximated one. Two of such approximations, on which most electronic structure methods are based, separate the nuclear degrees of freedom from one another (classical nuclei approximation) and from the electronic ones (Born-Oppenheimer approximation [44] [2]). The former approximation amounts to neglecting exchange and correlation effects among the nuclei, as well as considering each nucleus as an individual and well-localised wave packet. The Born-Oppenheimer approximation is inspired in the classical picture of electrons moving much faster than the nuclei owing to their mass difference. It is more accurate to describe it as a separation in energy and time scales of the electronic excitations form the nu-

[2] While some of the sources cited in Section 2.1 are in German, the corresponding topics have been covered in numerous solid state physics and electronic structure textbooks, e.g., [45–47].

clear ones (phonons), which results in ignoring non-radiative transitions between electronic states. This allows us to factor the wavefunction into a nuclear and an electronic part, i.e., $\Psi = \Theta(\mathbf{R}_1, \mathbf{R}_2 ... \mathbf{R}_P, t)\Phi(\mathbf{r}_1, \mathbf{r}_2 ... \mathbf{r}_N)$, where the nuclear wavefunction, Θ, is also a product of individual wave packets. The electronic wavefunction, Φ, depends only parametrically on the nuclear coordinates and is an (adiabatic) eigenstate,

$$\hat{\mathcal{H}}_e \Phi_i(\mathbf{r}_1, \mathbf{r}_2 ... \mathbf{r}_N) = E_i \Phi_i(\mathbf{r}_1, \mathbf{r}_2 ... \mathbf{r}_N) \tag{2.2}$$

of the so called electronic Hamiltonian,

$$\hat{\mathcal{H}}_e = -\sum_{I=1}^{P} \frac{\hbar^2}{2m} \nabla_i^2 + \frac{e^2}{2} \sum_{i=1}^{N} \sum_{j \neq i}^{N} \frac{1}{|\mathbf{r}_i - \mathbf{r}_j|} - e^2 \sum_{I=1}^{P} \sum_{i=1}^{N} \frac{Z_I}{|\mathbf{R}_I - \mathbf{r}_i|}, \tag{2.3}$$

of a given nuclear configuration, $\{\mathbf{R}_I\}$.

These approximations have turned the original problem into a much simpler but still unsolvable one, i.e., finding the eigenfunctions of the electronic Hamiltonian. This is referred to as **the electronic problem** and consists of N interacting electrons in the external Coulomb field generated by the nuclei. The main obstacle in its solution is that this time independent electronic Schrödinger equation is, again, non separable. Hence, its solution depends, in principle, on the 3N electronic coordinates. Unsurprisingly, the origin of this problem is the same as before, namely, the two-body nature of the Coulombic interactions between electrons. However, in the case of electrons, correlation effects are very important and cannot be safely ignored as in the case of nuclei (where a product of individual wavepackets gives a good approximation to the nuclear wavefunction). Indeed, electron correlation is the essence of the electronic problem, to which much of this thesis will be devoted.

Mathematically, electron correlation means that the electronic wavefunction cannot be written as a product of non-interacting one electron wavefunctions. Nevertheless, solving the electronic problem *via* DFT will involve doing exactly that, but only as a reference

system within a framework where correlation is nonetheless accounted for and, more importantly, the wavefunction is no longer the fundamental variable.

2.1.1 Density Functional Theory

The density as a fundamental quantity

The idea that the electronic density could be as fundamental as the wavefunction in the many-body problem was first intuitive [48–50]. In what is known as Thomas-Fermi-Dirac (TFD) theory, an inhomogeneous electron gas was considered as locally homogeneous and its energy was written as a functional of the electronic density. The obvious advantage of this framework is that the density depends only on the three spatial coordinates, while the electronic wavefunction has 3N degrees of freedom. This ideas of the late 1920's formed the basis for the later development of Density Functional Theory (1964), where these statements were proven and formalised by Hohenberg and Kohn [30].

The first Hohenberg and Kohn (HK) theorem indicates that the external potential is, to within a constant, a unique functional of the electron density [30]. The implications of this statement arise from the fact that, by defining the external potential, the electronic Hamiltonian is completely specified and so are the many-body energy eigenstates $\Phi(\mathbf{r}_1, \mathbf{r}_2 ... \mathbf{r}_N)$. As a result, the many-body ground state (and evidently the ground state energy) must be a unique functional of the electron density. This means that there must exist a one-to-one mapping between the ground state wavefunction of a system and its ground state electron density. The latter is as fundamental as the wavefunction and both carry the same information. The second HK theorem, known as the variational principle, proves that the energy functional assumes its minimum value for the correct electron density. This means that obtaining the ground state energy and density of any external potential amounts to minimising the energy functional of the electronic density, a function of the three spatial variables. The complexities of the many-body problem are then confined to determining the form of this energy functional.

The HK theorems tell us that the energy functional exists, but not what it looks like. In general, the energy functional, $\mathsf{E}[\rho]$, should have kinetic, electrostatic and exchange-correlation terms,

$$\mathsf{E}[\rho] = \mathsf{T}[\rho] + \mathsf{U}_{ext}[\rho] + \mathsf{U}_{ee}[\rho] + \mathsf{E}_C[\rho] + \mathsf{E}_X[\rho] \tag{2.4}$$

The electron-nuclei interaction, $\mathsf{U}_{ext}[\rho]$, does not pose any problems at this stage. The electron-electron interaction is formulated as that of a system of non-interacting electrons (Hartree term), $\mathsf{U}_{ee}[\rho]$, plus the exchange and correlation contributions, $\mathsf{E}_X[\rho]$ and $\mathsf{E}_C[\rho]$. For the latter two terms, reasonably good approximations exist and will be discussed below. We shall now focus on the kinetic energy term, $\mathsf{T}[\rho]$, for which the TFD expression (local in density) poses severe limitations. The most widely used approach to this issue was proposed by Kohn and Sham (1965) [31].

Kohn-Sham equations

As very often happens in many-body problems, the first approximation to a system of interacting particles is one where they do not interact at all. In this case, the electronic wavefunction would be given by a Slater determinant of many one-electron wavefunctions. As stated above, this decoupling is not correct because electron correlation plays a very important role in the physics being described. Nevertheless, Kohn and Sham (KS) managed to find a non-interacting reference system that has some physical significance for the problem at hand. They defined an auxiliary, non-interacting system that nonetheless produces the correct electron density, i.e., that of the interacting system. Therefore, the scheme of KS results in the eigenproblem,

$$\hat{H}^{\mathrm{KS}}\phi_i^{\mathrm{KS}}(\mathbf{r}) = E_i^{\mathrm{KS}}\phi_i^{\mathrm{KS}}(\mathbf{r}), \tag{2.5}$$

where $\phi_i^{\mathrm{KS}}(\mathbf{r})$ and E_i^{KS} represent the eigenstates and eigenvalues of the so-called KS Hamiltonian,

$$\hat{H}^{\mathrm{KS}} = -\sum_{i=1}^{N} \frac{\hbar^2}{2m}\nabla_i^2 + v_{\mathrm{KS}}(\mathbf{r}), \tag{2.6}$$

a one-particle operator that depends on three spatial variables. One can then obtain the electron density of the interacting system *via* the KS wavefunctions,

$$\rho(\mathbf{r}) = \sum_{i=1}^{N} f_i |\phi_i^{\mathrm{KS}}(\mathbf{r})|^2, \tag{2.7}$$

where f_i is the occupation factor of state i. The resulting density is then used in the energy functional, $\mathsf{E}[\rho]$ (Eq. 2.4).

The re-introduction of *some* wavefunctions in an otherwise wavefunctionless theory is particularly appealing when it comes to finding the expectation value of the kinetic energy operator. One can then calculate the kinetic energy of the reference system exactly,

$$\mathsf{T}_{\mathrm{R}} = -\frac{\hbar^2}{2m}\sum_{i=1}^{N} f_i \langle \phi_i^{\mathrm{KS}} | \nabla^2 | \phi_i^{\mathrm{KS}} \rangle, \tag{2.8}$$

and carry over the difference with respect to the true kinetic energy, i.e., the kinetic correlation energy, to the correlation functional. Computing the kinetic energy *via* Eq. 2.8 supposed a great improvement with respect to the density functionals derived from TFD theory. Important shortcomings of the latter such as the prediction of infinite densities around atomic nuclei and the lack of quantum density fluctuations in accordance to the atomic shell structure are avoided by Eq. 2.8 [31].

All that is left is to formulate a *reference* potential, v_{KS}, such that the energy eigenstates of the KS Hamiltonian produce the same electron density as the true many-body system. Applying the variational principle to both the reference and the interacting systems, and equating the resulting chemical potentials leads to,

$$v_{\mathrm{KS}}(\mathbf{r}) = v_{ext}(\mathbf{r}) + \int \frac{\rho(\mathbf{r}')}{|\mathbf{r}-\mathbf{r}'|} d\mathbf{r}' + v_{\mathrm{XC}}[\rho](\mathbf{r}), \tag{2.9}$$

where $v_{\mathrm{XC}}[\rho](\mathbf{r}) = \frac{\delta(\mathsf{E_C}[\rho]+\mathsf{E_X}[\rho])}{\delta\rho}$ is the exchange-correlation potential and the integral term represents the Hartree potential. We observe that the reference potential, v_{KS}, depends on the electron density, thus imposing the requirement for a self-consistent solution of the KS equations.

Exchange-correlation functional

As mentioned before, electron-electron interaction is the main obstacle in the quantum many-body problem, which includes complex physical effects as exchange and correlation. An appropriate description of these effects is of utmost importance for the success of any *ab-initio* framework and, within DFT, it is attempted *via* approximated functionals of the electronic density.

A suitable starting point is the local density approximation (LDA), which was employed in the seminal papers by Hohenberg, Kohn and Sham [30, 31]. It considers an inhomogeneous electron gas as locally homogeneous, therefore using available functionals for the homogeneous electron gas. While this approach has been successful in describing many solids over the years (e.g., Perdew-Zunger [51]), it also shows some limitations, particularly around inhomogeneities of the charge density like those found in low-dimensional systems.

The obvious improvement over LDA consists on expanding the functional in terms of the gradient of the density, which somehow introduces non-locality. This is the main idea behind the so-called generalised gradient approximations (GGA), of which many formulations have been proposed (e.g., PW91 [52] or PBE [53]). GGA functionals provided an improvement over LDA in many respects and have been extensively used in electronic structure methods. There is a wide variety of more advanced functionals one could choose from, like meta-GGA, hybrid functionals incorporating Fock exact exchange, functionals including Van der Waals interactions or those adding a Hubbard 'U' on-site interaction term (see, e.g., [46, 47]). Nevertheless, we consider LDA and GGA to be reasonably good approximations for the purposes of this thesis. This is because DFT will only be used as a starting point, while electron-electron correlation will be accounted for *via* the many-body perturbation theory

framework (see Section 2.2). Moreover, this thesis is generally concerned with validating methods against each other, rather than making quantitative predictions in agreement with experiments.

Bloch's theorem and plane waves

There is an important aspect related to the form that the one-electron wavefunctions take in a periodic potential, which is particularly relevant for DFT calculations on solids and other systems with periodic boundary conditions. According to Bloch's theorem [54], the eigenstates of any operator with translational invariance, such as a single-particle Hamiltonian with a periodic potential, will be of the form,[3]

$$\phi(\mathbf{r}) = e^{i\mathbf{k}\cdot\mathbf{r}}\mu(\mathbf{r}), \tag{2.10}$$

i.e., the product of a pure phase, where $\mathbf{k}$ is a vector in reciprocal space, and a periodic function, $\mu(\mathbf{r})$, with the periodicity of the lattice. While any wavevector $\mathbf{k}$ should be allowed in principle, it can be proven that only those in the first Brillouin zone (BZ) lead to distinct wavefunctions. As this is still an infinite number of vectors, one has to sample the BZ discretely with a grid of $\mathbf{k}$-points. The latter must be carefully selected so that results are roughly insensitive to the inclusion of additional $\mathbf{k}$-points. This is referred to as achieving convergence with respect to $\mathbf{k}$-points or the sampling of the BZ.

Another key element in solving electronic structure methods involves representing the one-electron wavefunctions in a way that facilitates their computational implementation. The energy eigenstates are then expanded in a basis set and the problem is now to find the coefficients of such expansion. The choice of basis sets will depend on characteristics of the system under study, seeking to make the problem more amenable. Wavefunctions of electrons in extended systems with periodic boundary conditions are usually expanded in plane waves [46, 47]. This would be equivalent to replacing the periodic part of the wavefunction,

[3] An analogous statement in one dimension had been proven earlier by Floquet in an analysis of differential equations with constant or periodic coefficients (see Section 2.4).

$\mu(\mathbf{r})$, by its Fourier series. Importantly, these basis functions do not depend on energy, so the Schrödinger equation becomes a linear eigenvalue problem [46]. In addition, the kinetic energy operator is a diagonal matrix in this representation, which is computationally convenient.

Although the Fourier series of the one-electron wavefunctions is infinite, they must be truncated to a finite number of terms for any computational implementation. This imposes a maximum wavevector $\mathbf{G}_{\max}$, or an energy cutoff, which also determines the the minimum distance in real space that can be resolved. The number of functions in the basis set must be carefully selected through convergence studies and, in this regard, plane-waves offer a systematic way of doing so by simply increasing the energy cutoff [46].

Practical aspects

There are numerous practical aspects that must be considered when solving the KS equations and it is not possible to cover them all here, so we will briefly mention some of them. The first one concerns the widely used pseudopotential approach (see, e.g., [55–57]), in which only the valence electrons are treated explicitly. Conversely, the core electrons form an effective core with the nucleus, thus screening the nuclear potential. Some numerical aspects include the use of density-mixing schemes to prevent charge sloshing and facilitate convergence of the self-consistent loop (see, e.g., [58]), or the inclusion of smearing in the occupations to deal with integrals across the BZ (see, e.g., [59]). Much attention is also devoted to the choice of minimisation algorithms to avoid full diagonalisation of the KS Hamiltonian (see, e.g., [60]). Finally, it is worth mentioning that the DFT formalism can be extended to consider spin polarisation in the so-called local spin density approximation (LSDA – see, e.g., [46]). Non-collinear calculations can also be performed *via* the spinorial formulation of DFT, which also takes into account the orientation of the spins in the lattice and allows for the inclusion of spin-orbit coupling.

2.2 Optical excitations in the linear regime

Let us start by discussing three approximations used throughout this thesis for the calculation of optical spectra, which are also widely adopted in the literature. First, we consider a semi-classical approach to the problem, where the electrons are described quantum mechanically while the electric field is treated classically, i.e., not quantised. Second, we assume that the electric field is spatially constant within a unit cell and invoke the dipole approximation [61], which is reasonable considering the photon energy range explored in this work in comparison with the atomic lengths involved. This approximation enables a gauge transformation such that the effect of the electric field on the electrons can be expressed solely by a scalar potential (i.e., the vector potential is zero within this framework) [61]. This scalar potential is of the form $-e\mathbf{r}\mathcal{E}(t)$, where the electric field $\mathcal{E}$ is constant in space. We therefore work within the so-called length gauge (or density-density approach), which is less susceptible to numerical issues and instabilities than the velocity gauge (or current-current approach) [62].

Finally, we use the fixed-nuclei approximation, thus ruling out any non-radiative electronic transition assisted by lattice vibrations (phonons). This eliminates an important energy dissipation mechanism of electronic excitations, which has to be accounted for phenomenologically instead. In practice, a phenomenological dissipation term is included when calculating response functions, thus providing broadening to the spectra. This term can take various forms depending on the formalism it is applied to, as will be pointed out throughout this thesis. We note these three approximations, as well as the use of the length gauge, will also apply to our study of the nonlinear regime (see Section 2.3).

2.2.1 Response functions *via* perturbative methods

As anticipated, the calculation of optical properties in the linear regime is usually carried out *via* perturbative methods, i.e., formulating expressions for $\chi^{(1)}$ based on the charge density induced by an external potential. While real-time approaches can certainly be used

to obtain this first-order response function, perturbative methods are much preferred in the linear regime, as they are simpler and more efficient. The derivation of these perturbative expressions has been predominantly conducted *via* two contrasting frameworks [38], i.e., many-body perturbation theory (MBPT) and time-dependent density functional theory (TD-DFT). The latter has been successfully applied to finite systems [63] and benefits computationally from a mean-field treatment of the electron-electron interaction. However, the use of approximated functionals in this framework, usually lacking spatial non-locality, makes it difficult to properly account for excitonic effects [38]. This imposes severe limitations on its ability to describe absorption spectra in semiconductors and insulators, where excitons play a crucial role (see e.g., [64–66]). Therefore, this thesis will not address TD-DFT specifically, only referring to it for comparison or completeness whenever appropriate. We will focus on MBPT instead, which offers a well established framework for the description of excitons in solids *via* a non-local, energy dependent, multivariable object, i.e., the self-energy [38, 39, 67]. This inevitably leads to a more cumbersome formalism, as it involves four-point quantities such as the BSE kernel or the two-particle Green's function. As a result, MBPT entails higher numerical complexity than TD-DFT, which can be expressed in terms of a two-point kernel based on a local exchange-correlation potential [38]. Indeed, overcoming these computational limitations of MBPT by proposing methods with improved numerical efficiency is a key motivation in this thesis (see Chapter 3).

Screening

Much of the complexity of dealing with electronic excitations in solids can be ascribed to the idea of *screening*. The latter will be intuitively introduced with an example involving two electrons at positions $\mathbf{r}_1$ and $\mathbf{r}_2$ (they are considered static for simplicity). In a vacuum, those electrons interact *via* a Coulomb potential $v_{\mathrm{Co}}(\mathbf{r}_1, \mathbf{r}_2) = \frac{1}{|\mathbf{r}_2 - \mathbf{r}_1|}$. Inside a material, one must also consider the impact of these electrons on the system as a whole, comprising many other electrons and charged particles. In particular, the presence of an electron at position $\mathbf{r}_1$ will induce rearrangements of electrons leading to a charge density difference everywhere

else in space, $\delta\rho(\mathbf{r}_3)$, that will then act on the electron at position $\mathbf{r}_2$,

$$W_{\mathrm{Co}}(\mathbf{r}_1, \mathbf{r}_2) = v_{\mathrm{Co}}(\mathbf{r}_1, \mathbf{r}_2) + \int d\mathbf{r}_3 \; v_{\mathrm{Co}}(\mathbf{r}_1, \mathbf{r}_3) \; \delta\rho(\mathbf{r}_3), \tag{2.11}$$

where the sum of both contributions is the screened Coulomb interaction, W_{Co}. In the linear regime, one can assume this so-called polarisation density is linear with respect to the perturbation that created it,

$$\delta\rho(\mathbf{r}_3) = \int d\mathbf{r}_4 \; \chi_{\rho\rho}(\mathbf{r}_3, \mathbf{r}_4) \; v_{\mathrm{Co}}(\mathbf{r}_4, \mathbf{r}_2), \tag{2.12}$$

where $\chi_{\rho\rho}$, is the density-density linear response function. We can then formulate the screened Coulomb interaction as,

$$W_{\mathrm{Co}}(\mathbf{r}_1, \mathbf{r}_2) = \int d\mathbf{r}_5 \; \varepsilon^{-1}(\mathbf{r}_1, \mathbf{r}_5) \; v_{\mathrm{Co}}(\mathbf{r}_5, \mathbf{r}_2), \tag{2.13}$$

where the static inverse dielectric function was introduced,

$$\varepsilon^{-1}(\mathbf{r}_1, \mathbf{r}_5) = \delta(\mathbf{r}_1 - \mathbf{r}_5) + \int d\mathbf{r}_3 \; v_{\mathrm{Co}}(\mathbf{r}_1, \mathbf{r}_3) \; \chi_{\rho\rho}(\mathbf{r}_3, \mathbf{r}_5). \tag{2.14}$$

As a result, the Coulomb repulsion between the two electrons is, in general, greatly reduced by the presence of the material. This simple example misses a crucial aspect of the dielectric function, i.e., its time/energy dependence, as the electrons were considered static. Nevertheless, it provides an intuitive picture of the physics involved in charged excitations like those occurring in photoemission spectroscopy experiments. One could also consider a similar situation between an electron-hole pair created in the material by an incoming photon, resulting in a screened Coulomb attraction between these particles. This sort of neutral excitations dominate the physics involved in absorption spectroscopies. In these experiments, it is also useful to think of an external potential applied to a material, V_{ext}, and the resulting total potential inside the material, $V_{\mathrm{tot}} = \varepsilon^{-1} V_{\mathrm{ext}}$, which includes a po-

tential induced by the rearrangement of electrons. This picture will help us formalise the dielectric function.

Linear response theory

We introduce this topic following the discussions in Refs. [39] and [68]. We start by considering a system taken out of equilibrium by a time-dependent perturbation, e.g., a potential $V_{\text{ext}}(\mathbf{r}, t)$ switched on at t_0. This potential will couple to the density operator adding a perturbing contribution to the Hamiltonian of the system, i.e., $\hat{H}(t) = \hat{H}^0 + \int d\mathbf{r}_2\ \hat{\rho}(\mathbf{r}_2)\ V_{\text{ext}}(\mathbf{r}_2, t)$. We now evaluate how a given observable evolves in time under this Hamiltonian by taking the expectation value of the associated operator in the Heisenberg picture. In light of the previous discussion on screening effects, we are interested in the density operator,

$$\langle \hat{\rho}_H(\mathbf{r}_1, t_1) \rangle = \langle U_S^\dagger(t_1, t_0) \hat{\rho}(\mathbf{r}_1) U_S(t_1, t_0) \rangle, \tag{2.15}$$

with the time-evolution operators defined in the Schrödinger picture as,

$$U_S(t_1, t_0) = e^{-i \int_{t_0}^{t_1} dt_2 \hat{H}^0 + \int d\mathbf{r}_2\ \hat{\rho}(\mathbf{r}_2)\ V_{\text{ext}}(\mathbf{r}_2, t_2)}. \tag{2.16}$$

This exponential can be expanded as a power series in V_{ext},

$$U_S(t_1, t_0) \approx e^{-i \int_{t_0}^{t_1} dt_2 \hat{H}^0} \left(1 - i \int_{t_0}^{t_1} dt_2 \int d\mathbf{r}_2\ \hat{\rho}(\mathbf{r}_2)\ V_{\text{ext}}(\mathbf{r}_2, t_2) + \mathcal{O}(V_{\text{ext}}^2) \right). \tag{2.17}$$

The leading term of this expansion would recover the equilibrium density, $\langle \hat{\rho}_H(\mathbf{r}_1, t_1) \rangle^0$, in Eq. 2.15 (the superscript indicates that the expectation value does not include the effect of the perturbation V_{ext}). Since we are interested in the linear response of the system, we only consider terms up to first order in V_{ext} and replace this expansion in Eqs. 2.15 and 2.16. In this process, a dynamical retarded correlation function between the two instances

of the density operator is formed,

$$-iC^R_{\rho\rho}(\mathbf{r}_1,t_1,\mathbf{r}_2,t_2) = -i\Theta(t_1-t_2)\langle[\hat{\rho}_H(\mathbf{r}_1,t_1),\hat{\rho}_H(\mathbf{r}_2,t_2)]_-\rangle \equiv \chi^{(1)}_{\rho\rho}(\mathbf{r}_1,t_1,\mathbf{r}_2,t_2), \quad (2.18)$$

where Θ is the Heaviside function. Defining the first order density-density response function, $\chi^{(1)}_{\rho\rho}$, as in Eq. 2.18, we arrive at the change in the electron density to first order in the external perturbation,

$$\delta\rho(\mathbf{r}_1,t_1) \equiv \langle\hat{\rho}_H(\mathbf{r}_1,t_1)\rangle - \langle\hat{\rho}_H(\mathbf{r}_1,t_1)\rangle^0 = \int dt_2 d\mathbf{r}_2\, \chi^{(1)}(\mathbf{r}_1,t_1,\mathbf{r}_2,t_2)\, V_{\text{ext}}(\mathbf{r}_2,t_2), \quad (2.19)$$

where we eliminated the $\rho\rho$ subscript as we only work with density-density response functions in this thesis. Moreover, in the MBPT literature, this response function is referred to as the reducible polarisability, χ^{red}. We will use this nomenclature for the rest of Section 2.2 (we eliminate the superscript indicating first order as it should be clear from context).

We now calculate the total potential inside the material as the sum of the external and induced potentials. We suppose the latter is created by the induced density of Eq. 2.19 through the Coulomb interaction,

$$\begin{aligned}\delta V_{\text{tot}}(\mathbf{r}_1,t_1) &= V_{\text{ext}}(\mathbf{r}_1,t_1) + \int dt_3 d\mathbf{r}_3\, v_{\text{Co}}(\mathbf{r}_1,t_1,\mathbf{r}_3,t_3)\delta\rho(\mathbf{r}_3,t_3) \\ &= V_{\text{ext}}(\mathbf{r}_1,t_1) + \int dt_3 d\mathbf{r}_3 \int dt_2 d\mathbf{r}_2\, v_{\text{Co}}(\mathbf{r}_1,t_1,\mathbf{r}_3,t_3)\chi^{red}(\mathbf{r}_3,t_3,\mathbf{r}_2,t_2)V_{\text{ext}}(\mathbf{r}_2,t_2).\end{aligned} \quad (2.20)$$

We then re-write Eq. 2.20 as,

$$\delta V_{\text{tot}}(\mathbf{r}_1,t_1) = \int dt_2 d\mathbf{r}_2\, \varepsilon^{-1}(\mathbf{r}_1,\mathbf{r}_2,t_1-t_2)V_{\text{ext}}(\mathbf{r}_2,t_2), \quad (2.21)$$

with the inverse dielectric function defined as,

$$\varepsilon^{-1}(\mathbf{r}_1, \mathbf{r}_2, t_1 - t_2) = \delta(\mathbf{r}_2 - \mathbf{r}_1)\delta(t_1 - t_2) + \int d\mathbf{r}_3 \; v_{\mathrm{Co}}(\mathbf{r}_1, \mathbf{r}_3)\chi^{red}(\mathbf{r}_3, \mathbf{r}_2, t_3 - t_2)\delta(t_3 - t_1). \tag{2.22}$$

We can write this magnitude in frequency space as,

$$\varepsilon^{-1}(\mathbf{r}_1, \mathbf{r}_2; \omega) = \delta(\mathbf{r}_2 - \mathbf{r}_1) + \int d\mathbf{r}_3 \; v_{\mathrm{Co}}(\mathbf{r}_1, \mathbf{r}_3)\chi^{red}(\mathbf{r}_3, \mathbf{r}_2; \omega), \tag{2.23}$$

thus making its energy dependence explicit. In addition, if the system presents translational invariance, we can express the inverse dielectric function in **G**-space,

$$\varepsilon^{-1}_{\mathbf{G},\mathbf{G}'}(\mathbf{q}, \omega) = \delta_{\mathbf{G},\mathbf{G}'} + v_{\mathrm{Co}}(\mathbf{q} + \mathbf{G})\chi^{red}_{\mathbf{G},\mathbf{G}'}(\mathbf{q}, \omega), \tag{2.24}$$

where $\mathbf{q}$ represents the transferred momentum.

Micro-macro connection

In order to transition from the microscopic quantities obtained *via* linear response to macroscopic properties that one can associate with experiments, the former should be averaged over the spatial variables. To this end, the macroscopic dielectric function is defined as the reciprocal of the long-wavelength part of the inverse dielectric function [69, 70],

$$\varepsilon_{\mathrm{M}}(\mathbf{q}, \omega) \equiv \frac{1}{\varepsilon^{-1}_{\mathbf{G}=0,\mathbf{G}'=0}(\mathbf{q}, \omega)}. \tag{2.25}$$

In particular, the imaginary part of the macroscopic dielectric function in the limit $\mathbf{q} \to 0$ represents optical absorption, since the momentum of the incoming photon in the energy range studied in absorption spectroscopies is negligible.

It is insightful to formulate an expression analogous to Eq. 2.23 but for the dielectric

function instead of its inverse,

$$\varepsilon(\mathbf{r}_1, \mathbf{r}_2; \omega) = \delta(\mathbf{r}_2 - \mathbf{r}_1) - \int d\mathbf{r}_3 \; v_{\mathrm{Co}}(\mathbf{r}_1, \mathbf{r}_3)\chi^{irr}(\mathbf{r}_3, \mathbf{r}_2; \omega). \tag{2.26}$$

Eq. 2.26 contains the so-called irreducible polarisability, χ^{irr}, which is related to χ^{red} *via* a Dyson-like equation,

$$\chi^{red}(\mathbf{r}_1, \mathbf{r}_2; \omega) = \chi^{irr}(\mathbf{r}_1, \mathbf{r}_2; \omega) + \int d\mathbf{r}_3 \int d\mathbf{r}_4 \; \chi^{irr}(\mathbf{r}_1, \mathbf{r}_4; \omega) v_{\mathrm{Co}}(\mathbf{r}_4, \mathbf{r}_3)\chi^{red}(\mathbf{r}_3, \mathbf{r}_2; \omega). \tag{2.27}$$

Then, if χ^{irr} was available in some approximation (see Section 2.2.2), one should perform a matrix inversion to solve Eq. 2.27 for χ^{red} before obtaining ε_{M} from Eqs. 2.23 and 2.25. Alternatively, one could think of simply evaluating Eq. 2.26 and taking the head of the dielectric matrix in reciprocal space, $\varepsilon_{0,0}(\mathbf{q}, \omega)$, in order to obtain ε_{M} without any matrix inversion. However, this procedure would not be correct in general since the averaging procedure has to be done over ε^{-1} and not ε. In order to understand this, we can apply spatial averages on both sides of $V_{\mathrm{tot}} = \varepsilon^{-1} V_{\mathrm{ext}}$ and realise that V_{ext} could be taken out of the average as it is a slowly varying potential. The same argument would not be true on $V_{\mathrm{ext}} = \varepsilon V_{\mathrm{tot}}$, since V_{tot} presents fluctuations in the inter-atomic scale, and we could only obtain an average of the product $\varepsilon V_{\mathrm{tot}}$. In fact, it is precisely these microscopic variations of V_{tot} that we are concerned with in this section, the so-called local field effects. More formally, the fact that all matrix elements of $\varepsilon_{\mathbf{G},\mathbf{G}'}$ contribute to the head of the inverse dielectric function, $\varepsilon^{-1}_{0,0}$, through a matrix inversion reflects the local field effects and stems from the inhomogeneities of the system. In an homogeneous system, all quantities would depend on the distance $|\mathbf{r}_1 - \mathbf{r}_2|$ rather than explicitly on $\mathbf{r}_1$ and $\mathbf{r}_2$. This would result in the dielectric function being a diagonal matrix reciprocal space, in which case Eq. 2.25 would reduce to simply $\varepsilon_{\mathrm{M}}(\mathbf{q}, \omega) = \varepsilon_{\mathbf{G}=0,\mathbf{G}'=0}(\mathbf{q}, \omega)$, i.e., only a single matrix element would need to be computed.

Given the computational incentives of potentially avoiding a matrix inversion in **G**-space

or requiring only one matrix element, it would be useful to find an expression for ε_{M} with the mathematical structure of the homogeneous case. This can be achieved by defining an interacting polarisability [38],

$$\overline{\chi} = \chi^{irr} + \chi^{irr}\ \overline{v_{\mathrm{Co}}}\ \overline{\chi}, \tag{2.28}$$

where the integrals of Eq. 2.27 are implied. In Eq. 2.28, a modified Coulomb potential, $\overline{v_{\mathrm{Co}}}$, was defined as being equal to the regular Coulomb potential, v_{Co}, except for the long-range component ($\mathbf{q} + \mathbf{G} = 0$), which is set to zero. With these definitions, the macroscopic dielectric function can be calculated as,

$$\varepsilon_{\mathrm{M}}(\mathbf{q},\omega) = 1 - v_{\mathrm{Co}\mathbf{G}=0}(\mathbf{q})\ \overline{\chi}_{\mathbf{G}=0,\mathbf{G'}=0}(\mathbf{q},\omega) \tag{2.29}$$

which will be useful in solving the Bethe-Salpeter equation (See Section 2.2.2).

2.2.2 Many-body perturbation theory

We now turn to MBPT [4] in order to find suitable approximations for the calculation of the response functions introduced in Section 2.2.1. This vast formalism has been discussed at length in several reviews [38, 40, 41, 67] and textbooks [39, 68, 71]. In this section, we only present a brief account of some aspects of MBPT based on their relevance for the present thesis.

A central quantity in this framework is given by the propagators, which are defined as the probability amplitude of finding an electron at $\mathbf{r}_2$ and t_2 having created an electron at $\mathbf{r}_1$ and t_1 (this would represent a one-particle propagator). If an independent particle Hamiltonian is considered, it can be proven that the independent-particle retarded propagator is the Green's function (i.e., mathematically, the resolvent) of the corresponding Schrödinger

[4] Much of this thesis revolves around the comparison between perturbative and non-perturbative approaches for the calculation of optical properties. In this context, the term 'perturbative' refers to the external electric field applied in spectroscopic measurements, and this is how it should be interpreted within this thesis. As an exception, we clarify that what is treated perturbatively in the MBPT framework is the electron-electron interaction.

equation,

$$[i\partial_{t_2} - \hat{H}^0(\mathbf{r}_2)]\, G^0(\mathbf{r}_1, t_1, \mathbf{r}_2, t_2) = i\delta(\mathbf{r}_1 - \mathbf{r}_2)\delta(t_1 - t_2). \tag{2.30}$$

For this reason, these propagators are normally referred to as Green's functions in electronic structure theory, be it at the independent particle level or beyond. These Green's functions carry important information about a given system of interacting electrons, e.g., charge density, electron addition or removal energies, etc, and are a much simpler object to work with compared to any approximation to a many-body wavefunction.

In trying to obtain an expression for a one-particle propagator, one usually resorts to its equation of motion (EOM). However, it can be shown that said equation will contain a two-particle Green's function. If one tries to find the latter writing its EOM, four-particle Green's functions will appear in the expressions. With the exception of some particular cases, this usually goes on indefinitely, i.e., the EOMs for the Green's functions do not *close*. This is normally referred to as a hierarchy of Green's functions. An approach to deal with this issue implies forcing the EOM of the one-particle Green's function to close by expressing the two-particle Green's function as a functional derivative of the former respect to an external perturbation. As a result, the self-energy operator is introduced, i.e., a non-local frequency-dependent one-particle operator that holds information of all higher-order Green's functions. This technique eventually leads to a *closed* set of five coupled integral equations known as the Hedin equations [72],

$$G(1,2) = G^0(1,2) + G^0(1,\bar{3})\Sigma_{\text{xc}}(\bar{3},\bar{4})G(\bar{4},2), \tag{2.31}$$

$$\widetilde{\Gamma}(1,2,3) = \delta(1,2)\delta(1,3) + \frac{\delta\Sigma_{\text{xc}}(1,2)}{\delta G(\bar{4},\bar{5})}\, G(\bar{4},\bar{6})G(\bar{7},\bar{5})\widetilde{\Gamma}(\bar{6},\bar{7},3), \tag{2.32}$$

$$\chi^{irr}(1,2) = -iG(1,\bar{3})G(\bar{4},1)\widetilde{\Gamma}(\bar{4},\bar{3},2), \tag{2.33}$$

$$W_{\text{Co}}(1,2) = v_{\text{Co}}(1,2) + v_{\text{Co}}(1,\bar{3})\chi^{irr}(\bar{3},\bar{4})W_{\text{Co}}(\bar{4},2), \tag{2.34}$$

$$\Sigma_{\text{xc}}(1,2) = iG(1,\bar{4})W_{\text{Co}}(1^+,\bar{3})\widetilde{\Gamma}(\bar{4},2,\bar{3}), \tag{2.35}$$

where the bar over a numeric coordinate denotes integration. Eq. 2.31 is the Dyson equation for the interacting one-particle propagator. The kernel of this equation is the above-mentioned self-energy, which can be seen as a dynamical non-local exchange-correlation potential acting on an excited electron or hole. Eq. 2.32 provides an expression for the vertex function, which represents the interaction between an electron and a hole. Indeed, in Eq. 2.33 for the polarisability, the vertex function modulates a product of said propagators which, on its own, would represent a non-interacting electron-hole pair (each Green's function in Eq. 2.33 represents a particle or a hole, depending on the time indexes). In Eq. 2.34, an expression for the screened Coulomb potential is given along the lines of the results found in Eqs. 2.13 and 2.14. Finally, the self-energy can be calculated with Eq. 2.35 as a function of already known quantities and fed into Eq. 2.31 to continue cycling through this set of equations.

The Hedin equations constitute a central result of MBPT that allows one to calculate the one-particle propagator of an interacting system including dynamical screening effects *via* the self-energy. The self-consistent solution of this set of equations is a formidable task and rarely pursued, not least because it has to be done analytically, rather than numerically. Nonetheless, part of the success behind the Hedin equations lies on including all the relevant physical effects explicitly in such way that even the strongest approximation, i.e., no self-consistency at all, leads to useful results (e.g., electron energy loss spectra at the RPA level or quasi-particle energies *via* the G_0W_0 scheme).

Random-phase approximation

In the context of MBPT, the random-phase approximation (RPA) implies calculating the inverse screening matrix, $\varepsilon^{-1}_{\mathrm{RPA}}$, with less than one cycle through Hedin's equations. We start by taking some approximation for the one-particle propagator, G^0. In this thesis, we will use the DFT ground state to formulate a non-interacting one-particle propagator, as it is

often the case elsewhere in the literature. We achieve so using the Lehmann representation,

$$G^0(\mathbf{r}_1, \mathbf{r}_2, \omega) = \sum_i \frac{\phi_i^{\mathrm{KS}}(\mathbf{r}_1)\, \phi_i^{\mathrm{KS}*}(\mathbf{r}_2)}{\omega - E_i^{\mathrm{KS}} + i\nu_i}, \tag{2.36}$$

where ν_μ is a real infinitesimal that takes a negative or positive value for occupied or unoccupied states, respectively. This means that the non-interacting propagator, G^0, can be readily calculated once the KS energies and wavefunctions are known, following the solution of the KS eigenproblem (see Eq. 2.5). Next, we enter Hedin's scheme in Eq. 2.31 with G^0 and assuming $\Sigma_{\mathrm{xc}} = 0$, thus obtaining $G \approx G^0$. This also results in neglecting the vertex corrections, i.e., $\widetilde{\Gamma} = 1$ after evaluating Eq. 2.32. Then, Eq. 2.33 is simplified to,

$$\chi^{\mathrm{irr}}(1, 2) = -iG^0(1, 2)G^0(2^+, 1). \tag{2.37}$$

Using Eq. 2.36 in Eq. 2.37, we obtain

$$\chi^{\mathrm{irr}}(\mathbf{r}_1, \mathbf{r}_2, \omega) = \sum_{i,j} (f_j - f_i) \frac{\phi_j^{\mathrm{KS}*}(\mathbf{r}_1)\, \phi_i^{\mathrm{KS}}(\mathbf{r}_1)\, \phi_i^{\mathrm{KS}*}(\mathbf{r}_2)\, \phi_j^{\mathrm{KS}}(\mathbf{r}_2)}{\omega - (E_j^{\mathrm{KS}} - E_i^{\mathrm{KS}}) + i\nu}, \tag{2.38}$$

where f_i represent occupation factors and ν is a positive real infinitesimal. With this irreducible polarisability, one can solve the Dyson-like Eq. 2.27 for χ^{red} and the calculate the inverse dielectric function at the RPA level evaluating Eq. 2.23.

It is interesting to note that a perturbative first-order scheme derived from the TD-DFT formalism arrives at a similar result [73]. Identifying the response function with the functional derivative of the electron density respect to the external potential, one obtains a Dyson-like equation,

$$\chi^{\text{TD-DFT}} = \chi^{\mathrm{KS}} + \chi^{\mathrm{KS}}[v_{\mathrm{Co}} + f_{\mathrm{XC}}]\chi^{\text{TD-DFT}}, \tag{2.39}$$

where the integrals are implied and the so-called exchange correlation kernel is defined as,

$$f_{\mathrm{XC}}(\mathbf{r}_1, \mathbf{r}_2) = \delta(\mathbf{r}_2 - \mathbf{r}_1) \frac{\delta v_{\mathrm{XC}}(\rho(\mathbf{r}_1), \mathbf{r}_1)}{\delta \rho(\mathbf{r}_1)}. \tag{2.40}$$

In Eq. 2.39, χ^{KS} can be calculated with the KS wavefunctions and energies as shown in Eq. 2.38. Then, if one neglects f_{XC} in Eq. 2.39, the RPA polarisability is recovered. Finally, ignoring the local field effects, v_{Co}, either in TD-DFT (Eq. 2.39) or in the RPA (Eq. 2.27) results in what we call the independent-particle response, $\varepsilon^{-1}_{\mathrm{IPA}}$.

In general, the RPA fails to reproduce absorption spectra, often even qualitatively, due to a poor description of excitonic effects. This is because the polarisability is calculated in terms of a non-interacting electron-hole pair, since the vertex function has been ignored (see the product of propagators in Eq. 2.37). TD-DFT improves upon the RPA by including exchange and correlation effects *via* the kernel in Eq. 2.39. However, despite this being formally correct, currently available functionals for f_{XC} usually fail to compute absorption spectra of extended systems in agreement with experiments. Overall, the description of excitons and the interactions between the electron and the hole are crucial for the quality of theoretical optical spectra, particularly in semiconductors and insulators [64–66]. One can account for these effects by computing the vertex corrections in a second iteration through Hedin's equations (see Eq. 2.35). This formulation introduces a two-particle propagator for the electron-hole pair and a Dyson-like equation to obtain it, which is in fact the Bethe-Salpeter equation.

Bethe-Salpeter Equation

In order to avoid a matrix inversion in **G**-space, we will use the interacting polarisability defined in Eq. 2.28, $\overline{\chi}$, which allows us to take the $\mathbf{q} \to 0$ limit directly on the dielectric

function (see Eq. 2.29). This interacting polarisation is obtained as,

$$\lim_{\mathbf{q}\to 0} \bar{\chi}_{\mathbf{G}=0,\mathbf{G}'=0}(\mathbf{q},\omega) = -i \lim_{\mathbf{q}\to 0} \sum_{nm\mathbf{k}} \sum_{n'm'\mathbf{k}'} [\Lambda^*_{nm\mathbf{k}}(\mathbf{q},\mathbf{G}=0)\Lambda_{n'm'\mathbf{k}'}(\mathbf{q},\mathbf{G}'=0)]\ \bar{L}_{\substack{nm\mathbf{k}\\ n'm'\mathbf{k}'}}(\omega), \tag{2.41}$$

which is analogous to Eq. 2.37 but replaces the product of one-particle propagators with a single two-particle propagator. This electron-hole (e-h) two-particle Green's function, $\bar{L}_{\substack{nm\mathbf{k}\\ n'm'\mathbf{k}'}}(\omega)$, is a key quantity in the BSE scheme as it describes the dynamics of an exciton. We express this Green's function in e-h space, i.e., a basis comprising all vertical transitions at every **k**-point in the BZ between an occupied band v and an empty band c, $\{vc\mathbf{k}\}$. Eq. 2.41 implies a change of basis from e-h space to **G**-space, from which the oscillator strengths emerge,

$$\Lambda_{nm\mathbf{k}}(\mathbf{q},\mathbf{G}) = \langle n\mathbf{k}|e^{i(\mathbf{q}+\mathbf{G})\cdot\mathbf{r}}|m\mathbf{k}-\mathbf{q}\rangle. \tag{2.42}$$

The Bethe-Salpeter equation is then a Dyson-like equation for $\bar{L}$,

$$\bar{L}_{\substack{nm\mathbf{k}\\ n'm'\mathbf{k}'}}(\omega) = L^0_{nm\mathbf{k}}(\omega)[\delta_{nn'}\delta_{mm'}\delta_{\mathbf{k}\mathbf{k}'} + i\sum_{vc\mathbf{k_1}} \Xi_{\substack{nm\mathbf{k}\\ vc\mathbf{k_1}}}(\omega)\bar{L}_{\substack{vc\mathbf{k_1}\\ n'm'\mathbf{k}'}}(\omega)], \tag{2.43}$$

where the matrix Ξ is the so-called BSE kernel,

$$\Xi_{\substack{nm\mathbf{k}\\ vc\mathbf{k_1}}} = W_{\substack{nm\mathbf{k}\\ vc\mathbf{k_1}}} - 2\bar{V}_{\substack{nm\mathbf{k}\\ vc\mathbf{k_1}}}. \tag{2.44}$$

The first contribution to the BSE kernel is the e-h attraction,

$$W_{\substack{nm\mathbf{k}\\ vc\mathbf{k_1}}} = \sum_{\mathbf{G},\mathbf{G}'} \Lambda_{nv\mathbf{k}}(\mathbf{q}=\mathbf{k}-\mathbf{k_1},\mathbf{G})\Lambda^*_{mc\mathbf{k_1}}(\mathbf{q}=\mathbf{k}-\mathbf{k_1},\mathbf{G}')\ \varepsilon^{-1}_{\mathbf{G},\mathbf{G}'}(\mathbf{q},\omega=0)\ v_{\mathrm{Co}}(\mathbf{q}+\mathbf{G}'), \tag{2.45}$$

where the inverse dielectric matrix is calculated at the RPA level and, usually, in the static limit, $\omega = 0$. This term represents the statically screened interaction between the electron

and the hole within an exciton. The second term is the e-h exchange,

$$\bar{V}_{\substack{nm\mathbf{k}\\vc\mathbf{k_1}}} = \sum_{\mathbf{G}\neq\mathbf{0}} \Lambda_{nm\mathbf{k}}(\mathbf{q}=0,\mathbf{G})\Lambda^{*}_{vc\mathbf{k_1}}(\mathbf{q}=0,\mathbf{G})\; v_{\mathrm{Co}}(\mathbf{G}), \tag{2.46}$$

which depends on the bare Coulomb interaction.

In order to compute excitonic spectra at the BSE level, one option is then to solve the Dyson-like Eq. 2.43 for $\bar{L}$. However, this requires an inversion of the BSE kernel, which can be prohibitively costly for systems with many electrons that require several unoccupied states for convergence and dense sampling of the BZ. Alternatively, the problem can be re-cast as a two-particle Hamiltonian in e-h space [38],

$$H^{2p}_{\substack{nm\mathbf{k}\\n'm'\mathbf{k}'}} = E_{nm\mathbf{k}}\;\delta_{nn'}\delta_{mm'}\delta_{\mathbf{k}\mathbf{k}'} + \;(f_{n\mathbf{k}} - f_{m\mathbf{k}})\;\Xi_{\substack{nm\mathbf{k}\\n'm'\mathbf{k}'}}, \tag{2.47}$$

where $E_{nm\mathbf{k}}$ is the energy of the vertical transition from band n to band m at point $\mathbf{k}$ according to either the KS or quasi-particle (QP) energies. The definition of H^{2p} in Eq. 2.47 allows us to express the two-particle Green's function as,

$$\bar{L}_{\substack{nm\mathbf{k}\\n'm'\mathbf{k}'}}(\omega) = [H^{2p} - I\omega]^{-1}_{\substack{nm\mathbf{k}\\n'm'\mathbf{k}'}}(f_{m\mathbf{k}} - f_{n\mathbf{k}}), \tag{2.48}$$

where I is the identity matrix. Replacing Eq. 2.48 in Eqs. 2.41 and 2.29 leads to,

$$\varepsilon_{\mathrm{M}}(\omega) = 1 - \lim_{\mathbf{q}\to 0}\frac{4\pi}{|\mathbf{q}|^2}\sum_{nm\mathbf{k}}\sum_{n'm'\mathbf{k}'}\Lambda^{*}_{nm\mathbf{k}}(\mathbf{q},0)\Lambda_{n'm'\mathbf{k}'}(\mathbf{q},0)\;[H^{2p} - I\omega]^{-1}_{\substack{nm\mathbf{k}\\n'm'\mathbf{k}'}}. \tag{2.49}$$

We seek to express the matrix $[H^{2p} - I\omega]^{-1}_{\substack{nm\mathbf{k}\\n'm'\mathbf{k}'}}$ in its spectral representation, for which we need to solve the eigenproblem,

$$H^{2p}_{\substack{nm\mathbf{k}\\n'm'\mathbf{k}'}} A^{n'm'\mathbf{k}'}_{\lambda} = E_{\lambda}\; A^{nm\mathbf{k}}_{\lambda}, \tag{2.50}$$

thus obtaining the excitonic energies, E_{λ}, and wavefunctions, $A^{n'm'\mathbf{k}'}_{\lambda}$. We therefore arrive

at an expression for the calculation of optical spectra at the BSE level,

$$\varepsilon_{\mathrm{M}}(\omega) = 1 - \lim_{\mathbf{q}\to 0} \frac{4\pi}{|\mathbf{q}|^2} \sum_{nm\mathbf{k}} \sum_{n'm'\mathbf{k}'} [\Lambda^*_{nm\mathbf{k}}(\mathbf{q},0)\Lambda_{n'm'\mathbf{k}'}(\mathbf{q},0)] \sum_{\lambda} \frac{A^{nm\mathbf{k}}_{\lambda}[A^{n'm'\mathbf{k}'}_{\lambda}]^*}{\omega - E_{\lambda}}. \tag{2.51}$$

However, computing spectra with Eq. 2.51 requires the diagonalisation of H^{2p} (see Eq. 2.50), which can become prohibitively costly as the size of the e-h space increases.

Haydock solution of the BSE

Apart from the above-mentioned inversion and full diagonalisation approaches for solving the BSE, Lanczos-based methods [74] offer a cost-effective alternative for sparse matrices [75]. Lanczos approaches eliminate the need for inverting the BSE kernel or fully diagonalising the two-particle Hamiltonian. Rather, the latter is re-expressed as a tridiagonal matrix based on recursive relations, which leads to an iterative solution of the problem that is computationally cheaper than full diagonalisation. While previously described solvers produce the full set of both excitonic energies and wavefunctions of the system at hand, Lanczos schemes lead to a partial solution of the problem, e.g., it may only provide the eigenvalues. In particular, Haydock's implementation [76] of the Lanczos approach can only provide matrix elements of the resolvent of the eigenproblem in Eq. 2.50), $\langle V_0|(H^{2p} - I\omega)^{-1}|V_0\rangle$, in a given initial (normalised) state, $|V_0\rangle$. Defining the latter as $|V_0\rangle = \frac{|P\rangle}{\|P\|}$ with,

$$|P\rangle = \lim_{\mathbf{q}\to 0} \frac{1}{|\mathbf{q}|} \sum_{nm\mathbf{k}} \Lambda^*_{nm\mathbf{k}}(\mathbf{q}, \mathbf{G}=0)\ |nm\mathbf{k}\rangle, \tag{2.52}$$

allows us to re-write the macroscopic dielectric function in Eq. 2.49 simply as,

$$\varepsilon_{\mathrm{M}}(\omega) = 1 - 4\pi\|P\|^2\ \langle V_0|(H^{2p} - I\omega)^{-1}|V_0\rangle, \tag{2.53}$$

and make use of this resolvent. Therefore, Haydock's algorithm can provide the optical spectrum, but not the excitonic wavefunctions [65, 76, 77]. Haydock's scheme [76] is based on mapping a stationary quantum problem into a semi-infinite chain model consisting of

basis states $|V_{it}\rangle$, which we call Haydock vectors. The subscript it stands for iteration and highlights the fact that these states are obtained recursively. In this basis, the Hamiltonian of the problem is a tri-diagonal matrix described by the coefficients a_{it} and b_{it}. Haydock then provides a set of recursive relations to compute these coefficients and basis vectors iteratively starting from $|V_0\rangle$,

$$a_{it} = \langle V_{it}|H^{2p}|V_{it}\rangle, \tag{2.54}$$

$$b_{it+1} = \|(H^{2p} - a_{it})|V_{it}\rangle - b_{it}|V_{it-1}\rangle\|, \tag{2.55}$$

$$|V_{it+1}\rangle = \frac{1}{b_{it+1}}[(H^{2p} - a_{it})|V_{it}\rangle - b_{it}|V_{it-1}\rangle]. \tag{2.56}$$

Eqs. 2.54-2.56 correspond to Hermitian Hamiltonians (the pseudo-Hermitian case has a slightly more complicated form [78]). Finally, Haydock's algorithm provides a recipe for the calculation of the resolvent matrix element in the form of a continued fraction of the Hamiltonian coefficients, a_{it} and b_{it}. We can then use this continued fraction to calculate the optical spectrum at each iteration it according to,

$$\epsilon_M^{(it)}(\omega) = 1 - \|P\|^2 \frac{1}{(\omega - a_1) - \frac{b_2^2}{(\omega - a_2) - \frac{b_3^2}{\cdots}}}, \tag{2.57}$$

until the difference between spectra of successive iterations is below an acceptable threshold. We note that the number of denominators in the continued fraction of Eq. 2.57 is determined by the iteration, e.g., the dielectric function at the tenth iteration, $\epsilon_M^{(10)}(\omega)$, is calculated with coefficients up to a_{10} and b_{10}.

Despite the numerical advantages offered by Lanczos solvers, a given system could still be too big for computing optical spectra at the BSE level. As the diagonalisation itself ceases to be a problem with Lanczos schemes, the bottleneck now shifts to the previous step of computing and storing the BSE kernel, which can render the calculation impracticable depending on the size of the e-h basis. For instance, a material with 10 bands that requires a 30×30×30 **k**-grid would imply a (resonant) BSE kernel matrix of dimension 675000, thus

requiring a few TB of memory. While this may be covered by some state-of-the-art high-memory nodes, it is quite close to the limits of today's supercomputers. Any increase in the size of the system could easily become prohibitive, e.g., duplicating the number of bands to include spin-orbit coupling or requiring a supercell. At this point, there is little alternative for solving the BSE and computing optical spectra, which is the challenge we intend to tackle in Chapter 3. We attempt to do so by proposing double-grid approach to **k**-sampling compatible with Haydock's solution of the BSE. Our method prioritises simplicity and distinguishes from previous double-grid approaches (see brief review below) by requiring minimal extra computation and memory.

Double k-grid strategies for BZ sampling

A crucial point in the efficiency of BSE calculations lies in the dense **k**-grids required to achieve an accurate description of excitons. This is because excitonic wavefunctions are usually quite spread out, with a periodicity well beyond the unit cell, and in order to expand them in a basis of transitions $\{vc\mathbf{k}\}$, very dense **k**-grids are required. The computational requirements imposed by **k**-sampling then represent a major bottleneck in the BSE scheme. Therefore, the introduction of alternative numerical methods and approximations that can effectively deal with **k**-point convergence in the BSE is of utmost importance.

This issue has been the target of many research efforts over the years, usually approached with the use of double **k**-grids. Rohlfing *et al.* introduced a scheme to interpolate the BSE matrix in the BZ [66, 79]. Their strategy is based on a double grid approach by which the kernel matrix elements are properly calculated on a coarse **k**-grid and approximated on a fine **k**-grid. As a function of **q**, the **k**-point difference between two transitions in e-h space, the BSE kernel is sharply peaked at the origin and a regular interpolation in the BZ would fail. However, expressing these matrix elements as $a\mathbf{q}^{-2} + b\mathbf{q}^{-1} + c$ results in the coefficients varying slowly in the BZ. These coefficients are then interpolated by virtue of knowing them exactly in the coarse **k**-grid. Their approximation also considers the varying phases of the single-particle states in the BZ, which requires knowledge of the wavefunctions in the fine

k-grid. This crucial point becomes a drawback when one is limited by memory and disk storage rather than computation, which is increasingly the case nowadays.

More recently, Fuchs *et al.* proposed the use of hybrid **k**-meshes in the form of a coarse **k**-grid for the whole BZ and a denser **k**-grid around the Γ-point [80]. Even though the kernel matrix elements are properly calculated on both grids, this method allows to refine **k**-sampling only where is needed, resulting in fewer **k**-points in total. The downside of using non-uniform grids becomes apparent in the calculation of the electron-hole attraction term of the BSE kernel, since it requires knowledge of the screening matrix, $\varepsilon^{-1}(\mathbf{q}, 0)$, at $\mathbf{q} = \mathbf{k} - \mathbf{k}'$ (see Eq. 2.45). If $\mathbf{k}$ and $\mathbf{k}'$ are part of a non-uniform grid, $\mathbf{q}$ will likely not belong to this grid. This poses no complication for model dielectric functions, as is the case in Ref. [80]. However, if one intends to use the RPA screening, non-uniform grids require computation of the screening matrix at many more **q**-points than if a uniform grid had been used (or at least an interpolation).

Kammerlander *et al.* applied double grid techniques to solving the BSE by inversion [81]. In the latter, the BSE kernel is calculated on the coarse **k**-grid while the fine **k**-grid is used to compute the independent particle part of the two-particle response function. This technique, which also benefits from Wannier interpolation of the KS wavefunctions, has proven successful in accurately reproducing the spectra of several materials. However, as it ultimately relies on matrix inversion, its application is limited to *small* systems, i.e., systems which could be computed by the inversion solver in the coarse grid, albeit underconverged.

Finally, an interesting generalisation of the method in Ref. [66] has been proposed by Gillet *et al.* [82], where the interpolation of the BSE kernel matrix element at a given fine-grid **k**-point considers eight coarse-grid **k**-points around it. Importantly, this method is compatible with Haydock's solution scheme to the BSE. Moreover, substantial savings in memory requirements and disk storage are achieved by interpolating kernel matrix elements on the fly. Nevertheless, this method still requires knowledge of the KS wavefunctions in the fine grid. Depending on the number of bands and density of the fine grid, this can entail prohibitive memory requirements.

2.3 Non-linear optics

We now focus on the study of response functions beyond the linear regime, i.e., $\chi^{(n)}$ with $n > 1$. High-harmonic generation (HHG) phenomena can reach orders of around a few tens and beyond, which requires real-time non-perturbative methods for its theoretical description. On the opposite end of the nonlinear regime, we find second and third harmonic generation (SHG and THG), i.e., $n = 2 - 3$. In this area of nonlinear optics, and for $\chi^{(2)}$ in particular, there may still be an argument for perturbative approaches as an alternative to real-time, non-perturbative formalisms. Therefore, both perturbative and non-perturbative methods are available in the literature (see below). However, the latter are usually preferred over perturbative approaches due to their relative simplicity, especially when electron-electron correlation is included.

As far as nonlinear optics is concerned, this thesis focuses on SHG and, to a lesser extent, THG (See Chapters 4-6). We note that the three approximations stated at the beginning of Section 2.2 are still used in our study of the nonlinear regime.

2.3.1 Perturbative vs non-perturbative approaches

Perturbative approaches are often extensions of frameworks that proved successful for linear optics. For instance, Sipe *et al.* presented a scheme for the calculation of nonlinear optical response of semiconductors at the IPA level and derived expressions for the second order susceptibility, $\chi^{(2)}$ [83]. A study by Dal Corso *et al.* introduced a Sternheimer approach for the second order response of insulators based on the TD-DFT action functional within the LDA [84]. Luppi *et al.* derived perturbative expressions for $\chi^{(2)}$ in extended systems from TD-DFT [85]. The latter included excitonic effects by means of a long-range contribution to the exchange-correlation kernel and proved valid for weakly bound excitons [85]. Finally, the inclusion of many-body effects at the BSE level warranted a few attempts up to the second order [86, 87]. Crucially, perturbative approaches require a specific formulation for each order in the response one intends to calculate and their generalisation to higher

orders is not straightforward. Indeed, the resulting expressions for nonlinear susceptibilities become extremely complex with increasing orders in the perturbation and increasing levels of theory as regards correlation.

At variance, non-perturbative approaches involve explicit time propagation and can describe nonlinear phenomena to several orders in the electric field simultaneously, thus offering a convenient workaround to the shortcomings described above. Moreover, they are flexible in the sense that including many-body effects amounts to just adding the relevant operators into the effective Hamiltonian. In these methods, the integration of an EOM allows for the calculation of the dynamical polarisation, from which susceptibilities to any order (in principle) can be extracted. The quantity evolved in the EOMs varies among the different time-propagation methods. For instance, TD-DFT implies the time evolution of the electron density and is typically applied to isolated systems [63,88–91]. Propagating the Green's function was proposed in the so-called Kadanoff-Baym equations (KBE) [92]. A simplification of the KBE using the time-diagonal of said Green's function, i.e., the density matrix, was proposed by Attaccalite, Grüning and Marini [93]. Subsequently, Attaccalite and Grüning proposed a scheme based on evolving the periodic part of the Bloch functions [42]. Crucially, this method is valid for systems with periodic boundary conditions (PBCs) since it is based on the modern theory of polarisation [94–96] and uses the Berry-phase formulation of the dynamical polarisation [97] (see Section 2.3.2). This real-time approach [42] has been successfully applied for the calculation of nonlinear optical properties in extended systems [98–102]. We proceed to describe this real-time method in detail since much of the present thesis focuses on improving it (See Chapters 4-6).

2.3.2 Real-time approach

We consider the Hamiltonian of a crystalline solid coupled to a time-dependent electric field,

$$\hat{\mathcal{H}} = \hat{H}^0 + \hat{H}^{\mathcal{E}}, \tag{2.58}$$

where $\hat{H}^0$ is the zero-field unperturbed Hamiltonian while $\hat{H}^{\mathcal{E}}$ represents the perturbation. We denote the Bloch eigenstates of the cell-periodic unperturbed Hamiltonian, $e^{-i\mathbf{k}\cdot\mathbf{r}}\hat{H}^0 e^{i\mathbf{k}\cdot\mathbf{r}}$, as $\mu_{\mathbf{k}n}(\mathbf{r})$. Then, the wavefunctions $\psi_{\mathbf{k}n}(\mathbf{r}) = e^{i\mathbf{k}\cdot\mathbf{r}}\ \mu_{\mathbf{k}n}(\mathbf{r})$ are the eigenstates of the unperturbed Hamiltonian, $\hat{H}^0$. In what follows, the periodic part of these functions will be referred to as the zero-field time-zero states, $|\mu_{\mathbf{k}n}\rangle$, and will be used as a starting point for time integration or as a basis. In practice, these time-zero states will be defined at the DFT level, i.e., $\psi_{\mathbf{k}n}(\mathbf{r}) \equiv \phi^{\mathrm{KS}}_{\mathbf{k}n}(\mathbf{r})$.

Equation of motion

The real-time approach to nonlinear optics, as referred to within this thesis, was set out by Attaccalite and Grüning [42, 43], and follows the scheme introduced by Souza *et al.* for the dynamical Berry-phase polarisation [97]. The central objects in this formalism are the time-dependent Bloch states, $|v_{\mathbf{k}n}\rangle$, which represent the periodic part of the states, $\psi_{\mathbf{k}n}(\mathbf{r},t) = e^{i\mathbf{k}\cdot\mathbf{r}}\ v_{\mathbf{k}n}(\mathbf{r},t)$. The states $|v_{\mathbf{k}n}\rangle$ are obtained upon time-evolution of the time-zero states, $|\mu_{\mathbf{k}n}\rangle$, according to the EOM,

$$\left(\hat{H}^{\mathrm{eff}}_{\mathbf{k}} - i\partial_t\right)|v_{\mathbf{k}n}\rangle = 0, \tag{2.59}$$

with the boundary condition,

$$|v_{\mathbf{k}n}\rangle(t=0) = |\mu_{\mathbf{k}n}\rangle, \tag{2.60}$$

and the effective Hamiltonian,

$$\hat{H}^{\mathrm{eff}} = \hat{H}^0 + \hat{W}(\mathcal{E}). \tag{2.61}$$

The unperturbed Hamiltonian in Eq. 2.61, $\hat{H}^0$, is a single-particle operator that varies according to the level of theory considered [43,103] while the perturbation, $\hat{W}(\mathcal{E})$, represents the coupling with the external field, $\mathcal{E}$.

The real-time approach is then based on integrating the EOM (Eq. 2.59) numerically,

for which the linearised Crank-Nicolson method is used [42, 97],

$$|v_{\mathbf{k}n}\rangle(t+\Delta t) = \frac{1 - i\Delta t/2\ \hat{H}^{\text{eff}}_{\mathbf{k}}(t)}{1 + i\Delta t/2\ \hat{H}^{\text{eff}}_{\mathbf{k}}(t)}\ |v_{\mathbf{k}n}\rangle(t). \tag{2.62}$$

This is carried out in KS space, thus resulting in several EOMs for the projections, $\langle \mu_{\mathbf{k}i}|v_{\mathbf{k}n}\rangle(t)$. The accuracy and stability of this numerical integration depends on having a short time-step, usually in the order of 1-10 as. The latter parameter is material-dependent and reflects how fast the dynamics of a given system are. Ultimately, having access to the time-dependent Bloch states, $|v_{\mathbf{k}n}\rangle$, will allows us to compute dynamical properties, such as the polarisation as a function of time. From the latter, susceptibilities to any order in the electric field can be extracted (see below).

Levels of theory

Three levels of theory are considered in the real-time approach as regards electron-electron correlation, which manifest in the expressions for the effective Hamiltonian in Eq. 2.61. Let us start by the IPA level [42, 93],

$$\hat{H}^{\text{IPA}} = \underbrace{\hat{H}^{KS}[\rho_0] + \hat{\Delta}_{\text{QP}}[\varrho_0]}_{\hat{H}^{\text{IPA},0}} + \hat{W}(\mathcal{E}), \tag{2.63}$$

where $\hat{H}^{\text{IPA},0}$ represents the corresponding unperturbed Hamiltonian. This includes the KS Hamiltonian, $\hat{H}^{KS}[\rho_0]$, which is a functional of the ground-state density, ρ_0, plus the quasi-particle corrections, $\Delta_{\text{QP}}[\varrho_0]$. The latter could simply reflect a rigid shift (scissor operator) or involve QP corrections obtained from a G_0W_0 scheme, thus formally depending on the ground-state density matrix, ϱ_0. In any case, $H^{\text{IPA},0}$ is a functional of only ground-state quantities and, therefore, time-independent. The time dependence of the effective Hamiltonian at the IPA level is then confined to the electron-field coupling operator, $\hat{W}(\mathcal{E})$.

The first step beyond the IPA level is including the Hartree potential, $\hat{V}^H[\rho]$, in the

effective Hamiltonian [43, 93],

$$\hat{H}^{\mathrm{TDH}} = \hat{H}^{KS}[\rho_0] + \hat{\Delta}_{\mathrm{QP}}[\varrho_0] + \hat{V}^{H}[\rho] + \hat{W}(\mathcal{E}), \tag{2.64}$$

which represents the so-called time-dependent Hartree (TDH) level. The Hartree term is simply the classical Coulomb potential originating from the time-dependent electron density. Its expression can be derived from the Poisson equation in **G**-space,

$$V^{H}[\rho(\mathbf{G},t)] = (\rho(\mathbf{G},t) - \rho_0(\mathbf{G}))\,\frac{4\pi}{|\mathbf{G}|^2}, \tag{2.65}$$

leading to a linear functional of the density, $V^{H}[\rho(\mathbf{G},t)]$, which we will write as $V^{H}(\mathbf{G},t)$ for simplicity. In Eq. 2.65 the $\mathbf{G}$=0 term is omitted for the reasons explained in Section 2.2.1. $V^{H}(\mathbf{G},t)$ represents a local potential that inherits its time dependence from the density. We note that the ground-state Hartree potential is already taken into account at the DFT level (see U_{ee} in Eq. 2.4) and, therefore, included in $\hat{H}^{\mathrm{IPA,0}}$. As a result, the Hartree potential added at the TDH level should represent the difference respect to the ground state contribution. This is achieved by subtracting the ground state density, i.e., $\rho - \rho_0$ in Eq. 2.65, which takes advantage of the linearity of the functional.

Finally, we turn to the inclusion of correlation effects in the real-time approach. In principle, this could be done by adding a time-dependent exchange-correlation functional to Eq. 2.64, thus arriving at the TD-DFT level. However, currently-available approximations to this functional face limitations when attempting to describe excitons in extended systems [38], as explained above. Therefore, we chose to consider correlation effects through the addition of the screened-exchange self-energy, $\Sigma^{\mathrm{SEX}}[\varrho]$, into the effective Hamiltonian [43, 93],

$$\hat{H}^{\mathrm{H+SEX}} = \hat{H}^{KS}[\rho_0] + \hat{\Delta}_{\mathrm{QP}}[\varrho_0] + \hat{V}^{H}[\rho] + \hat{\Sigma}^{\mathrm{SEX}}[\varrho] + \hat{W}(\mathcal{E}), \tag{2.66}$$

as a functional of the density matrix, ϱ. We will refer to this as the Hartree plus screened exchange (H+SEX) level of theory. Formally, this implies taking the static limit of the GW

self-energy to arrive at the Coulomb hole plus screened exchange (COHSEX) self-energy,

$$\Sigma^{\mathrm{COHSEX}} = \underbrace{-1/2\; W_{\mathrm{Co}}(\mathbf{r}_1, \mathbf{r}_2; \varrho)\; \delta(\mathbf{r}_1 - \mathbf{r}_2)}_{\Sigma^{\mathrm{COH}}} + \underbrace{i\; W_{\mathrm{Co}}(\mathbf{r}_1, \mathbf{r}_2; \varrho)\; \varrho(\mathbf{r}_1, \mathbf{r}_2, t)}_{\Sigma^{\mathrm{SEX}}}, \tag{2.67}$$

where the screened Coulomb interaction, W_{Co}, is calculated at the RPA level in the static limit ($\omega = 0$). A further approximation entails neglecting the functional derivative $\frac{\delta W_{\mathrm{Co}}}{\delta \varrho}$, in which case Σ^{COH} becomes time independent [93]. Therefore, the EOM is only concerned with Σ^{SEX} (see Eq. 2.66), provided we remove the initial contribution at time zero. Since Σ^{SEX} is now a linear functional of the density matrix, ϱ, this can be achieved by subtracting the ground state density matrix, ϱ^0, before evaluating said functional. This operator is then obtained in KS space as,

$$\Sigma^{\mathrm{SEX}}_{ii'\mathbf{k}} = \sum_{jj'\mathbf{q}} M^{\mathbf{k}}_{ii'jj'\mathbf{q}}\; (\varrho_{jj'\mathbf{k}-\mathbf{q}}(t) - \varrho^0_{jj'\mathbf{k}-\mathbf{q}}), \tag{2.68}$$

where the Coulomb integrals,

$$M^{\mathbf{k}}_{ii'jj'\mathbf{q}} = \sum_{\mathbf{G},\mathbf{G}'} \Lambda_{ij\mathbf{k}}(\mathbf{q}, \mathbf{G}')\; \Lambda^*_{i'j'\mathbf{k}}(\mathbf{q}, \mathbf{G})\; W_{\mathrm{Co}_{\mathbf{G},\mathbf{G}'}}(\mathbf{q}), \tag{2.69}$$

are pre-computed and stored in a database. As a result, each step in the time evolution requires computing the density matrix, ϱ, and evaluating Eq. 2.68.

Overall, the real-time approach includes electron-electron correlation in a non-perturbative framework, thus allowing for the description of excitonic effects in nonlinear optical phenomena [43]. We note that the TDH and H+SEX levels of theory reduce to the RPA and BSE, respectively, in the linear response limit [93]. Crucially, Eqs. 2.63, 2.64 and 2.66 highlight one of the main advantages of the real-time approach, i.e., the inclusion of many-body effects is as simple as adding terms to the effective Hamiltonian in Eq. 2.59 [43]. This flexibility is in stark contrast with perturbative approaches, where the complexity of the formulations increases dramatically as correlation is added into the formalism (e.g., [83]).

Berry-phase formulation of the electron-field coupling operator

A direct coupling to the electric field in the length gauge, i.e., $-e\mathbf{r}\mathcal{E}$, should be avoided in extended systems since the position operator is ill-defined in the presence of periodic boundary conditions [94–96]. In the linear regime, this is usually circumvented using the commutation relation $[\hat{H}, \hat{\mathbf{r}}] = \hat{\mathbf{p}} + [V_{nl}, \hat{\mathbf{r}}]$, where V_{nl} is the non-local part of the Hamiltonian. However, since the real-time approach is meant to describe nonlinear optical processes, an electron-field coupling operator valid beyond the linear regime is required.

This is achieved by a Berry-phase formulation of the dynamical polarisation, resulting in a dipole operator in the form of a covariant $\mathbf{k}$-derivative that makes its way into the electron-field coupling operator [97],

$$\hat{W}_{\mathbf{k}}(\mathcal{E}) = \hat{w}_{\mathbf{k}}(\mathcal{E}) + \hat{w}^{\dagger}_{\mathbf{k}}(\mathcal{E}). \tag{2.70}$$

In Eq. 2.70, $\hat{w}_{\mathbf{k}}(\mathcal{E})$ is the electron-field coupling operator in its Berry-phase formulation as outlined in Refs. [42] and [97],

$$\hat{w}_{\mathbf{k}}(\mathcal{E}) = i\frac{e}{4\pi}\sum_{\alpha=1}^{3} N_{\alpha}^{\parallel}\left(\mathcal{E}\cdot\mathbf{a}_{\alpha}\right)\sum_{\sigma}\sigma\hat{P}_{\mathbf{k}\mathbf{k}_{\alpha}^{\sigma}}, \tag{2.71}$$

where $\mathbf{a}_{\alpha}$ represents a lattice vector and $N_{\alpha}^{\parallel}$ is the number of $\mathbf{k}$-points along a *string* parallel to the direction of the corresponding reciprocal lattice vector $\mathbf{b}_{\alpha}$. Also, $\sigma = \pm 1$ and $\mathbf{k}_{\alpha}^{\sigma} = \mathbf{k} + \sigma\Delta\mathbf{k}_{\alpha}$, i.e., the *next* $\mathbf{k}$-point in the grid along the direction of $\mathbf{b}_{\alpha}$ (the definition of *next* depends on the sign of σ). The projector operator in Eq. 2.71 has the form,

$$\hat{P}_{\mathbf{k}\mathbf{k}_{\alpha}^{\sigma}} = \sum_{m=1}^{M} |\tilde{v}_{\mathbf{k}_{\alpha}^{\sigma}m}\rangle\langle v_{\mathbf{k}m}|, \tag{2.72}$$

where m runs over the occupied bands, M. The state $|\tilde{v}_{\mathbf{k}_{i}^{\sigma}m}\rangle$ is the so-called dual of the state $|v_{\mathbf{k}m}\rangle$, namely,

$$|\tilde{v}_{\mathbf{k}_{\alpha}^{\sigma}n}\rangle = \sum_{m=1}^{M} [S^{-1}_{\mathbf{k}\mathbf{k}_{\alpha}^{\sigma}}]_{m,n}\, |v_{\mathbf{k}_{\alpha}^{\sigma}m}\rangle, \tag{2.73}$$

with the overlap matrix elements

$$[S_{\mathbf{k}\mathbf{k}_\alpha^\sigma}]_{n,m} = \langle v_{\mathbf{k}n} | v_{\mathbf{k}_\alpha^\sigma m} \rangle. \tag{2.74}$$

Within this Berry-phase scheme [97], the Lagrangian of the system leads to the EOM for the time-dependent Bloch states used in the real-time approach, Eq. 2.59 [42, 43]. As mentioned above, numerically integrating Eq. 2.59 allows us to obtain the time-dependent states $|v_{\mathbf{k}n}\rangle$ at every time step t_i, with which we can update the overlaps $[S_{\mathbf{k}\mathbf{k}_\alpha^\sigma}]_{n,m}$ (Eq. 2.74). Ultimately, we can use these overlaps to calculate the polarisation in its Berry-phase formulation,

$$\mathbf{P}_\alpha = -\frac{e\,f}{2\pi v}\frac{\mathbf{a}_\alpha}{N_\alpha^\perp}\sum_{\mathbf{k}_\alpha^\perp} \mathrm{Im}\left[\ln\left(\prod_{i=1}^{N_\alpha^\parallel - 1} \det\left(\mathbf{S}_{\mathbf{k}_i \mathbf{k}_\alpha^\sigma}\right)\right)\right], \tag{2.75}$$

with the electron charge e, occupation factor f, unit cell volume v. Eq. 2.75 provides the dynamical polarisation in the direction α of the lattice vector $\mathbf{a}_\alpha$. The corresponding reciprocal lattice vector $\mathbf{b}_\alpha$ is used to determine the number of $\mathbf{k}$-points in a *string* along its direction, $N_\alpha^\parallel$, as well as the number of $\mathbf{k}$-points in a plane perpendicular to $\mathbf{b}_\alpha$, namely $N_\alpha^\perp$.

Response functions

Within the regime where the dynamical polarisation is time-periodic with the periodicity of the perturbation, ω_0, it can be formulated as a Fourier series,

$$\mathrm{P}(t) = \sum_n \mathrm{p}^{(n)} e^{in\omega_0 t}, \tag{2.76}$$

where scalar magnitudes are used for simplicity. In addition, one can consider its expansion in orders of the electric field $\mathcal{E}$ (cf. Eq. 1.2),

$$\mathrm{P}(t) = \chi^{(1)}\mathcal{E}(t) + \chi^{(2)}\mathcal{E}^2(t) + \chi^{(3)}\mathcal{E}^3(t) + \mathcal{O}(\mathcal{E}^4(t)), \tag{2.77}$$

where the tensor nature and time dependence of the susceptibilities $\chi^{(n)}$ are omitted for brevity. Comparing Eqs. 2.76 and 2.77 finally allows us to extract susceptibilities to any order. The relation between the Fourier coefficients, $\mathrm{p}^{(n)}$, and the desired susceptibilities will depend on the order, n, and the shape of the electric field, typically chosen to be a sine function, $(e^{i\omega_0 t} - e^{-i\omega_0 t})/2i$.

This procedure shows another main advantage of the real-time approach. As a non-perturbative scheme, it allows for the simultaneous determination of susceptibilities to different orders in the electric field. This is also facilitated by having a Berry-phase derived electron-field coupling operator that remains valid to every order in the electric field. At variance, perturbative approaches require a different formulation for each order they intend to consider.

Dephasing

The electronic systems solved throughout this thesis are perfectly isolated due to the approximations introduced, e.g., Born-Oppenheimer, fixed nuclei, etc. This implies neglecting important dissipative effects that occur in excited electronic systems, such as inelastic electron scattering or scattering processes with other degrees of freedom like phonons or defects. These effects represent the interaction of the electrons with the environment and contribute to the decay of excited electronic populations, providing a finite lifetime to the excitations. Ignoring these processes altogether results in failing to reproduce the dynamics of open systems.

In order to mitigate this shortcoming, dissipation effects are included phenomenologically in the real-time approach by means of a dephasing term. This implies adding the dephasing operator,

$$\mathbf{\Gamma}_{ph} = -i\nu \ (|v_{\mathbf{k}n}\rangle\langle v_{\mathbf{k}n}| - |\mu_{\mathbf{k}n}\rangle\langle \mu_{\mathbf{k}n}|) \tag{2.78}$$

to the EOM for state $|v_{\mathbf{k}n}\rangle$, Eq. 2.59. In Eq. 2.78, ν is a positive number in eV chosen to provide a desired broadening to the spectra. In the EOM, this operator acts as a restoring

force proportional to the departure of the state $|v_{\mathbf{k}n}\rangle$ from equilibrium, $|\mu_{\mathbf{k}n}\rangle$, thus limiting the population of empty states upon excitation.

Another function of this dephasing term relates to the fact that, in order to extract non-linear response functions at frequency ω_0, one must drive the system with a monochromatic perturbation of the same frequency, which in turn produces a time-periodic dynamical polarisation with the same period. This is a necessary condition for the expansion of the latter as a Fourier series (see Eq. 2.76) and the extraction procedure described above. Only then one can ensure that, e.g., $\mathrm{p}^{(2)}$ of Eq. 2.76 contains the information for $\chi^{(2)}$ in Eq. 2.77. Let us, for the sake of argument, add a second electric field to the system, $\mathcal{E}'(t)$, of frequency $\omega' = 2\omega_0$. It becomes clear that the Fourier transform of the dynamical polarisation evaluated at $2\omega_0$, i.e., $\widetilde{\mathrm{p}}(2\omega_0)$ (which was equal to $\mathrm{p}^{(2)}$ in the case with only one electric field), will now contain information about the second order response of the system to the original electric field, $\chi^{(2)}$, plus the first order response, $\chi'^{(1)}$, to the new electric field, $\mathcal{E}'(t)$. Moreover, this first order response will overshadow $\chi^{(2)}$, as the latter is orders of magnitude smaller. The situation would be worse if one had multiple electric fields, e.g., if one has a non-periodic field that has non-zero Fourier components at a continuum of frequencies (i.e., infinitely many electric fields). At this point, the Fourier transform of the polarisation at frequency ω will only be able to provide the linear response of the system at ω (plus various higher order contributions due to excitations at different frequencies that would be impossible to pick apart).

In a real-time calculation, the system is taken out of equilibrium by switching on an electric field at t_0. Essentially, the electric field around this initial time is non-periodic, implying the above-described complications. Hence, regardless of how smoothly one tries to introduce it, the system feels a *kick* at t_0, which excites every electronic transition in the material. These unwanted excitations are then suppressed by means of the dephasing term until the system is purely driven by a monochromatic electric field with frequency ω_0, at $t \gg t_0$. At this point, the periodicity of the solution is restored, the dynamical polarisation is time-periodic with the same frequency as the perturbation and nonlinear

susceptibilities can be extracted. The amount of simulated time required to reach this point, i.e., to properly *dephase* the response, is therefore a convergence parameter of the real-time approach (see Section 4.2 and Fig. 4.5).

Computational cost

Despite its many virtues, the real-time approach often presents challenges regarding its elevated computational cost. This is its biggest disadvantage and originates from its time-propagation nature, due to the the short time steps and long simulated times required. This implies repeating a handful of operations, e.g., building a Hamiltonian matrix, for tens of thousands of time steps. The computational cost of these schemes renders the calculation of nonlinear optical properties prohibitively costly in many cases, certainly for large systems and complex materials. Therefore, finding alternative formulations and methods that could alleviate these computational demands is of utmost importance.

Arguably, there is a particular case in which much of this cost is avoidable, i.e., computing nonlinear optical susceptibilities. In these calculations, the system is driven by a periodic perturbation and the response is sampled at a handful of times within one period, i.e., only one period worth of dynamical polarisation data is needed to extract susceptibilities. However, a considerably longer time is required to dephase the response before sampling it, in order to filter out all the eigenfrequencies that are excited when the electric field is first introduced. This amounts to a total simulated time that greatly exceeds the time window actually used to probe the response and, combined with the expensive numerical integration of the EOMs (often with short time steps), is responsible for the elevated computational cost of this scheme. It would then be desirable to devise a strategy where the dephasing is not needed, numerical time-evolution is avoided and/or the problem becomes time-independent altogether. Floquet theory, outlined in Section 2.4, offers a framework in which all of the above are possible for periodically-driven systems, which motivates much of the present thesis (see Chapters 4-6).

2.4 Floquet theory

The semi-classical approximation to light-matter interaction phenomena usually results in Hamiltonian operators exhibiting time periodicity in their explicit time dependence (Schrödinger picture), which originates from the coupling of the electrons to, e.g., a monochromatic light beam. The intrinsically time-dependent problem posed by optical excitations could certainly benefit from this characteristic. However, neither response-based perturbative methods nor the real-time approach make use of the time periodicity in the Hamiltonian governing the time evolution. In fact, this extra symmetry of the Hamiltonian is exploited to a much lesser extent than its spatial counterpart, i.e., the analogous translational invariance of extended systems that motivates Bloch's theorem and underpins much of solid-state electronic structure theory.

2.4.1 Quasi-energy eigenproblem

Floquet theory offers a suitable framework to address the time evolution of so-called periodically-driven quantum systems in light of the additional symmetry given by time-periodicity, as initially proposed in the seminal works of Shirley [104], Sambe [105] and Salzman [106]. This relies on the fact that, provided a time-periodic Hamiltonian, the corresponding time-dependent Schrödinger equation is a differential equation with periodic coefficients,

$$(\hat{\mathcal{H}} - i\partial_t)\ \psi(\mathbf{r}, t) = 0, \tag{2.79}$$

where $\hat{\mathcal{H}}(t+T) = \hat{\mathcal{H}}(t)$. A differential equation of these characteristics admits the application of Floquet's theorem [107] [5], which states that its solutions would be of the form,

$$\psi(\mathbf{r}, t) = e^{-i\xi t}\ \phi(\mathbf{r}, t), \tag{2.80}$$

[5] Floquet theory has been covered in numerous textbooks, e.g., [108, 109]

i.e., a pure phase times a periodic function that retains the periodicity of the Hamiltonian, $\phi(\mathbf{r}, t+T) = \phi(\mathbf{r}, t)$. The latter represents a so-called Floquet state while the argument in the pure phase contains the Floquet quasi-energy, ξ. Given their periodicity, Floquet states can be expanded in a Fourier series,

$$\phi(\mathbf{r}, t) = \sum_{\gamma=-\infty}^{+\infty} e^{-i\gamma\omega_0 t}\, \widetilde{\phi}_\gamma(\mathbf{r}), \tag{2.81}$$

where the coefficients, $\widetilde{\phi}_\gamma(\mathbf{r})$, receive the name of time-independent Floquet states, γ runs over the Floquet modes and $\omega_0 = \frac{2\pi}{T}$ is the frequency of the perturbation in $\hat{\mathcal{H}}$. These exponentials form an orthonormal basis for the Hilbert space of periodic functions of time, $\mathcal{L}_2[0, T]$, with the inner product,

$$\frac{1}{T}\int_0^T dt\; e^{+i\eta\omega_0 t}\, e^{-i\gamma\omega_0 t} = \delta_{\eta,\gamma}. \tag{2.82}$$

In this basis, the time derivative operator, ∂_t, is multiplicative, much like the momentum operator in the space of eigenfunctions of the translation operator, i.e., plane-waves. With this in mind, we replace Eqs. 2.81 and 2.80 in Eq. 2.79, take the inner product with $e^{+i\eta\omega_0 t}$ and arrive at the eigenproblem,

$$\sum_{\gamma=-\infty}^{+\infty} \hat{\mathcal{K}}_{\eta,\gamma}\, \widetilde{\phi}_\gamma(\mathbf{r}) = \xi\, \widetilde{\phi}_\eta(\mathbf{r}), \tag{2.83}$$

where the matrix elements of the so-called quasi-energy operator, $\hat{\mathcal{K}} \equiv \hat{\mathcal{H}} - i\partial_t$, take the form,

$$\hat{\mathcal{K}}_{\eta,\gamma} = \langle\eta|\hat{\mathcal{H}}|\gamma\rangle\; - \gamma\omega_0\delta_{\eta,\gamma}. \tag{2.84}$$

The matrix element formed in Eq. 2.84, $\langle\eta|\hat{\mathcal{H}}|\gamma\rangle$, can be written in terms of an unperturbed time-independent Hamiltonian, $\hat{H}^0$, and a time-dependent part which represents the coupling of the electrons with the electric field, $\hat{H}^{\mathcal{E}}$ (cf. Eq. 2.58). Since the latter is time

periodic, one can expand it as a Fourier series,

$$\hat{H}^{\mathcal{E}}(t) = \sum_{\zeta=-\infty}^{+\infty} e^{-i\zeta\omega_0 t}\ \widetilde{H}^{\mathcal{E}}_{\zeta}. \tag{2.85}$$

This Fourier expansion together with the orthonormality condition in Eq. 2.82 leads to,

$$\langle\eta|\hat{\mathcal{H}}|\gamma\rangle \equiv \frac{1}{T}\int_0^T dt\ e^{+i\eta\omega_0 t}\ \hat{\mathcal{H}}\ e^{-i\gamma\omega_0 t} = \hat{H}^0\delta_{\eta,\gamma} + \sum_{\zeta}\widetilde{H}^{\mathcal{E}}_{\zeta}\ \delta_{\zeta,\eta-\gamma}, \tag{2.86}$$

which has a diagonal part arising from the time-independent unperturbed Hamiltonian plus an electron-field coupling operator which is given by the Fourier coefficient of Eq. 2.85 evaluated at $\zeta = \eta - \gamma$. It is precisely the time dependence of this operator that makes it non-diagonal in Floquet space, thus coupling different Floquet modes in the eigenproblem of Eq. 2.83. Finally, using Eq. 2.86 in Eq. 2.84, we write the quasi-energy operator as,

$$\hat{\mathcal{K}}_{\eta,\gamma} = \widetilde{H}^{\mathcal{E}}_{\eta-\gamma} + (\hat{H}^0 - \gamma\omega_0)\delta_{\eta,\gamma}. \tag{2.87}$$

Eqs. 2.79-2.87 show how Floquet theory offers a suitable framework for reformulating the time-dependent Schrödinger equation as a time-independent eigenproblem (a more detailed account of this procedure will be presented in Section 4.1). In this eigenproblem, the time-independent Floquet states represent the eigenvectors while the Floquet quasi-energies assume the role of the eigenvalues. While the quasi-energy operator in Eq. 2.87 takes the form of an infinite matrix, any practical implementation of this formalism would truncate the number of Floquet modes to a well-converged $\eta_{\max}$.

The use of Floquet theory to solve the time-dependent Schrödinger equation resulted in *ab-initio* methods like Sturmian-Floquet theory [110, 111] and R-matrix-Floquet theory [112, 113], typically used to describe atomic multiphoton processes in intense laser fields [114, 115]. Floquet approaches to the time evolution of the density matrix operator of atoms and molecules have also been attempted, leading to the Liouville supermatrix framework [116, 117]. More recently, Floquet formulations of TD-DFT have been pro-

posed (see below a discussion on its limitations) and applied to atomic and molecular systems [118–120]. In Chapter 4, we present yet another Floquet method, obtained by reformulating the EOMs of the real-time approach to nonlinear optics [42, 43] (Eq. 2.59). Nonetheless, a crucial feature of our scheme, which distinguishes it from previous Floquet approaches, is that it can be applied to extended systems. This is achieved by deriving the electron-field coupling operator from the dynamical Berry-phase formulation of the polarisation [97], thus remaining valid in the presence of PBCs. Besides, the proposed method shows some similarities respect to Floquet-TD-DFT, like the effective nature of the Hamiltonian operators involved, the requirement for a self-consistent solution and the use of the adiabatic approximation [121] (see below). In fact, the addition of an exchange-correlation potential to the TDH level of our Floquet formulation (see Section 5.1.1) would represent a Floquet-TD-DFT scheme. However, the proposed Floquet scheme can also include many-body effects *via* a non-local COHSEX self-energy (see Section 5.1.4).

2.4.2 Practical aspects

In practical implementations, it is customary to further expand the time-independent Floquet states, $\widetilde{\phi}_\gamma(\mathbf{r})$, in the basis of eigenstates of the unperturbed Hamiltonian, $\hat{H}^0$, which we can call $\mu(\mathbf{r})$ in agreement with Section 2.3.2. These functions form an orthonormal set for the Hilbert space we denote $\mathcal{R}$. Therefore, the eigenproblem in Eq. 2.83 is solved in a composite Hilbert space, $\mathcal{L}_2[0,T] \otimes \mathcal{R}$, with the inner product,

$$\langle\langle \cdot | \cdot \rangle\rangle \equiv \frac{1}{T} \int_0^T dt \, \langle \cdot | \cdot \rangle, \tag{2.88}$$

where $\langle \cdot | \cdot \rangle$ is the usual inner product in $\mathcal{R}$. This composite space was originally introduced by Sambe as the Hilbert space for Floquet *steady states* and the functions $e^{-i\eta\omega_0 t}\mu(\mathbf{r})$ form an (infinite) orthonormal basis for it [105].

Another interesting feature of this Floquet formulation relates to the fact that the quasi-energies are defined modulo ω_0. In essence, if ϕ_0 is an eigenstate of the quasi-energy operator

with eigenvalue ξ_0, then $\phi_n = e^{-in\omega_0 t}\phi_0$ is also an eigenstate with eigenvalue $\xi_n = \xi_0 - n\omega_0$. Therefore, ϕ_0 and ϕ_n lead to the same physical state, ψ, in Eq. 2.80. This is equivalent to the folding of reciprocal space into the BZ for periodic systems. Indeed, we can define any interval of length ω_0 in the real axis as an ω-BZ, e.g., $[-\omega_0/2, \omega_0/2]$.

Since all quasi-energies can be mapped into a finite interval of length ω_0, the use of an infinite basis set determines that the quasi-energy spectrum becomes dense in the ω-BZ, i.e., there are infinitely many eigenfunctions, infinitely close to any quasi-energy in ω-BZ, which also adds complexity to the structure of avoided crossings of the quasi-energy operator. This problem has been identified as the absence of an adiabatic limit [122], meaning that the state to which the system evolves in an adiabatic switching-on of the electric field is not unique. It was nonetheless concluded that these pathologies are circumvented whenever a finite basis for $\mathcal{L}_2 \otimes \mathcal{R}$ is employed, which is, in any case, required for practical implementations [122].

A somewhat related issue concerns the compatibility between Floquet theory and the TD-DFT formalism. The initial Floquet formulation of TD-DFT [118] was met with strong criticism, as it was later recognised that the mapping between a time-periodic density of a Floquet state and the time-periodic potential it evolves in is not unique, certainly for strong electric fields [123]. The application of the TD-DFT equations to Floquet states is nonetheless correct [124], given an initial state that will determine the form of the exchange-correlation functional. However, the requirement of time-periodicity in the exchange-correlation functional is in general not met [121]. Two assumptions are needed to achieve this, which are only valid for weak fields. First, that the memory effects of the exchange-correlation potential, inherently incompatible with time periodicity, can be neglected in favour of a functional that is local in time, e.g. adiabatic LDA (ALDA). Such functional would be periodic provided the density presents periodicity. However, the latter is also not true in general and requires, as a second assumption, that each zero-field state evolve adiabatically to a single Floquet state. This so-called adiabatic approximation will also be used in the Floquet method proposed here (see Sections 4.1.1 and 5.1.1 for details).

Finally, we briefly mention that the Floquet quasi-energies do not have a direct phys-

ical interpretation. Despite being the eigenvalues of an eigenproblem resembling a time-independent Schrödinger equation, it has been argued that their identification with the energy of the system as a physical magnitude is misleading [125]. Moreover, the so-called average energy has been proposed as the 'energy' of a Floquet ground state. In analogy with Bloch's theorem, the quasi-energies play the role of the quasi-momentum or crystal-momentum, while the band energies would find their counterpart in the average energy. This lead to a variational formulation of the Floquet eigenproblem in terms of the average energy [126], which disputes previous attempts based on the quasi-energy alone [127]. The average energy formalism is revisited in Section 6.3.2.

Chapter 3

Double grid for k-sampling in BSE-Haydock

We propose an efficient double-grid approach to **k***-sampling for the calculation of absorption spectra compatible with Haydock's iterative solution of the BSE (see Section 2.2.2). Our method relies on a coarse* **k***-grid that drives the computational cost, while a dense* **k***-grid is responsible for approximately capturing excitonic effects with minimal extra computational requirements. Tests performed on bulk Si, bulk GaAs and monolayer MoS_2 produced spectra in relatively good agreement with data reported elsewhere. The validity of the approximations involved and the strong limitations of the approach are also discussed, particularly regarding strongly-bound excitons.* [1]

As discussed in Section 2.2.2, **k**-point convergence is a critical issue for the calculation of optical absorption spectra *via* the BSE scheme. The dense **k**-grids required for the description of excitonic wavefunctions often render these calculations prohibitively costly. Double **k**-grid approaches where the *full* BSE is solved in a coarse **k**-grid while a denser **k**-grid is included in some approximated way have been useful in reducing the computational cost of these calculations [66, 80–82] (See Section 2.2.2). Nonetheless, the availability of efficient Lanczos-based solvers of the BSE results in the computational limitations gravitating towards memory footprint and disk storage rather than computational power, i.e., being able

[1] The work presented in Chapter 3 was carried out as part of this PhD and first appeared published in Alliati, Sangalli & Grüning, Frontiers in Chemistry, 9, 763946 (2022). Content from the published article is used here, with some emendations and changes of phrase to better elaborate the work.

to compute and store the two-particle Hamiltonian matrix. In this Chapter, we propose a double **k**-grid approach compatible with the Haydock solver of the BSE that requires no additional memory compared to a coarse **k**-grid calculation and implies minimal extra computation. In particular, knowledge of the wavefunctions in the fine **k**-grid is not needed, nor is the calculation of the RPA screening at any extra **k**-point. Therefore, the computational cost remains roughly at the level of the coarse **k**-grid. The proposed method and its computational implementation are described in Section 3.1. Absorption spectra computed with this method for a number of materials are presented in Section 3.2 and compared with experimental results where available. This is followed by a discussion on several aspects of the approach, including its computational cost, the approximations it entails and its limitations. Supplemental material regarding this development is provided in Appendix A.

3.1 Implementation

We start by considering a coarse **k**-grid where no new approximations are introduced by our approach, i.e., the BSE kernel and two-particle Hamiltonian are computed for all vertical transitions involving **k**-points in this grid, which requires knowledge of the KS wavefunctions and energies at each of these **k**-points (see Eqs. 2.44-2.47). The solution of the BSE in this grid would typically be computationally manageable but produce underconverged optical spectra. Therefore, a much denser fine **k**-grid will be added to the system. We will denote **k**-points belonging to the fine grid with the letter $\boldsymbol{\kappa}$, while those in the coarse grid will be labelled **K**. Moreover, $\boldsymbol{\kappa}$-points will be grouped in domains centred around the **K**-points in such way that $\mathbf{Dom}(\mathbf{K_i})$ will be composed by the $\boldsymbol{\kappa}$-points that are closer to $\mathbf{K_i}$ than to any other **K**-point (as an example, see Fig. 3.1 for a visual representation of these domains in monolayer MoS_2). The number of **k**-points in this fine grid would ordinarily be too large for the BSE to be solved in full, and hence, additional approximations will be introduced for the fine grid. The two-particle Hamiltonian in Eq. 2.47 can be thought of as a shift (the diagonal matrix containing the energies of each transition) plus a rotation (the BSE

kernel). The approximation proposed here implies that the diagonal matrix is calculated in the fine **k**-grid, for which knowledge of *only* the KS energies of each band at every $\boldsymbol{\kappa}$-point is required. The BSE kernel, however, will not be calculated in the fine **k**-grid but rather, only in the coarse **k**-grid. Hence, every matrix element involving at least one transition in the fine grid will be approximated based on the kernel matrix elements in the coarse grid. This allows us to dispense with the KS wavefunctions in the fine **k**-grid, which has a great impact on memory requirements.

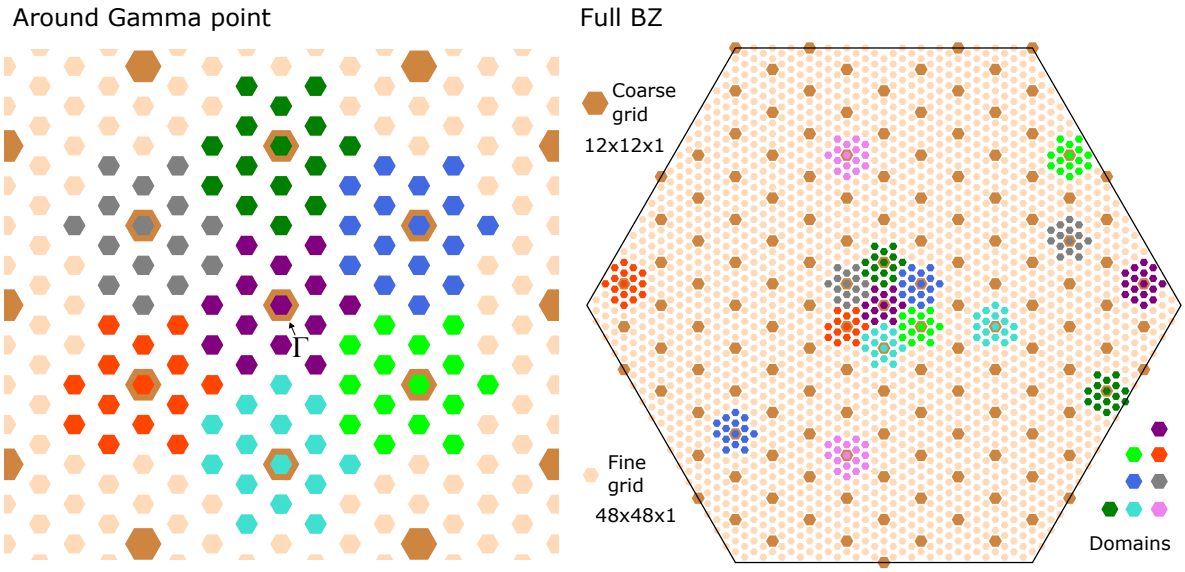

Figure 3.1: Visual representation of the coarse 12×12×1 and fine 48×48×1 **k**-grids in monolayer MoS_2. There is a fine-grid $\boldsymbol{\kappa}$-point underneath every coarse-grid **K**-point. The fine-grid domains centred around a selection of **K**-points are shown in different colours (key in bottom-right corner). Both the full BZ (right panel) and the region around the Γ point (left panel) are represented.

The way in which the BSE kernel is extended from the coarse to the fine **k**-grid has been carefully considered as it has significant impact on the results. The best agreement with experimental spectra was achieved with an approach we refer to as diagonal kernel extension (DKE). Let us consider one **k**-point in the coarse grid, $\mathbf{K_I}$. There will be a group of $\boldsymbol{\kappa}$-points in the fine grid that map to it, namely those in the domain $\mathbf{Dom}(\mathbf{K_I})$. We will label those with a second numerical sub-index as $\boldsymbol{\kappa}_{\mathbf{I}_1}, \boldsymbol{\kappa}_{\mathbf{I}_2}, \boldsymbol{\kappa}_{\mathbf{I}_3}, ..., \boldsymbol{\kappa}_{\mathbf{I}_i}, ...$ Given that the fine grid contains the coarse grid, we have that $\boldsymbol{\kappa}_{\mathbf{I}_1} = \mathbf{K_I}$, while $\boldsymbol{\kappa}_{\mathbf{I}_i}$ with $i \neq 1$ are other fine

grid points close to $\mathbf{K_I}$. Having established the nomenclature in this way, then the DKE would imply the definition

$$\Xi_{\substack{nm\boldsymbol{\kappa}_{\mathbf{I}_i} \\ n'm'\boldsymbol{\kappa}_{\mathbf{I}'_{i'}}}} \equiv \Xi_{\substack{nm\mathbf{K}_{\mathbf{I}} \\ n'm'\mathbf{K}_{\mathbf{I}'}}} \delta_{ii'}, \tag{3.1}$$

where the R.H.S can be calculated according to Eqs. 2.44-2.47 while the L.H.S is the unknown matrix element we are trying to approximate (see Eq. A.4 in Appendix A for a visual representation of Eq. 3.1). Thus, Eq. 3.1 is only exact for transitions involving $\mathbf{k}$-points that belong both the coarse and the fine grids simultaneously ($i = i' = 1$), and approximated otherwise. Even though the BSE kernel is not, in general, a diagonally-dominant matrix, it is true that the diagonal matrix elements usually have values orders of magnitude higher than those of immediately close off-diagonal elements. The DKE approach preserves this character when extending the kernel from the coarse grid to the fine grid. Essentially, each matrix element of the coarse grid BSE kernel expands into a block in the fine grid matrix. The DKE method ensures that each block is strictly diagonal, which is very relevant when expanding one of the diagonal matrix elements of the coarse grid matrix. In practice, Eq. 3.1 implies setting to zero some fine-grid kernel matrix elements (if not most, depending of the ratio between the number of $\boldsymbol{\kappa}$-points and $\mathbf{K}$-points). The remaining fine-grid matrix elements are made equal to a corresponding coarse-grid matrix element (see Eq. A.4). Other possible strategies for kernel extension that ignore this guiding principle of the DKE tend to produce poorer results (see Section 3.2.3).

Finally, let us discuss how this double grid method fits within Haydock's algorithm. It is apparent from Eqs. 2.54-2.56 that this scheme relies mainly on the matrix vector multiplication $H^{2p}|V_n\rangle$, so we will focus on how this is adapted to account for the fine $\mathbf{k}$-grid. The matrix in question (H^{2p}) has already been described above, i.e., the BSE kernel is approximated by DKE (Eq. 3.1) and the diagonal part needs no such approximation as the KS energies are known in the fine $\mathbf{k}$-grid. All there is left is then to define how the Haydock vectors $|V_n\rangle$ are extended to the fine grid and initialised. The initial Haydock vector $|V_0\rangle$ is calculated in the coarse $\mathbf{k}$-grid according to Eq. 2.52. Each component is

associated to one transition $vc\mathbf{k}$ and thus, when moving from the coarse to the fine grid, the number of components will increase according to the ratio between the number of $\boldsymbol{\kappa}$-points and $\mathbf{K}$-points. From Eq. 2.52, it is clear that the KS wavefunctions at the $\boldsymbol{\kappa}$-points would be required to properly initialise the Haydock vector in the fine $\mathbf{k}$-grid. As our method is designed so that these fine-grid wavefunctions are not needed nor loaded into memory, those components will be initialised as being equal to the corresponding transition in the coarse $\mathbf{k}$-grid. In other words,

$$|P\rangle_{\mathrm{FG}} = \sum_{vc\mathbf{K_I}} \lim_{\mathbf{q}\to 0} \frac{1}{|\mathbf{q}|} \Lambda^*_{vc\mathbf{K_I}}(\mathbf{q}, \mathbf{G}=0) \sum_{\substack{\boldsymbol{\kappa}_{\mathbf{I}_i} \in \\ \mathbf{Dom}(\mathbf{K_I})}} |vc\boldsymbol{\kappa}_{\mathbf{I}_i}\rangle, \tag{3.2}$$

where FG denotes the fine grid. It is apparent that $|P\rangle_{\mathrm{FG}}$ has many more components than $|P\rangle$, due to each coarse grid transition (at $\mathbf{K_I}$) being replicated into many transitions at all the $\boldsymbol{\kappa}$-points in the domain of $\mathbf{K_I}$. The recursive relations in Eqs. 2.54-2.56 would formally require the multiplication of the fine grid (full) BSE kernel times Haydock vectors of the size of $|P\rangle_{\mathrm{FG}}$. In our implementation, we calculate this matrix-vector multiplication without allocating the (DKE-approximated) fine-grid BSE kernel into memory. Instead, we perform this operation having only allocated the coarse-grid kernel. This choice has a large impact in the memory footprint of our double-grid method, since the fine-grid BSE matrix can reach tens of TB in size, e.g., for a 60×60×60 $\mathbf{k}$-grid. This matrix-vector multiplication can be expressed in the fine-grid e-h space as,

$$r_{nm\boldsymbol{\kappa}_{\mathbf{I}_i}} = \sum_{n'm'\boldsymbol{\kappa}_{\mathbf{I}'}{}_{i'}} \Xi^{nm\boldsymbol{\kappa}_{\mathbf{I}_i}}_{n'm'\boldsymbol{\kappa}_{\mathbf{I}'}{}_{i'}} c_{n'm'\boldsymbol{\kappa}_{\mathbf{I}'}{}_{i'}} , \tag{3.3}$$

where $c_{vc\boldsymbol{\kappa}_{\mathbf{I_i}}} = \langle vc\boldsymbol{\kappa}_{\mathbf{I_i}}|V\rangle$ are the components of the vector to be multiplied and r are, analogously, the coefficients of the resulting vector. The summation in Eq. 3.3 runs over the fine-grid e-h space. However, applying the DKE (Eq. 3.1) to the BSE matrix in Eq.

3.3, we obtain,

$$r_{nm\boldsymbol{\kappa}_{\mathbf{I}_i}} = \sum_{n'm'\mathbf{K}_{\mathbf{I}'}} \sum_{\substack{i' \in \\ \mathbf{Dom}(\mathbf{K}_{\mathbf{I}'})}} \Xi_{\substack{nm\mathbf{K}_{\mathbf{I}} \\ n'm'\mathbf{K}_{\mathbf{I}'}}} \delta_{i,i'}\, c_{n'm'\boldsymbol{\kappa}_{\mathbf{I}'i'}} = \sum_{n'm'\mathbf{K}_{\mathbf{I}'}} \Xi_{\substack{nm\mathbf{K}_{\mathbf{I}} \\ n'm'\mathbf{K}_{\mathbf{I}'}}} c_{n'm'\boldsymbol{\kappa}_{\mathbf{I}'i}}, \tag{3.4}$$

where the BSE matrix elements in the R.H.S are those of the coarse-grid kernel and the resulting summation runs over the **K**-points in the coarse grid only (see Eqs. A.5 and A.6 in Appendix A for a visual representation of Eq. 3.4). Computationally, this means adding a loop over the $\boldsymbol{\kappa}$-points in the domain of each **K**, which can alternatively be recast as a matrix-matrix multiplication (see Eq. A.7). In practice, we divide a given Haydock vector $|V\rangle$ in *fragments* by grouping its components, $c_{nm\boldsymbol{\kappa}_{\mathbf{I}_i}}$, according to their $\boldsymbol{\kappa}$-point index, i. Hence, instead of evaluating Eq. 3.4 for each i index, we build a matrix with those *fragments* as columns and multiply the coarse-grid BSE kernel by it (see Eq. A.7).

We highlight that the implementation conducted as part of this thesis involves the extension of Haydock's algorithm to the double grid, while the Haydock solver itself, alongside the BSE scheme, were already coded.

3.2 Results and discussion

The double grid method proposed here to calculate optical spectra via the BSE has been implemented in the Haydock solver of the Yambo code [128, 129] and tested on a variety of semiconductors. In this section, we present the resulting optical spectra of bulk Si, bulk GaAs and monolayer MoS_2. An assessment of the computational cost of this scheme in comparison with the *full* BSE is also provided. We conclude this section discussing the approximations made in our double **k**-grid approach and its limitations. Although Gamma-centred **k**-grids were used throughout this study, our method can also be used with shifted grids (see an example in Appendix A). The starting KS wavefunctions and energies were computed with Quantum Espresso [130] using norm-conserving pseudopotentials and the Perdew-Zunger LDA exchange-correlation functional [51]. The calculation of optical spectra

was performed in the length gauge and within the dipole approximation.

3.2.1 Absorption spectra

Fig. 3.2 shows the absorption spectrum of bulk Si, which is notoriously difficult to converge with respect to **k**-points since a very dense **k**-sampling is required to properly describe its excitons. The starting point for our Si calculations is a severely under-converged $8 \times 8 \times 8$ **k**-point grid. Indeed, the spectrum produced by this coarse grid alone shows numerous spurious peaks (see left panel of Fig. 3.2), which reveals a high degree of artificial localisation of the excitons imposed by the $8 \times 8 \times 8$ **k**-grid. We then took the latter as the coarse grid for the double grid method and added a fine grid of $\boldsymbol{\kappa}$-points to it. Fig. 3.2 shows that a fine (double) grid of $24 \times 24 \times 24$ $\boldsymbol{\kappa}$-points on top of this coarse grid immediately suppresses this artificial localisation. Denser double grids improve upon this result. Ultimately, the spectrum obtained with a $60 \times 60 \times 60$ fine $\boldsymbol{\kappa}$-grid on top of an $8 \times 8 \times 8$ coarse **K**-grid is in relatively good agreement with experimental data available in the literature for Si bulk at 10 K [131] (see Fig. 3.2). The right panel of Fig. 3.2 shows a comparison with other theoretical results obtained from the literature. Among the latter, Ref. [79] uses the BZ-interpolation of Rohlfing *et al.* [66] (described in Section 2.2.2) while Refs. [64] and [132] solve the BSE in shifted **k**-grids without any such interpolation. Importantly, Ref. [133] includes the coupling to the lattice (zero-point) vibrations and the resulting renormalisation of optical strengths. All five theoretical spectra presented in the right panel of Fig. 3.2 show relatively good agreement with the experimental data.

As in the case of Si, GaAs also requires very dense k-sampling for its optical response to be converged. The coarse grid in this case is an under-converged $10 \times 10 \times 10$ Gamma-centred **k**-point grid. Various spurious peaks are present in the spectrum calculated with this coarse grid alone, which points to a high degree of artificial localisation of the excitonic wavefunctions (see left panel of Fig. 3.3). It is apparent that adding a fine (double) $\boldsymbol{\kappa}$-grid of $20 \times 20 \times 20$ does not solve the problem fully. However, the spectra with $40 \times 40 \times 40$ or

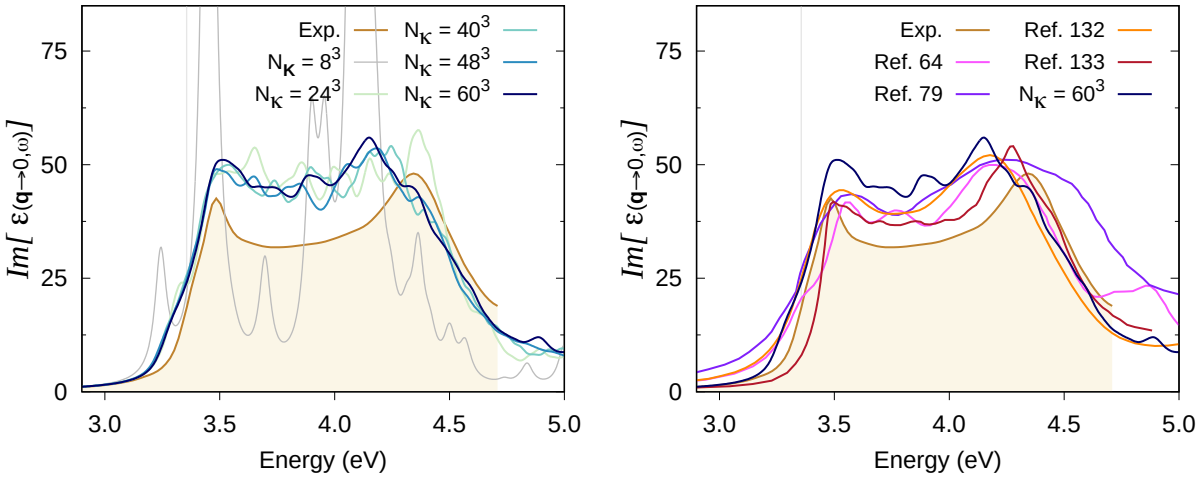

Figure 3.2: Optical absorption spectra of bulk Si calculated at the BSE level and compared with experimental data at 10 K [131] (labelled Exp.). Left: Results obtained with the double-grid method proposed here. The label $N_{\mathbf{K}} = 8^3$ corresponds to a regular BSE calculation on a single $8 \times 8 \times 8$ coarse $\mathbf{k}$-grid. The label $N_{\boldsymbol{\kappa}} = 60^3$ corresponds to a double-grid BSE calculation with an $8 \times 8 \times 8$ coarse $\mathbf{k}$-grid and a $60 \times 60 \times 60$ fine $\mathbf{k}$-grid. We consider all e-h pairs from the top 4 valence bands to the 4 bottom conduction bands. All $\mathbf{k}$-grids are Gamma-centred. Right: A comparison with other theoretical spectra available in the literature.

$60 \times 60 \times 60$ $\boldsymbol{\kappa}$-grids match the experimental data relatively well (see Fig. 3.3, respectively). The right panel in Fig. 3.3 shows a comparison with available experimental data for GaAs at 22 K [134]. In addition, other theoretical results obtained from the literature are displayed, both with BZ-interpolation [66] and without it [65]. All three theoretical spectra agree relatively well with the experimental data.

The $\mathbf{k}$-point convergence of the absorption spectrum of monolayer MoS_2 within the BSE scheme has been previously discussed [135,136], where the splitting of the first exciton was attributed to spin-orbit coupling. Moreover, it was argued that several studies obtain a similar splitting due to an underconverged $\mathbf{k}$-sampling of the BZ and mistakenly report it as matching experimental results. In fact, the appendix of Ref. [135] shows that a calculation in which spin-orbit coupling is not accounted for should not show any splitting in the first exciton.

Here, we intend to investigate whether our double-grid method can eliminate this un-

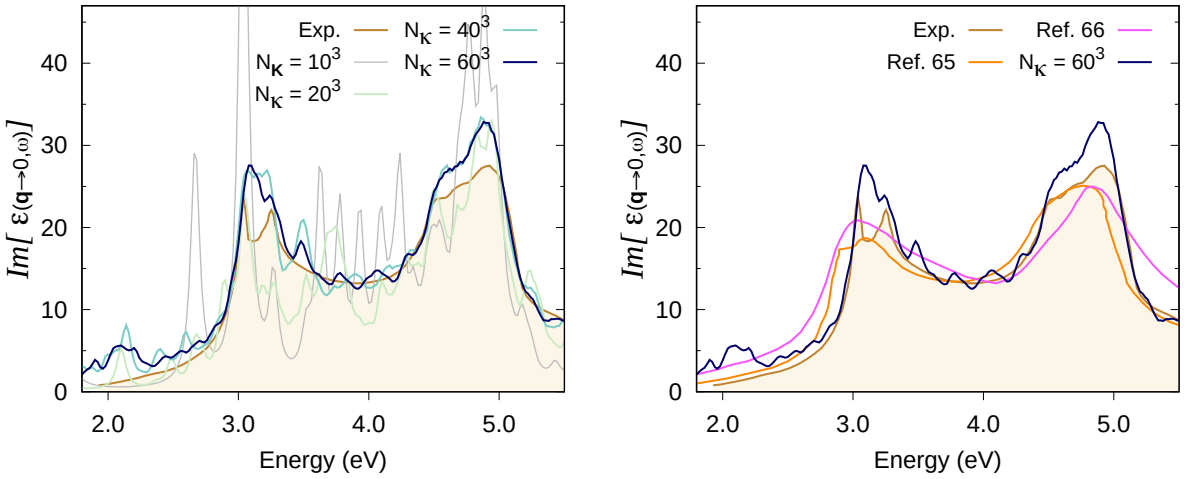

Figure 3.3: Optical absorption spectra of bulk GaAs calculated at the BSE level and compared with experimental data at 22 K [134] (labelled Exp.). Left: Results obtained with the double-grid method proposed here. The label $N_{\mathbf{K}} = 10^3$ corresponds to a regular BSE calculation on a single $10 \times 10 \times 10$ coarse $\mathbf{k}$-grid. The label $N_{\boldsymbol{\kappa}} = 60^3$ corresponds to a double-grid BSE calculation with a $10 \times 10 \times 10$ coarse $\mathbf{k}$-grid and a $60 \times 60 \times 60$ fine $\mathbf{k}$-grid. We consider all e-h pairs from the top 4 valence bands to the 4 bottom conduction bands. All $\mathbf{k}$-grids are Gamma-centred. Right: A comparison with other theoretical spectra available in the literature.

physical splitting in a calculation without spin-orbit coupling. We start with the spectra computed on a (single) grid of $12 \times 12 \times 1$ $\mathbf{k}$-points, which splits the first exciton into two peaks at around 2.2 and 2.5 eV (see left panel of Fig. 3.4). Indeed, adding successive double grids results in suppressing the splitting in favour of just one peak at around 2.3 eV. Moreover, this is achieved with a negligible computational overhead respect to the underconverged $12 \times 12 \times 1$ $\mathbf{k}$-points calculation (See Section 3.2.2).

In any case, dense $\mathbf{k}$-grids in monolayer MoS_2 still amount to a manageable total number of $\mathbf{k}$-points owing to its two-dimensional nature, which requires only one $\mathbf{k}$-point in the vertical direction. Therefore, *full* BSE calculations on dense grids could be conducted for this material using high-memory computing nodes, e.g., requiring around 500 GB of memory per processor for a single-grid $60 \times 60 \times 1$ BSE calculation. This is much less severe than a $60 \times 60 \times 60$ calculation for bulk Si, in which case the BSE kernel required tens of TB of memory, thus resulting prohibitively costly. The spectra of monolayer MoS_2

calculated in dense (single) grids is presented in the right panel of Fig. 3.4, showing a noticeable reduction in the above-mentioned splitting of the exciton. These results also feature a gradual shift in the position of the first and second excitons with increasing **k**-sampling. A comparison with the double-grid spectrum indicates that our method fails to reproduce this shift as a result of the stark approximations made in the BSE kernel.

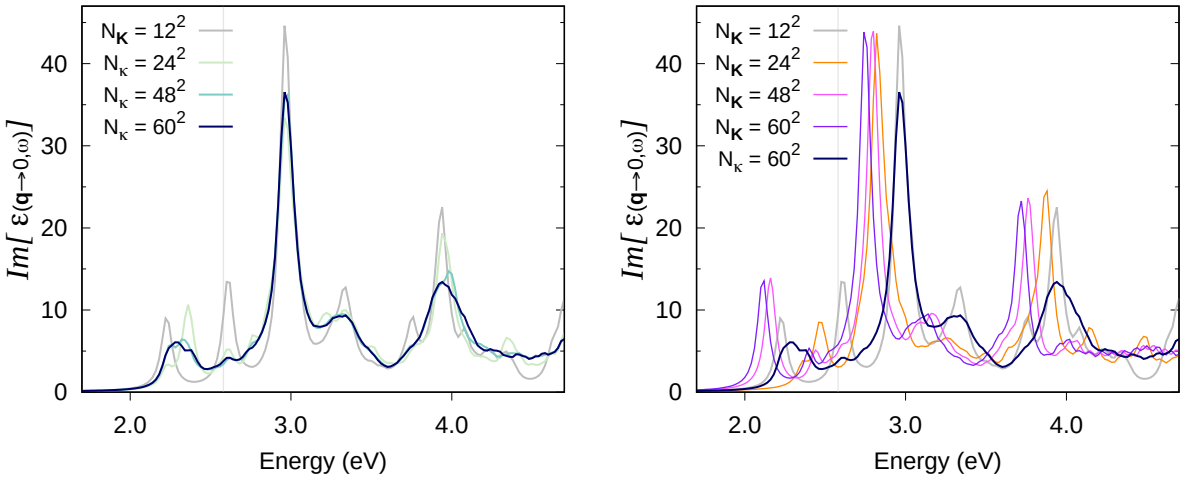

Figure 3.4: Optical absorption spectra of monolayer MoS_2 at the BSE level. The label $N_{\mathbf{K}} = N^2$ corresponds to a regular BSE calculation on a single $N \times N \times 1$ coarse **k**-grid. The label $N_{\boldsymbol{\kappa}} = 60^2$ corresponds to a double-grid BSE calculation with a $12 \times 12 \times 1$ coarse **k**-grid and a $60 \times 60 \times 1$ fine **k**-grid. Left: Results obtained with the double-grid method proposed here. Right: Comparison with *full* BSE calculations on dense (single) grids. We consider all e-h pairs from the top 3 valence bands to the 5 bottom conduction bands. All **k**-grids are Gamma-centred.

Finally, we discuss the impact of the coarse-grid starting point for a double-grid calculation. The first observation derived from our experience with this method indicates that, if the coarse grid is very far from convergence (e.g., 3×3×1 for MoS_2), the double grid spectrum would not be correct or meaningful (see, e.g., Fig. A.3). Therefore, around these low densities of **k**-points, we conclude that a denser coarse-grid will usually represent a better starting point. However, upon increasing the **k**-point density of the coarse grid, we reach a point where the advantage of doing so is not always clear. For example, the left panel of Fig. 3.5 shows absorption spectra of Si bulk obtained with a 60×60×60 fine grid and two

different coarse grids, 12×12×12 and 8×8×8 (the latter is the result from Fig. 3.2). While the 12×12×12 coarse grid shows better agreement with the experimental data in the region between the two peaks and beyond, the quality of the spectrum around the first peak has deteriorated respect to the 8×8×8 coarse-grid result. In the case of GaAs, the comparison with experimental spectra worsens slightly upon increasing the **k**-point density of the coarse grid from 10×10×10 to 14×14×14 (see right panel of Fig. 3.5). The exception to this is the feature around 2.1 eV, which improves with a denser coarse grid (see Sec. 3.2.4). For MoS_2, Fig. 3.6 shows a comparison between double-grid spectra obtained with different coarse grids and the *full* BSE calculation on a 60×60×1 **k**-grid. The description of the first exciton with a 24×24×1 coarse grid worsens respect to the one obtained using a 12×12×1 coarse grid (see left panel of Fig. 3.6). This is due to a sizeable shift in the position of the first exciton when going from a *full* 12×12×1 BSE calculation to a *full* 24×24×1 one, which then gets reversed upon using even denser grids (see right panel of Fig. 3.4). As a result, a 48×48×1 coarse grid represents a better starting point regarding this first exciton (see right panel of Fig. 3.6). The rest of the spectrum appears to improve with denser coarse-grids. Overall, this analysis highlights the dependence of the double-grid result on the quality of the coarse-grid spectrum as an important shortcoming of this approach. This hinders the predictive power of the double-grid method presented in this Chapter (we revisit this issue in Section 3.2.4).

3.2.2 Computational cost

As described in Section 2.2.2, Lanczos approaches to the BSE eliminate the need to invert the BSE kernel or fully diagonalise the two-particle Hamiltonian, which would become the bottleneck of the calculation whenever required. Instead, Lanczos solvers replace these highly demanding tasks by very efficient and computationally inexpensive iterative schemes. This numerical advantage means that the solution step itself does not drive the computational cost any longer, but rather, computing and storing the BSE matrix now becomes

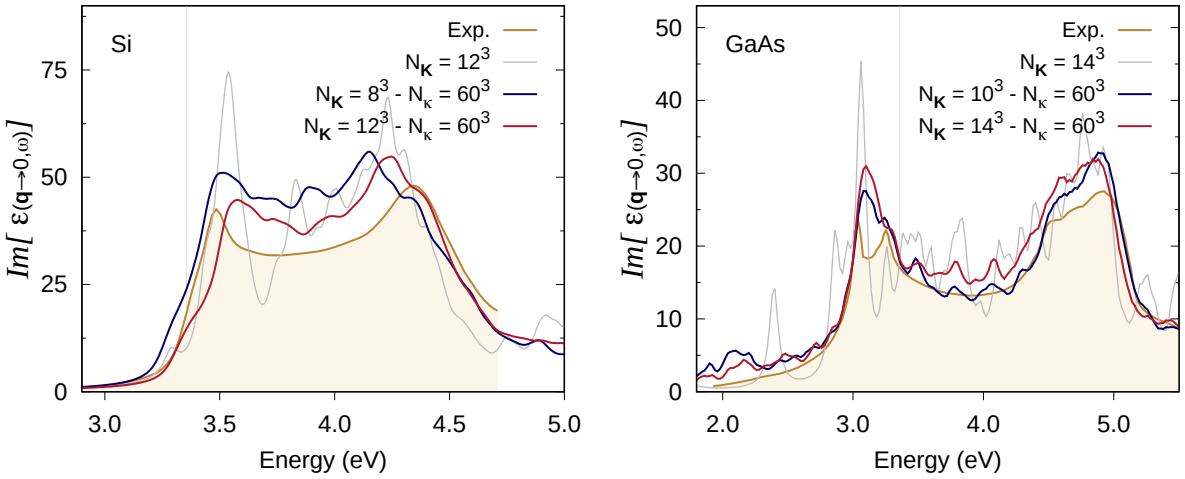

Figure 3.5: Optical absorption spectra of bulk Si (left) and GaAs (right) at the BSE level *via* the double-grid approach using different coarse grids. We consider all e-h pairs from the top 4 valence bands to the 4 bottom conduction bands. All **k**-grids are Gamma-centred.

the bottleneck of the calculation. The method proposed in this work addresses this issue directly. First, the KS wavefunctions in the fine grid need not be available, i.e., not stored nor loaded into memory. Moreover, the kernel matrix elements in the fine grid, and consequently, the corresponding oscillator strengths, need not be calculated. As a result, the size of the BSE kernel matrix will effectively be that of the coarse grid kernel. For instance, if we consider a coarse grid of $10 \times 10 \times 10$ and a fine grid of $60 \times 60 \times 60$, then there would be 1000 **K**-points and 216000 $\boldsymbol{\kappa}$-points. The full BSE kernel would have $\sim (200 \times N_v \times N_c)^2$ more matrix elements than the approximated one, where N_v and N_c denote the number of valence and conduction bands, respectively. Depending on the number of bands required for convergence, the steps of computing and storing that many matrix elements may draw the line between what is feasible and what is not, not only in terms of processing power, but also due to memory and disk-storage limitations.

Let us consider monolayer MoS_2 to address how the computational cost compares between our double grid approach with a given fine $\boldsymbol{\kappa}$-grid and the regular (*full*) BSE calculation using that same fine grid as the only (single) **k**-grid. While this Section focuses on the computational cost comparison, the spectra produced by all calculations involving, e.g., a

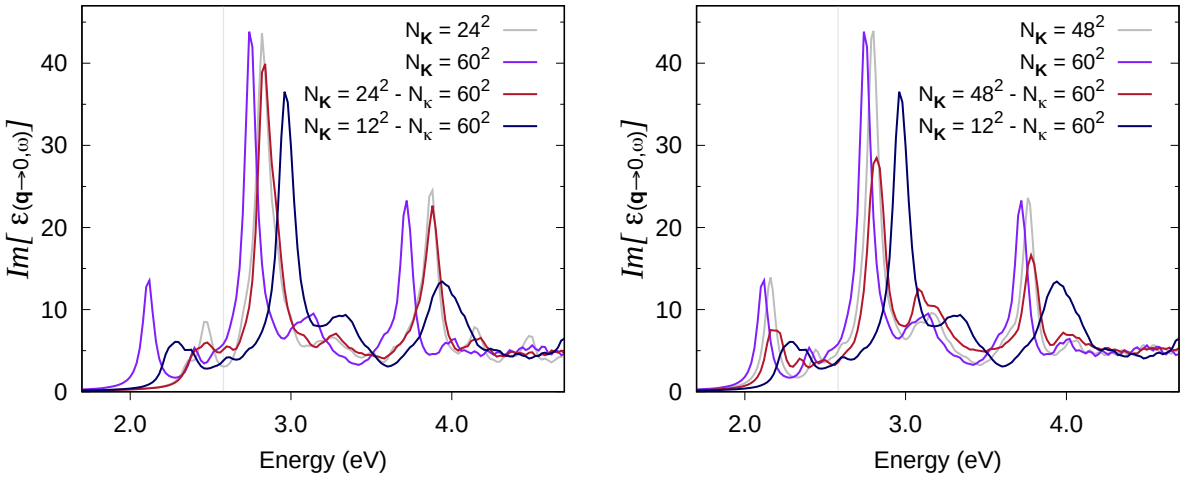

Figure 3.6: Optical absorption spectra of monolayer MoS_2 at the BSE level *via* the double-grid approach using different coarse grids. Left: Using a $24 \times 24 \times 1$ coarse **k**-grid. Right: Using a $48 \times 48 \times 1$ coarse **k**-grid. We consider all e-h pairs from the top 3 valence bands to the 5 bottom conduction bands. All **k**-grids are Gamma-centred.

$24\times24\times1$ **k**-grid, is presented in Fig. A.3. Fig. 3.7 shows the combined time required to calculate the BSE kernel and compute the absorption spectra via Haydock's scheme as a function of **k**-points used in each calculation. For comparability purposes, all the calculations shown in Fig. 3.7 have been carried out with just one processor. For the *full* solution of the problem (brown circles) the number of **k**-points has quadratic scaling from one **k**-grid to another (as it does for any 2D material) and the CPU time scales quadratically with the total number of **k**-points. This latter dependence stems from the size of the e-h basis set and the number of matrix elements of the BSE kernel, i.e., $(N_{\mathbf{K}} \times N_v \times N_c)^2$. The computational cost of the double grid approach proposed in this work (green-blue diamonds connected by lines) increases only slightly with the size of the fine-grid, when the same coarse grid is used. Since the BSE kernel is calculated only in the coarse-grid, this increase is due to the Haydock solver, which now has to process larger Haydock vectors. Nonetheless, it is apparent that the Haydock-related increase in CPU time is minor and far more manageable than the scaling of the *full* BSE problem. Overall, the fine grid has little impact on the CPU time required by the method we propose. In fact, Fig. 3.7 clearly shows that the

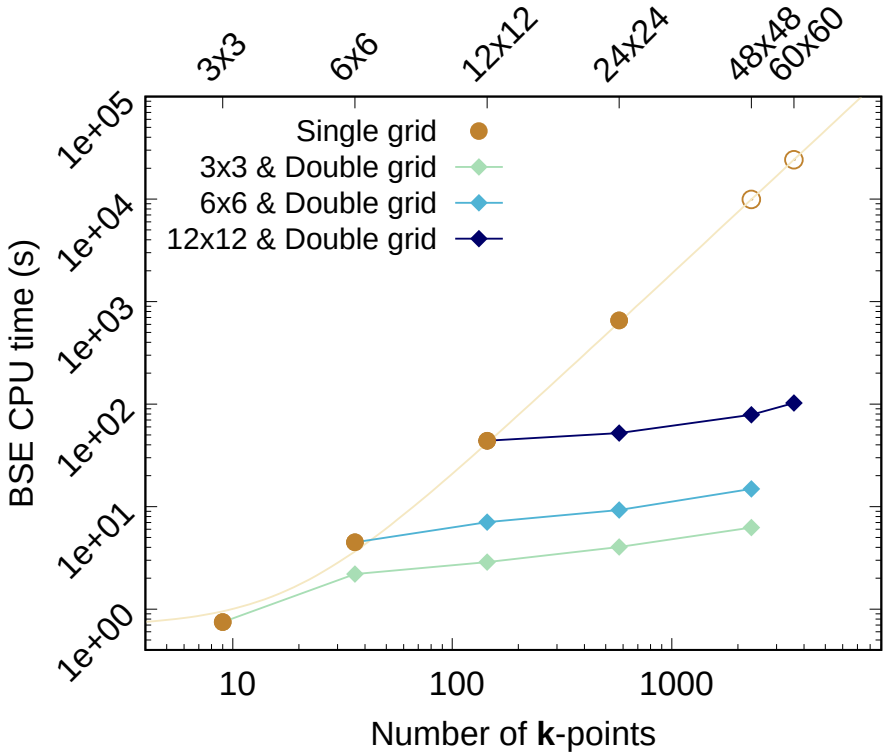

Figure 3.7: CPU time in seconds required to calculate and store the BSE kernel, and solve it via Haydock's iterative scheme as a function of the number of **k**-points. Brown circles represent *full* BSE calculations. The data for $48 \times 48 \times 1$ and $60 \times 60 \times 1$ **k**-grids have been estimated via a quadratic fitting. The diamonds denote double-grid BSE calculations. Lines connect double-grid calculations that use the same coarse-grid. All calculations were carried out in one processor for comparability purposes. We consider all e-h pairs from the top 3 valence bands to the 5 bottom conduction bands.

computational cost of the double grid method is roughly driven by the coarse grid.

3.2.3 Kernel extension to the fine grid

The extension of the BSE kernel from the coarse to the fine **k**-grid is the key approximation of the double-grid approach proposed in this thesis. There are a number of strategies one could use, many of which require knowledge of the KS wavefunctions in the fine **k**-grid [66, 82]. At variance, we only considered strategies where said wavefunctions were not needed and the fine-grid BSE kernel matrix was not allocated in order to limit the memory footprint of our method, such as the DKE approximation we defined in Eq. 3.1. As explained in Sec. 3.1, the latter was chosen for this implementation given its simplicity

and low computational cost. Nevertheless, there are other possible strategies for kernel extension one can consider, which have similar characteristics to the DKE. In particular, we also examined the so-called full kernel extension (FKE). We define the FKE approach so that each matrix element of the coarse **k**-grid BSE kernel is expanded into an all-ones block in the fine grid times the original matrix element,

$$\Xi_{\substack{nm\boldsymbol{\kappa}_{\mathbf{I}_i} \\ n'm'\boldsymbol{\kappa}_{\mathbf{I}'_{i'}}}} \equiv \Xi_{\substack{nm\mathbf{K}_{\mathbf{I}} \\ n'm'\mathbf{K}_{\mathbf{I}'}}} \quad \forall i, i', \tag{3.5}$$

(see Eq. A.8 in Appendix A for a visual representation of Eq. 3.5). As a result, the way in which the fine-grid matrix vector multiplication is carried out also differs from the DKE. In the FKE, this operation is performed as

$$r_{nm\boldsymbol{\kappa}_{\mathbf{I}_i}} = \sum_{n'm'\mathbf{K}_{\mathbf{I}'}} \Xi_{\substack{nm\mathbf{K}_{\mathbf{I}} \\ n'm'\mathbf{K}_{\mathbf{I}'}}} \sum_{\substack{i' \in \\ \mathbf{Dom}(\mathbf{K}_{\mathbf{I}'})}} c_{n'm'\boldsymbol{\kappa}_{\mathbf{I}'_{i'}}}, \tag{3.6}$$

(see Eqs. A.9 and A.10 in Appendix A for a visual representation of Eq. 3.6). We note that Eqs. 3.5 and 3.6 of the FKE are analogous to Eqs. 3.1 and 3.4 of the DKE, respectively.

In terms of the spectra produced by either kernel extension strategy, the comparison consistently favoured the DKE over the FKE in all the materials tested in Sec. 3.2.1, as shown in Fig. 3.8. The difference may be less noticeable in systems with weaker excitonic effects. In the case of bulk Si, it is apparent that the DKE is better than the FKE at suppressing the artificial localisation found around 3.6 eV. For GaAs, the DKE also shows an improvement with respect to the FKE when dealing with the artificial localisation at around 3.1 eV. Finally, monolayer MoS_2 shows a greater difference between both approaches. In fact, the FKE approach shows little to none improvement with respect to the $12 \times 12 \times 1$ single **k**-grid as far as the first exciton is concerned (cf. Fig. 3.4). Overall, the trend found in this work indicates that the DKE is consistently better than the FKE, which is why we chose the former for this implementation.

In order to explain the better performance of DKE over FKE, we will discuss the

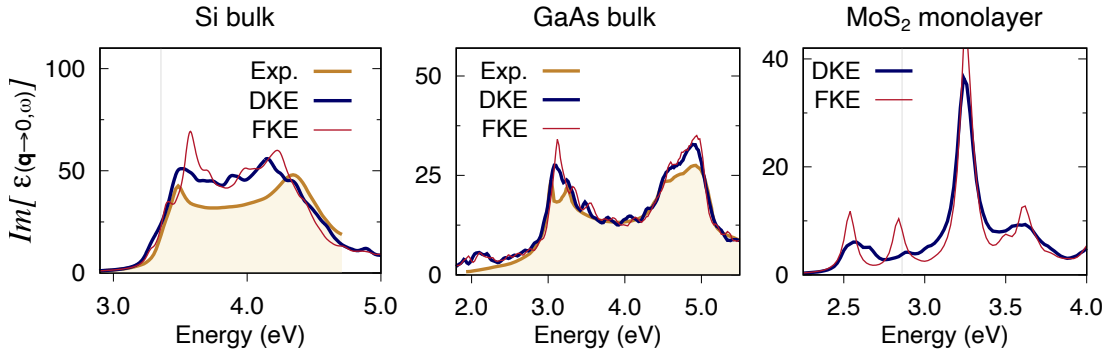

Figure 3.8: Optical absorption spectra of bulk Si (left panel), bulk GaAs (middle panel) and monolayer MoS_2 (right panel). Comparison of spectra obtained by using the diagonal kernel extension (DKE) and full kernel extension (FKE) approximations. Computational details as in Figs. 3.2-3.4.

properties of the BSE kernel and the two-particle Hamiltonian matrices, which are related by Eq. 2.47. In general, the kernel matrix elements $\Xi^{nm\mathbf{k}}_{n'm'\mathbf{k}'}$ are sharply peaked at $\mathbf{q} = 0$ [66, 79], i.e., for $\mathbf{k} = \mathbf{k}'$. This does not mean that every matrix element with $\mathbf{q} = 0$ will have a higher value than the remaining matrix elements. In fact, that is only true for the diagonal elements $\Xi_{nm\mathbf{k}}^{nm\mathbf{k}}$, while the $\mathbf{q} = 0$ elements coupling different sets of bands ($\Xi^{nm\mathbf{k}}_{n'm'\mathbf{k}}$) are closer in value to all other $\mathbf{q} \neq 0$ matrix elements. We exemplify this with monolayer MoS_2 in Fig. 3.9. The latter shows the modulus of every matrix element between a given transition ($v = 13$, $c = 14$ and $\mathbf{k}_1 = (-0.166, -0.166, 0)$) and every other transition in the e-h space, i.e., one row of the BSE kernel matrix. This data is plotted as a function of the magnitude $||\mathbf{q}||/||\mathbf{q}||_{max}\ sgn(q_x)$, where $\mathbf{q} = \mathbf{k} - \mathbf{k_1}$. Fig. 3.9A shows the BSE kernel as obtained with a single grid of $6 \times 6 \times 1$ $\mathbf{k}$-points, where we can see that the diagonal matrix element (the selected transition with itself) is an order of magnitude higher than all other matrix elements (many of which also have $\mathbf{q} = 0$). The fine grid of $12 \times 12 \times 1$ $\mathbf{k}$-points better captures the build-up to the peak of the graph as it has many more $\mathbf{k}$-points around $\mathbf{k}_1$ (see Fig. 3.9B). Unfortunately, the double grid approach proposed here cannot capture this feature because it is meant not to imply any extra computation or storage of matrix elements at fine grid $\boldsymbol{\kappa}$-points. However, the reader should bear in mind that while this feature is missing in our approximated BSE kernel, the benefits of this double grid approach

reside in exactly knowing the transition energies at the fine grid $\boldsymbol{\kappa}$-points (see Appendix A for a detailed discussion). Therefore, what we require from the approximated kernel is to avoid introducing unphysical matrix elements, and in this regard the DKE performs much better than the FKE. Fig. 3.9C shows how the BSE kernel matrix elements approximated by DKE still represent a function of $\mathbf{q}$ that is sharply peaked at the origin. Conversely, the FKE approach means that many matrix elements in $\mathbf{Dom}(\mathbf{k}_1)$, and consequently at $\mathbf{q} \neq \mathbf{0}$, will take the value of the peak. We know that such behaviour as a function of $\mathbf{q}$ would not arise should more $\mathbf{k}$-points be included (see 3.9B). Hence, we believe DKE constitutes a better approximation of the BSE kernel than FKE. Further arguments in favour of the DKE over the FKE are presented in Appendix A.

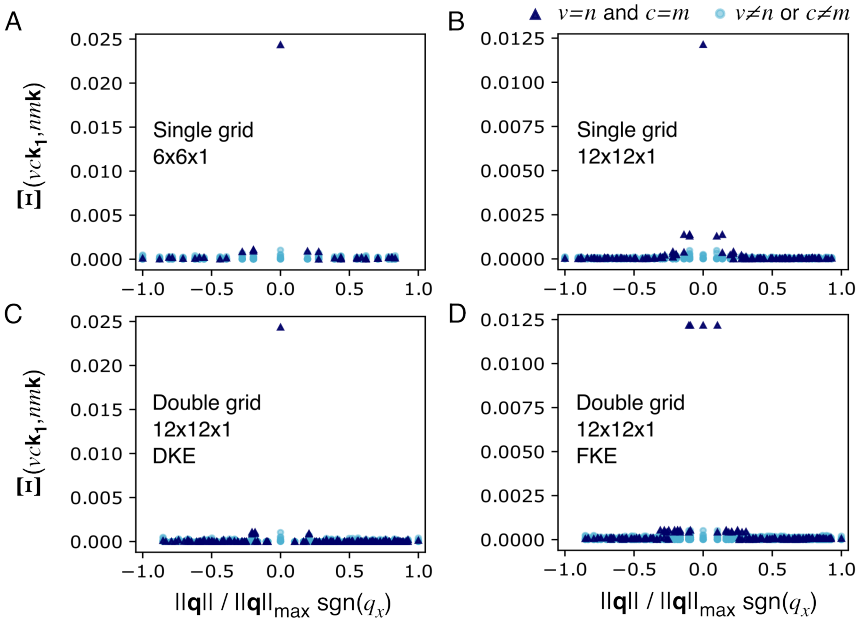

Figure 3.9: Modulus of the BSE Kernel matrix element between one transition ($vc\mathbf{k}_1$) and every other transition in the e-h space ($nm\mathbf{k}$). The data plotted here corresponds to MoS_2 with all the bands required for convergence. Panel A shows the matrix elements considering only a single grid of $6 \times 6 \times 1$ $\mathbf{k}$-points. The DKE (panel C) and FKE (panel D) matrix elements are obtained from a $6 \times 6 \times 1$ coarse $\mathbf{K}$-grid and a $12 \times 12 \times 1$ double $\boldsymbol{\kappa}$-grid. The fine grid data (panel B) is simply what DKE and FKE try to approximate, i.e., the kernel matrix elements obtained with one single grid of $12 \times 12 \times 1$ $\mathbf{k}$-points.

3.2.4 Limitations of the approach

The double-grid approach presented in Sec. 3.1 is based on two approximations: the DKE (Eq. 3.1) and the approximation of the starting Haydock vector (Eq. 3.2). The DKE has been extensively analysed in Sec. 3.2.3. From the analysis, it emerges that the predominance of the matrix elements with $\mathbf{q} \approx 0$ is crucial to the success of the approximation. This is consistent with the spatial de-localisation of the exciton over many unit cells. Conversely, when the exciton is localised on few unit cells, as it is the case for instance in wide-gap insulators, the approximation may break down because of the significant contribution to the BSE kernel of matrix elements with $\mathbf{q} \neq 0$. We verified this is the case, for example, for bulk h-BN. The breakdown of the approach for these cases is, however, not critical. In fact, excitons that are localised on few unit cells can be described accurately with a modest $\mathbf{k}$-point sampling and the double-grid is not needed.

The approximation for the starting Haydock vector (Eq. 3.2) implies the assumption that (within the length gauge and the dipole approximation) the dipole matrix elements in the fine grid can be approximated by those in the coarse grid, namely,

$$\langle n\boldsymbol{\kappa}_{\mathbf{I}_i}|\ \hat{\mathbf{r}}\ |m\boldsymbol{\kappa}_{\mathbf{I}_i}\rangle \approx \langle n\mathbf{K}_{\mathbf{I}}|\ \hat{\mathbf{r}}\ |m\mathbf{K}_{\mathbf{I}}\rangle, \tag{3.7}$$

for $\boldsymbol{\kappa}_{\mathbf{I}_i} \in \mathbf{Dom}(\mathbf{K}_{\mathbf{I}})$, where $\hat{\mathbf{r}}$ is the position operator. This assumption can be verified at the level of the independent particle approximation (IPA) by comparing the IPA spectrum obtained with the double-grid approach (which we call Haydock-IP) with the IPA spectrum calculated on the fine grid. In fact, in the independent particle case, Eq. 3.7 is the only approximation introduced by the double grid. For the systems considered in Sec. 3.2, we verified that indeed the IPA spectra obtained within the double-grid approach agree well with the IPA calculated on the corresponding fine grid (see Fig. 3.10). It is also interesting to note that this particular approximation is valid for h-BN, which singles out the BSE kernel ($\mathbf{q} \approx 0$) approximation as the only factor hindering the application of the double-grid method to this material. In particular, GaAs shows a minor discrepancy in the IPA

spectra around 2.1 eV (see Fig. 3.10), a region of the spectrum where **k**-point convergence is markedly difficult. This is due to the steep dispersion of the conduction band of GaAs around the Gamma point, where the optical gap occurs (see, for example, [134]). As a result, the approximation of the oscillator strengths around Gamma by the corresponding matrix element at Gamma (Eq. 3.7) is a rather poor one, which translates into an unphysical feature around 2.1 eV in the BSE spectrum as well (see Fig. 3.3).

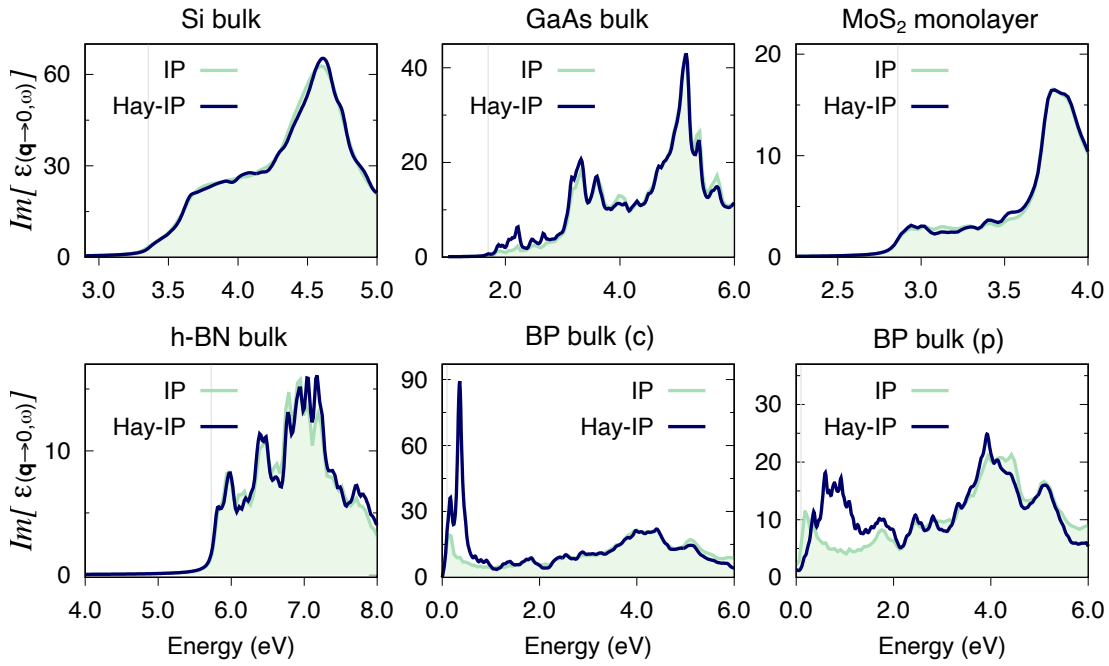

Figure 3.10: Optical absorption spectra calculated at the IP level using the double grid method (labelled Hay-IP) and *via* a regular (*full*) calculation on a dense grid (labelled IP). In all cases, the fine grid in the double-grid Haydock-IP calculation is of the same dimensions as the dense grid used in the regular IP calculation. The coarse grids and fine/dense grids used for each material are as follows. Si: $8 \times 8 \times 8$ and $60 \times 60 \times 60$, GaAs: $10 \times 10 \times 10$ and $40 \times 40 \times 40$, MoS_2: $12 \times 12 \times 1$ and $60 \times 60 \times 1$, h-BN: $12 \times 12 \times 4$ and $24 \times 24 \times 8$, BP(c): $14 \times 10 \times 4$ and $42 \times 30 \times 12$, BP(p): $5 \times 5 \times 6$ and $30 \times 30 \times 36$. All **k**-grids are Gamma-centred. The PW91 exchange-correlation functional [52] was used for BP.

There are also instances in which the approximation in Eq. 3.7 breaks down substantially. As an example, Fig. 3.10 shows this breakdown for the optical absorption of bulk black-phosphorus (BP) along the armchair direction (this material has been studied in Ref. [137]). The IPA spectrum obtained within the double-grid approach has strong peaks

around 0.3 eV which are not present in the reference calculation. The appearance of this artefact can be understood considering how the dipole matrix elements (Eq. 3.7) are calculated given that the position operator is ill-defined in a system with periodic boundary conditions. Within the linear regime, we use the commutation relation,

$$[\hat{H}, \mathbf{r}] = \hat{\mathbf{p}} + [V_{nl}, \hat{\mathbf{r}}], \tag{3.8}$$

where V_{nl} is the non-local part of the Hamiltonian $\hat{H}$ and $\hat{\mathbf{p}}$ is the momentum operator. This results in the dipole matrix elements being expressed as,

$$\langle n\mathbf{K_I}|\ \hat{\mathbf{r}}\ |m\mathbf{K_I}\rangle = \frac{\langle n\mathbf{K}_I|\ \hat{\mathbf{p}} + [V_{nl}, \mathbf{r}]\ |m\mathbf{K}_I\rangle}{E_{n\mathbf{K}_I} - E_{m\mathbf{K}_I}}. \tag{3.9}$$

BP has a minimum KS band-gap of about 0.2 eV (0.1 eV at the DFT level) and thus the corresponding dipole matrix element is large. Within the double-grid approach, all fine-grid $\boldsymbol{\kappa}$-points in the domain of the **K**-point corresponding to the minimum KS band-gap use the same value, which largely overestimates the actual dipole matrix element. Notably, carrying out the calculations in the primitive rather than in the conventional unit cell (see Fig. 3.10), improves the agreement with the reference IPA fine-grid spectrum, suggesting that in this case the coarse grid does a better job at sampling the Brillouin zone around the **K**-point corresponding to the minimum KS band-gap. Nevertheless, this Haydock-IP spectrum still presents artificial features between 0.5–1.0 eV, preventing the application of the double-grid method presented in this work to BP.

Overall, the intention of our double-grid approach was to reduce the computational and memory requirements of the BSE scheme by virtue of not using the fine-grid wavefuctions and avoiding the allocation of a matrix with the dimensions of the fine-grid e-h space. However, this resulted in very crude approximations and imposed severe limitations on the validity of the our method. In addition, the double-grid results are strongly dependent on the quality of the coarse-grid spectrum, which hinders the reliability and predictive power of

this approach. For these reasons, other BZ-interpolation schemes available in the literature are still preferable. In particular, the methods of Rohlfing *et al.* [66,79] and Gillet *et al.* [82] are able to deal with strongly bound excitons. Moreover, while they require the fine-grid wavefunctions, only the method by Rohlfing *et al.* allocates memory for a fine-grid BSE kernel. Instead, Gillet *et al.* avoid storing said matrix in memory by proposing an on-the-fly interpolation.

3.2.5 Usage recommendations

We now provide some recommendations for using the double-grid method presented here. Based on the discussion in Section 3.2.4, a minimal coarse grid must be identified, i.e., the coarser grid that nonetheless satisfies the approximation in Eq. 3.7. This is done in two steps. First, a *full* fine grid IPA calculation must be converged with respect to **k**-points, arriving, e.g., at a $60 \times 60 \times 60$ **k**-grid. The next stage would entail running several double-grid calculations at the IPA level with varying coarse grids and a fine grid of $60 \times 60 \times 60$ until the spectrum agrees with the *full* fine-grid IPA calculation (e.g., see top row of Fig. 3.10). We highlight this is a fairly inexpensive procedure as it only involves calculations at the IPA level.

We can then perform double-grid BSE calculations using the recently found minimal coarse grid. Alternatively, one may choose to go beyond that minimal coarse grid in an attempt to provide a better starting point for the double-grid BSE calculation (which is not always guaranteed, as explained in Section 3.2.1). With the chosen coarse grid, successive double-grid BSE calculations of increasing fine grid should be carried out in order to converge the dimensions of the latter. However, we highlight that convergence of the fine-grid in the double-grid method does not guarantee the validity of the DKE approximation. At this point, one should turn to available data, either experimental or theoretical, in order to assess the validity of the results on physical grounds. As mentioned above, this limits the reliability and predictive power of our method.

Chapter 4

Floquet approach to nonlinear optics at IPA level

We use Floquet theory (see Section 2.4) to reformulate the real-time approach to nonlinear optics (see Section 2.3.2) as a self-consistent time-independent eigenvalue problem. The proposed method applies to periodically-driven Hamiltonians and makes use of the dynamical Berry-phase polarisation, thus remaining valid for extended systems. We implemented this Floquet scheme at the independent particle level and compared it with the real-time approach. Our reformulation reproduces real-time-calculated 2^{nd} and 3^{rd} order susceptibilities for a number of bulk and two-dimensional materials, while reducing the associated computational cost by one or two orders of magnitude. [1]

As discussed in Section 2.3.2, the main drawback of the real-time approach to nonlinear optics [42] lies in the elevated computational cost associated with it. The latter stems from the expensive numerical integration of the EOMs (Eq. 2.59) combined with the long simulated times required to properly *dephase* the response. For periodically-driven systems, Floquet theory offers a time-independent framework which would naturally circumvent these shortcomings (See Section 2.4). In this work, we invoke Floquet theory to re-cast the EOM of the real-time approach as a time-independent self-consistent eigenproblem. This reformulation and its computational implementation are described in Section 4.1. Considerable atten-

[1] The work presented in Chapter 4 was carried out as part of this PhD and first appeared published in Alliati & Grüning, Electronic Structure, 5, 017001 (2023). Content from the published article is used here, with some emendations and changes of phrase to better elaborate the work.

tion is devoted to dealing with the Berry-phase expression for the electron-field coupling operator [42, 97], which makes our approach valid for extended systems and distinguishes it from previous Floquet works (e.g., [118]). In Section 4.2, the proposed Floquet approach is validated by computing nonlinear optical susceptibilities for a number of materials and comparing the spectra with the real-time results. An assessment of the computational cost required by our Floquet method is also provided, followed by a discussion on its limitations. The present Chapter is concerned exclusively with the IPA, while more advanced levels of theory are deferred to Chapter 5. Supplemental material regarding this development is presented in Appendix B.

4.1 Implementation

Throughout Chapters 4-6, we choose the IPA to be defined at the DFT level plus a static quasi-particle correction. With this assumption, the effective Hamiltonian in Eq. 2.61 takes the form of Eq. 2.63, which we repeat here for clarity,

$$\hat{H}^{\mathrm{IPA}} = \underbrace{\hat{H}^{KS}[\rho_0] + \hat{\Delta}_{\mathrm{QP}}[\varrho_0]}_{\hat{H}^{\mathrm{IPA},0}} + \hat{W}(\mathcal{E}), \tag{4.1}$$

where $\hat{H}^{\mathrm{IPA},0}$ represents the unperturbed Hamiltonian at the IPA level. It is composed of the KS Hamiltonian, $\hat{H}^{KS}[\rho_0]$, and the quasi-particle corrections, $\Delta_{\mathrm{QP}}[\varrho_0]$, for which we will use a rigid (scissor) shift. As explained in Section 2.3.2, the unperturbed Hamiltonian at the IPA level is time-independent while the time dependence of $\hat{H}^{\mathrm{IPA}}$ is confined to the electron-field coupling operator, $\hat{W}(\mathcal{E})$. Finally, since the unperturbed Hamiltonian, $\hat{H}^0$, is formulated at the DFT level, we can also refer to the zero-field states, $|\mu_{\mathbf{k}n}\rangle$, simply as KS states.

4.1.1 Time independent Floquet-Kohn-Sham basis

We start by defining the so-called Floquet-Kohn-Sham (FKS) basis. Let us assume that the effective Hamiltonian in Eq. 2.59 is time-periodic with a period, $T = \frac{2\pi}{\omega_0}$, given by the frequency of the perturbing electric field, ω_0. Invoking Floquet's theorem, one can assert this EOM will admit solutions in the form of Eq. 2.80, i.e., $e^{-i\xi_\alpha t}\ \phi_\alpha(t)$, where ξ_α is the Floquet quasi-energy and the time-dependent Floquet states, $\phi_\alpha(t)$, retain the periodicity of the Hamiltonian, $\phi_\alpha(t) = \phi_\alpha(t+T)$. The general solution to Eq. 2.59 would then be a linear combination of said functions,

$$|v_{\mathbf{k}n}\rangle = \sum_\alpha c^\alpha_{\mathbf{k}n}\ e^{-i\xi_\alpha t}\ |\phi_\alpha\rangle. \tag{4.2}$$

Making use of the adiabatic approximation for weak fields [121], we can assume each time-zero KS state will evolve adiabatically into a single Floquet state and retain only one term in the summation of Eq. 4.2, i.e.,

$$|v_{\mathbf{k}n}\rangle \approx e^{-i\xi_\alpha t}\ |\phi_\alpha\rangle = e^{-i\xi_{\mathbf{k}n} t}\ |\phi_{\mathbf{k}n}\rangle, \tag{4.3}$$

where we replaced the label α with the index of the state at $\mathbf{k}$-point $\mathbf{k}$ and band n. Projecting over the zero-field KS states, $|\mu_{\mathbf{k}n}\rangle$, we get,

$$|v_{\mathbf{k}n}\rangle = e^{-i\xi_{\mathbf{k}n} t}\ \sum_i^{+\infty} |\mu_{\mathbf{k}i}\rangle\langle\mu_{\mathbf{k}i}|\phi_{\mathbf{k}n}\rangle = e^{-i\xi_{\mathbf{k}n} t}\ \sum_i^{+\infty} d_{\mathbf{k}ni}(t)\ |\mu_{\mathbf{k}i}\rangle, \tag{4.4}$$

where the index i runs over both occupied and empty bands. As the coefficients $d_{\mathbf{k}ni}(t) \equiv \langle\mu_{\mathbf{k}i}|\phi_{\mathbf{k}n}\rangle$ retain the time periodicity of the Floquet states, $d_{\mathbf{k}ni}(t) = d_{\mathbf{k}ni}(t+T)$, they can be expanded in a Fourier series,

$$d_{\mathbf{k}ni}(t) = \sum_{\eta=-\infty}^{+\infty} e^{-i\eta\omega_0 t}\ \widetilde{d}_{\mathbf{k}ni}(\eta), \tag{4.5}$$

where η will be referred to as the Floquet mode. Finally, with Eqs. 4.4 and 4.5, we arrive at the representation of the time-dependent Bloch states we will use in this work,

$$|v_{\mathbf{k}n}\rangle = e^{-i\xi_{\mathbf{k}n}t} \sum_{\eta=-\infty}^{+\infty} e^{-i\eta\omega_0 t} \sum_{i}^{+\infty} \widetilde{d}_{\mathbf{k}ni}(\eta)\ |\mu_{\mathbf{k}i}\rangle, \tag{4.6}$$

where the coefficients $\widetilde{d}_{\mathbf{k}ni}(\eta)$ depend on the band index i and the Floquet mode η. The states given by $|\mathbf{k}ni;\eta\rangle \equiv e^{-i\xi_{\mathbf{k}n}t}\ e^{-i\eta\omega_0 t}\ |\mu_{\mathbf{k}i}\rangle$ form a basis for FKS space. This composite Hilbert space includes $\mathcal{L}_2[0,T]$ plus the space spanned by KS eigenvectors, i.e., $\mathcal{R}$. The inner product in $\mathcal{L}_2[0,T]\otimes\mathcal{R}$ is defined as $\langle\langle\cdot|\cdot\rangle\rangle \equiv \int_0^T dt\ \langle\cdot|\cdot\rangle$, with $\langle\cdot|\cdot\rangle$ the usual inner product in $\mathcal{R}$. The dimension of FKS space must be truncated to $N_b \times (2\eta_{\max}+1)$ for any practical calculation. N_b is the number of bands in the summation of Eq. 4.4 while $\eta_{\max}$ is the maximum Floquet mode used for the expansion in Eq. 4.5. In this work, we define $\eta_{\max}$ in relation to the FKS states, i.e., $\eta_{\max}$ implies the definition,

$$\widetilde{d}_{\mathbf{k}ni}(\eta) \equiv 0 \ \text{ if } |\eta| > \eta_{\max}. \tag{4.7}$$

4.1.2 Quasi-energy eigenproblem

The use of FKS basis in the EOM of the real-time approach (Eq. 2.59) allows us to turn it into a self-consistent time-independent eigenproblem. Choosing the Hamiltonian in Eq. 2.59 at the IPA level (Eq. 4.1) and expanding the time-dependent Bloch states in FKS basis (Eq. 4.6), we arrive at the EOM,

$$\sum_{j}^{+\infty}\sum_{\gamma=-\infty}^{+\infty} \left(\hat{H}^{\mathrm{IPA}}_{\mathbf{k}} - i\partial_t\right) e^{-i\xi_{\mathbf{k}n}t} e^{-i\gamma\omega_0 t}\ \widetilde{d}_{\mathbf{k}nj}(\gamma)|\mu_{\mathbf{k}j}\rangle = 0. \tag{4.8}$$

Acting the operators $\hat{H}^0$ and $-i\partial_t$ we obtain,

$$\sum_{j}^{+\infty}\sum_{\gamma=-\infty}^{+\infty} \left(E^{\mathrm{IPA}}_{\mathbf{k}j} + \hat{W}_{\mathbf{k}}(t) - \xi_{\mathbf{k}n} - \gamma\omega_0\right) e^{-i\xi_{\mathbf{k}n}t} e^{-i\gamma\omega_0 t}\ \widetilde{d}_{\mathbf{k}nj}(\gamma)|\mu_{\mathbf{k}j}\rangle = 0, \tag{4.9}$$

where E^{IPA} are the KS energies shifted by the quasi-particle corrections and the time-dependence of $\hat{W}_{\mathbf{k}}(\mathcal{E})$ is shown explicitly. We multiply to the left by $\int dt\; e^{+i\xi_{\mathbf{k}n}t}\; e^{+i\eta\omega_0 t}\; \langle\mu_{\mathbf{k}i}|$ and arrive at,

$$\sum_{j}^{+\infty}\sum_{\gamma=-\infty}^{+\infty}\Big[\left(E^{\mathrm{IPA}}_{\mathbf{k}j}-\xi_{\mathbf{k}n}-\gamma\omega_0\right)\delta_{i,j}\delta_{\eta,\gamma}\;+W_{\mathbf{k}ij}(\eta,\gamma)\Big]\;\widetilde{d}_{\mathbf{k}nj}(\gamma)=0, \tag{4.10}$$

where $W_{\mathbf{k}ij}(\eta,\gamma)$ are the matrix elements of $\hat{W}_{\mathbf{k}}(t)$ in FKS space. It is also worth noting that the operator $\left(\hat{H}^0_{\mathbf{k}}-i\partial_t\right)$ is diagonal in FKS space, with matrix elements given by $\left(E^{\mathrm{IPA}}_{\mathbf{k}j}-\xi_{\mathbf{k}n}-\gamma\omega_0\right)$. Now, Eq. 4.10 can be rearranged as an eigenvalue problem for the Floquet quasi-energies,

$$\sum_{j}^{+\infty}\sum_{\gamma=-\infty}^{+\infty}\Big[\left(E^{\mathrm{IPA}}_{\mathbf{k}j}-\gamma\omega_0\right)\delta_{i,j}\delta_{\eta,\gamma}\;+W_{\mathbf{k}ij}(\eta,\gamma)\Big]\;\widetilde{d}_{\mathbf{k}nj}(\gamma)=\xi_{\mathbf{k}n}\;\widetilde{d}_{\mathbf{k}ni}(\eta). \tag{4.11}$$

We define the operator on the LHS of Eq. 4.11 as the quasi-energy operator $\hat{\mathcal{K}}^{\mathrm{IPA}}_{\mathbf{k}}$. Its matrix elements in FKS space are (cf. Eq. 2.87),

$$\mathcal{K}^{\mathrm{IPA}}_{\mathbf{k}ij}\left(\eta,\gamma\right)=\left(E^{\mathrm{IPA}}_{\mathbf{k}j}-\gamma\omega_0\right)\delta_{i,j}\delta_{\eta,\gamma}\;+W_{\mathbf{k}ij}(\eta,\gamma), \tag{4.12}$$

and the eigenvalue problem in Eq. 4.11 reduces to the shorthand notation (cf. Eq. 2.83),

$$\sum_{j}^{+\infty}\sum_{\gamma=-\infty}^{+\infty}\mathcal{K}^{\mathrm{IPA}}_{\mathbf{k}ij}\left(\eta,\gamma\right)\;\widetilde{d}_{\mathbf{k}nj}(\gamma)=\xi_{\mathbf{k}n}\;\widetilde{d}_{\mathbf{k}ni}(\eta), \tag{4.13}$$

Formally, the matrix elements $W_{\mathbf{k}ij}(\eta,\gamma)$ can be obtained by expressing the time-periodic electron-field coupling operator in Floquet space, i.e., $\hat{W}_{\mathbf{k}}(t)=\sum_{\zeta=-\infty}^{+\infty}e^{-i\omega_0\zeta t}\;\tilde{W}_{\mathbf{k}}(\zeta)$, and taking the inner product,

$$W_{\mathbf{k}ij}(\eta,\gamma)=\int dt\;e^{+i\omega_0\eta t}\sum_{\zeta=-\infty}^{+\infty}e^{-i\omega_0\zeta t}\;e^{-i\omega_0\gamma t}\;\langle\mu_{\mathbf{k}i}|\tilde{W}_{\mathbf{k}}(\zeta)|\mu_{\mathbf{k}j}\rangle. \tag{4.14}$$

Replacing the time integral with a delta function, we arrive at,

$$\begin{aligned} W_{\mathbf{k}ij}(\eta,\gamma) &= \sum_{\zeta=-\infty}^{+\infty} \delta_{\zeta,\eta-\gamma}\, \langle \mu_{\mathbf{k}i}|\tilde{W}_{\mathbf{k}}(\zeta)|\mu_{\mathbf{k}j}\rangle \\ &= \langle \mu_{\mathbf{k}i}|\tilde{W}_{\mathbf{k}}(\eta-\gamma)|\mu_{\mathbf{k}j}\rangle. \end{aligned} \tag{4.15}$$

An expression for $W_{\mathbf{k}ij}(\eta,\gamma)$ will be obtained in Section 4.1.3. We can anticipate from Eq. 4.15 that $W_{\mathbf{k}ij}(\eta,\gamma)$ will couple different Floquet modes in the eigenproblem of Eq. 4.11.

4.1.3 Electron-field coupling operator $\hat{W}(\mathcal{E})$

In order to obtain the matrix elements $W_{\mathbf{k}ij}(\eta,\gamma)$ (Eq. 4.15), we consider a sinusoidal electric field of amplitude $\mathcal{E}_0$ and frequency ω_0, and re-write Eq. 2.71 as,

$$\begin{aligned} \hat{w}_{\mathbf{k}} &= i\tfrac{e}{4\pi} \sum_{i=1}^{3} N_{\alpha}^{\parallel} \left(\mathcal{E}_0 \cdot \mathbf{a}_i\right) \sum_{\sigma} \sigma \left(\tfrac{e^{i\omega_0 t} - e^{-i\omega_0 t}}{2i}\right) \hat{P}_{\mathbf{k}\mathbf{k}_{\alpha}^{\sigma}} \\ &= \tfrac{e}{8\pi} \sum_{i=1}^{3} N_{\alpha}^{\parallel} \left(\mathcal{E}_0 \cdot \mathbf{a}_i\right) \sum_{\sigma} \sigma \sum_{\sigma_2} \sigma_2\, e^{\sigma_2\, i\omega_0 t} \hat{P}_{\mathbf{k}\mathbf{k}_{\alpha}^{\sigma}}, \end{aligned} \tag{4.16}$$

where $\sigma_2 = \pm 1$. The summations in Eq. 4.16 add up to twelve equivalent terms. In what follows, we will work with just one of them for simplicity. Choosing the positive exponential ($\sigma_2 = +1$) and replacing $\mathbf{k}_{\alpha}^{\sigma}$ by $\mathbf{k}^{+}$, we define,

$$\hat{\mathcal{P}}_{\mathbf{k}\mathbf{k}^{+}}^{+} = e^{+i\omega_0 t} \hat{P}_{\mathbf{k}\mathbf{k}^{+}}. \tag{4.17}$$

We start by acting $\hat{\mathcal{P}}_{\mathbf{k}\mathbf{k}^{+}}^{+}$ on a time-dependent Bloch state,

$$\hat{\mathcal{P}}_{\mathbf{k}\mathbf{k}^{+}}^{+}\, |v_{\mathbf{k}n}\rangle = \hat{\mathcal{P}}_{\mathbf{k}\mathbf{k}^{+}}^{+}\, e^{-i\xi_{\mathbf{k}n}t} \sum_{\gamma=-\infty}^{+\infty} e^{-i\gamma\omega_0 t} \sum_{j}^{+\infty} \widetilde{d}_{\mathbf{k}nj}(\gamma)|\mu_{\mathbf{k}j}\rangle, \tag{4.18}$$

where we have expanded the state $|v_{\mathbf{k}n}\rangle$ in FKS basis as shown in Eq. 4.6. Multiplying the RHS of Eq. 4.18 to the left by $\int dt\; e^{+i\xi_{\mathbf{k}n}t}\; e^{+i\eta\omega_0 t}\; \langle\mu_{\mathbf{k}i}|$, we arrive at

$$\sum_{\gamma=-\infty}^{+\infty}\sum_{j}^{+\infty}\int dt \quad e^{+i\eta\omega_0 t}\;\langle\mu_{\mathbf{k}i}|\;\hat{\mathcal{P}}^{+}_{\mathbf{k}\mathbf{k}^{+}}\;|\mu_{\mathbf{k}j}\rangle\;e^{-i\gamma\omega_0 t}\;\widetilde{d}_{\mathbf{k}nj}(\gamma)$$
$$= \textstyle\sum_{\gamma=-\infty}^{+\infty}\sum_{j}^{+\infty}\mathcal{P}^{+}_{\mathbf{k}\mathbf{k}^{+}ij}(\eta,\gamma)\;\widetilde{d}_{\mathbf{k}nj}(\gamma). \tag{4.19}$$

In Eq. 4.19, we have extracted an expression for the matrix elements of the projector,

$$\mathcal{P}^{+}_{\mathbf{k}\mathbf{k}^{+}ij}(\eta,\gamma) = \int dt\; e^{+i\eta\omega_0 t}\;\langle\mu_{\mathbf{k}i}|\;\hat{\mathcal{P}}_{\mathbf{k}\mathbf{k}^{+}}\;|\mu_{\mathbf{k}j}\rangle\;e^{-i\gamma\omega_0 t}. \tag{4.20}$$

Using Eqs. 2.72 and 4.17, we find,

$$\mathcal{P}^{+}_{\mathbf{k}\mathbf{k}^{+}ij}(\eta,\gamma) = \int dt\; e^{+i(\eta+1)\omega_0 t}\;\langle\mu_{\mathbf{k}i}|\sum_{m}^{M}|\tilde{v}_{\mathbf{k}^{+}m}\rangle\langle v_{\mathbf{k}m}|\mu_{\mathbf{k}j}\rangle\;e^{-i\gamma\omega_0 t}. \tag{4.21}$$

The dual $|\tilde{v}_{\mathbf{k}^{+}m}\rangle$ can be expressed via the overlaps matrix as in Eq. 2.73,

$$\mathcal{P}^{+}_{\mathbf{k}\mathbf{k}^{+}ij}(\eta,\gamma) = \int dt\; e^{+i(\eta+1)\omega_0 t}\;\langle\mu_{\mathbf{k}i}|\sum_{m}^{M}\sum_{m_1}^{M}[S^{-1}_{\mathbf{k}\mathbf{k}^{+}}]_{m_1,m}\;|v_{\mathbf{k}^{+}m_1}\rangle\langle v_{\mathbf{k}m}|\mu_{\mathbf{k}j}\rangle\;e^{-i\gamma\omega_0 t}. \tag{4.22}$$

Eq. 4.22 contains the inverse of the matrix $\mathbf{S}_{\mathbf{k}\mathbf{k}^{+}}$, i.e., the time-dependent overlap already defined in Eq. 2.74. Transforming Eq. 2.74 to FKS basis (Eq. 4.6), we arrive at,

$$[S_{\mathbf{k}\mathbf{k}^{+}}]_{m,m_1} \;=\; e^{+i\xi_{\mathbf{k}m}t}\;e^{-i\xi_{\mathbf{k}^{+}m_1}t}\textstyle\sum_{\zeta_2=-\infty}^{+\infty}\sum_{\eta_2=-\infty}^{+\infty}e^{+i\zeta_2\omega_0 t}e^{-i\eta_2\omega_0 t}\;\times$$
$$\textstyle\sum_{j_2}^{+\infty}\sum_{i_2}^{+\infty}\widetilde{d}^{*}_{\mathbf{k}mj_2}(\zeta_2)\langle\mu_{\mathbf{k}j_2}|\mu_{\mathbf{k}^{+}i_2}\rangle d_{\mathbf{k}^{+}m_1 i_2}(\eta_2). \tag{4.23}$$

Defining the time-zero zero-field overlaps as $[S^{0}_{\mathbf{k}\mathbf{k}^{+}}]_{j_2,i_2} = \langle\mu_{\mathbf{k}j_2}|\mu_{\mathbf{k}^{+}i_2}\rangle$ and making the replacement $\eta_2' = \eta_2 - \zeta_2$, we get to,

$$[S_{\mathbf{k}\mathbf{k}^{+}}]_{m,m_1} = \qquad e^{+i\xi_{\mathbf{k}m}t}\;e^{-i\xi_{\mathbf{k}^{+}m_1}t}\textstyle\sum_{\eta_2'=-\infty}^{+\infty}e^{-i\eta_2'\omega_0 t}\;\times$$
$$\left(\textstyle\sum_{\zeta_2=-\infty}^{+\infty}\sum_{j_2}^{+\infty}\sum_{i_2}^{+\infty}\widetilde{d}^{*}_{\mathbf{k}mj_2}(\zeta_2)[S^{0}_{\mathbf{k}\mathbf{k}^{+}}]_{j_2,i_2}d_{\mathbf{k}^{+}m_1 i_2}(\eta_2'+\zeta_2)\right). \tag{4.24}$$

We now define the terms in the parentheses of Eq. 4.24 as $[\widetilde{S}_{\mathbf{k}\mathbf{k}^+}]_{m,m_1}(\eta_2')$ and obtain,

$$[S_{\mathbf{k}\mathbf{k}^+}]_{m,m_1} = e^{+i\xi_{\mathbf{k}m}t}\, e^{-i\xi_{\mathbf{k}^+m_1}t} \sum_{\eta_2'=-\infty}^{+\infty} e^{-i\eta_2'\omega_0 t}[\widetilde{S}_{\mathbf{k}\mathbf{k}^+}]_{m,m_1}(\eta_2'), \tag{4.25}$$

which implies the need for a self-consistent solution to the eigenproblem in Eq. 4.11, given that the matrix elements $W_{\mathbf{k}ij}(\eta,\gamma)$ will depend on the solutions $\{\widetilde{d}_{\mathbf{k}ni}(\eta)\}_{\mathbf{k},n,i,\eta}$ through the overlap matrices $[S_{\mathbf{k}\mathbf{k}^+}]_{m,m_1}$.

According to Eq. 4.22, we need the inverse of the matrix $\mathbf{S}_{\mathbf{k}\mathbf{k}^+}$. How this inversion is performed will be discussed in Section 4.1.4. For now, we will assume we can find an expression for $[S^{-1}_{\mathbf{k}\mathbf{k}^+}]_{m_1,m}$ expanded in Floquet modes as,

$$[S^{-1}_{\mathbf{k}\mathbf{k}^+}]_{m_1,m} = e^{-i\xi_{\mathbf{k}m}t}\, e^{+i\xi_{\mathbf{k}^+m_1}t} \sum_{\eta_2'=-\infty}^{+\infty} e^{-i\eta_2'\omega_0 t}[\widetilde{D}_{\mathbf{k}\mathbf{k}^+}]_{m_1,m}(\eta_2'), \tag{4.26}$$

where the signs of the quasi-energy exponentials have been inverted with respect to Eq. 4.25. Inserting Eq. 4.26 into Eq. 4.22, we arrive at,

$$\begin{aligned}\mathcal{P}^+_{\mathbf{k}\mathbf{k}^+ij}(\eta,\gamma) = \int dt\; e^{-i(\gamma-\eta-1)\omega_0 t} \textstyle\sum_m^M \sum_{m_1}^M e^{-i\xi_{\mathbf{k}m}t}\, e^{+i\xi_{\mathbf{k}^+m_1}t} \;\times \\ \langle\mu_{\mathbf{k}i}|\left(\textstyle\sum_{\eta_2'=-\infty}^{+\infty} e^{-i\eta_2'\omega_0 t}[\widetilde{D}_{\mathbf{k}\mathbf{k}^+}]_{m_1,m}(\eta_2')|v_{\mathbf{k}^+m_1}\rangle\langle v_{\mathbf{k}m}|\right)|\mu_{\mathbf{k}j}\rangle.\end{aligned} \tag{4.27}$$

Furthermore, we now use Eq. 4.6 to replace the time-dependent Bloch states in Eq. 4.27 as,

$$\langle v_{\mathbf{k}m}| = e^{+i\xi_{\mathbf{k}m}t} \sum_{\zeta_1=-\infty}^{+\infty} e^{+i\zeta_1\omega_0 t} \sum_{i_3}^{+\infty} \widetilde{d}^*_{\mathbf{k}mi_3}(\zeta_1)\langle\mu_{\mathbf{k}i_3}| \tag{4.28}$$

and

$$|v_{\mathbf{k}^+m_1}\rangle = e^{-i\xi_{\mathbf{k}^+m_1}t} \sum_{\eta_1=-\infty}^{+\infty} e^{-i\eta_1\omega_0 t} \sum_{i_1}^{+\infty} \widetilde{d}_{\mathbf{k}^+m_1i_1}(\eta_1)|\mu_{\mathbf{k}^+i_1}\rangle. \tag{4.29}$$

Inserting Eqs. 4.28 and 4.29 into Eq. 4.27, the quasi-energy exponentials cancel each other

out and we arrive at,

$$\mathcal{P}^{+}_{\mathbf{k}\mathbf{k}^{+}ij}(\eta,\gamma) = \int dt\; e^{-i(\gamma-\eta-1)\omega_0 t} \sum_{m}^{M}\sum_{m_1}^{M}\sum_{\eta_2'=-\infty}^{+\infty} e^{-i\eta_2'\omega_0 t}[\widetilde{D}_{\mathbf{k}\mathbf{k}^{+}}]_{m_1,m}(\eta_2') \;\times$$
$$\sum_{\eta_1=-\infty}^{+\infty} e^{-i\eta_1\omega_0 t} \sum_{i_1}^{+\infty} \widetilde{d}_{\mathbf{k}^{+}m_1 i_1}(\eta_1)\langle\mu_{\mathbf{k}i}|\mu_{\mathbf{k}^{+}i_1}\rangle \sum_{\zeta_1=-\infty}^{+\infty} e^{+i\zeta_1\omega_0 t} \sum_{i_3}^{+\infty} \widetilde{d}^{*}_{\mathbf{k}mi_3}(\zeta_1)\langle\mu_{\mathbf{k}i_3}|\mu_{\mathbf{k}j}\rangle, \quad (4.30)$$

where $\langle\mu_{\mathbf{k}i_3}|\mu_{\mathbf{k}j}\rangle = \delta_{i_3,j}$ eliminates the summation over i_3 and a new zero-field overlap is formed, namely $[S^0_{\mathbf{k}\mathbf{k}^{+}}]_{i,i_1} = \langle\mu_{\mathbf{k}i}|\mu_{\mathbf{k}^{+}i_1}\rangle$. Grouping all the Floquet mode summations and exponentials together, we obtain,

$$\mathcal{P}^{+}_{\mathbf{k}\mathbf{k}^{+}ij}(\eta,\gamma) = \textstyle\sum_{\eta_2'=-\infty}^{+\infty}\sum_{\eta_1=-\infty}^{+\infty}\sum_{\zeta_1=-\infty}^{+\infty}\left(\int dt\; e^{-i(\gamma-\eta-1+\eta_2'+\eta_1-\zeta_1)\omega_0 t}\right) \;\times$$
$$\textstyle\sum_{m}^{M}\sum_{m_1}^{M}\;[\widetilde{D}_{\mathbf{k}\mathbf{k}^{+}}]_{m_1,m}(\eta_2')\;\sum_{i_1}^{+\infty}\;\widetilde{d}_{\mathbf{k}^{+}m_1 i_1}(\eta_1)[S^0_{\mathbf{k}\mathbf{k}^{+}}]_{i,i_1}\;\widetilde{d}^{*}_{\mathbf{k}mj}(\zeta_1), \quad (4.31)$$

where the first parenthesis encapsulates the time dependence. This term results in the condition $(\gamma-\eta-1+\eta_2'+\eta_1-\zeta_1)=0$. Choosing to replace ζ_1 and thus eliminating this summation via $\delta_{\zeta_1,\gamma-\eta-1+\eta_2'+\eta_1}$, we finally arrive at,

$$\mathcal{P}^{+}_{\mathbf{k}\mathbf{k}^{+}ij}(\eta,\gamma) = \sum_{m}^{M}\;\; \textstyle\sum_{\eta_2'=-\infty}^{+\infty}\sum_{\eta_1=-\infty}^{+\infty}\widetilde{d}^{*}_{\mathbf{k}mj}(\gamma-\eta-1+\eta_2'+\eta_1)\;\times$$
$$\textstyle\sum_{m_1}^{M}\;[\widetilde{D}_{\mathbf{k}\mathbf{k}^{+}}]_{m_1,m}(\eta_2')\;\sum_{i_1}^{+\infty}[S^0_{\mathbf{k}\mathbf{k}^{+}}]_{i,i_1}\widetilde{d}_{\mathbf{k}^{+}m_1 i_1}(\eta_1). \quad (4.32)$$

The expressions for the eleven remaining instances of $\hat{\mathcal{P}}^{\sigma_2}_{\mathbf{k}\mathbf{k}^{\sigma}_i}$ can be derived by analogy to Eq. 4.32. Once all these projectors are computed, we can go back to Eqs. 4.16, 4.17 and 2.70 to finally obtain the matrix elements of the electron-field coupling operator $W_{\mathbf{k}ij}(\eta,\gamma)$ in FKS space.

To summarise, we have laid out all the steps needed to reformulate the time-dependent real-time EOM (Eq. 2.59) into a time-independent eigenproblem (Eq. 4.11) in FKS basis (Eq. 4.6). Crucially, our scheme is valid for extended systems since we use the Berry-phase derived electron-field coupling operator. The latter depends on the solutions $\{\widetilde{d}_{\mathbf{k}ni}(\eta)\}_{\mathbf{k},n,i,\eta}$

and thus the eigenproblem in Eq. 4.11 must be solved self-consistently. As our Floquet reformulation is time-independent, it does not require expensive numerical time-integrations, which will alleviate the computational burden. Nonetheless, we retain the main advantage of the real-time approach, i.e., the scheme remains non-perturbative in the electric field, allowing for the simultaneous calculation of susceptibilities to different orders in the electric field.

4.1.4 Computational implementation

The Floquet scheme presented here involves, for each frequency ω_0, a self-consistency cycle where the eigenvectors calculated in one iteration (solving Eq. 4.11) are fed to the next one (Eqs. 4.24 and 4.32) until convergence is reached. The condition for convergence is based on the absolute error in the real and imaginary parts of the susceptibility to every order requested by the user. Algorithm 4.1.4 shows the main steps in a Floquet calculation as implemented in our code. As the real-time approach [42], our Floquet code offers parallelisation in frequencies and **k**-points. Moreover, it works both in the non-magnetic (spin unpolarised) and magnetic non-collinear (spinorial) formulations.

In general, the size of the various matrices in Algorithm 4.1.4 is determined by number of bands in KS space, N_b, and the total number of Floquet modes, $(2\eta_{\max}+1)$. For instance, the matrices $\hat{\mathcal{P}}^{\pm}_{\mathbf{k}\mathbf{k}^{\sigma}_{i}}$, $W_{\mathbf{k}}$ and $\mathcal{K}_{\mathbf{k}}$ are of dimension $N_b \times (2\eta_{\max}+1)$, which would amount to 40 in a SHG calculation ($\eta_{\max}=2$) of a system with 8 bands. We note that the number of **k**-points in the system does not enter in the size of the matrices. Instead, it determines the number of matrices, e.g., there is one $\mathcal{K}_{\mathbf{k}}$ eigenproblem per IBZ **k**-point. In the case of the projector, $\hat{\mathcal{P}}^{\pm}_{\mathbf{k}\mathbf{k}^{\sigma}_{i}}$, the number of matrices scales with the pairs of adjacent **k**-points. Finally, the dimension of the overlap matrices, $S_{\mathbf{k}\mathbf{k}^{\sigma}_{i}}$, is given by the number of occupied bands, M. The number of said matrices is determined by the pairs of adjacent **k**-points times the magnitude $(2\times 2\eta_{\max}+1)$, which arises from subtraction of Floquet modes (see step between Eqs. 4.23-4.24).

Algorithm 1 Workflow of a Floquet calculation as implemented in this work. A simplified convergence condition is shown for clarity, while the code checks both real and imaginary parts of the susceptibilities to every order requested by the user. The subscript *it* refers to the iteration number while *thr* denotes an accuracy threshold specified by the user.

for ω in frequency range **do**
  while self-consistency not reached **do**
    for **k**-point in IBZ **do**
      invert overlap matrices $S_{\mathbf{k}\mathbf{k}_i^\sigma}$ (Eqs. 4.24-4.26)
      compute projectors $\hat{\mathcal{P}}^{\pm}_{\mathbf{k}\mathbf{k}_i^\sigma}$ (Eq. 4.32)
      build $W_{\mathbf{k}ij}(\eta,\gamma)$ matrix elements (Eqs. 2.71,4.16,4.17)
      build $\mathcal{K}_{\mathbf{k}ij}(\eta,\gamma)$ matrix elements (Eq. 4.12)
      diagonalise $\mathcal{K}_{\mathbf{k}ij}(\eta,\gamma)$
    end for
    calculate Polarisation $\mathbf{P}_\alpha$ (Eq. 2.75)
    extract susceptibilities $\chi^{(n)}$ (Eq. 2.76,2.77)
    if ($\mathrm{Im}(\chi^{(n)}_{it} - \chi^{(n)}_{it-1}) < thr$) **then**
      break while loop at ω
    end if
  end while
end for

One of the challenges met during this implementation concerns the inversion of the overlap matrix $\mathbf{S}_{\mathbf{k}\mathbf{k}^+}$, which is required to obtain the coefficients $[\widetilde{D}_{\mathbf{k}\mathbf{k}^+}]_{m_1,m}(\eta_2')$ as defined in Eq. 4.26. To this end, two strategies were implemented and compared. The first one would entail avoiding the time domain entirely and remaining in Floquet space, i.e., one could obtain the coefficients $[\widetilde{D}_{\mathbf{k}\mathbf{k}^+}]_{m_1,m}(\eta_2')$ (see Eq. 4.26) directly from the coefficients $[\widetilde{S}_{\mathbf{k}\mathbf{k}^+}]_{m_1,m}(\eta_2')$ (see Eq. 4.25). This is indeed possible for scalar functions [138] and was extended to matrices as part of this work. The alternative option is to trivially go to the time domain evaluating Eq. 4.25 for several sample times t_i, invert the matrices $[S_{\mathbf{k}\mathbf{k}^+}]_{m_1,m}(t_i)$ numerically at each t_i, and Fourier transform the resulting $[S^{-1}_{\mathbf{k}\mathbf{k}^+}]_{m_1,m}(t_i)$ back to Floquet space, i.e., solve Eq. 4.26 for $[\widetilde{D}_{\mathbf{k}\mathbf{k}^+}]_{m_1,m}(\eta_2')$. This numerical inversion in time domain

resulted both more robust and less time-consuming than the approach based on Duffin's theorems [138].

The calculation of the polarisation *via* Eq. 2.75 proved to be another obstacle in our implementation. As before, the problem originates from the fact that what is available to us are the Floquet coefficients of each overlap matrix, $[\widetilde{S}_{\mathbf{kk}^+}]_{m_1,m}(\eta_2')$, rather than the matrix itself, $[S_{\mathbf{kk}^+}]_{m_1,m}$. Inserting Eq. 4.25 into Eq. 2.75, we see that we would need to calculate the logarithm of a sum, which should be linearised by expanding it into a logarithmic series if the $\eta_2' = 0$ term dominates. While this does indeed lead to a manageable set of equations to solve, it would turn our scheme into a perturbative one, thus losing one of the great advantages of the real-time approach. In fact, the issue of what order in this perturbative expansion corresponds to which order of the response in the electric field does not seem to be a trivial one. As before, the alternative is to switch to the time domain, i.e., evaluate Eq. 4.25 for a handful of sample times t_i, calculate the polarisation at each t_i with Eq. 2.75 and proceed with the usual steps in Eq. 2.77 to extract the required susceptibilities.

This resembles the usual choice one has in systems with translational invariance of going back and forth from real to reciprocal space to calculate whatever operator is simpler in either basis. By analogy, we can switch to time domain to perform a series of operations and then Fourier transform back to Floquet space. It is key to understand that transforming to the time domain does not necessarily imply the long simulated times and short time steps (i.e., tens of thousands of sample times) characteristic of the real-time approach to nonlinear optics. Rather, the assumed time periodicity means that one just needs to calculate the observables across one time period only. Moreover, the number of time steps required within that period is very limited as it corresponds to the total number of Floquet modes one needs for $[\widetilde{D}_{\mathbf{kk}^+}]_{m_1,m}(\eta_2')$, which happens to be $(2 \times 2\eta_{\max} + 1)$, i.e., $\eta_{\max}^S = 2\eta_{\max}$.

4.1.5 Dissipation effects

The inclusion of dissipation effects in the context of periodically-driven systems has been previously accomplished by adding an imaginary diagonal matrix to the quasi-energy operator [106]. In this work, we propose introducing these effects *via* a phenomenological dissipation term we define as,

$$i\,\Gamma^{(1)}_{\mathbf{k}ij}(\eta,\gamma)\;\equiv\; i\,\nu_1\,(1-\delta_{\gamma,0})\,\delta_{i,j}\delta_{\eta,\gamma}\;, \tag{4.33}$$

where ν_1 is a positive real number that provides the broadening to the spectra. The factor $(1-\delta_{\gamma,0})$, denoted by the subscript 1 or superscript (1), ensures that processes to all orders are damped to the same extent and will be further discussed in Section 5.1.3. Including the dissipation term into the quasi-energy operator of Eq. 4.12,

$$\mathcal{K}^{\mathrm{IPA}}_{\mathbf{k}ij}\,(\eta,\gamma) = \left(E^{\mathrm{IPA}}_{\mathbf{k}j} - \gamma\omega_0 - i\nu_1\,(1-\delta_{\gamma,0})\right)\delta_{i,j}\delta_{\eta,\gamma} + W_{\mathbf{k}ij}\,(\eta,\gamma)\,, \tag{4.34}$$

modifies the eigenproblem in Eq. 4.11 as,

$$\sum_{j}^{+\infty}\sum_{\gamma=-\infty}^{+\infty}\left[\left(E^{\mathrm{IPA}}_{\mathbf{k}j} - \gamma\omega_0 - i\nu_1\,(1-\delta_{\gamma,0})\right)\delta_{i,j}\delta_{\eta,\gamma} + W_{\mathbf{k}ij}(\eta,\gamma)\right]\,\widetilde{d}_{\mathbf{k}nj}(\gamma) = \xi_{\mathbf{k}n}\,\widetilde{d}_{\mathbf{k}ni}(\eta). \tag{4.35}$$

This addition can be understood in terms of an adiabatic switch-on of the electric field that happens at $t\to-\infty$. Let us multiply the RHS of Eq. 4.6 by a real exponential of the form,

$$|v_{\mathbf{k}n}\rangle = e^{-i\xi_{\mathbf{k}n}t}\sum_{\eta=-\infty}^{+\infty} e^{-i\eta\omega_0 t}\,\sum_{i}^{+\infty}\widetilde{d}_{\mathbf{k}ni}(\eta)\,|\mu_{\mathbf{k}i}\rangle\,e^{\nu_1(1-\delta_{\eta,0})\,t}, \tag{4.36}$$

where the limit $\nu_1\to 0$ is implied. We then act the time derivative operator of Eq. 2.59, $-i\partial_t$, on these newly defined time-dependent states, $|v_{\mathbf{k}n}\rangle$, as done to obtain Eq. 4.9 from Eq. 4.8. This results in adding the term $-i\nu_1\,(1-\delta_{\gamma,0})$ to Eq. 4.9, thus arriving at Eq. 4.34. We now consider what this term means for the time-dependent states themselves.

Evaluating Eq. 4.36 at $t \to -\infty$ results in suppressing all terms with $\eta \neq 0$,

$$|v_{\mathbf{k}n}\rangle(t \to -\infty) = e^{-i\xi_{\mathbf{k}n}t} \sum_{i}^{+\infty} \widetilde{d}_{\mathbf{k}ni}(\eta = 0)\, |\mu_{\mathbf{k}i}\rangle \; . \tag{4.37}$$

Formally, this requires that the time-dependent states, $|v_{\mathbf{k}n}\rangle$, be a superposition of KS states, $|\mu_{\mathbf{k}i}\rangle$, when the field is introduced at $t \to -\infty$. In practice, as we shall see in Chapter 6, the so-called central component ($i = n, \eta = 0$) of the eigenvector representing a state at **k**-point **k** and band n departs from unity only to a negligible extent, i.e., $\widetilde{d}_{\mathbf{k}n\; i=n}(\eta = 0) \approx 1$. Other $\eta = 0$ amplitudes, i.e., $\widetilde{d}_{\mathbf{k}n\; i\neq n}(\eta = 0)$, are usually in the order of $10^{-5} - 10^{-9}$. Therefore, the introduction of this dissipation term requires that, at $t \to -\infty$, a time-dependent state, $|v_{\mathbf{k}n}\rangle$, be equal to the corresponding KS state, $|\mu_{\mathbf{k}n}\rangle$.

This damping term deals with the rich structure of avoided crossings characteristic of Floquet quasi-energy operators, effectively removing the singularities that appear at resonant frequencies. At the IPA level, these Floquet crossings occur whenever a multiple of the frequency of the perturbation, ω_0, matches the energy difference between two states of the system, i.e., the unperturbed (diagonal) part of the quasi-energy operator becomes degenerate as a function of ω_0 (see Eq. 4.12).

As an example, we consider a two-state model with $\eta_{\max} = 1$. Let us focus on the crossing shown on the left side of Fig 4.1 between the zeroth mode of the valence state and the first positive mode of the conduction state, i.e., $(v, 0)$ and $(c, +1)$, respectively. This crossing occurs when the frequency of the perturbation, ω_0, matches the energy difference between the states, $E_c - E_v \equiv \omega_{res}$. In the absence of any coupling between these modes, i.e., $W_{ij}(\eta, \gamma) = 0$, the quasi-energy operator is diagonal and the eigenvectors are just the canonical vectors in the basis of choice (see top vector in Fig. 4.1). This means that the time-dependent state is simply the static (zeroth mode) valence state of the basis set, i.e., $\widetilde{d}_{\mathbf{k}vi=v}(\eta = 0) = 1$. The introduction of the electron-field coupling operator would imply non-zero off-diagonal matrix elements coupling the two modes in question. Even couplings in the order of $(E_c - E_v) \times 10^{-10}$ would result in an unreasonably high mixing of these

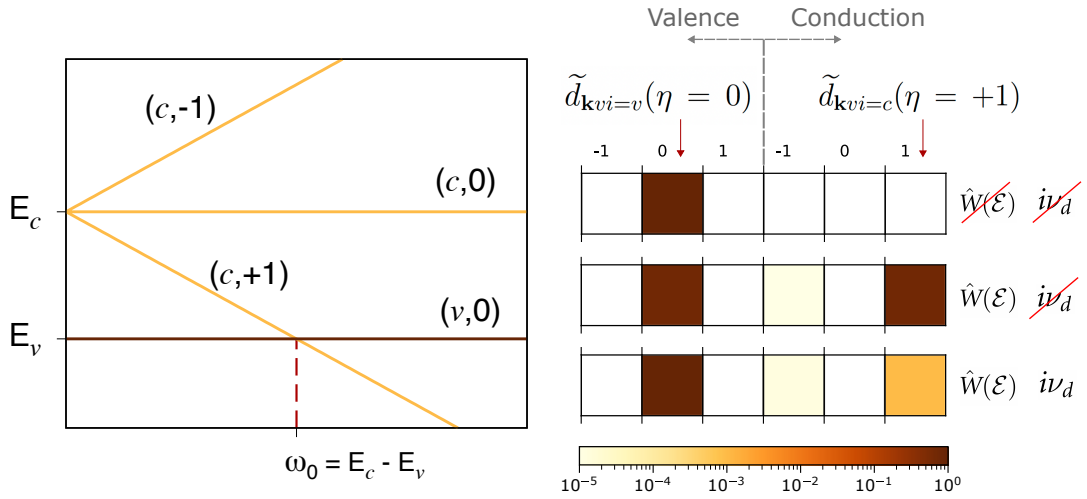

Figure 4.1: Left: representation of a Floquet crossing between the zeroth mode of the valence band and the first positive mode of the conduction band, which happens when the frequency of the perturbation, ω_0, matches the energy difference between the states, $E_c - E_v$. Right: colour-coded representation of a Floquet eigenvector $\widetilde{d}_{\mathbf{k}vi}(\eta)$ in a system with two-bands and $\eta_{\max} = 1$. The left (right) side of each vector represents projections over the valence (conduction) state, while the numbers on top of the first vector indicate the Floquet mode η. Each square represents a component (or amplitude) within the eigenvector, e.g., $\widetilde{d}_{\mathbf{k}vv}(0)$ is the so-called central component while $\widetilde{d}_{\mathbf{k}vc}(+1)$ represents the coupling component. The three eigenvectors shown correspond to different situations regarding the inclusion or not of the electron-field coupling operator and the dissipation effects.

states, i.e., $\widetilde{d}_{\mathbf{k}vi=v}(\eta = 0) \approx \widetilde{d}_{\mathbf{k}vi=c}(\eta = +1) \approx \frac{1}{\sqrt{2}}$ (see middle vector in Fig. 4.1). Not only this implies a far greater population inversion than expected for such a weak field, but also, it prevents the self-consistent loop from achieving convergence since the response function diverges. Upon including damping in the system, the imaginary contribution $-i\nu$ lifts the degeneracy between these eigenstates. This results in an eigenvector where the projection over the zeroth mode valence state remains close to one, $\widetilde{d}_{\mathbf{k}vi=v}(\eta = 0) \approx 1$, and the amplitude of the $(c, +1)$ mode is orders of magnitude smaller, e.g., 10^{-3} (see bottom vector in Fig. 4.1). As we will see in Chapter 6, this degree of coupling between the $(v, 0)$ and $(c, +1)$ modes gives the correct response function for the nonlinear regime under consideration.

In the real-time approach [42], this demotion of electrons from the conduction band back to the valence band is achieved by the dephasing term (see Eq. 2.78). The latter prevents

high population inversions and provides broadening to the spectra. For this reason, we tried formulating this operator in FKS basis and including it into the eigenproblem. While it did provide the correct broadening to the spectra, it also introduced instabilities into the self-consistent loop and was hence discarded. We note that other possible expressions for the dephasing operator result in imaginary contributions to the diagonal of the quasi-energy operator when transformed to FKS basis, which is similar to the dissipation included in Eq. 4.34.

We note that the quasi-energy matrix in Eq. 4.34 is no longer Hermitian due to the addition of these imaginary contributions to its diagonal. Therefore, we used a diagonalisation routine suitable for non-Hermitian matrices and verified that the imaginary part of the Floquet quasi-energies remained negligible. Finally, we also introduced a small imaginary contribution to some KS eigenenergies (typically $\nu_1 \times 10^{-4}$) in order to avoid singularities arising from degeneracies or crossings in the KS band structure. This applies to those eigenvalues that differ in less than, e.g., 1×10^{-7} Ha, and is only added at the zeroth Floquet mode.

4.2 Results and discussion

The Floquet approach to nonlinear optics presented in this Chapter has been implemented into the Yambo code [128,129] and tested with a number of well-known materials. The latter have been studied before from an *ab-initio* perspective [85,139–141] and within the real-time formalism in particular [42, 43], which makes them ideal for validating and benchmarking our method. To this end, a systematic comparison between the real-time [42] and Floquet approaches has been conducted, where the real-time calculations were also performed using the Yambo code [128,129]. The starting KS wavefunctions and energies were computed with Quantum Espresso [130] using norm-conserving pseudopotentials and the Perdew-Zunger LDA exchange-correlation functional [51]. The calculation of optical spectra was performed in the length gauge and within the dipole approximation.

	AlAs	h-BN	MoS_2
k-grids (nscf)	$30 \times 30 \times 30$	$48 \times 48 \times 1$	$24 \times 24 \times 1$
Bands (full,empty)	3 , 6	4 , 4	5 , 5
Band-gap correction [eV]	0.9	3.3	0.72
Broadening [eV]	0.04	0.15	0.15
Total time [fs]	118	83	85
Time step [as]	10 (2.5)	2.5	10
Floquet modes [$\eta_{\max}$]	2	2	2

Table 4.1: Computational details of the SHG calculations presented in Figs. 4.2-4.4. The total time and time step have been selected through convergence tests available in Appendix B. The time step in parentheses applies to the inset in Fig. 4.2

4.2.1 Second Harmonic Generation

In this section, we report selected SHG spectra for bulk AlAs, monolayer h-BN and monolayer MoS_2 calculated both *via* the real-time and Floquet approaches (see computational details in Table 4.1). Fig. 4.2 presents SHG spectra for bulk AlAs calculated by both methods. The agreement between the two spectra is almost complete, despite the small broadening deliberately used to highlight differences. The small discrepancies towards the 4 eV to 6 eV region are due to the choice of time-step in the real-time approach (see discussion below) and vanish with a shorter time step (see inset in Fig. 4.2 and details in Table 4.1). Nevertheless, we consider the larger time step in Fig. 4.2 (10 as) to be well converged for this calculation. Fig. 4.3 shows the spectra for h-BN while Fig. 4.4 presents data for MoS_2. It is apparent that the results produced by either method are indistinguishable from one another on this scale. This close matching between our Floquet method and the real-time approach was found across a variety of **k**-point grids and broadening conditions for all three materials, extending also to the linear response regime (the full set of SHG and linear response results is provided in Appendix B).

Both real-time and Floquet calculations were carefully converged with respect to the relevant parameters in each case (see convergence tests in Appendix B and the resulting parameters in Table 4.1). The Floquet approach requires convergence with respect to the number of Floquet modes included in each calculation, i.e., $\eta_{\max}$ as defined in Eq. 4.7. Our tests indicate that convergence with respect to $\eta_{\max}$ is very fast for SHG spectra, e.g., $\eta_{\max} =$

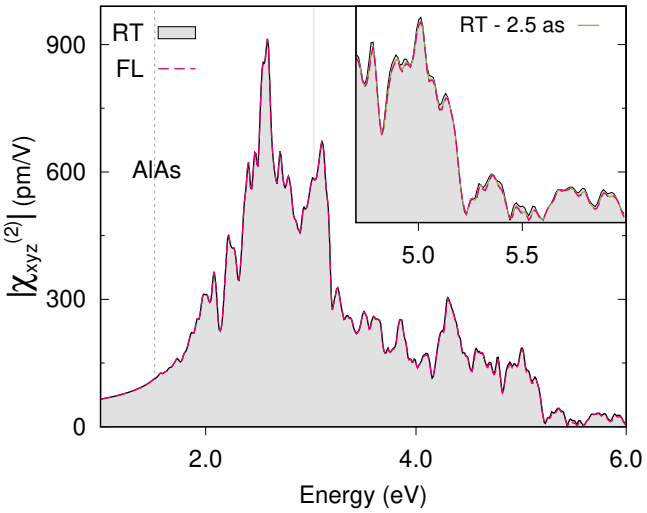

Figure 4.2: Bulk AlAs SHG spectra on a $30 \times 30 \times 30$ **k**-grid with a broadening of 0.04 eV, calculated by the real-time (RT) approach (black line with grey filling) and our Floquet (FL) method (pink dashed line). The intensity of the electric field is $1{\times}10^6$ W cm^{-2}. The real-time spectrum is calculated with a 10-as time step. The inset shows a portion of the spectrum re-calculated with a 2.5-as time step (green line), which reduces the discrepancies found in the 4 eV to 6 eV range between the Floquet and 10-as real-time spectra.

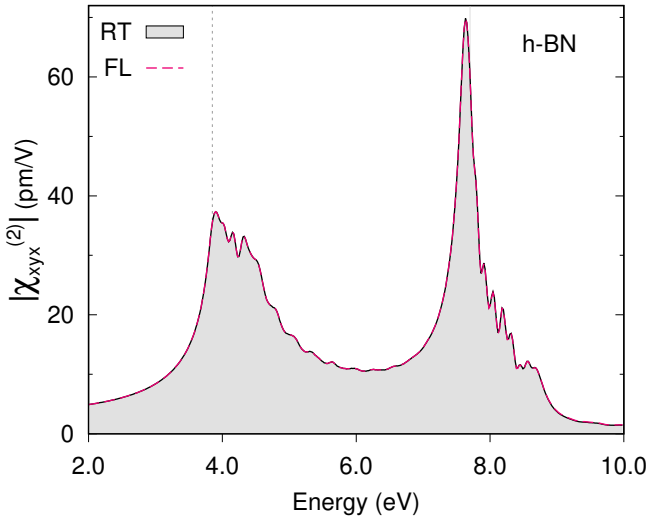

Figure 4.3: Monolayer h-BN SHG spectra on a $48 \times 48 \times 1$ **k**-grid with a broadening of 0.15 eV, calculated by the real-time (RT) approach (black line with grey filling) and our Floquet (FL) method (pink dashed line). The intensity of the electric field is $1{\times}10^6$ W cm^{-2}.

2 is enough to compute a well-converged SHG spectrum, even at higher intensities where higher-order contributions should play a greater role (see convergence tests in Appendix B). In addition, our Floquet method requires an accuracy threshold to control the self-

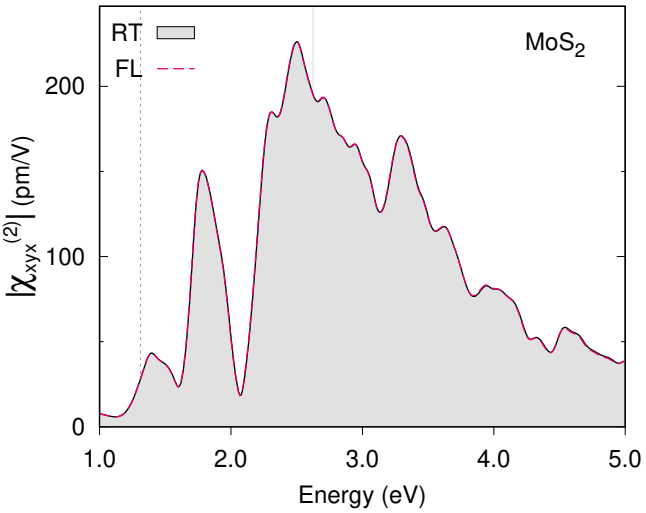

Figure 4.4: Monolayer MoS_2 SHG spectra on a $24 \times 24 \times 1$ **k**-grid with a broadening of 0.15 eV, calculated by the real-time (RT) approach (black line with grey filling) and our Floquet (FL) method (pink dashed line). The intensity of the electric field is 1×10^6 W cm^{-2}.

consistency loop. This threshold should be selected according to the magnitude of the response and will impact the computational cost of our approach through the number of iterations required. For SHG, we chose an accuracy threshold of 2.44×10^{-5} pm V^{-1}, which must be satisfied individually by both the real and imaginary parts of the second order susceptibility. This resulted in off-resonant frequencies converging within three iterations, while energies close to resonance took four or five iterations.

Convergence in the case of real-time calculations must be studied with respect to two crucial parameters, the total simulated time and the time step used in the numerical integration of the EOMs. Both are system-dependent and must be subjected to convergence tests for every material. Regarding the former parameter, failure to allow for sufficient simulated time would result the response not being properly dephased. In this case, some eigenmodes of the system will still be excited since the introduction of the electric field at time zero, manifesting as oscillations in the real-time spectrum. For instance, the well converged spectrum in Fig. 4.4 was obtained with 85 fs of total time. Fig. 4.5(a) shows the same spectra of Fig. 4.4 alongside an underconverged spectrum calculated with a total simulated time of 65 fs, which is evidently not enough to suppress these oscillations (see

blue curve in Fig. 4.5(a)).

In terms of the time step, this needs to be sufficiently small since longer steps, albeit more efficient, will introduce unphysical features in the spectra. For instance, the well-converged h-BN spectrum in Fig. 4.3 was obtained with a time step of 2.5 as. A portion of this spectrum was re-calculated with a low broadening (0.04 eV) to highlight these unphysical features and is shown in Fig. 4.5(b). While the well-converged 2.5-as spectrum matches Floquet closely, the real-time spectrum integrated with a 10 as step (thus, four times faster) is severely underconverged, as is apparent from the blue curve in Fig. 4.5(b). In our experience, a steeper dispesion in the band structure of a material correlated with faster dynamics, and therefore, the need for shorter time steps. This is in line with interpreting large curvatures at the extrema of the band dispersion as a small effective mass of the electrons. Overall, real-time spectra tend to the Floquet solution upon progressively increasing the total simulated time and decreasing the time step, as inferred from Fig. 4.5. Summarising, the convergence with numerical parameters impacts the execution time of the real-time approach to a larger extent with respect to the present formalism, which is not based on explicit time integration. The computational advantage of the Floquet approach over the real-time one is presented in Section 4.2.3.

4.2.2 Third Harmonic Generation

In this section, we report selected third harmonic generation (THG) spectra of bulk Si calculated both *via* the real-time and Floquet approaches. The full set of THG results can be found in Appendix B. Fig. 4.6 shows very good agreement between the spectra calculated by either method. Convergence of the Floquet approach was also fast in this case, requiring only $\eta_{\max} = 3$ for THG spectra. However, additional Floquet modes may be required at higher intensities in case one wants to capture higher-order contributions to the third order response, which are present in the real-time result. These contributions depend on the intensity of the electric field and thus gain relevance at high intensities. In order to

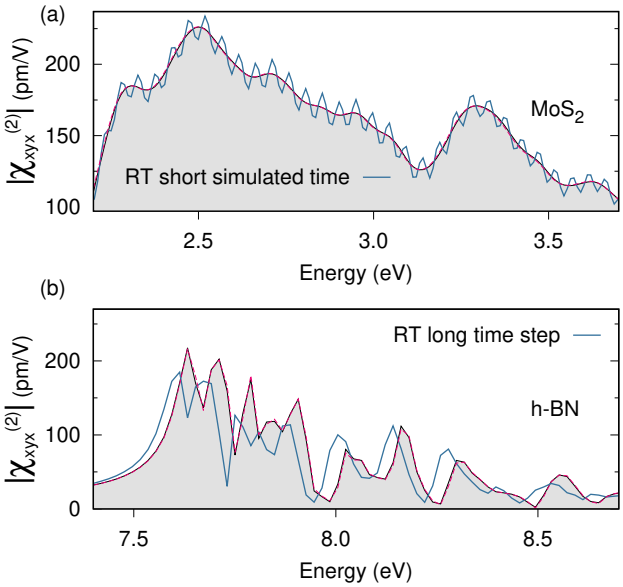

Figure 4.5: Effects of underconvergence with respect to total simulated time (a) and time step (b). Panel (a) shows the same spectra as Fig. 4.4 plus an underconverged real-time (RT) spectrum obtained with 65 fs of total time (blue line). The latter compares poorly with the 85 fs required to properly dephase the system (black line with grey filling) and approach the Floquet solution (pink dashed line). Panel (b) displays the spectra for h-BN obtained with a well-converged time step of 2.5 as (black line with grey filling), plus an underconverged real-time spectrum with 10 as (blue line) that fails to approach the Floquet solution (pink dashed line). At variance with Fig. 4.3, these spectra were calculated with a broadening of 0.04 eV to highlight the differences.

demonstrate this, we re-calculated a portion of these spectra with a perturbation of higher intensity and compared the results in Fig. 4.7. The latter shows that $\eta_{\max} = 3$ suffices to reproduce the low-intensity real-time result while additional Floquet modes ($\eta_{\max} = 5$) are required at higher intensities to capture these higher-order contributions.

4.2.3 Computational cost

We compared the computational cost of the real-time and Floquet approaches across the entire data set of SHG calculations. Our results account for a so-called Floquet speed-up of 1-2 orders of magnitude (see Fig. 4.8). This speed-up is calculated as the ratio of the CPU time required by either approach to perform the exact same calculation (see Appendix B for CPU time of each approach individually). Controlling the accuracy and convergence

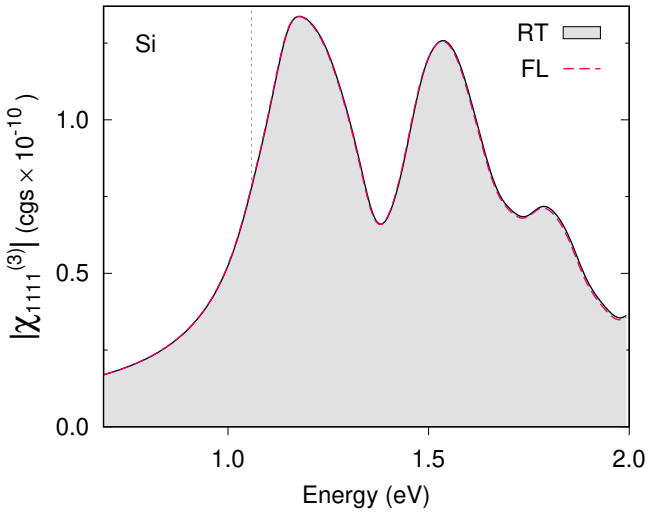

Figure 4.6: Bulk Si THG spectra on a $32 \times 32 \times 32$ **k**-grid with a broadening of 0.15 eV, calculated by the real-time (RT) approach (black line with grey filling) and our Floquet (FL) approach (pink dashed line). The intensity of the electric field is $1{\times}10^6$ W cm^{-2}. We used 4 occupied and 3 empty bands and a band gap correction of 0.6 eV. The real-time spectrum was calculated with a total time of 114 fs and a time step of 10 as. The Floquet spectrum was obtained with $\eta_{\max} = 3$.

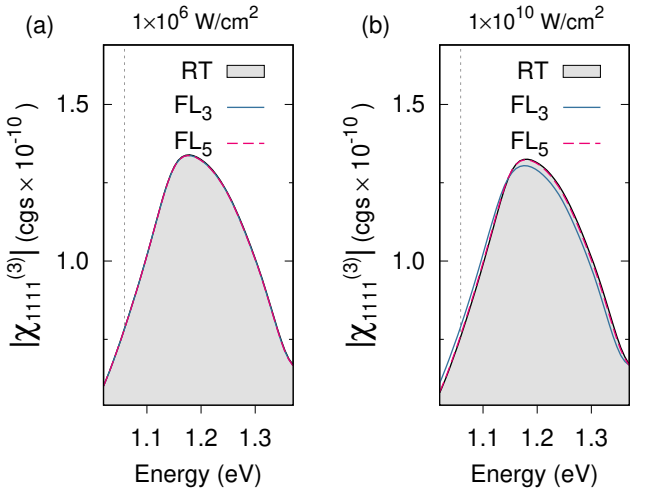

Figure 4.7: Higher-order contributions to THG spectra in bulk Si on a $32 \times 32 \times 32$ **k**-grid. Spectra are calculated by both the real-time (RT) and Floquet (FL) approaches with electric fields of two different intensities, i.e., $1{\times}10^6$ (a) and $1{\times}10^{10}$ W cm^{-2} (b). The number of Floquet modes is indicated in the legend as a subscript, e.g., FL_5 corresponds to $\eta_{\max} = 5$. Computational details in Fig. 4.6 apply, with two exceptions. A time step of 1 as was used to rule out underconvergence in the real-time spectrum as a reason for the discrepancies. The total simulated times were set in excess of those required by the convergence tests for the same reason.

of the spectra played an important role in this comparison. As regards Floquet, we used $\eta_{\max} = 2$, which is well converged, and a uniform self-consistent accuracy threshold for all calculations. We then verified the latter was smaller than 0.1% of the real-time result we intended to reproduce. We believe this is in line with what a regular user would do, however we note that there would have been potential for greater speed-ups had this threshold been fine-tuned in every calculation. As shown in Section 4.2.1, the systematic way of converging real-time calculations implies increasing the total simulated time and decreasing the time step, i.e., two choices that increase the associated computational cost. While this was carefully tested for each material, we avoided overconverging these parameters as it would have unduly penalised the real-time approach (see Appendix B for computational details, convergence tests and all spectra in the data set).

The results in Fig. 4.8 show the influence of the real-time convergence parameters, e.g., the speed-up is higher in h-BN as it required the longest simulated times and shortest time steps (2.5 as) to closely match the Floquet spectra. MoS_2 shows an intermediate speed-up since it was well converged with a 10-as time step but also needed long simulated times. Finally, AlAs was calculated with a time step of 10 as, which is well-converged in the region of interest despite the small discrepancies at 4 eV to 6 eV (see Fig. 4.2). While reducing the latter with a 2.5 as time step (see Fig. 4.2) would have quadrupled the Floquet speed-up, it would have unduly penalised the real-time approach in our view.

One parameter that *is* present in both methods and plays an important role in the speed-up achieved is the broadening of the spectra. In the real-time approach, the broadening is introduced through the dephasing term (see Eq. 2.78) and impacts its ability to filter out excited eigenfrequencies. In general, a small broadening will require a long time to properly dephase the system and converge the spectrum. Hence, the broadening has an inverse impact in the computational cost of the real-time method through the total simulated time needed. At variance, the computational cost of our Floquet approach is almost insensitive to the broadening, which is introduced *via* the damping term in Eq. 4.34. It would be expected that a smaller broadening could make convergence more difficult at some

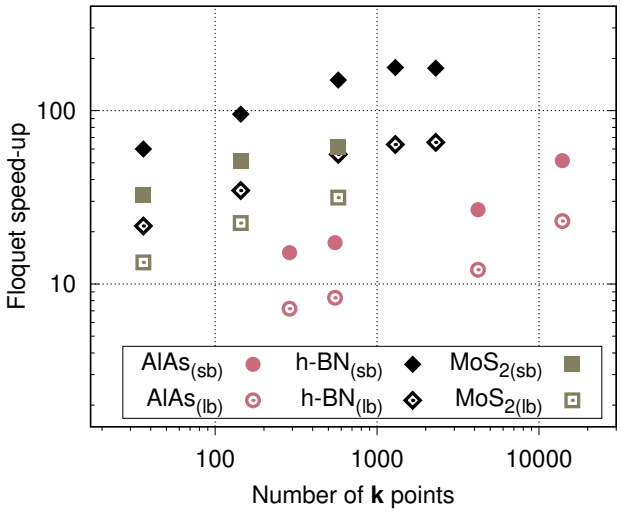

Figure 4.8: Computational cost comparison for SHG in the form of a CPU-time ratio between equivalent real-time and a Floquet calculations. Hollow markers represent calculations with 0.15 eV broadening ("lb" stands for large broadening), while filled ones are for 0.04 eV runs ("sb" or small-broadening). Floquet speed-ups are larger for the latter since the simulated times required are longer that in the former case, at the same time that Floquet CPU times are not significantly affected by the choice of broadening.

particular (resonant) frequencies. However, while it is true that the CPU time required by Floquet scales linearly with the average number of self-consistent iterations per frequency, adding one or two cycles at a handful of frequencies did not impact the total CPU time significantly. As a result, the speed-up achieved with Floquet is much larger in small-broadening calculations. In fact, Fig. 4.8 shows two groups of points per material. Within the data of a given material, the uppermost points correspond to small-broadening results (0.04 eV) while the lowermost ones reflect the large-broadening calculations (0.15 eV).

We also performed comparisons on bulk Si THG spectra, which were calculated for just one broadening (0.15 eV) but two intensities, i.e., 1×10^{6} and 1×10^{10} W cm^{-2} (referred to as low and high intensity, respectively). In line with Section 4.2.2, we report high-intensity calculations with $\eta_{\max} = 5$ and low-intensity runs with $\eta_{\max} = 3$. This results in larger Floquet speed-ups at low intensities, as shown in Fig. 4.9. Since high-intensity spectra require $\eta_{\max} = 5$, there is an increased computational cost related to the additional Floquet modes in comparison with low-intensity calculations, for which $\eta_{\max} = 3$ is well converged

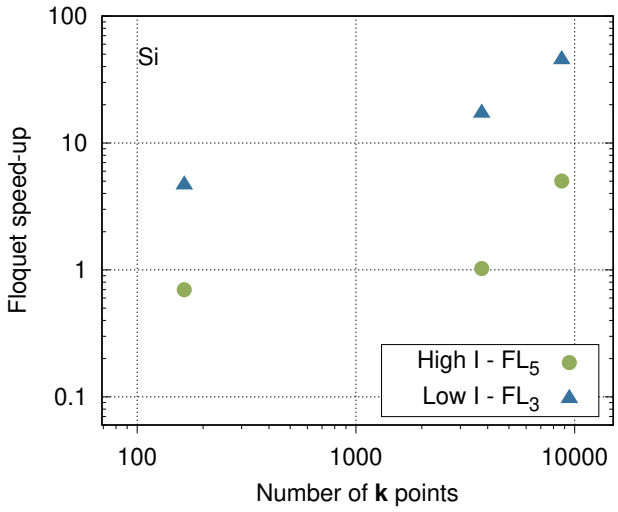

Figure 4.9: Computational cost comparison for bulk Si THG in the form of a CPU-time ratio between a real-time and a Floquet calculation producing the same spectra. In the labels, low and high I stand for intensities of $1{\times}10^6$ and $1{\times}10^{10}$ W cm^{-2}, respectively. The number of Floquet modes used is denoted by a subscript in the legend, e.g., FL_5 means $\eta_{\max} = 5$.

(see Appendix B for convergence tests). Nonetheless, the computational advantage offered by Floquet becomes clear close to convergence with respect to **k**-point sampling (see Fig. 4.9), regardless of the intensity. We point out that, with a broadening of 0.04 eV, the low-intensity speed-up for an 8×8×8 **k**-grid was 15.1 (not shown in Fig. 4.9). This allows us to reliably estimate a speed-up of around 146 for a 32×32×32 **k**-grid. Hence, at low intensities where $\eta_{\max} = 3$ is well converged, the speed-ups obtained for bulk Si THG spectra are comparable to those achieved for bulk AlAs SHG spectra.

The drop in Floquet speed-ups at high intensities, i.e., when including higher harmonics to capture higher-order processes, points to a poor scaling of our method with respect to the number of Floquet modes. This is because each additional mode enlarges the dimension of the quasi-energy matrices by $2N_b$, which in turns impacts the time required for their diagonalisation (see near-quadratic scaling in Appendix B). At the other end of the scale, linear response calculations are much more efficient with the present Floquet formalism than with the real-time approach. This is because the Floquet matrices are very small (of dimension $3N_b$) and convergence very fast (typically 2 self-consistent iterations are

sufficient for linear response). However, first-order Floquet is still more expensive than the usual frequency-domain response-based approach and the latter remains the best option in the linear response regime, at least at the independent particle level.

One of the main contributions to the computational cost in our scheme is the diagonalisation of the quasi-energy matrices. For this particular task, we use the QR algorithm (i.e., 'full' diagonalisation). There is room for improvement in this diagonalisation since the matrices are of dimension $N_b \times (2\eta_{\max}+1)$ but only M eigenvectors are needed (i.e., the number of occupied bands, which is a fraction of N_b). In the cases considered here, M represents between 5 and 10% of the dimension of the corresponding matrices. This opens the possibility of exploring more efficient eigensolvers (e.g., those in the SLEPc library [142]) such as Krylov subspace methods [143] or even variational approaches [125–127], which would further improve the performance of our Floquet method. Moreover, this would reduce the scaling of the computational cost with the number of Floquet modes.

Finally, we note that the scaling with the number of atoms is near cubic both for the real-time and the Floquet approaches (the exponents are 3.1 and 2.8, respectively). However, the pre-factor of this scaling resulted 17 times higher in the former. We therefore conclude that the speed-up attained by the Floquet approach respect to the real-time will also be present (in fact, greater) in systems with large number of atoms. These scaling tests are presented in Appendix B.

4.2.4 Limitations

The limitations of the Floquet approach proposed in this Chapter are mainly related to the requirement of time-periodicity in the Hamiltonian. First and foremost, this framework can only apply to continuous and monochromatic perturbations. Otherwise, the basic conditions for the application of Floquet's theorem would not be present. For instance, modelling pump-and-probe experiments is beyond what one can do with the present formalism, and falls within the broader capabilities of the real-time approach. Second, we use the adia-

batic approximation in order to ensure the periodicity of the effective Hamiltonian of our method, since the Berry-phase electron-field coupling operator depends self-consistently on the solution of the quasi-energy eigenproblem. This limits the validity of the approach to weak field intensities. We quantified this limit for the case of h-BN, in which signatures of non-adiabaticity started to appear at intensities of 1×10^{12} $\mathrm{W\,cm^{-2}}$ (see Section 6.5). However, the intensity at which this transition occurs is likely system-dependent and care should be taken when using our approach in this regime and beyond. In particular, we believe our method is not well-suited for the extreme nonlinear regime, where non-adiabaticity is expected to play an important role.

Chapter 5

Floquet approach to nonlinear optics beyond IPA level

We extend the Floquet formalism of Chapter 4 beyond the IPA level by implementing the Hartree potential and the screened-exchange self-energy into the quasi-energy eigenproblem. Only a handful of results could be achieved at this level of theory, since the Floquet self-consistent cycle presented instabilities and proved much harder to converge than in the IPA case. Strategies for mitigating these divergencies such as the use of Kerker mixing schemes and Padé approximants are discussed.

As explained in Section 2.3.2, one of the advantages of the real-time approach is its flexibility for the inclusion of many-body effects, i.e., they can be easily taken into account by adding the corresponding terms to the Hamiltonian in Eq. 2.61. Formally, our Floquet scheme retains this advantage. One has to take the relevant operators, i.e., the Hartree potential and the screened-exchange self-energy, find their matrix elements in FKS space and add them to the quasi-energy operator to be diagonalised. However, in practice, these extra terms bring instabilities into the self-consistent loop, affecting its convergence and leading to divergencies in the response functions. We will describe the implementation of these operators into the quasi-energy eigenproblem in Section 5.1, alongside two strategies to mitigate the instabilities found beyond the IPA level, i.e., Kerker preconditioning [144] and Padé approximants [145]. In Section 5.2, we present some preliminary results that

exemplify these convergence issues and assess the usefulness of said strategies.

5.1 Implementation

The effective Hamiltonian for the real-time approach to nonlinear optics with many-body effects has the form in Eq. 2.66, which we repeat here for clarity,

$$\hat{H}^{\text{eff}} = \overbrace{\underbrace{\hat{H}^{KS}[\rho_0] + \hat{\Delta}_{\text{QP}}[\varrho_0]}^{\hat{H}^{\text{MB},0}} + \hat{V}^{H}[\rho] + \hat{\Sigma}^{\text{SEX}}[\varrho]}^{\hat{H}^{\text{IPA},0}} + \hat{W}(\mathcal{E}), \tag{5.1}$$

where the added terms respect to Eq. 2.61 are the Hartree potential, $\hat{V}^{H}[\rho]$, and the screened-exchange self-energy $\hat{\Sigma}^{\text{SEX}}[\varrho]$. The time dependence of these magnitudes is given by their functional dependence on the density, ρ, and density matrix, ϱ, respectively. This marks a difference respect to the IPA case, where $\hat{W}(\mathcal{E})$ was the only time-dependent operator (as explained in Section 2.3.2, $\hat{H}^{\text{IPA},0}$ is time-independent as it only depends on ground-state quantities).

5.1.1 Hartree potential

The first step beyond the IPA level consists on including the Hartree potential in the Hamiltonian (see Eq. 5.1). We refer to this level of theory as TDH in accordance with Section 2.3.2 and note it reduces to the RPA in the linear response limit [43]. This contribution represents a local and time-dependent potential, which is simply the Coulomb potential arising from the electron density at a given point in space and time. As such, it can be obtained in **G**-space as a linear functional of the electron density derived from the Poisson equation (see Eq. 2.65). This functional is local in space and time and will thus be time-periodic provided the density also presents time-periodicity. The latter is ensured by the adiabatic approximation introduced in Eq. 4.3 (see below for details). It is worth mentioning that the Hartree potential depends on the solution of the quasi-energy eigenproblem through

the electron density and will thus require self-consistency (which was already the case at the IPA level due to the electron-field coupling operator).

Ultimately, we need to find the matrix elements of the Hartree potential in FKS space, $V^H_{\mathbf{k}ij}(\eta,\gamma)$. Since some of the operations required for this will be performed in the time domain, we will start by calculating the time-dependent KS states in phase space, $v_{\mathbf{k}n}(\mathbf{x},t)$. Projecting Eq. 4.6 over $\langle\mathbf{x}|$, one obtains,

$$v_{\mathbf{k}n}(\mathbf{x},t) = e^{-i\xi_{\mathbf{k}n}t} \sum_{\eta=-\infty}^{+\infty} e^{-i\eta\omega_0 t} \sum_{i}^{+\infty} \widetilde{d}_{\mathbf{k}ni}(\eta)\ \mu_{\mathbf{k}i}(\mathbf{x}). \tag{5.2}$$

In practice, the KS time-zero, zero-field states are available in a real-space grid from the DFT calculation, i.e., $\mu_{\mathbf{k}i}(\mathbf{x}_\mathrm{R})$, where $\mathbf{x}_\mathrm{R}$ represents a point in such grid. Using the eigenvectors from a previous iteration, $\{\widetilde{d}_{\mathbf{k}ni}(\eta)\}$, we compute the sum over Floquet modes in Eq. 5.2 and arrive at a phase-space equivalent of Eq. 4.4,

$$v_{\mathbf{k}n}(\mathbf{x}_\mathrm{R},t) = e^{-i\xi_{\mathbf{k}n}t} \sum_{i}^{+\infty} d_{\mathbf{k}ni}(t)\ \mu_{\mathbf{k}i}(\mathbf{x}_\mathrm{R}). \tag{5.3}$$

We evaluate this expression for a handful of sample times t_s within one period and obtain the time-dependent KS bands in a real-space grid at each time step, $v_{\mathbf{k}n}(\mathbf{x}_\mathrm{R},t_s)$. With this, we can evaluate the electron density at each time t_s in the same real-space grid,

$$\rho(\mathbf{x}_\mathrm{R},t_s) = \sum_{\mathbf{k}} \sum_{n}^{M} |v_{\mathbf{k}n}(\mathbf{x}_\mathrm{R},t_s)|^2, \tag{5.4}$$

where the index n runs over the occupied bands only. The quasi-energy exponentials in Eq. 5.3 cancel out in Eq. 5.4, leading to a time-periodic density, which in turns imply a time-periodic Hartree potential and ultimately ensures that the Hamiltonian remains periodic at the TDH level. This is the intended effect of the adiabatic approximation introduced in Eq. 4.3. If Eq. 5.4 contained a sum over time-dependent Floquet states as in Eq. 4.2, it would give rise to exponentials of the form $e^{-i(\xi_{\alpha_1}-\xi_{\alpha_2})t}$, which would not be commensurate with the frequency of the perturbation, ω_0, and therefore render the density non-periodic.

Such a term in the Hamiltonian would make it impossible to eliminate the time variable from the EOMs and prevent us from arriving at a time-independent eigenproblem as in Eq. 4.11.

As mentioned in Section 2.3.2, the time-zero Hartree potential is already included in the exchange-correlation potential from the DFT ground state. This means the term $V^H[\rho]$ we add to Eq. 5.1 in TDH should be the difference with respect to that DFT Hartree potential. In order to do so, we subtract the reference density from the result of Eq. 5.4. The reference (ground-state) density is simply obtained with the time-zero, zero-field KS wavefunctions, i.e., $\rho_0(\mathbf{x}_\mathrm{R}) = \sum_\mathbf{k} \sum_n^M |\mu_{\mathbf{k}n}(\mathbf{x}_\mathrm{R})|^2$. We can define the subtraction as $\rho^\Delta(\mathbf{x}_\mathrm{R}, t_s) \equiv \rho(\mathbf{x}_\mathrm{R}, t_s) - \rho_0(\mathbf{x}_\mathrm{R})$ and use it thereafter. This exploits the fact that the Hartree potential is linear in the density.

Having the density $\rho^\Delta(\mathbf{x}_\mathrm{R}, t_s)$ in real space, we can use a Fast Fourier Transform (FFT) routine to transform it to $\mathbf{G}$-space for each time t_s, i.e., $\rho^\Delta(\mathbf{G}, t_s)$. With this, we can calculate the Hartree potential in $\mathbf{G}$-space as (cf. 2.65),

$$V^H(\mathbf{G}, t_s) = \rho^\Delta(\mathbf{G}, t_s)\, \frac{4\pi}{|\mathbf{G}|^2}, \tag{5.5}$$

where the $\mathbf{G} = 0$ term is omitted for the reasons presented in Section 2.2.1. Then, using FFT routines we can obtain the Hartree potential in a real-space grid $V^H(\mathbf{x}_\mathrm{R}, t_s)$ at each time t_s and proceed to calculate the matrix elements in KS space,

$$V^H_{\mathbf{k}ij}(t_s) \equiv \langle \mu_{\mathbf{k}i} | \hat{V}^H(t_s) | \mu_{\mathbf{k}j} \rangle = \sum_{\mathbf{x}_\mathrm{R}}^{grid} \mu^*_{\mathbf{k}i}(\mathbf{x}_\mathrm{R})\; V^H(\mathbf{x}_\mathrm{R}, t_s)\; \mu_{\mathbf{k}j}(\mathbf{x}_\mathrm{R}). \tag{5.6}$$

Given that each matrix element $V^H_{\mathbf{k}ij}(t_s)$ is individually a periodic function of time, we can find the corresponding Floquet coefficients from,

$$V^H_{\mathbf{k}ij}(t_s) = \sum_{\zeta=-\infty}^{+\infty} e^{-i\omega_0 \zeta t_s}\; \widetilde{V}^H_{\mathbf{k}ij}(\zeta). \tag{5.7}$$

With this, we have available all the quantities required to calculate the matrix elements of the Hartree potential in FKS space, $V^H_{\mathbf{k}ij}(\eta,\gamma)$. Analogously to Eqs. 4.14 and 4.15, we do

$$V^H_{\mathbf{k}ij}(\eta,\gamma) = \int dt\; e^{+i\omega_0\eta t} \sum_{\zeta=-\infty}^{+\infty} e^{-i\omega_0\zeta t}\; e^{-i\omega_0\gamma t}\; \widetilde{V}^H_{\mathbf{k}ij}(\zeta), \tag{5.8}$$

$$V^H_{\mathbf{k}ij}(\eta,\gamma) = \sum_{\zeta=-\infty}^{+\infty} \delta_{\zeta,\eta-\gamma}\; \widetilde{V}^H_{\mathbf{k}ij}(\zeta), \tag{5.9}$$

$$V^H_{\mathbf{k}ij}(\eta,\gamma) = \widetilde{V}^H_{\mathbf{k}ij}(\eta-\gamma). \tag{5.10}$$

As a result of the Hartree potential being time dependent, its matrix elements in FKS basis couple different Floquet modes with one another. Finally, the quasi-energy eigenproblem for the TDH case would be obtained by simply adding this term to the IPA eigenproblem (see Eq. 4.11), resulting in,

$$\sum_{j}^{+\infty}\sum_{\gamma=-\infty}^{+\infty} \mathcal{K}^{\mathrm{TDH}}_{\mathbf{k}ij}(\eta,\gamma)\;\; \widetilde{d}_{\mathbf{k}nj}(\gamma) = \xi_{\mathbf{k}n}\; \widetilde{d}_{\mathbf{k}ni}(\eta), \tag{5.11}$$

with

$$\mathcal{K}^{\mathrm{TDH}}_{\mathbf{k}ij}(\eta,\gamma) = \left(E^{\mathrm{IPA}}_{\mathbf{k}j} - \gamma\omega_0 - i\nu_1\left(1-\delta_{\gamma,0}\right)\right)\delta_{i,j}\delta_{\eta,\gamma}\; + W_{\mathbf{k}ij}(\eta,\gamma) + V^H_{\mathbf{k}ij}(\eta,\gamma). \tag{5.12}$$

As anticipated, part of this procedure was performed in the time domain, which required to transform the Floquet eigenvectors to time (Eq. 5.2) and transform the Hartree potential back to Floquet space (Eq. 5.7). We could have chosen to remain in Floquet space and dispense with the time domain completely. Both alternatives were implemented in our code and tested, showing a consistent computational advantage in favour of using the time domain. Therefore, we used the time-domain route for the calculation of the Hartree potential in FKS space.

5.1.2 Mixing schemes and Kerker preconditioning

As will be shown in Section 5.2.1, the introduction of the Hartree potential alone is usually enough to result in the above mentioned convergence issues. This is expected as small changes in the density from one iteration to the next one are amplified into big variations in the potential by long-wavelength (small $\mathbf{G}$) terms in Eq. 5.5, which may be a source of these instabilities. This problem shares some features with DFT schemes, i.e., both entail a self-consistent eigenproblem where a term in the Hamiltonian has a functional dependence on the density (our Floquet formulation is not variational, otherwise the similarity would be greater). For this reason, a mixing scheme was proposed to improve the performance of our code. We started with a linear mixing scheme for the density at each time step, t_s,

$$\rho_{\mathrm{In}}^{(it+1)}(x,t_s) = \beta\, \rho_{\mathrm{Out}}^{(it)}(x,t_s) + (1-\beta)\, \rho_{\mathrm{In}}^{(it)}(x,t_s), \tag{5.13}$$

where ρ_{In} is the density used to construct the Hartree potential of the Hamiltonian at a given iteration and ρ_{Out} is the density calculated with the wavefunctions obtained after diagonalisation of the quasi-energy operator. However, our tests indicate that this mixing scheme has limited impact in the stability of our code. We also tried mixing other quantities like the Floquet eigenvectors or the Hartree potential, but without success. We note that a linear mixing of the Hartree potential is equivalent to Eq. 5.13, since V^H is obtained through a series of operations that are linear on the density (the same applies to mixing ρ or ρ^{Δ}). A double self-consistency loop was also considered, where the outer loop would update the density every time the inner loop converged for a given Hartree potential. We highlight that the first iteration of the outer loop represented an IPA-level calculation. Nevertheless, this showed no improvement in the stability of the code.

We also implemented a Kerker preconditioning method [144]. This represents a $\mathbf{G}$-dependent mixing where the long-wavelength components of the Hartree potential are heavily mixed (i.e., remain almost at their ground-state value) while highly localised contributions are mixed to a lesser extent (i.e., they are free to change considerably from one

iteration to the next one). This Kerker preconditioning implies solving [144],

$$V^{H(it+1)}(\mathbf{G}, t_s) = \left(\rho^{\Delta(it)}(\mathbf{G}, t_s) + \frac{\lambda^2}{4\pi} V^{H(it)}(\mathbf{G}, t_s) \right) \frac{4\pi}{|\mathbf{G}|^2 + \lambda^2}, \tag{5.14}$$

which effectively introduces a screening length of $\frac{2\pi}{\lambda}$. In essence, this formulation defines a sphere beyond which the effects of the Hartree potential are considered to be long-range and therefore screened. Hence, only contributions within that sphere are taken into account (i.e., local field effects). This is achieved by Eq. 5.14, which approximates Eq. 5.5 in the $\lambda \ll |\mathbf{G}|$ case,

$$V^{H(it+1)}(\mathbf{G}, t_s) \approx \rho^{\Delta(it)}(\mathbf{G}, t_s) \frac{4\pi}{|\mathbf{G}|^2}. \tag{5.15}$$

In other words, for wavelengths shorter than the screening length (*inside* the sphere), the corresponding high-$|\mathbf{G}|$ components of the Hartree potential are simply generated from the output density of the previous iteration. This means that the information of these components at a given iteration is not carried over to the next one, i.e., mixing is minimal and the high-$|\mathbf{G}|$ contributions to the potential vary greatly throughout the iterations. At variance, for wavelengths larger than the screening length ($|\mathbf{G}| \ll \lambda$), Eq. 5.14 reduces to

$$V^{H(it+1)}(\mathbf{G}, t_s) \approx V^{H(it)}(\mathbf{G}, t_s) + \rho^{\Delta(it)}(\mathbf{G}, t_s) \frac{4\pi}{\lambda^2}. \tag{5.16}$$

As shown in Eq. 5.16, the long-range (small-$|\mathbf{G}|$) contributions to the Hartree potential are heavily mixed with their values from previous iterations, thus remaining close to their ground-state value calculated at the DFT level. While this strategy improves the stability of the self-consistency cycle, one must carefully verify that all relevant local field effects are captured and that what is left *outside* the sphere does not affect the response significantly.

5.1.3 Padé approximant

Our experience with the proposed Floquet approach indicates that, as a general trend, increasing the broadening of a calculation brings stability into the Floquet self-consistent

loop. However, beyond IPA, the broadening required to achieve convergence at resonant frequencies is usually much too large. As explained in Section 4.1.5, the broadening in the spectra we calculate is a result of introducing dissipation effects into the electronic problem in a phenomenological way. Therefore, this parameter should be chosen on physical grounds and cannot take any value. For instance, 1-4 eV would probably overestimate the effect of the environment on the electrons, thus failing to reproduce the dynamics of open systems. Usually, we choose broadening values below 0.2 eV in order to match experimental spectra obtained at low temperatures. While a broadening in the region 0.25-0.5 eV would not be unreasonable from a physical point of view, it normally results in very broad spectra where features are difficult to pick apart.

The overall impact of the dissipation term (Eq. 4.33) in the response function can be understood as an imaginary contribution to the frequency, i.e., $\tilde{\omega} \equiv \omega + i\nu_1$. This is common practice when dealing with the pole structure of perturbative expressions obtained for response functions (e.g., 2.38). Mathematically, any response function $\chi(\omega)$ is complex-valued function $\mathbb{R} \to \mathbb{C}$ with poles at resonant frequencies $\omega \equiv \omega_{\text{res}}$. Let us then consider the introduction of broadening as an analytical continuation of this function into the complex plane, $\chi(\widetilde{\omega}) : \mathbb{C} \to \mathbb{C}$. The imaginary part of the frequency would then shift the poles away from the real axis and circumvent the associated singularities. In this context, one can think of solving the Floquet eigenproblem with a large broadening and using an analytical continuation procedure to shift the poles back to a desired value of broadening. This would benefit from the stability gained by using a large broadening at the same time as turning the resulting broad spectrum into a useful one.

We implemented this strategy making use of Padé approximants [145]. The latter have been employed in several areas of electronic structure, e.g., they can be applied to Green's functions [146], the screened Coulomb potential [147] or absorption spectra of molecules [148]. In particular, we will use an N-point Padé approximant to obtain a response function $\chi^{\text{Padé}}(\tilde{\omega}^{\text{TB}})$, where the complex frequency, $\tilde{\omega}^{\text{TB}} \equiv \omega + i\nu^{\text{TB}}$, contains the desired or target broadening (TB), e.g., $\nu^{\text{TB}} = 0.15$ eV. We start with a collection of N

points belonging to a spectrum calculated *via* the Floquet approach using a large broadening (LB), $\chi^{\mathrm{LB}}(\tilde{\omega}^{\mathrm{LB}})$. The argument of this broadened response function is a complex number, $\tilde{\omega}^{\mathrm{LB}} \equiv \omega + i\nu^{\mathrm{LB}}$, in which ω represents the frequencies for which the Floquet approach was solved and ν^{LB} is the deliberately large broadening used to facilitate convergence, e.g., $\nu^{\mathrm{LB}} = 0.4$ eV. With this data, we can construct the auxiliary functions [145],

$$g_0(z) = \chi^{\mathrm{LB}}(z), \tag{5.17}$$

$$g_p(z) = \frac{g_{p-1}(\tilde{\omega}^{\mathrm{LB}}_{p-1}) \; - \; g_{p-1}(z)}{(z - \tilde{\omega}^{\mathrm{LB}}_{p-1}) \; - \; g_{p-1}(z)}, \tag{5.18}$$

where z is any number in the complex plane and the index p runs over the N data points of χ^{LB}. Evaluating these functions at the frequencies of the broad spectrum we obtain the a coefficients,

$$a_p \equiv g_p(z = \tilde{\omega}^{\mathrm{LB}}_p). \tag{5.19}$$

With these coefficients, we construct a set of recursive formulas [145],

$$\frac{A_{p+1}}{B_{p+1}} = \frac{A_p + (z - \tilde{\omega}^{\mathrm{LB}}_p)\; a_{p+1}\; A_{p-1}}{B_p + (z - \tilde{\omega}^{\mathrm{LB}}_p)\; a_{p+1}\; B_{p-1}}, \tag{5.20}$$

$$A_{-1} = 0,\; A_0 = a_0,\; B_{-1} = 1,\; B_0 = 1. \tag{5.21}$$

We can then compute these recursive relations for any complex number, z, in order to obtain the N^{th}-order Padé approximant, $\frac{A_N}{B_N}$, evaluated at that point, z, in the complex plane. In particular, we are interested in calculating the approximants at or close to the real axis, e.g., at the complex frequencies with the target broadening we defined above,

$$\chi^{\mathrm{Padé}}(\tilde{\omega}^{\mathrm{TB}}) \equiv \; \frac{A_N}{B_N}(z = \tilde{\omega}^{\mathrm{TB}}), \tag{5.22}$$

thus obtaining an approximation to the response function with the desired broadening, e.g., $\nu^{\mathrm{TB}} = 0.15$ eV. In practice, we enforce some relations within our initial data set, $\chi^{\mathrm{LB}}(\tilde{\omega}^{\mathrm{LB}})$,

in order to enhance the numerical accuracy of the method,

$$\chi(\tilde{\omega}^*) = \chi^*(\tilde{\omega}), \tag{5.23}$$

$$\chi(-\tilde{\omega}) = \chi^*(\tilde{\omega}), \tag{5.24}$$

where the LB superscript was omitted for simplicity. Eqs. 5.23 and 5.24 come from the pole structure of the susceptibility and the Kramers-Kronig relations, respectively [10, 148]. As we have quadrupled the number of initial data points, we will obtain a Padé approximant of order $4N$.

While this approach works well for first order response functions (see Section 5.2.2 or Ref. [148]), second order susceptibilities present some issues. In particular, second order processes appear underdamped if the Padé approximant is calculated as described above, even showing divergencies in some cases (see Section 5.2.2). In terms of Floquet crossings (see Fig. 4.1), second order processes arise from couplings between zeroth and second Floquet modes, therefore involving Floquet modes higher than $\eta = 1$. All these arguments point to the dissipation term in Eq. 4.33, which does not show a proportionality with η. At variance, one could propose an η-dependent dissipation term in analogy with Eq. 4.33,

$$i\,\Gamma^{(\eta)}_{\mathbf{k}ij}(\eta,\gamma) \;\equiv\; i\,\nu_\eta\,|\gamma|\,\delta_{i,j}\delta_{\eta,\gamma}\;, \tag{5.25}$$

which will dampen second order processes twice as much as first order processes. We believe the dissipation term as defined in Chapter 4 (Eq. 4.33) is correct for the Floquet implementation proposed in this thesis. However, an η-dependent dissipation term may be more appropriate for the purpose of an analytic continuation. In perturbative expressions of second order response functions, one usually encounters the factor $\frac{1}{\Delta E - 2\omega}$ associated to second order processes. It is clear that an analytic continuation of this factor would result in a damping term that goes as $i2\nu$, which is what we try to reproduce when introducing the η-dependent dissipation term. If we want the second order susceptibility $\chi^{(LB)}$ produced

by our Floquet code to be an analytic continuation of a second order response function, then surely processes associated with 2ω should be damped twice as much as first order processes.

After testing a few possibilities (see results in Section 5.2.2), we arrived at the conclusion that both dissipation terms were required when solving the Floquet approach to calculate $\chi^{(LB)}$, i.e., with the intention of analytically continuating the resulting response function. This entails diagonalising the quasi-energy operator with two dissipation terms,

$$\mathcal{K}^{\mathrm{TDH}}_{\mathbf{k}ij}(\eta,\gamma) = \left(E^{\mathrm{IPA}}_{\mathbf{k}j} - \gamma\omega_0 - i\nu_1\left(1-\delta_{\gamma,0}\right) - i\nu_\eta|\gamma|\right)\delta_{i,j}\delta_{\eta,\gamma} + W_{\mathbf{k}ij}(\eta,\gamma) + V^{H}_{\mathbf{k}ij}(\eta,\gamma). \quad (5.26)$$

In particular, we obtained the best Padé approximants when we associated ν_1 with the target broadening of the Padé approximant. This leaves the η-dependent broadening linked to the part of the broadening that should vanish after the analytic continuation procedure. This implies solving the Floquet approach with the conditions,

$$\begin{aligned} \nu_1 &= \nu^{TB} \\ \nu_\eta &= \nu^{LB} - \nu^{TB} \end{aligned} \quad (5.27)$$

which can be understood as the poles being permanently shifted above the real axis to the desired broadening. Then, the additional broadening introduced to help convergence of the Floquet self-consistent loop will be effectively removed when analytically continuating from ν^{LB} to ν^{TB}.

5.1.4 Screened-exchange self-energy

As discussed in Section 2.3.2, adding the screened-exchange self-energy (Eq. 2.68) to the Hamiltonian in the EOM of the real-time approach (Eq. 2.59) allows for a description of many-body effects at the H+SEX level of theory. In the Floquet formalism, this implies including the self-energy operator in the quasi-energy eigenproblem, for which we need to obtain its matrix elements in FKS space, $\Sigma^{\mathrm{SEX}}_{\mathbf{k}ij}(\eta,\gamma)$. Using a similar strategy as for

the Hartree potential, part of this operation can be performed in the time domain. This implies computing the density matrix at a handful of time steps within one period, $\varrho(t_s)$, and evaluating Eqs. 2.68-2.69 to obtain the corresponding self-energy in KS space, $\Sigma^{\mathrm{SEX}}_{\mathbf{k}ij}(t_s)$. Once this quantity is known in the time domain, it can be then transformed back to Floquet space by finding its Fourier coefficients,

$$\Sigma^{\mathrm{SEX}}_{\mathbf{k}ij}(t_s) = \sum_{\zeta=-\infty}^{+\infty} e^{-i\omega_0\zeta t}\, \widetilde{\Sigma}^{\mathrm{SEX}}_{\mathbf{k}ij}(\zeta). \tag{5.28}$$

Next, we proceed in analogy with Eqs. 5.8-5.10 and obtain the matrix elements of the self-energy in FKS space,

$$\Sigma^{\mathrm{SEX}}_{\mathbf{k}ij}(\eta,\gamma) = \int dt\; e^{+i\omega_0\eta t} \sum_{\zeta=-\infty}^{+\infty} e^{-i\omega_0\zeta t}\, e^{-i\omega_0\gamma t}\, \widetilde{\Sigma}^{\mathrm{SEX}}_{\mathbf{k}ij}(\zeta), \tag{5.29}$$

$$\Sigma^{\mathrm{SEX}}_{\mathbf{k}ij}(\eta,\gamma) = \sum_{\zeta=-\infty}^{+\infty} \delta_{\zeta,\eta-\gamma}\, \widetilde{\Sigma}^{\mathrm{SEX}}_{\mathbf{k}ij}(\zeta), \tag{5.30}$$

$$\Sigma^{\mathrm{SEX}}_{\mathbf{k}ij}(\eta,\gamma) = \widetilde{\Sigma}^{\mathrm{SEX}}_{\mathbf{k}ij}(\eta-\gamma). \tag{5.31}$$

With this, we can finally formulate the Floquet quasi-energy eigenproblem at the H+SEX level,

$$\sum_{j}^{+\infty}\sum_{\gamma=-\infty}^{+\infty} \mathcal{K}^{\mathrm{H+SEX}}_{\mathbf{k}ij}(\eta,\gamma)\;\widetilde{d}_{\mathbf{k}nj}(\gamma) = \xi_{\mathbf{k}n}\,\widetilde{d}_{\mathbf{k}ni}(\eta), \tag{5.32}$$

with

$$\mathcal{K}^{\mathrm{H+SEX}}_{\mathbf{k}ij}(\eta,\gamma) = \left(E^{\mathrm{IPA}}_{\mathbf{k}j} - \gamma\omega_0 - i\nu_1\left(1-\delta_{\gamma,0}\right)\right)\delta_{i,j}\delta_{\eta,\gamma} + W_{\mathbf{k}ij}(\eta,\gamma) + V^{H}_{\mathbf{k}ij}(\eta,\gamma) + \Sigma^{\mathrm{SEX}}_{\mathbf{k}ij}(\eta,\gamma). \tag{5.33}$$

5.2 Results from current implementation

As anticipated, our Floquet implementation faces convergence issues in the self-consistency cycle beyond the IPA level. Tests were carried out at the TDH and H+SEX levels of theory on the same materials as in Chapter 4, i.e., bulk AlAs, 2D h-BN and 2D MoS_2. Every calculation performed at the H+SEX level showed instabilities and divergencies in the response function. These issues are less severe at the TDH level, as suggested by cases where divergencies occurred only at particular features in the spectra, leaving some energy ranges free from instabilities. While no general solution to these problems could be found yet, there are nonetheless a handful of results where convergence has been achieved across an entire spectrum at the TDH level, both for h-BN and MoS_2. These results are all particular cases where the specifics of each calculation helped or allowed for convergence.

5.2.1 Time-dependent Hartree with Kerker preconditioning

As mentioned above, there is a general trend whereby a larger broadening increases the stability of the calculations. However, the minimum broadening required to converge h-BN at the TDH level was 0.4 eV, which is hardly a useful result on its own (see Section 5.2.2). Moreover, for MoS_2, some frequencies would still present instabilities at 1.0 eV. This means that none of the cases studied at the IPA level (0.04 and 0.15 eV, labelled small and large broadening in Chapter 4) achieved convergence upon inclusion of the Hartree potential.

A possible strategy to help mitigate these divergencies consists on using the Kerker preconditioning scheme, which was introduced in Section 5.1. The latter added stability to the system and allowed us to obtain a handful of fully converged calculations. These results were achieved with 0.15 eV in the case of h-BN while MoS_2 required an even greater 0.2 eV. None of them would converge in the small broadening case (0.04 eV) despite using the preconditioning. All calculations presented in this Chapter were performed on a coarse 6×6×1 **k**-grid for simplicity, given that tests carried out on denser **k**-grids showed no improvement in terms of their stability.

Fig. 5.1 presents absorption and SHG spectra for h-BN with varying strengths of the Kerker preconditioning. This shows how decreasing the screening length of the preconditioning improved the stability of the Floquet self-consistency loop until all frequencies were converged (see right panel in Fig. 5.1). Moreover, the converged result obtained with the smallest screening length is indistinguishable from the real-time TDH solution at this scale. Calculations on MoS_2 could also be converged with a sufficiently small screening length for the preconditioning, as shown in Fig. 5.2. However, in this case, the Floquet solution deviated from the spectrum obtained with the real-time approach.

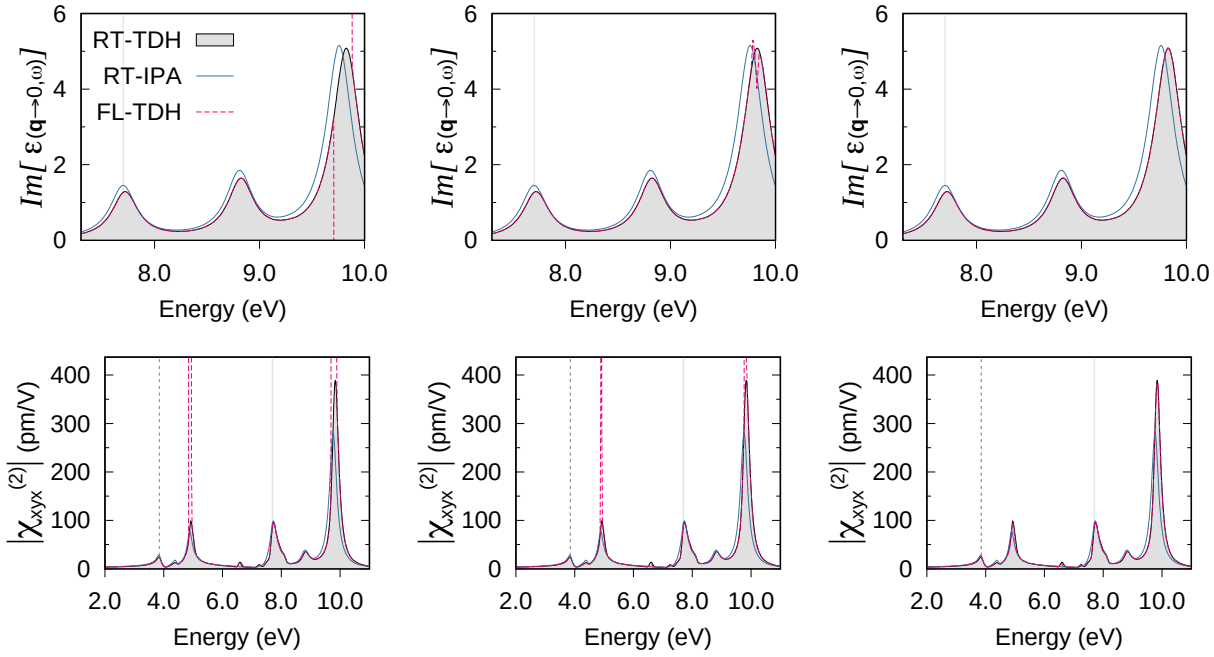

Figure 5.1: Absorption (top row) and SHG (bottom row) spectra of 2D h-BN (0.15 eV of broadening) at the TDH level with decreasing screening lengths for the Kerker preconditioning. Left: $\frac{2\pi}{\lambda} = 3.5$ Å, 3.4 % divergent frequencies. Centre: $\frac{2\pi}{\lambda} = 2.6$ Å, 1.8 % divergent frequencies. Right: $\frac{2\pi}{\lambda} = 1.9$ Å, 0 % divergent frequencies. In the legend, RT and FL indicate results were obtained *via* the real-time and Floquet approaches, respectively, while IPA and TDH represent the levels of theory.

The reason why h-BN converged to the correct TDH spectrum while MoS_2 deviated from it simply relates to the screening length used in each case, i.e., h-BN achieved convergence with 1.9 Å while MoS_2 required a much lower 0.8 Å. In fact, we can recognise there is an important trade-off between stability and accuracy when using the Kerker preconditioning.

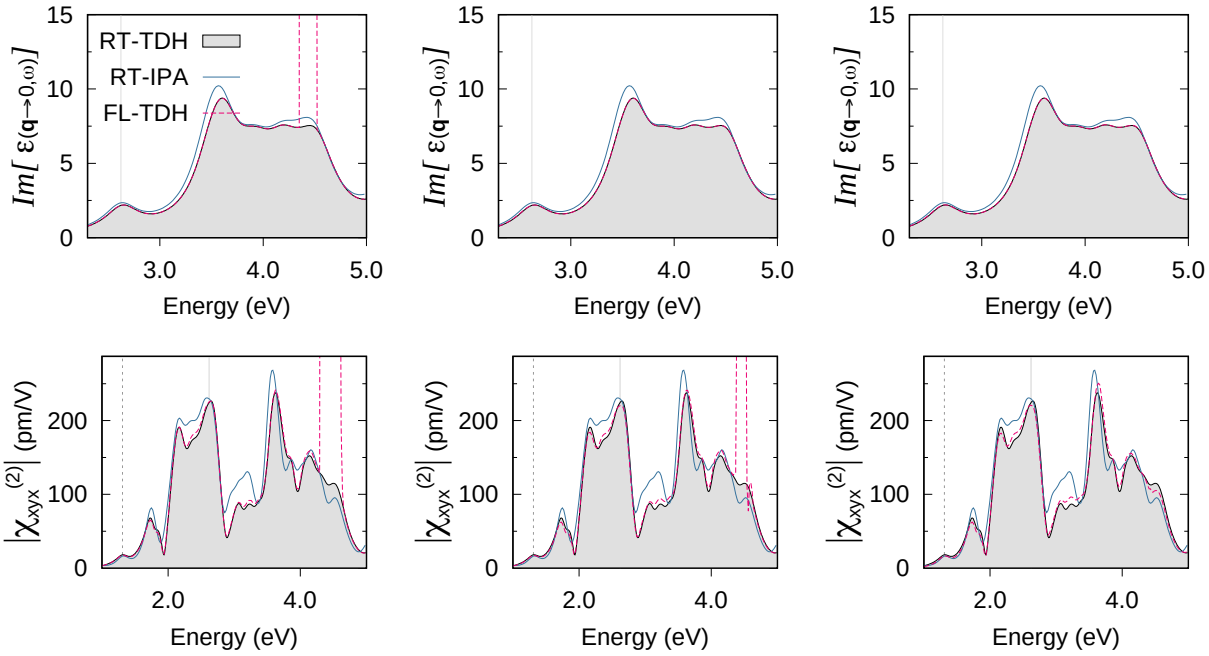

Figure 5.2: Absorption (top row) and SHG (bottom row) spectra of 2D MoS_2 (0.2 eV of broadening) at the TDH level with decreasing screening lengths for the Kerker preconditioning. Left: $\frac{2\pi}{\lambda} = 3.0$ Å, 8% divergent frequencies. Centre: $\frac{2\pi}{\lambda} = 1.7$ Å, 5 % divergent frequencies. Right: $\frac{2\pi}{\lambda} = 0.8$ Å, 0 % divergent frequencies.

As the screening length of the preconditioning is decreased, the system gains stability but, at the same time, a growing number of contributions to the Hartree potential are neglected (contributions of decreasing wavelength). There are two milestones in this progression, one consists on gaining enough stability so as to converge the self-consistent loop for every frequency in the spectrum. The second milestone implies reaching the wavelength where relevant local-field effects start being neglected, thus altering the resulting spectra. In other words, since the Hartree potential is meant to represent the physics of local fields, screening its long-range contributions should not affect the result. However, if the screening length required to ensure stability is too small, then part of those local field effects are lost and the result will naturally deviate from the correct real-time solution. If the stability milestone happens *before* the second one is reached, one can successfully calculate spectra with the Kerker preconditioning as in the case of h-BN (Fig. 5.1). At variance, MoS_2 (Fig. 5.2) represents a case where the opposite happens and the Kerker preconditioning does not

provide a satisfactory result when computing SHG with our Floquet method.

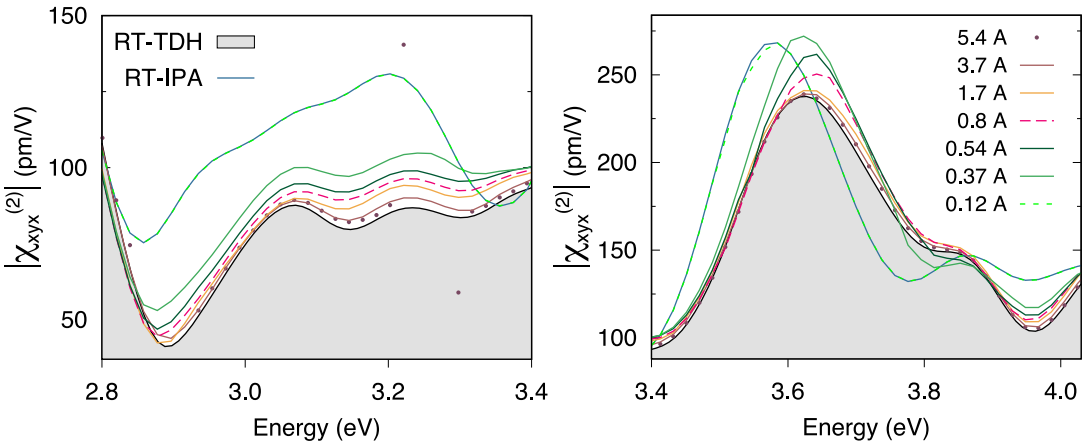

Figure 5.3: Floquet-calculated SHG spectra of MoS_2 (0.2 eV of broadening) at TDH level with various screening lengths showing the TDH-to-IPA transition. Both panels present data from the same set of calculations, showing different energy regions and scales. The dashed pink line is the Floquet result obtained with $\frac{2\pi}{\lambda} = 0.8$ Å (same as in bottom-right panel of Fig. 5.2). Curves in different tones of green were obtained with smaller screening lengths, thus tending to the IPA solution. Data in different tones of brown/beige correspond to larger screening lengths. These spectra tend to the RT-TDH solution but become unstable before reaching it (e.g., brown dots). The screening length of every curve is shown in the key of the right panel.

In order to better illustrate this trade-off, we re-calculated the response of MoS_2 with a greater range of screening lengths and focused on specific portions of the SHG spectrum, i.e., those where the difference between IPA and TDH is large (see Fig. 5.3). As shown with brown dots in Fig 5.3, the largest screening length is the closest result to the real-time TDH spectrum, however it presents some divergent frequencies. As the screening length is reduced, the spectrum starts to deviate from the TDH solution, which we show in different tones of brown/beige. Further into this progression, convergence is achieved for all frequencies in the spectrum. At this point, we obtain the dashed pink line (same result as in Fig. 5.2), which already deviates from the TDH solution. If we keep on decreasing the screening length, the solution continues to deviate from the correct result and tends to the IPA solution (see different tones of green in Fig. 5.3). Finally, the Floquet solution becomes almost indistinguishable from the IPA spectrum for the smallest screening length used. It is important to mention that Fig. 5.3 focuses an energy range where the system

presents fewer divergencies, i.e., while the second largest screening may seem to be the best solution, it does present divergent frequencies elsewhere in the spectrum.

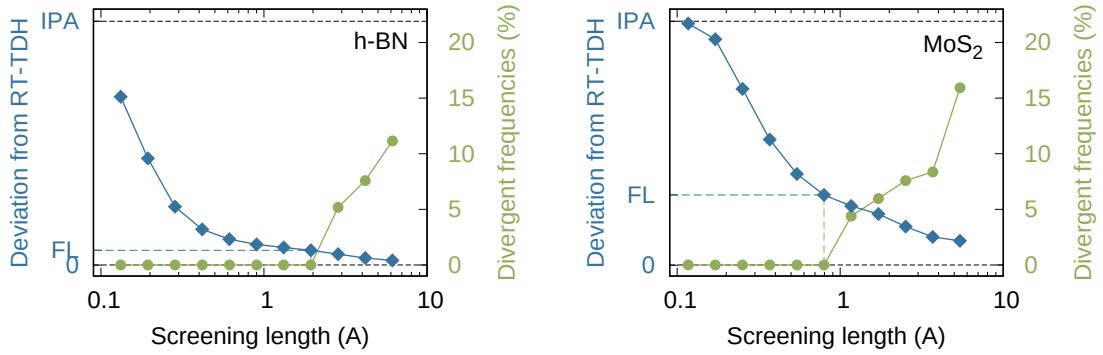

Figure 5.4: Data extracted from SHG spectra of h-BN (left) and MoS_2 (right) computed with a range of screening lengths. The green lines show the percentage of divergent frequencies of each calculation (0% corresponds to a converged spectrum) and the blue lines represent the deviation respect to the RT-TDH solution. The data is normalised by the so-called maximum deviation, i.e., that of the IPA spectrum respect to the RT-TDH solution. The magnitude of this maximum deviation is 558 (317) pm V^{-1} for h-BN (MoS_2). In the scale of the left-vertical axis, the label IPA indicates maximum deviation, while 0 represents the RT-TDH spectrum. Upon reaching convergence, the deviation of the Floquet spectrum (labelled FL) is of 34 (92) pm V^{-1} for h-BN (MoS_2).

We can quantify this trade-off by contrasting the proportion of divergent frequencies of a given Floquet run with the deviation of its solution with respect to the RT-TDH spectrum. This deviation was computed as the l^2-norm of a multi-dimensional vector containing difference between two spectra at each frequency. We performed this analysis for SHG spectra of h-BN and MoS_2 calculated at various screening lengths (see Fig. 5.4). The latter shows that as the screening length is reduced, the percentage of divergent frequencies decreases (green curve) and the deviation respect to the RT-TDH spectrum increases (blue curve). When the former reaches 0%, the calculation becomes stable and converges at every frequency. At this point, h-BN remains close to the RT-TDH solution while MoS_2 shows a more significant deviation. This is in part a result of MoS_2 requiring a smaller screening length to achieve stability, as mentioned above. Since one would not normally have access to the RT-TDH solution when calculating a spectrum *via* Floquet, there is no reliable way

of assessing whether a Floquet solution misses important local field effects or not. For this reason, we can conclude that the Kerker preconditioning does not offer a robust and general solution to the convergence issues faced by our Floquet formalism with local field effects.

In terms of performance, the instabilities originated by the inclusion of the Hartree potential had an impact on the efficiency of our Floquet implementation. Despite having mitigated the divergencies described above, converging the self-consistent loop at resonant frequencies took several tens of iterations, which can compromise the computational advantage offered by our scheme. In the case of h-BN, around 40 iterations were required at resonant frequencies, while non-resonant ones needed fewer than 10. In MoS_2, some resonant frequencies required almost 100 iterations to converge. The efficiency of these calculations was still satisfactory, resulting over 50 and 10 times faster than their real-time counterpart, respectively. However, we believe the number of iterations could be reduced with a more robust approach to deal with divergencies and much greater speed-ups should be reached with additional stability.

5.2.2 Time-dependent Hartree *via* Padé approximant

We calculated the same spectra as in Section 5.2.1 by means of Padé approximants. As explained in Section 5.1.3, this implies solving the Floquet approach with a large broadening, ν^{LB}, and performing an analytic continuation of the resulting response functions, χ^{LB}, to the desired or target broadening, ν^{TB}. In this case, it is primarily this large broadening that brings stability into the Floquet self-consistent cycle and facilitates convergence (rather than the Kerker preconditioning as in Section 5.2.1). The main trend found in these results indicates that keeping the difference $\nu^{LB} - \nu^{TB}$ as low as possible is crucial for the quality of the approximation and the resulting Padé response function, $\chi^{\text{Padé}}$. Hence, the procedure involved running several Floquet calculations with increasing broadening up to the minimum value that ensured convergence at all frequencies. In order to limit ν^{LB} as much as possible, the Kerker preconditioning was still used in these calculations but only to

a minimal degree (one that would not guarantee convergence on its own). This means that very large screening lengths were used (greater than 10 Å) in order to ensure no important contributions to the Hartree potential were missed (as explained in Section 5.2.1).

As anticipated in Section 5.1.3, first order response functions were straightforward to obtain with Padé approximants. First, no η-dependent dissipation terms were required, i.e., the dissipation term as introduced in Eq. 4.33 with $\nu_1 = \nu^{LB}$ allowed for a satisfactory Padé spectrum at ν^{TB}. Moreover, relatively high values of $\nu^{LB} - \nu^{TB}$ were well handled by the method, e.g., 0.85 and 0.5 eV for h-BN and MoS_2, respectively. As we will show in the rest of this Section, the situation with changed considerably when trying to approximate second order susceptibilities, i.e., much smaller values of $\nu^{LB} - \nu^{TB}$ were required and the η-dependent dissipation term (Eq. 5.25) was needed alongside the relations in Eq. 5.27. This is related to the nature of the processes involved in the second order response. Moreover, numerical issues may also be at play since the first order response is orders of magnitude larger than the second order susceptibility, which implies a better numerical stability for the former.

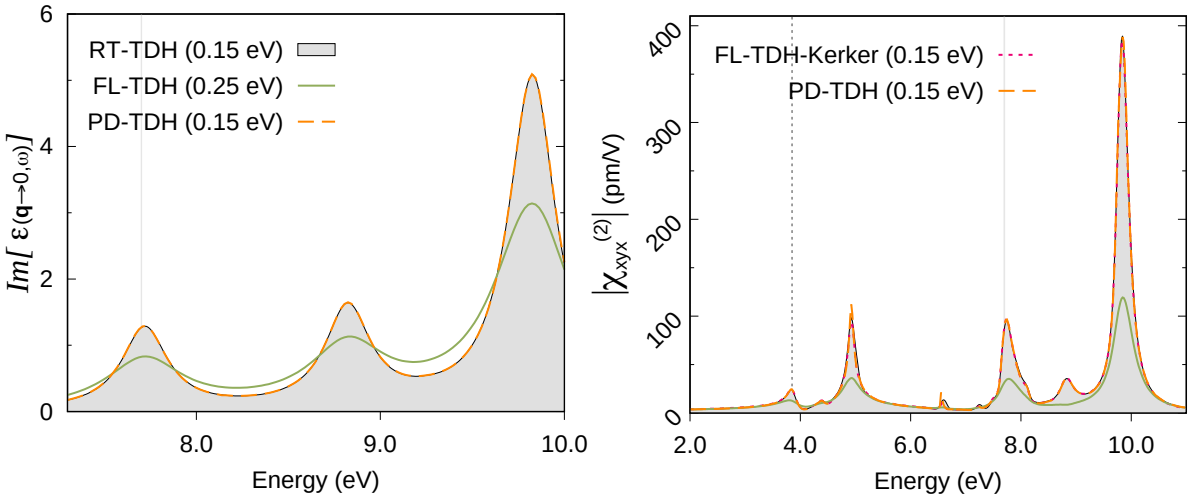

Figure 5.5: Absorption (left) and SHG (right) spectra of 2D h-BN at the TDH level with Padé approximants (labelled PD in the legend). Dissipation parameters: $\nu_1 = \nu^{TB} = 0.15$ eV, $\nu_1 + \nu_\eta = \nu^{LB} = 0.25$ eV. The best SHG spectrum achieved with Kerker preconditioning (bottom right panel in Fig. 5.1) and the real-time solution are also shown.

Fig. 5.5 presents the results for h-BN at $\nu_1 = \nu^{TB} = 0.15$ eV, both in terms of optical absorption and SHG. The green curve represents the broad spectrum obtained *via* the Floquet approach with $\nu_1 + \nu_\eta = \nu^{LB} = 0.25$ eV, i.e., an additional broadening of only $\nu_\eta = 0.1$ eV was enough to achieve convergence in this case. The orange dashed line shows the Padé approximant at $\nu^{\mathrm{TB}} = 0.15$ eV, which represents a very good approximation to the absorption spectrum as it is indistinguishable from the real-time result at this scale (see left panel in Fig. 5.5). While the approximation to the SHG spectrum is also satisfactory (see right panel in Fig. 5.5), some issues appear around 5 and 6.5 eV, i.e., when describing second order processes. The best result achieved with the Kerker preconditioning (i.e., bottom right panel in Fig. 5.1) is also shown in the right panel of Fig. 5.5 with a pink dashed line for comparison. The minor shortcomings found in the Padé approximant to the SHG spectrum make the use of Kerker preconditioning preferable in this particular case.

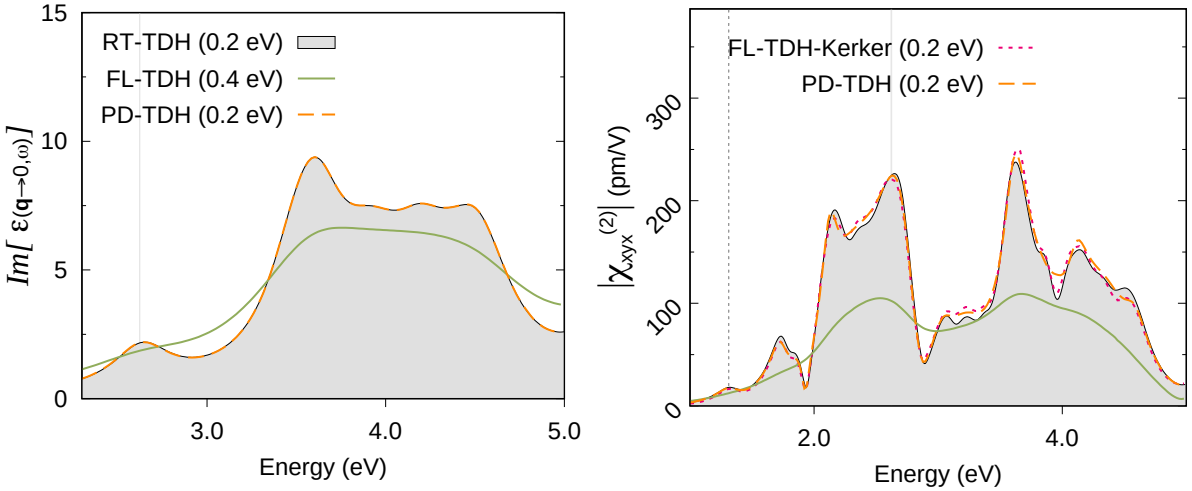

Figure 5.6: Absorption (left) and SHG (right) spectra of 2D MoS_2 at the TDH level with Padé approximants (labelled PD in the legend). Dissipation parameters: $\nu_1 = \nu^{TB} = 0.2$ eV, $\nu_1 + \nu_\eta = \nu^{LB} = 0.4$ eV. The best SHG spectrum achieved with Kerker preconditioning (bottom right panel in Fig. 5.2) and the real-time solution are also shown.

The results for MoS_2 at $\nu_1 = \nu^{TB} = 0.2$ are shown in Fig. 5.6, in which case an additional broadening of $\nu_\eta = 0.2$ eV was required to avoid divergencies in the Floquet approach at all frequencies in the spectrum. The latter then produced broad spectra at

$\nu^{LB} = 0.4$ eV (green curves). Again, the Padé approximation to the absorption spectrum is very good in comparison with the correct real-time result (see left panel in Fig. 5.6). Moreover, the Padé approximant to the SHG spectrum does not present issues reproducing second order processes (see right panel in Fig. 5.6). However, it does show some limitations when reproducing fine features such as the sharp valley around 4 eV.

Overall, the main shortcoming of this Padé approximant scheme is the reliance on a small additional broadening, $\nu^{LB} - \nu^{TB}$, particularly when calculating SHG spectra. Fig. 5.7 shows how the quality of the Padé SHG spectra deteriorates in the case of MoS_2 when increasing ν^{LB} (or ν_η) while keeping ν_1 fixed. Even an increase of 0.05 eV in ν_η respect to the solution presented in Fig. 5.6 results in noticeable discrepancies between the Padé spectrum and the real-time solution, particularly around second order processes (see left panel of Fig. 5.7). As shown in the centre and right panels of Fig. 5.7, subsequent increases in ν_η cause further deviations. The effect of increasing ν^{LB} in the case of h-BN (not shown here) is less severe.

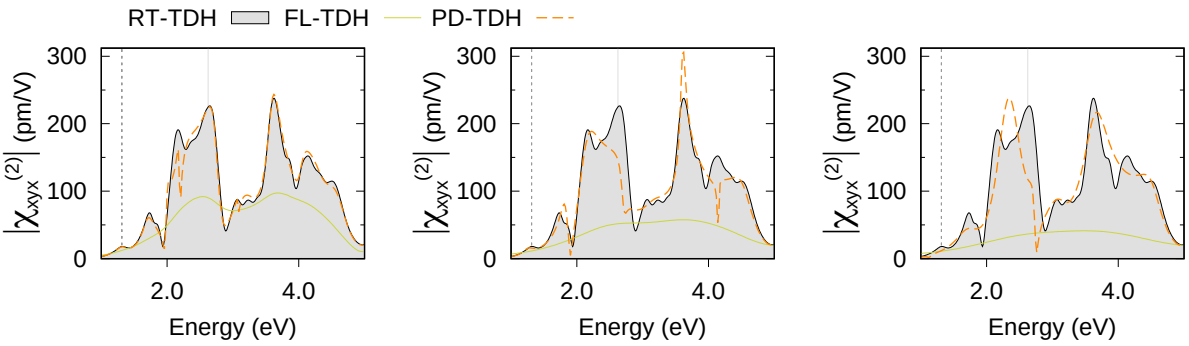

Figure 5.7: SHG spectra of 2D MoS_2 at the TDH level *via* Padé approximants at 0.2 eV calculated with increasing ν_η. The real-time solution at 0.2 eV is also shown. All plots have, $\nu_1 = \nu^{TB} = 0.2$ eV (orange dashed lines show Padé spectra at 0.2 eV). Left: $\nu_\eta = 0.25$ eV and $\nu^{LB} = 0.45$ eV (green line shows broad spectra at 0.45 eV). Centre: $\nu_\eta = 0.55$ eV and $\nu^{LB} = 0.75$ eV (green line shows broad spectra at 0.75 eV). Right: $\nu_\eta = 0.8$ eV and $\nu^{LB} = 1$ eV (green line shows broad spectra at 1 eV).

In addition, we present how the Padé spectra depend on the type of dissipation introduced in the Floquet calculation. The results in Figs. 5.5-5.7 were obtained with a mixture

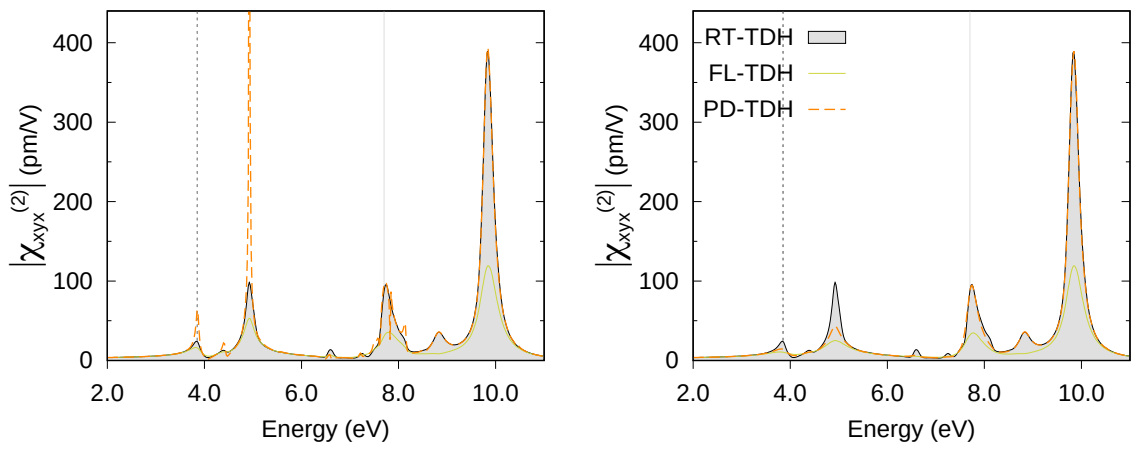

Figure 5.8: SHG spectra of 2D h-BN at the TDH level *via* Padé approximants at 0.15 eV calculated with different types of dissipation terms, i.e., only $\Gamma^{(1)}$ (left) or only $\Gamma^{(\eta)}$ (right). Both graphs were calculated with $\nu^{TB} = 0.15$ eV and $\nu^{LB} = 0.25$ eV. The plot on the left considers $\nu_1 = 0.25$ eV (and $\nu_\eta = 0$ eV). The plot on the left considers $\nu_\eta = 0.25$ eV (and $\nu_1 = 0$ eV).

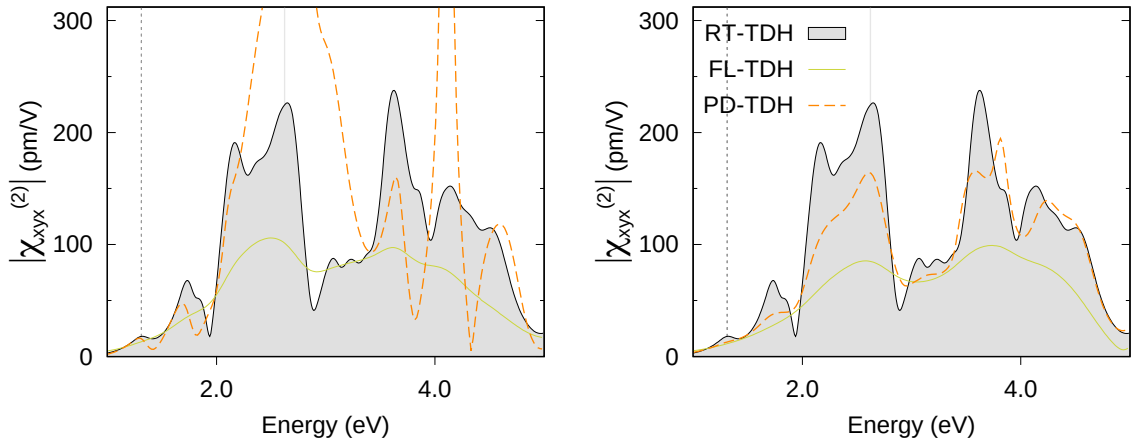

Figure 5.9: SHG spectra of 2D MoS_2 at the TDH level *via* Padé approximants at 0.2 eV calculated with different types of dissipation terms, i.e., only $\Gamma^{(1)}$ (left) or only $\Gamma^{(\eta)}$ (right). Both graphs were calculated with $\nu^{TB} = 0.2$ eV and $\nu^{LB} = 0.4$ eV. The plot on the left considers $\nu_1 = 0.4$ eV (and $\nu_\eta = 0$ eV). The plot on the left considers $\nu_\eta = 0.4$ eV (and $\nu_1 = 0$ eV).

of regular dissipation, $\Gamma^{(1)}$ (Eq. 4.33), and η-dependent dissipation, $\Gamma^{(\eta)}$ (Eq. 5.25), according to the conditions in Eq. 5.27. Fig. 5.8 shows the Padé spectra obtained for h-BN in the cases where only $\Gamma^{(1)}$ (left panel) or only $\Gamma^{(\eta)}$ (right panel) are considered. In essence, second order processes appear underdamped with only $\Gamma^{(1)}$ and overdamped with only $\Gamma^{(\eta)}$. The spectra are more complex for MoS_2 but the general trends are the same (see Fig. 5.9). These results validate the use of the conditions in Eq. 5.27.

In terms of performance, we mention that this Padé procedure is inexpensive and adds negligible computational cost. Moreover, a Floquet calculation with large broadening is easier to converge than one with smaller broadening, thus requiring fewer iterations. As a result, the former will generally be faster than the latter. While this difference was not noticeable in the case of h-BN, the MoS_2 calculation with $\nu_1^{\mathrm{LB}} = 0.4$ eV was over two times faster than the best result using Kerker preconditioning at 0.2 eV (see Section 5.2.1).

5.2.3 Hartree plus screened-exchange self-energy

Let us briefly discuss what we obtained at the Hartree + SEX level (or real-time BSE) with our Floquet formalism. Convergence issues are much more severe in this case than at the TDH level, as we found while calculating the linear response of 2D h-BN *via* Floquet (6×6×1 **k**-grid, 0.15 eV and only two bands). All frequencies below the position of the first exciton (5.43 eV according to an equivalent real-time calculation) were converged to roughly the right result (see Fig. 5.10). It is important to note that the response at this frequency would be zero at the IPA and TDH levels. Hence, the fact that our code is able to find this bound exciton somewhat validates our implementation of the self-energy. Convergence could not be achieved at any frequency beyond this first exciton, showing divergencies throughout the spectrum. The behaviour at the exciton energy is rather curious, as can be seen in the inset in Fig. 5.10. The response at that frequency seems to oscillate through the iterations around the correct value, but never converge to it. On the contrary, the amplitude of these oscillations increases with the number of iterations.

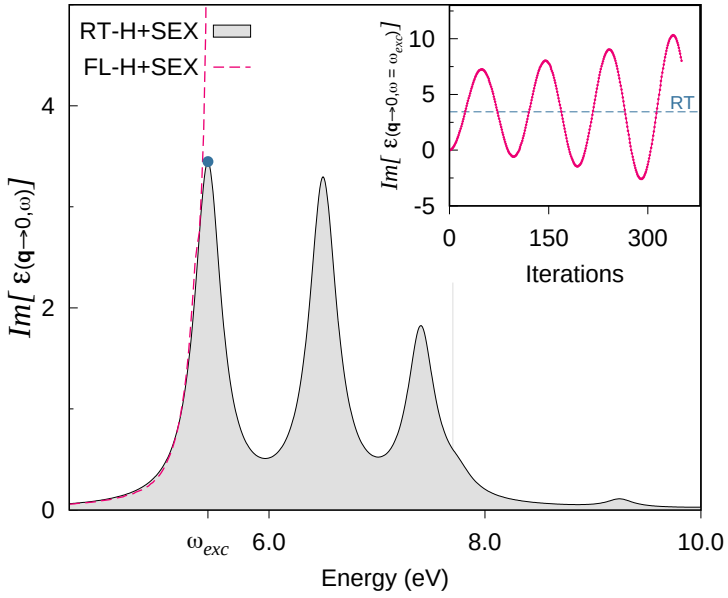

Figure 5.10: Absorption spectra of 2D h-BN (0.15 eV of broadening) at the H+SEX level. The Floquet-calculated spectrum (dashed pink line) present divergencies and does not compare well with the real-time solution (black line with grey filling) beyond the frequency of the first exciton, ω_{exc}. The inset shows the response calculated *via* Floquet at ω_{exc} throughout the iterations. The correct result at ω_{exc}, calculated with the real-time approach, is shown as a blue dot in the main figure and a blue dashed line in the inset.

Finally, we mention that the use of Padé approximants was not possible at this level of theory. The convergence issues introduced by the self-energy are so severe that around 4-5 eV of broadening were required to mitigate instabilities. With such a high additional broadening, the Padé approximant was unable to reproduce the real-time spectrum even in qualitative terms.

Chapter 6

Floquet analysis of real-time solution

We present a Floquet analysis tool capable of calculating Floquet eigenvectors provided that the time-dependent states, i.e., the solutions of the real-time approach, are known. This allows us to further characterise the instabilities affecting the self-consistent loop of our Floquet approach beyond the IPA level (see Chapter 5). We discuss the potential origin of said instabilities and gain insights into possible remedies for this problem.

As shown in Chapter 5, the proposed Floquet approach presents instabilities in the self-consistent cycle at any level of theory beyond IPA, which results in divergent response functions. A key quantity in this loop are the eigenvectors of the quasi-energy eigenproblem (e.g., Eq. 5.32). Once these Floquet eigenvectors are known, the time-dependent states can be recovered *via* Eq. 4.6, as we do, e.g., to calculate the dynamical polarisation. In principle, one could think of reversing this problem and obtaining the Floquet eigenvectors provided the time-dependent states are known. Therefore, besides our implementation of the Floquet approach (Chapters 4-5), we developed a python module with several tools to post-process the time-dependent quantities calculated by the real-time scheme in Yambo [42, 43]. The main objective is to take the correct solution of the EOMs in Eq. 2.59 as input and extract the Floquet eigenvectors from it. The latter are precisely the solutions we should arrive at by solving the Floquet eigenproblem (e.g., Eq. 5.32). This is useful in situations where our method struggles converge, as it allows us to understand what is wrong with the eigenvectors

it is producing. We describe this strategy and its implementation in Section 6.1, while the comparison between the Floquet states produced by either method is presented in Section 6.2. Further analysis of the convergence problems in our Floquet approach and the origin of these instabilities is provided in Section 6.3, together with an outlook on possible strategies for solving these issues. Finally, the validity of the adiabatic approximation invoked in Chapters 4 and 5 is assessed for a particular case based on the corresponding real-time result (see Section 6.5).

6.1 Floquet analysis tool

As explained in Section 2.3.2, the real-time approach integrates Eq. 2.59 in KS space and calculates the time-dependent Bloch states in this basis, i.e., $\langle \mu_{\mathbf{k}i} | v_{\mathbf{k}n} \rangle$. For periodically driven systems and under the adiabatic approximation introduced in Eq. 4.3, this magnitude is equal to the projection of Eq. 4.4 over the KS basis,

$$\langle \mu_{\mathbf{k}i} | v_{\mathbf{k}n} \rangle = \sum_j e^{-i\xi_{\mathbf{k}n}t} \, d_{\mathbf{k}nj}(t) \, \delta_{i,j} = e^{-i\xi_{\mathbf{k}n}t} \, d_{\mathbf{k}ni}(t), \tag{6.1}$$

where the coefficients $d_{\mathbf{k}ni}(t)$ retain the periodicity of the perturbation,

$$d_{\mathbf{k}ni}(t) = d_{\mathbf{k}ni}(t+T). \tag{6.2}$$

The idea is to take the output of a real-time calculation, $\langle \mu_{\mathbf{k}i} | v_{\mathbf{k}n} \rangle$, solve Eq. 6.1 for $d_{\mathbf{k}ni}(t)$ and Fourier transform the latter *via* Eq. 4.5 to obtain the Floquet eigenvectors, $\widetilde{d}_{\mathbf{k}ni}(\eta)$. This procedure would be trivial if the quasi-energy, $\xi_{\mathbf{k}n}$, was known. However, the latter is not computed by the real-time approach. In principle, one could take a pair of real-time results separated in time by one period, divide Eq. 6.1 by itself and apply Eq. 6.2 to obtain,

$$\frac{\langle \mu_{\mathbf{k}i} | v_{\mathbf{k}n} \rangle (t_s + T)}{\langle \mu_{\mathbf{k}i} | v_{\mathbf{k}n} \rangle (t_s)} = e^{-i\xi_{\mathbf{k}n}T}, \tag{6.3}$$

where one could easily solve for $\xi_{\mathbf{k}n}$. However, this would require the time step to be commensurate with the period, which imposes some practical limitations. A response function obtained in this way would have been computed with a different time step at each frequency in the spectrum. This would only be correct if the time step was very well converged, so as to ensure that slight variations would not affect the numerical integration. Moreover, if one decided to just run a single frequency and adjust the time step accordingly, this would require to have computed the spectra beforehand in order to choose this frequency of interest (e.g., at an excitonic peak). On the other hand, using an arbitrary time step that ignores the requirement of being commensurate with the period would mean that the computed quasi-energy would only be an approximation. However, a far simpler approximation to $\xi_{\mathbf{k}n}$ is be given by the KS energies, which are already known from the DFT ground state.

Instead, we preferred to formulate a procedure for computing quasi-energies that is independent of how the dynamical data was obtained. Moreover, the method is fairly inexpensive and uses information that is, in any case, required for the calculation of Floquet states. What we know is that if the *true* quasi-energy was used to solve Eq. 6.1 for $d_{\mathbf{k}ni}(t)$, then the result would be periodic, i.e., it would fulfil Eq. 6.2. Therefore, we propose an iterative solution to this problem where we essentially verify this condition for an assumed value of the quasi-energy that changes through the iterations.

In order to carry out this procedure we need the real-time results, $\langle \mu_{\mathbf{k}i} | v_{\mathbf{k}n} \rangle(t)$, at two different sets of time steps. The first one is the sampling set and should contain a handful of time steps, $\{t_s\}$, within one period. The second set is used to verify the periodicity condition at a later time steps, $\{t_v\}$, outside the sampling period. The latter can be, e.g., three periods after a given time step in the first set, $t_v = t_s + 3T$. We take all these real-time results, at $\{t_s\}$ and $\{t_v\}$, and use the assumed quasi-energy to solve Eq. 6.1 for $d^{\mathrm{RT}}_{\mathbf{k}ni}(t)$ at each time step (we use the RT superscript to indicate how this quantity was obtained). We then take the first set of these results, $d^{\mathrm{RT}}_{\mathbf{k}ni}(t_s)$, which are contained within one period, and perform a Fourier transform to compute the corresponding Floquet coefficients, $\widetilde{d}_{\mathbf{k}ni}(\eta)$. We will obtain an expansion with Floquet modes up to $\eta_{\max}$ provided that the sampling

set had $2\eta_{\max}+1$ time steps. With these coefficients, we can evaluate the Fourier series in Eq. 4.5 at any time, in particular, for those time steps in the verifying set,

$$d^{\mathrm{CALC}}_{\mathbf{k}ni}(t_v) = \sum_{\eta=-\eta_{\max}}^{+\eta_{\max}} e^{-i\eta\omega_0 t_v}\ \widetilde{d}_{\mathbf{k}ni}(\eta), \tag{6.4}$$

where we used the superscript to distinguish between this calculated value and those extracted from the real-time result, $d^{\mathrm{RT}}_{\mathbf{k}ni}(t_v)$. We now consider a series of equalities,

$$d^{\mathrm{CALC}}_{\mathbf{k}ni}(t_v = t_s + 3T) \ = \ d^{\mathrm{CALC}}_{\mathbf{k}ni}(t_s) \ = \ d^{\mathrm{RT}}_{\mathbf{k}ni}(t_s) \ \stackrel{?}{=} \ d^{\mathrm{RT}}_{\mathbf{k}ni}(t_v = t_s + 3T), \tag{6.5}$$

the first of which holds because $d^{\mathrm{CALC}}_{\mathbf{k}ni}$ is a Fourier series, while the second equality is true by construction of $d^{\mathrm{CALC}}_{\mathbf{k}ni}$. The third equality is only satisfied if the quasi-energy assumed is indeed correct, as it would imply the fulfilment of the periodicity condition, Eq. 6.2. Therefore, this procedure aims at finding a quasi-energy such that ,

$$d^{\mathrm{CALC}}_{\mathbf{k}ni}(t_v) = d^{\mathrm{RT}}_{\mathbf{k}ni}(t_v), \tag{6.6}$$

for all time steps in the verifying set, which allows us to define the error in our method as,

$$\mathrm{err}_{\mathbf{k}n} = \sum_{t_v,i} \left| d^{\mathrm{CALC}}_{\mathbf{k}ni}(t_v) - d^{\mathrm{RT}}_{\mathbf{k}ni}(t_v) \right| . \tag{6.7}$$

This deviation can be calculated for any time-dependent state obtained *via* the real-time approach, identified by its band index n and $\mathbf{k}$-point. For each state, $\mathbf{k}n$, the summation in Eq. 6.7 runs over the states i in the KS space and the time steps in the verifying set, t_v (this set could well have only one element). Ultimately, we can solve this problem by minimising $\mathrm{err}_{\mathbf{k}n}$ as a function of the assumed quasi-energy, $\xi_{\mathbf{k}n}$.

As an example, Fig. 6.1 shows the execution of this method for h-BN considering two-bands and assuming three different values for the quasi-energy. In this case, we intend to find the quasi-energy of the Floquet valence state at a given $\mathbf{k}$-point, $\xi_{\mathbf{k}v}$. While the i

index in Eq. 6.7 would run over both bands, Fig. 6.1 focuses on the projection over the conduction band only, $d_{\mathbf{k}vc}(t)$, to exemplify the method. The first 9 points of each plot represent the sampling set, where $d^{\mathrm{CALC}}_{\mathbf{k}vc}(t_s)$ and $d^{\mathrm{RT}}_{\mathbf{k}vc}(t_s)$ are the same by construction. The remaining 3 points constitute the verifying set, where the agreement between $d^{\mathrm{CALC}}_{\mathbf{k}vc}(t_v)$ and $d^{\mathrm{RT}}_{\mathbf{k}vc}(t_v)$ is guaranteed only for the correct quasi-energy. Any other value of the quasi-energy (except those shifted by ω_0) will not satisfy the periodicity condition in Eq. 6.2 and result in discrepancies between $d^{\mathrm{CALC}}_{\mathbf{k}vc}(t_v)$ and $d^{\mathrm{RT}}_{\mathbf{k}vc}(t_v)$, thus adding to $\mathrm{err}_{\mathbf{k}v}$ (see uppermost and middle panels of Fig. 6.1). At variance, the quasi-energy in the lowermost panel of Fig. 6.1 is close to the correct value and no deviation between $d^{\mathrm{CALC}}_{\mathbf{k}vc}(t_v)$ and $d^{\mathrm{RT}}_{\mathbf{k}vc}(t_v)$ can be distinguished at this scale.

In general, the error function in Eq. 6.7 depends on the number of time steps used for verification and how distant from the sampling set they are, providing a knob to tune the precision of this method. In order to automate the iterative procedure, we implemented a Newton-Raphson routine in our python module to perform this minimisation, where the derivative of the $\mathrm{err}_{\mathbf{k}n}$ function is evaluated numerically *via* finite differences. According to our tests, this method allows us to reduce the $\mathrm{err}_{\mathbf{k}n}$ function to values around 10^{-9} and calculate quasi-energies with an accuracy in the order of 10^{-10} eV.

6.2 Floquet eigenvectors from real-time solution

We used the Floquet analysis tool introduced in Section 6.1 to post-process the time-dependent solution produced by the real-time approach and extract the corresponding Floquet states. The latter were then compared with the Floquet eigenvectors produced *via* the Floquet approach in order to further characterise the convergence issues described in Section 5.2. We chose a small system to simplify this analysis, i.e., 2D h-BN with a 6×6×1 **k**-grid and two bands. All 36 transitions in the BZ were studied before reporting on the most relevant **k**-points. Regarding levels of theory, we considered TDH with a broadening of 0.04 eV and H+SEX with 0.15 eV (see Sections 6.2.1 and 6.2.2, respectively). Both

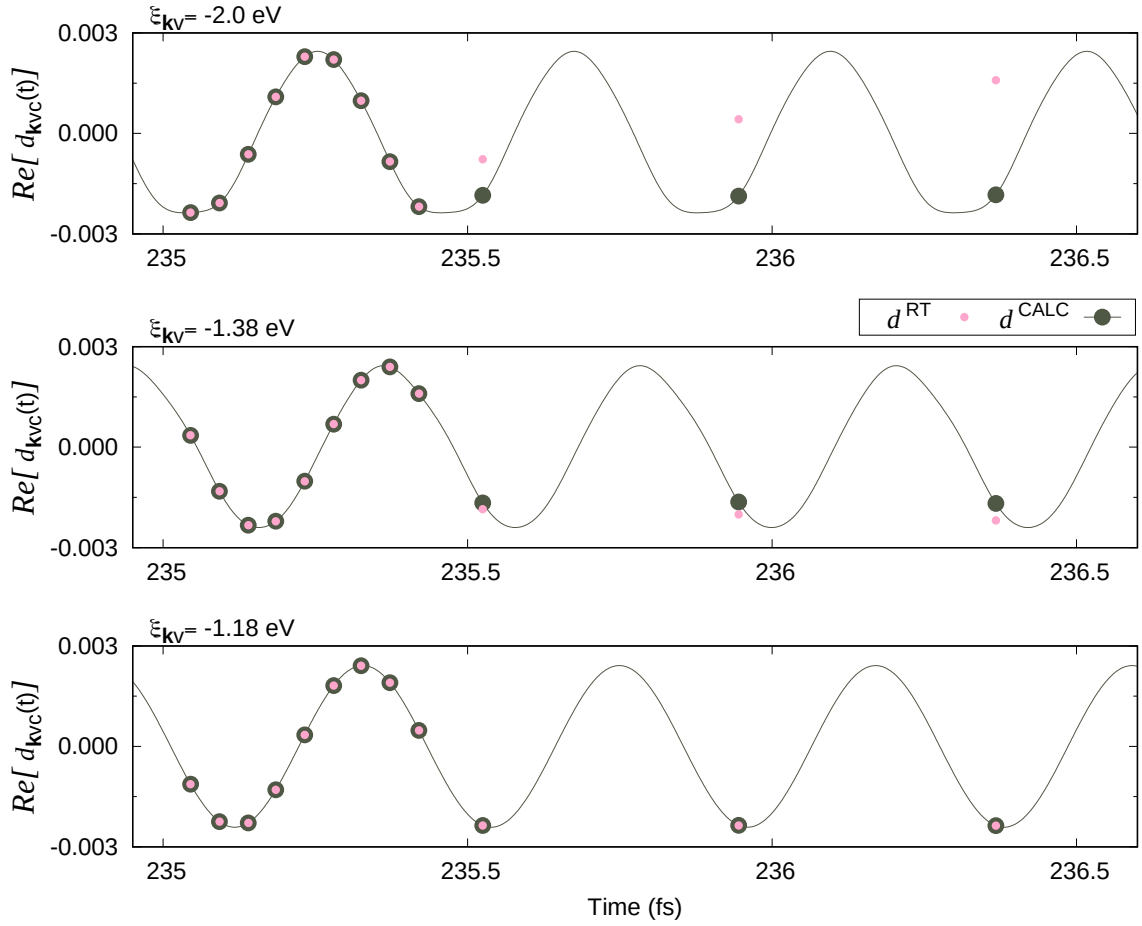

Figure 6.1: Agreement between $d^{\mathrm{CALC}}_{\mathbf{k}vc}(t_s)$ and $d^{\mathrm{RT}}_{\mathbf{k}vc}(t_s)$ for three trial values of the quasi-energy at a given $\mathbf{k}$-point, $\xi_{\mathbf{k}v}$. The pink dots represent $Re[d^{\mathrm{RT}}_{\mathbf{k}vc}(t_s)]$ at the time steps of the sampling and verifying sets (first nine and last three values, respectively). The grey curve corresponds to $Re[d^{\mathrm{CALC}}_{\mathbf{k}vc}(t)]$. Its value at the time steps of both sets is distinguished with a grey dot. The difference between the grey and pink dots are the contributions to the $\mathrm{err}_{\mathbf{k}n}$ function. The lowermost quasi-energy is close to the correct value.

cases are far from convergence when calculated *via* the Floquet approach and show severe discrepancies in the resulting eigenvectors respect to those obtained by post-processing the real-time solution. We verified that these discrepancies are not present when convergence of the Floquet self-consistent loop is achieved, e.g., 2D h-BN at TDH level with a broadening of 0.15 eV and Kerker preconditioning, which is the case shown in Fig. 5.1.

6.2.1 Time-dependent Hartree

The analysis at the TDH level focuses on the third peak of the absorption spectrum of h-BN, where our Floquet code normally presents divergencies (see Fig. 5.1). Moreover, the small broadening used here leads to more severe instabilities than those shown in Fig. 5.1, which could not be mitigated by the Kerker preconditioning. The results of this analysis are shown in Figs. 6.2 and 6.3, where all data corresponds to the frequency of the peak, $\omega_{\text{res}} = 9.8236$ eV, and to a particular $\mathbf{k}$-point, which showed the greatest response at that frequency.

First, we look at the Floquet eigenvector extracted from the real-time solution (top half of Fig. 6.2). This eigenvector, which corresponds to the Floquet state of the time-dependent valence band (solution of the real-time problem), is indicative of a Floquet crossing between the zeroth mode of the valence band and the first mode of the conduction band (cf. Fig. 4.1). For this reason, the central component ($\widetilde{d}_{\mathbf{k}vv}(0)$, or $(v, 0)$ for short) decreases slightly from unity while the second-to-highest amplitude corresponds to the first mode of the conduction band, i.e., the so-called coupling component ($\widetilde{d}_{\mathbf{k}vc}(+1)$, or $(c, +1)$). We verified the latter peaks at the same frequency as the response function, reaching an absolute value of 2.9×10^{-3} at ω_{res} (this will be revisited in Section 6.3).

We now turn to the eigenvectors calculated by the proposed Floquet formalism, shown in the bottom half of Fig. 6.2. From the data at iterations 2 and 6, we observe the Floquet solution progresses in the right direction and shows great similarity with the eigenvector extracted from the real-time solution. However, the code did not converge at that point and subsequent iterations started to diverge from the intended solution. This is better appreciated in the left panel of Fig. 6.3, where the value of individual components of the Floquet-calculated eigenvector are tracked throughout the iterations and the dashed lines represent the real-time solution for each component. From iteration 7 onwards, several components of the eigenvector start to grow out of control, overtaking their real-time counterpart by orders of magnitude. This leads to a situation where the coupling component

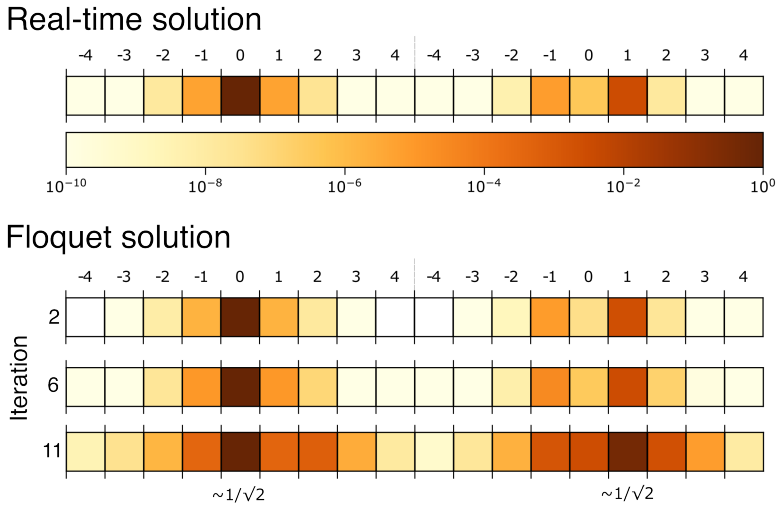

Figure 6.2: Colour-coded representation of Floquet eigenvectors at TDH level, as introduced in Fig. 4.1 The data corresponds to a selected **k**-point of real-time and Floquet calculations of two-band h-BN at $\omega_{\text{res}} = 9.8236$ eV. Top: Correct eigenvector as extracted from the real-time solution. Bottom: Eigenvectors calculated by the Floquet approach at different iterations. The Floquet code fails to converge in this case as a broadening of 0.04 eV was used.

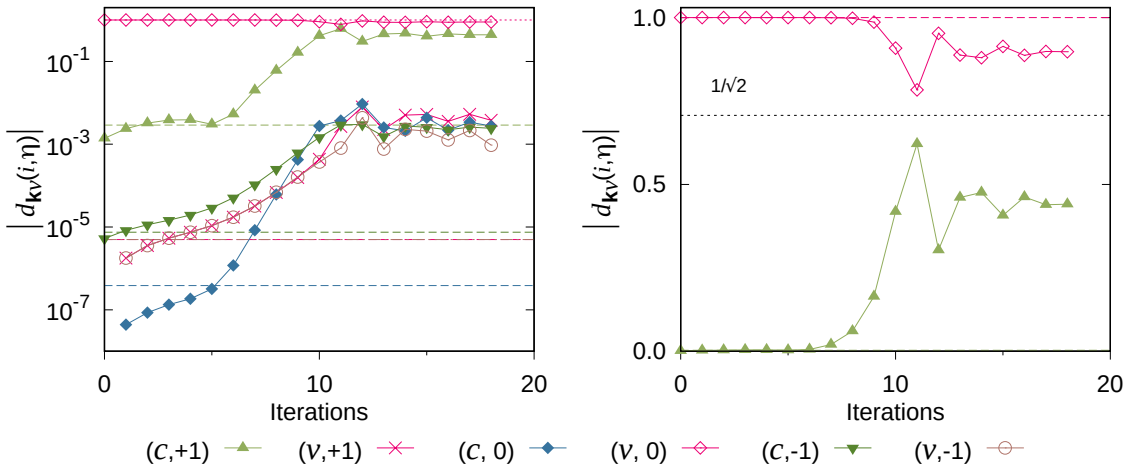

Figure 6.3: Selected components of the eigenvectors presented in Fig. 6.2 (TDH level). The left panel shows several components in logarithmic scale. The lines with points represent data calculated *via* the Floquet approach while the horizontal dashed lines correspond to the real-time solution. The right panel only shows two Floquet-calculated amplitudes in linear scale, namely the central and coupling components ($\widetilde{d}_{\mathbf{k}vv}(0)$ and $\widetilde{d}_{\mathbf{k}vc}(+1)$, respectively).

$(c,+1)$ reaches the same order of magnitude as the central component $(v,0)$, which decreases accordingly (see right panel of Fig. 6.3, where both values tend to $\frac{1}{\sqrt{2}}$). This eigenvector

implies a population inversion that greatly exceeds both what was found by post-processing the real-time result and what is expected with the weak fields used throughout this work. We are confident a population inversion of this magnitude is wrong and should not be produced by our Floquet code.

6.2.2 Hartree plus screened-exchange self-energy

The analysis at the H+SEX level focuses on the first exciton of h-BN, where the linear response calculated *via* Floquet did not achieve convergence (see Fig. 5.10). The results of this analysis are shown in Figs. 6.4 and 6.5, where all data corresponds to the exciton energy, $\omega_{\text{exc}} = 5.4332$ eV. We start by looking at the Floquet eigenvectors extracted from the real-time solution at two particular $\mathbf{k}$-points (top half of Fig. 6.4). The first one (of index number 7, i.e., $\mathbf{k}_7$) shows the largest response among all the transitions studied in terms of its coupling component $(c, +1)$, which reaches a maximum of 1×10^{-3} at ω_{exc}. At variance, $\mathbf{k}_{35}$ represents one of the many transitions showing a much more moderate coupling component of only 1×10^{-5}.

In terms of the eigenvectors calculated *via* Floquet (bottom half of Fig. 6.4), the one corresponding to $\mathbf{k}_7$ at iteration 7 looks reasonably close to the real-time result. However, some amplitudes of this eigenvector grow out of control in subsequent iterations, in particular, the ± 2 components both of the valence and conduction band, and the zeroth mode of the conduction band (see left panel of Fig. 6.5). They surpass the real-time solution (indicated with dashed lines) by several orders of magnitude but do not reach values closer to the central component $(v, 0)$, which remains at 0.99996. At variance, the eigenvector at $\mathbf{k}_{35}$ does show a $(c, +2)$ component that reaches the order of magnitude of the central component (see right panel of Fig. 6.5). Once again, this implies a population inversion far greater than expected or found in the real-time solution (see Fig. 6.4). As in the TDH case, we believe this population inversion is not correct and should not be predicted by this Floquet formalism.

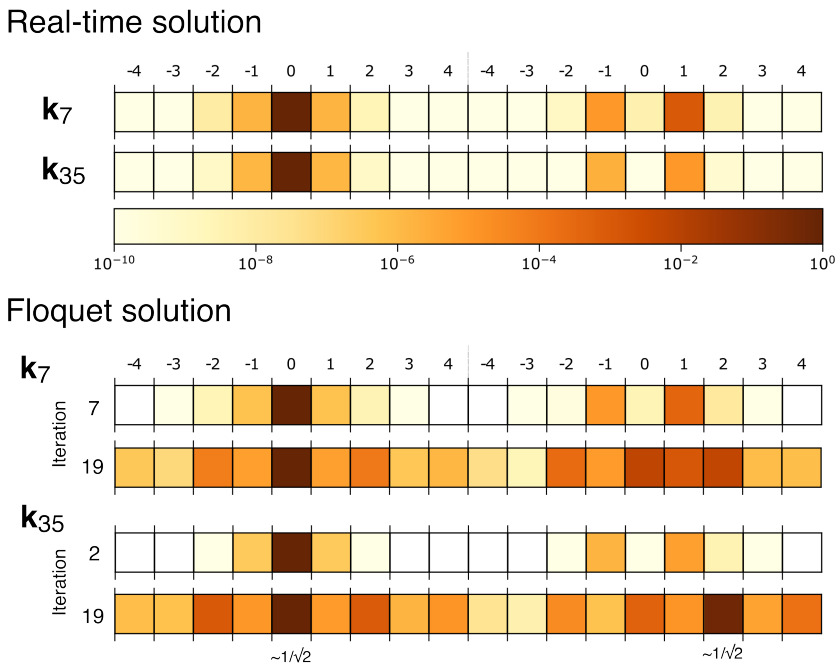

Figure 6.4: Colour-coded representation of Floquet eigenvectors at H+SEX level, as introduced in Fig. 4.1. The data corresponds to selected **k**-points of real-time and Floquet calculations of two-band h-BN at $\omega_{\text{exc}} = 5.4332$ eV. Top: Correct eigenvectors as extracted from the real-time solution. Bottom: Eigenvectors calculated by the Floquet approach at different iterations. The Floquet code fails to converge in this case.

6.3 Discussion and outlook

In Section 5.2, the divergencies in the spectra calculated by the proposed Floquet method were described, while Section 6.2 presented the big population inversions that our code wrongly predicts for these cases. In this Section, we will argue there is a causal link between the two and explore ways to limit the population inversion.

6.3.1 Population inversion

Let us first say that, in our experience of having programmed and debugged this code, every time the response function presented divergencies, there was an eigenvector showing a big population inversion such that the central amplitude $(v, 0)$ and some coupling component, e.g., $(c, +1)$ were of the same order of magnitude. For example, 0.92 and 0.4, respectively. Second, the real-time results in Section 6.2 indicate that, even at the peak of the response

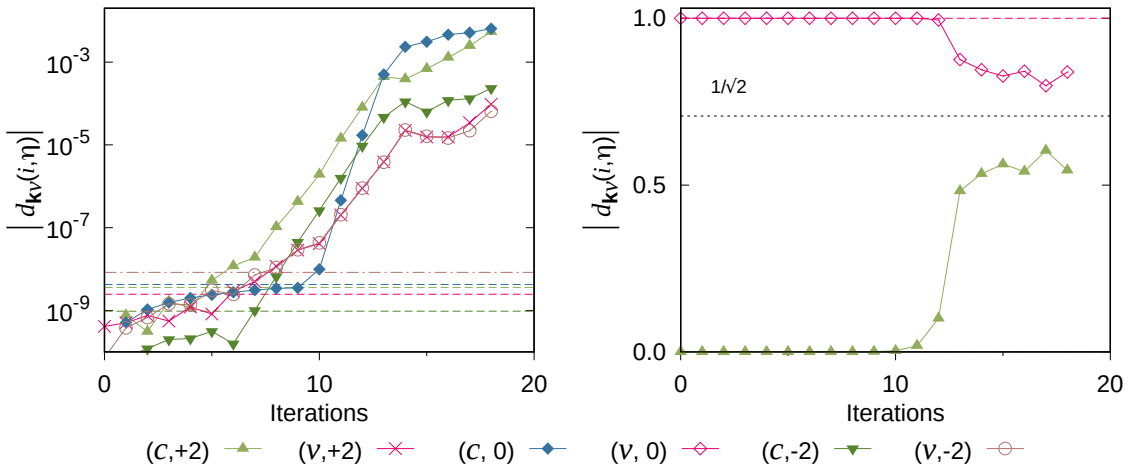

Figure 6.5: Selected components of the eigenvectors presented in Fig. 6.2 (H+SEX level). The left panel shows several components in logarithmic scale. The lines with points represent data calculated *via* the Floquet approach while the horizontal dashed lines correspond to the real-time solution. The right panel only shows two Floquet-calculated amplitudes in linear scale, namely the central and coupling components ($\widetilde{d}_{\mathbf{k}vv}(0)$ and $\widetilde{d}_{\mathbf{k}vc}(+2)$, respectively).

function, the coupling amplitude should be in the order of 10^{-3}. While the latter does show an inverse proportionality with the broadening, even the 0.04 eV calculations resulted in moderate coupling components. Finally, Fig. 6.6 shows that the absorption follows the magnitude of the coupling amplitude of the eigenvector corresponding to the **k**-point that drives that response (the eigenvectors in these two cases have been obtained by post-processing the real-time result). In light of this discussion, we can confidently say that if the coupling amplitude happens to be much too high, so will the response function.

Based on the correct Floquet states as obtained by post-processing the real-time result, it is apparent that we should now explore ways to limit the high population inversions wrongly produced by our Floquet code at the TDH and H+SEX levels (see Figs. 6.2 and 6.4). As discussed in Section 2.3.2, the dephasing term of Eq. 2.78 that prevents high population inversions in the real-time approach by demoting electrons back to the valence band. Moreover, it was already mentioned in Section 4.1.5 that the addition of a FKS-space formulation of this dephasing operator to the quasi-energy eigenproblem was not successful,

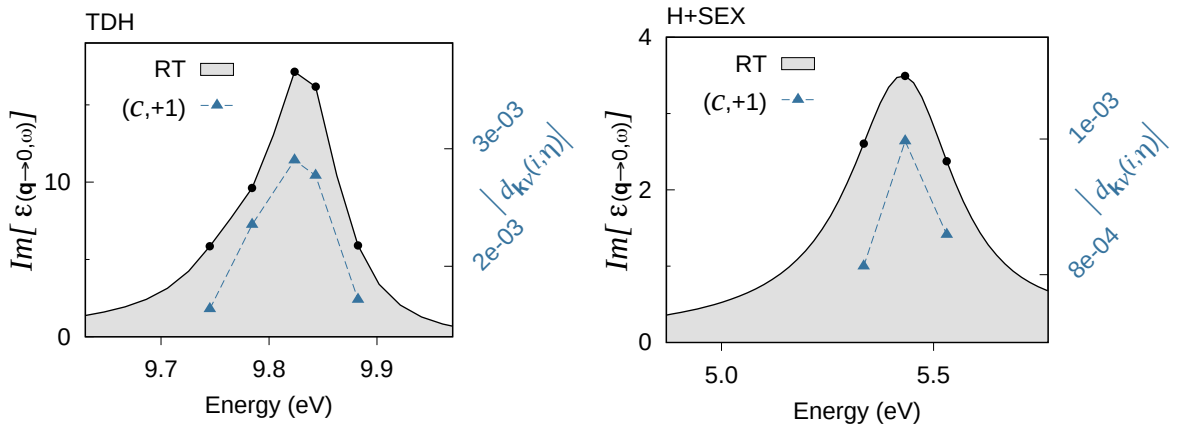

Figure 6.6: Comparison between the linear response function (black lines, left axis) and the maximum magnitude of the coupling component among all eigenvectors (blue dashed lines,right axis) at resonant or excitonic frequencies. The data corresponds to real-time calculations on two-band h-BN, both at the TDH (left panel) and H+SEX (right panel) levels.

i.e., it introduced convergence issues at the IPA level and it did not improve the stability of the TDH case.

It is interesting to note that this problem can also be found the IPA level in the absence of any dissipation mechanisms. This follows the logic of the two-state model presented in Fig. 4.1, where even the smallest of couplings would result in high populations inversions if not damped with an imaginary contribution to the diagonal of the quasi-energy operator. By a similar token, the population inversions at the IPA level were remedied by the introduction of the phenomenological damping term of Eq. 4.34. However, the results of Chapters 5-6 indicate that this operator is not enough to avoid high population inversions when local fields or many-body effects are included. It is possible that a more advance framework for the introduction of dissipation effects could result in a damping operator robust enough to stabilise these calculations, the form of which has not been found yet.

6.3.2 Floquet near-degeneracies

Another way of dealing with high population inversions consists on working in the (near) degenerate sub-space implied by the presence of a Floquet crossing. As explained in Fig. 4.1,

when a Floquet crossing occurs, two eigenstates of the quasi-energy operator will have (near) degenerate eigenvalues. The corresponding eigenvectors will then be 'complementary', in the sense that if one has amplitudes of 0.92 and 0.4 for $(v, 0)$ and $(c, +1)$, respectively, then the other eigenvector will have those amplitudes inverted, i.e., 0.4 and 0.92 for $(v, 0)$ and $(c, +1)$, respectively. Any linear combination in this degenerate sub-space will be a valid eigenvector with the same eigenvalue. In fact, there will be a linear combination that has precisely the correct population inversion and thus gives just the right response function. The problem would then be finding a correct framework to define said linear combination.

In this regard, the average energy formalism presents itself as providing such framework [125, 126]. The authors argue that the current method of obtaining Floquet states (see Eq. 2.83) is incomplete and unstable, and that the quasi-energy should not be interpreted as the energy of the system. Instead, they propose an average energy operator whose eigenvalues *are* the analogous of a static energy. The average energy would then lift degeneracies in the quasi-energy spectrum and define a Floquet ground state, thus acting as an additional quantum number. This average energy operator is built in the degenerate sub-space as,

$$\bar{H}_{\mathtt{IJ}} = \frac{1}{T}\int_0^T \langle \phi_{\mathtt{I}}(t)|\hat{H}|\phi_{\mathtt{J}}(t)\rangle, \tag{6.8}$$

where the labels `I` and `J` correspond to degenerate Floquet eigenvectors having the same quasi-energy. Diagonalising this operator and choosing the lowest eigenvalue would provide the appropriate linear combination within the degenerate subspace to define a Floquet ground state [125, 126].

We implemented the average energy formalism into our Floquet code and tested it with two-band h-BN at the IPA level (see Fig. 6.7). Away from any near-degeneracy, the code proceeds as described in Chapter 4. However, if a near-degeneracy is found in the quasi-energy spectrum, the average energy operator is built with the states of the degenerate sub-space and then diagonalised. The lowest average energy eigenvalue is chosen and the corresponding linear combination of degenerate eigenvectors is computed to continue with

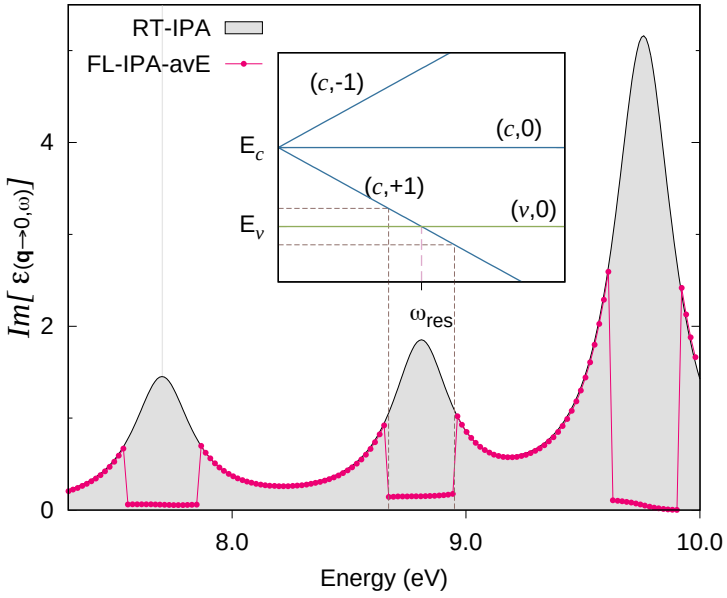

Figure 6.7: Absorption spectrum obtained with the average energy formalism (labelled avE in the legend) as implemented in our Floquet code. The data corresponds to a two-band calculation of h-BN at the IPA level with 0.04 eV of broadening. The inset shows a representation of a Floquet crossing and the resulting near-degeneracy in the quasi-energy (see horizontal dashed lines). The latter determines a range of frequencies for which the code executes the average energy subroutine (see vertical dashed lines). The vertical dashed lines overlap into the main figure to show an example of a frequency range where a near-degeneracy was found in the calculation.

the calculation. Whether the code finds a near-degeneracy or not depends on a user-defined threshold, which defaults to twice the broadening parameter.

As expected, the algorithm finds near-degeneracies at the positions of the peaks in the spectra, as represented by the dashed lines in the inset overlapping with the main plot in Fig. 6.7. However, the use of this formalism results in suppressing the absorption to nearly zero. After carefully considering the analytical example provided in Ref. [125], we concluded that, indeed, the Floquet ground state as calculated *via* this formalism implies recovering the valence state. This could indicate that the states we are looking for when calculating optical spectra are not Floquet ground states. Moreover, as suggested by the examples in Ref. [125], it is possible that the average energy formalism has been developed for electric fields with higher intensities than the ones used in our work. Nevertheless, we consider the use of some linear combination within the degenerate subspace to be a promising route for

addressing the instabilities found in the proposed Floquet method. Work should be done towards developing a formalism capable of uniquely defining such linear combination.

6.4 Application example

We briefly digress from the main narrative of the thesis to showcase how the Floquet analysis tool presented here can be used on its own right, providing further insights into a real-time calculation. In this example, we will analyse the SHG spectrum of 2D h-BN at the H+SEX level, as obtained *via* the real-time approach [43]. In order to simplify the analysis, only two bands will be included in the model, however we highlight that the procedure presented here is not limited to any particular number of states.

A criticism that could be made of the real-time approach concerns its inability to identify the individual contributions of each KS state or e-h transition to a given feature in the spectrum. This is because all the electronic degrees of freedom are integrated out in the calculation of the dynamical polarisation, before the latter is processed to extract the susceptibilities. Therefore, it is difficult to assess which states drive the response function at given frequency. At variance, this information is likely more accessible in formalisms based on response theory. For instance, in the BSE framework for linear response, the eigenvectors of the excitonic Hamiltonian provide the contributions (weights) of different transitions in e-h space to a given excitonic wavefunction. It would be desirable to perform an analysis of this kind over a real-time calculation, which can also describe nonlinear optical processes. In this section, we will demonstrate how a Floquet processing of the time-dependent states, solutions of the real-time approach, can facilitate said analysis.

As shown above, the Floquet analysis tool allows us to extract Floquet states from the time-dependent wavefunctions corresponding to each occupied band at every $\mathbf{k}$-point. As show in Fig. 6.8, we do this at two different frequencies in the SHG spectrum of h-BN, i.e. off resonance and at resonance, in order to compare the resulting Floquet eigenvectors. Our findings highlight the role of the $(c, +2)$ components of the eigenvectors, as they grow

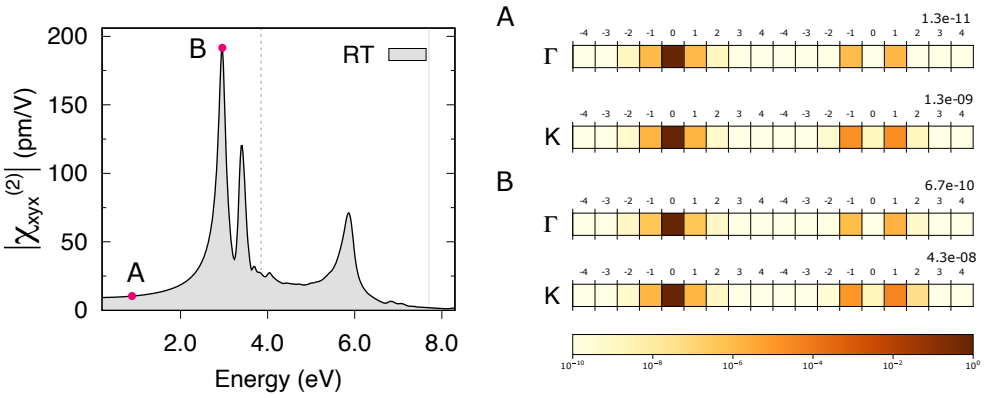

Figure 6.8: Left: Monolayer h-BN SHG spectra on a $24 \times 24 \times 1$ **k**-grid with a broadening of 0.15 eV, calculated by the real-time (RT) approach at the H+SEX level. The intensity of the electric field is 1×10^6 W cm^{-2}. The two frequencies at which the Floquet analysis is performed are highlighted with pink dots. Right: Colour-coded representation of Floquet eigenvectors, as introduced in Fig. 4.1. The data corresponds to selected **k**-points of the real-time calculation, both off-resonance (A) and at a resonant frequency (B), $\omega = 2.96$ eV. The numbers on the right hand side indicate the magnitude of $\widetilde{d}_{\mathbf{k}vc}(\eta = 2)$ on each eigenvector.

considerably more than any other amplitude when going from off-resonance to resonance. For instance, Fig. 6.8 shows that, at the high-symmetry K point of the BZ, $\widetilde{d}_{\mathbf{k}vc}(\eta = 2)$ increases over 33 times from frequencies 'A' to 'B' in the spectrum (while, e.g., $\widetilde{d}_{\mathbf{k}vc}(\eta = 1)$ less than doubles). This is consistent with the idea of a Floquet crossing between the $(v, 0)$ and $(c, +2)$ Floquet modes (cf. Fig 4.1), occurring at a frequency close to half the energy of a related feature in the absorption spectrum (see below).

Moreover, these $(c, +2)$ components show great disparities among different **k**-points in the BZ, as exemplified with the Γ and K high-symmetry points in Fig. 6.8. Since we can perform this Floquet analysis over the time-dependent states at any **k**-point, we can then map the magnitude of $\widetilde{d}_{\mathbf{k}vc}(\eta = 2)$ into the BZ, as shown in the right hand side of Fig. 6.9. This reveals that the first peak in the SHG spectrum of h-BN (peak 'B' in Fig. 6.8) originates from transitions at and around the optical gap (see K **k**-point in the band structure of Fig. 6.9). In reciprocal space, these contributions reach their highest values at the high-symmetry K **k**-points and extend along the $K - M$ boundaries of the BZ.

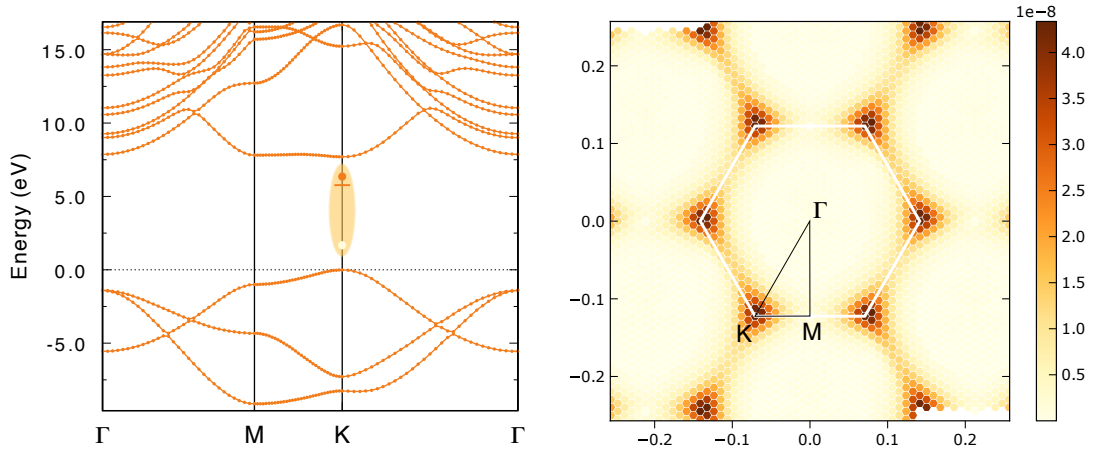

Figure 6.9: Left: band structure of monolayer h-BN. Right: absolute value of $\widetilde{d}_{\mathbf{k}vc}(\eta = 2)$ at different **k**-points in the BZ. These values were calculated with the Floquet analysis tool presented here, while the plot has been produced with tools available within Yambopy [129]. The scale in the colour map is linear.

In the absence of the information provided by the present Floquet analysis, the interpretation of this SHG peak would have been limited to an argument around frequencies, which remains valid nonetheless. The latter focuses on the fact that this feature occurs at 2.96 eV, which is half the frequency of the first exciton of h-BN ($\omega_{exc} = 5.92$ eV according to our calculations). Therefore, two-photon resonances with said exciton are thought to be involved. Having access to the contributions of the various e-h pairs to the SHG spectrum puts this interpretation on firmer footing, since this SHG peak and the first exciton of h-BN show a similar distribution of weights in the BZ (see Fig. 5 of Ref. [141] for a representation of this exciton in reciprocal space).

A limitation of this approach relates to the excitonic wavefunctions, which are not accessible *via* this Floquet analysis. As a result, this procedure overlooks the fact that the first exciton of h-BN is doubly degenerate, which would arise immediately from the BSE eigenvectors [141].

6.5 Signatures of non-adiabaticity

The Floquet approach presented in Chapters 4 and 5 requires the validity of the adiabatic approximation introduced in Eq. 4.3. Without this approximation, the time periodicity of the Hamiltonian in Eq. 2.59 cannot be guaranteed, thus failing to meet one of the conditions for the application of Floquet's theorem. At the IPA level, this reflects the fact that the Berry-phase electron-field coupling operator depends on the solution of the quasi-energy eigenproblem, as explained in Section 4.1.3. The inclusion of local-field and many-body effects requires this approximation to ensure the periodicity of the density and the density matrix, which in turn determines the periodicity of the Hartree potential and the self-energy (see Section 5.1).

In this section, we intend to numerically assess the validity of the adiabatic approximation for a particular case. We chose the system in Section 6.2.2, i.e., 2D h-BN driven by an electric field at the frequency of its first excitonic resonance, $\omega_{\text{exc}} = 5.4332$ eV. In order to do this, we performed a real-time calculation at the H+SEX level and extracted the matrix elements of the Hamiltonian in Eq. 2.66 as a function of time. This Hamiltonian included the electron-field coupling operator, the Hartree potential and the self-energy, according to the chosen level of theory. We then selected the matrix element that showed the greatest time dependence, i.e., oscillated with the largest amplitude. As expected, this was the off-diagonal matrix element between the valence and conduction bands at the same $\mathbf{k}$-point considered for Fig. 6.4 ($\mathbf{k}_7$). Finally, we studied the time periodicity of this matrix element. We conducted this same test for a range of electric-field intensities in order to quantify the limits of validity of the adiabatic approximation with regards to this parameter.

In order to study the time periodicity of this matrix element, we performed a FFT. Numerical issues related to spectral leakage were solved by using the Kaiser window function (with a large $\beta = 42$), which showed very good side-lobe behaviour. This required hundreds of fs worth of dynamical data, i.e., hundreds of thousands of data points. Fig. 6.10 presents the results at two different field intensities. The uppermost plot shows that

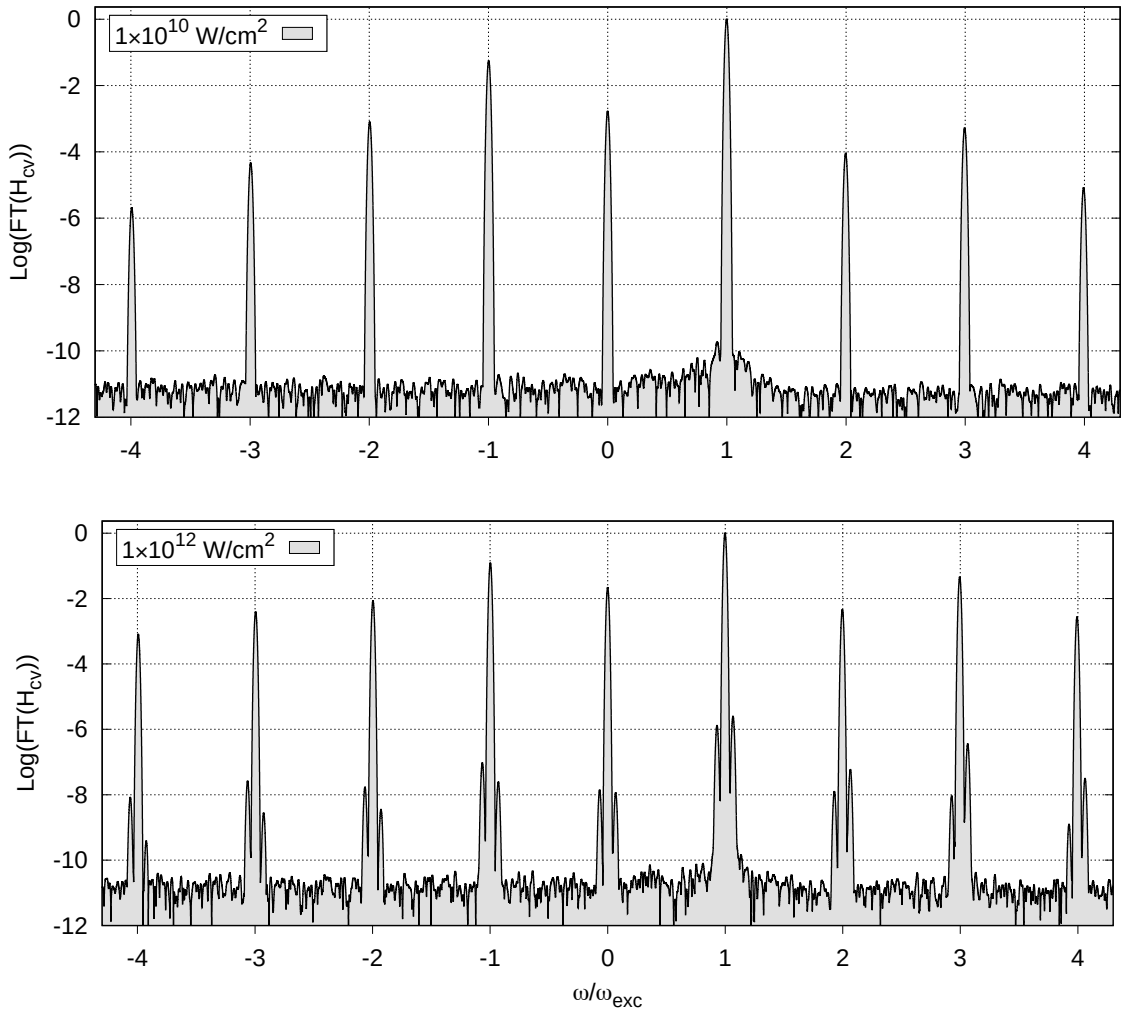

Figure 6.10: Fourier transform of a Hamiltonian matrix element extracted from a real-time calculation at H+SEX level as a function of time. The data corresponds to a selected **k**-points of two-band h-BN at $\omega_{\text{exc}} = 5.4332$ eV. Top (bottom): electric field intensity of $1{\times}10^{10}$ ($1{\times}10^{12}$) W cm^{-2}. The data obtained from the Fourier transform (FT) is normalised to a maximum value of 1.

the Fourier transform of the matrix element in question at $1{\times}10^{10}$ W cm^{-2} only has non-zero contributions at frequencies commensurate with the frequency of the excitation, ω_{exc}. Therefore, this quantity is a periodic function of time, which validates the adiabatic approximation at this field intensity. However, at $1{\times}10^{12}$ W cm^{-2}, the Fourier transform of the Hamiltonian matrix element presents side-bands to the main peaks (see lowermost plot in Fig. 6.10). This result is in line with the findings of a similar study of the exchange-correlation functional in the context of TD-DFT [121]. The presence of side-bands is a

signature of non-adiabaticity since it indicates the presence of Rabi oscillations. While it could be argued that this feature is small (six orders of magnitude smaller than the main peak), it is clear that the adiabatic approximation should not be assumed valid at intensities beyond 1×10^{12} W cm^{-2}. Nevertheless, the result reported in Fig. 6.10 at 1×10^{10} W cm^{-2} puts the validity of the adiabatic approximation at the intensities explored in Chapters 4 and 5 on firmer footing.

Chapter 7

Conclusions and future work

Computational materials science opens the possibility of accelerating the discovery of novel and functional materials by offering a *technology* capable of testing tens of thousands of compounds in a quick and relatively inexpensive way compared to experimental studies. This relies on its ability to make *ab-initio* predictions of properties in quantitative agreement with experiments. At the core of computational materials science we find the numerical methods used to compute these properties, which determine what is (or is not) possible within given computational resources. They represent the result of a decades-long cross-community effort that ranges from the formulation of the relevant theoretical frameworks, to the development of efficient algorithms and their computational implementation. Improving these methods in order to boost the capabilities of computational materials science is the overarching objective of this thesis.

While the calculation of ground-state properties finds an extremely efficient framework in DFT, the numerical methods available for the description of excited states within MBPT are more computationally demanding, often reaching the limits of today's supercomputers. This certainly applies to the calculation of optical properties, in which the description of excitons and phenomena beyond the linear regime are often met with computational barriers. Removing these limitations could enhance the contribution of computational materials science to the fields of optoelectronics and photonics. Crucially, these research areas stand

out for the hugely transformative technologies they have enabled and their remarkable potential for future applications. This conjunction of challenges and opportunities gives grounds for focusing our efforts in developing methods for optical properties in particular.

The first development we proposed concerns the calculation of optical absorption spectra in extended systems based on linear response theory, to which Chapter 3 was devoted. The state-of-the-art framework for the prediction of this property is given by the Bethe-Salpeter equation, which allows for an appropriate description of excitons. The latter requires very dense **k**-point grids, thus imposing a computational burden that often renders these calculations prohibitively costly. This is certainly a main limiting factor in the BSE scheme, both in terms of computational cost and memory footprint. We addressed this challenge by proposing a double-grid approach to **k**-sampling in the BSE. Our method is based on combining a coarse **k**-grid where both KS eigenvalues and eigenvectors are known with a fine **k**-grid where only KS energies are required, which eases memory and disk storage requirements. This results in having access to the oscillator strengths and BSE kernel matrix elements only in the coarse grid, and implies necessary approximations for both magnitudes in the fine grid.

As stated in Section 1.3, a key question relates to whether this approximated scheme can correctly describe excitonic effects, which we addressed by critically analysing its assumptions, as well as performing tests on a number of well-known materials. We concluded that the diagonal extension of the BSE kernel proposed here remains a good approximation for systems with excitons that are loosely bound and/or delocalised over many unit cells, as confirmed by satisfactory results on bulk Si, bulk GaAs and, to a lesser extent, monolayer MoS_2. This approximation fails in materials with spatially localised and strongly bound excitons, e.g., bulk h-BN, which are nonetheless usually well described by a relatively coarse **k**-grids. Finally, systems with rapidly varying oscillator strengths within the BZ also fall outside the limits of validity of our approach, e.g., BP. In any case, this can be verified with a procedure based on inexpensive IPA-level calculations.

An evaluation of the computational gains attained by the proposed double-grid ap-

proach constitutes another key question identified in Section 1.3. We verified that, within this strategy, the coarse **k**-grid drives the computational cost while the fine **k** grid requires minimal extra computation and memory. Therefore, based on its simplicity, the proposed method provides an approximated fine-grid result at roughly the cost of a coarse-grid calculation. Moreover, our approach is compatible with the most efficient BSE solver, i.e., the Lanczos-based Haydock scheme, thus maximising the size and range of materials for which this method could be useful.

In Chapters 4 and 5, we proposed a Floquet reformulation of the real-time approach to nonlinear optics in extended systems [42, 43]. In response to Section 1.3, our successful implementation of this framework indicates that, indeed, Floquet theory can be used to reformulate this time-dependent problem into a time-independent self-consistent eigenvalue problem. Due to the time-periodicity required of the Hamiltonian by Floquet's theorem, this reformulation applies to systems driven by a continuous monochromatic perturbation, which is useful to compute nonlinear susceptibilities. Particular attention was devoted to the electron-field coupling operator, which is based on the dynamical Berry-phase polarisation [97] and makes our approach valid for extended systems. This operator introduced the need for a self-consistent solution of the quasi-energy eigenproblem and required the use of the adiabatic approximation [121] in order to remain time-periodic. As a result, our Floquet approach is valid for weak electric fields, thus excluding the extreme nonlinear regime where the adiabatic approximation is likely to break down.

Whether this Floquet formulation retains the main advantages of the real-time approach is also a central issue, as stated in Section 1.3. We can confirm that our method maintains the non-perturbative nature of the real-time scheme, allowing for the simultaneous extraction of susceptibilities to different orders in the electric field and for treating several nonlinear phenomena within the same formalism. The flexibility for the inclusion of correlation effects is also retained. Formally, many-body effects can be considered by adding the relevant terms to the effective one-particle Hamiltonian, as it is done within the real-time approach. However, the formulation beyond the IPA level introduced instabilities into the

Floquet self-consistent loop, which could not yet be fully mitigated.

An extensive benchmark of the proposed Floquet approach was conducted at the IPA level, which demonstrated the validity and effectiveness of our scheme. We calculated SHG spectra of bulk AlAs, monolayer h-BN and monolayer MoS_2, plus THG spectra of bulk Si. In all cases, the Floquet method produced spectra in agreement with the real-time approach. Moreover, the proposed scheme showed a consistent computational advantage in comparison to the real-time formalism, resulting up to two orders of magnitude faster. Therefore, we were able to tackle the often prohibitive computational cost associated with real-time calculations, which originates from the expensive numerical integration of the EOMs (entirely avoided in our time-independent formalism).

A final point relates to the convergence issues appearing in the Floquet approach beyond the IPA level. Only a handful of results could be converged at the TDH level, assisted by the Kerker preconditioning scheme [144] or *via* Padé approximants. These calculations showed spectra in agreement with the real-time approach and still presented a sizeable computational advantage. However, considerable work has to be done in order to find a robust and general solution to these instabilities. In order to further characterise these shortcomings, a suite of post-processing tools capable of extracting Floquet states from the time-dependent solution of the real-time approach was developed in Chapter 6. The insights provided by these tools indicate that these divergencies are linked to high population inversions encountered throughout the Floquet self-consistent loop. Indeed, the correct Floquet states derived from the real-time result show small population of excited states regardless of the level of theory employed, in accordance to the weak electric fields considered in this work.

In light of the promising results achieved by the double-grid and Floquet approaches presented in this thesis, we believe our contribution can accelerate the *ab-initio* calculation of linear and nonlinear optical properties, reaching complex materials that are too demanding for currently available methods and, overall, boosting the capabilities within computational materials science.

Future work

The findings in this thesis can serve as motivation for prospective studies and future developments, both in terms of addressing the shortcomings of the methods presented here and building up on what has been achieved.

Let us start with the double-grid approach to **k**-sampling presented in Chapter 3. A straightforward way to improve this method implies removing the approximation to the dipole matrix elements in the fine **k**-grid (see Eq. 3.7). Instead of considering these matrix elements as being equal to their closest coarse-grid counterpart, we could calculate them for every κ-point in the fine grid, thus expanding the applicability of our method to systems where this approximation breaks down. However, computing these quantities would require access to the fine-grid wavefunctions, severely increasing the memory requirements of the scheme. Since our intention was to propose a method based on simplicity and with minimal computational overhead respect to a coarse-grid calculation, we opted against this idea in Chapter 3. Alternatively, one could think of formulating this approximation in the velocity gauge, rather than the length gauge (see Eq. 3.7), and evaluate its performance.

The other approximation used in our double-grid method concerns the treatment of the fine-grid matrix elements of the BSE kernel as an extension of coarse-grid analogues. As it was earlier pointed out, more complex schemes for double-grid **k**-sampling within the BSE scheme already exist [66, 79–82]. In fact, the DKE approximation proposed here is intended as a simplification of these other methods, in order to dispense with the fine-grid wavefunctions. Moreover, we believe it would not be sensible to try and simplify it even further. Therefore, any future development on improving the efficiency of BSE calculations would likely focus on some other aspect of their implementation. Since the size of the BSE kernel matrix determines the computational cost of a given BSE calculation, we could consider re-thinking the e-h basis and proposing an alternative one. For example, we could opt for the so-called optimal basis (OB) [149] and its extension to an optimal product basis (OPB) [150]. This idea has been successfully implemented in the SIMPLE code [150].

However, the latter only exploits the OPB for the calculation and storage of the excitonic Hamiltonian, reverting to e-h space for the solution of the eigenproblem. At variance, one could think of reformulating the Haydock solution of the BSE in the OPB, thus completely dispensing with the e-h basis. This could be attempted based on a similar example found in the theoretical chemistry literature for finite systems [151], where the Haydock algorithm was re-written in terms of a product basis of localised functions (linear combinations of atomic orbitals). At variance, any such proposal of our own would focus on extended systems. Moreover, a further element of novelty would lie on including the RPA screening, rather than model screening functions as previously done [150].

Regarding the Floquet approach to nonlinear optics presented in Chapters 4 and 5, prospective studies would likely focus on addressing the shortcomings found beyond the IPA level in terms of instabilities within the Floquet self-consistent loop. An interesting avenue to explore is the idea of a linear combination of Floquet eigenvectors within the degenerate subspace formed at Floquet crossings, as has been proposed in Section 6.3.2. This procedure would limit the population of excited states, thus dealing with the high population inversions encountered during self-consistency. However, this would require the development of a theoretical framework capable of defining such linear combination in order to avoid any *ad-hoc* formulations. The average energy formalism, or variations of it, certainly constitute a promising alternative. Moreover, we believe that the broadening parameter should play a role in the definition of this linear combination, as it is clear from the correlation between the population inversion and the magnitude of the response functions.

Besides approaches based on the degenerate sub-space, the phenomenological dissipation operator should be another clear target of any future efforts, as suggested in Section 6.3.1. The fact that the damping term as introduced in Chapter 4 works at the IPA level but struggles to mitigate divergencies beyond it suggests that a *better*, more general or more robust operator coupling the system to the environment could be the missing ingredient in Chapter 5. In this regard, ideas could be drawn from the literature around non-Hermitian

Floquet theory and multiphoton ionisation processes of atoms in intense laser fields [109, 114, 117, 119].

Further developments and improvements can also be considered, either for the current implementation at the IPA level or after eventually tackling the shortcomings found upon the inclusion of many-body effects. As mentioned in Section 4.2.3, one of such opportunities is the use of more efficient eigensolvers for the quasi-energy eigenproblem, like those based on Krylov subspaces [143] or variational approaches [125–127]. This would improve the efficiency of our Floquet method, resulting in higher computational gains respect to the real-time approach. Another interesting idea concerns the calculation of Floquet bandstructures based on the Floquet states and quasi-energies computed when solving the Floquet approach. While this implementation is currently in progress, some important questions remain open, e.g., how to define the occupation of Floquet states. Nevertheless, this development holds promise of paving the way towards an *ab-initio* framework for Floquet engineering of materials, a topic that is typically addressed at the level of model Hamiltonians (e.g., [152]).

An interesting application of the Floquet method presented in this thesis would be given by a high-throughput study oriented towards two-dimensional antiferromagnetism. As mentioned in Section 1.1.2, MOKE microscopy allowed for the detection of ferromagnetism in the monolayer limit, where regular magnetometric techniques fail due to the small sample volumes [27]. However, there is no Kerr rotation in systems with zero net magnetisation, which include interlayer antiferromagnets like bilayer CrI_3 [27] and monolayer systems with intralayer antiferromagnetic ordering , e.g., $MnPS_3$ [153]. Therefore, MOKE microscopy cannot detect magnetic ordering in these cases. Nevertheless, if the antiferromagnetic ordering breaks the inversion symmetry of an otherwise centrosymmetric material, then this phase transition could be detected using SHG as a symmetry-dependent probe.

One could then conceive a high-throughput computational study based on this principle, scanning a database of two-dimensional materials in search of compounds that have an energetically-favoured antiferromagnetic phase in which time-reversal plus inversion remains

a good symmetry. Then, one could select these materials and compute their SHG spectra, in order to determine frequencies with high-intensity second order response. This information could then assist the experimental validation of these potential two-dimensional antiferromagnets. Both bilayer CrI_3 and monolayer $MnPS_3$ fall within this category of materials, as do many other members of the family of transition-metal phosphorus tri-chalcogenides [154]. In fact, SHG has already been used experimentally to detect antiferromagnetism in bilayer CrI_3 [22] and few-layer $MnPS_3$ [24].

Finally, the suite of tools for Floquet analysis of time-dependent states presented in Chapter 6 can be considered a development on its own, beyond its application to characterise the shortcomings of our Floquet approach. It can be used to determine the degree to which different transitions (bands and **k**-points) contribute to a given peak in a SHG spectra. This can be thought of in analogy with the eigenvectors of a BSE Hamiltonian, which can be used to measure the contribution (weight) of each transition in e-h space to a given excitonic wavefunction. Moreover, this tool can be generalised to be agnostic of the code that produced the time-dependent states, and just return Floquet states in the same basis as the former were given.

Appendix A

Supplemental material for double-grid approach

The present Appendix provides supplemental material relative to the double-grid approach introduced in Chapter 3. This entails a visual representation of the main equations involved in the method and further discussions regarding the comparison between different strategies for the extension of the BSE kernel to the fine grid. We also present some supplementary figures referenced within Chapter 3. Finally, we include a statement regarding code and data availability.

A.1 Kernel matrix in the double-grid method

As discussed in Chapter 3, we explored two possible approaches for the extension of the BSE kernel from the coarse grid to the fine grid, namely, DKE and FKE. The DKE approach was chosen for the double grid Haydock implementation in the Yambo code as it has shown to consistently produce better results than the FKE method. In this Section, we will give a visual representation of the equations defining both approaches. Further arguments in favour of DKE are also presented here, apart from the **q**-dependence of the kernel matrix elements (already explored in Section 3.2.3).

A.1.1 Coarse grid

As an example, let us assume we have a system with two bands (c and v) and two $\mathbf{k}$-points ($\mathbf{k_1}$ and $\mathbf{k_2}$). This system would then have two transitions (T_1 and T_2). In this example, the e-h basis would have two components and the BSE kernel would be a 2-by-2 matrix,

$$\begin{bmatrix} \boldsymbol{\Xi_{11}} & \boldsymbol{\Xi_{12}} \\ \boldsymbol{\Xi_{21}} & \boldsymbol{\Xi_{22}} \end{bmatrix}. \tag{A.1}$$

The readily implemented Haydock algorithm requires matrix vector multiplications of the kind

$$\begin{bmatrix} \boldsymbol{\Xi_{11}} & \boldsymbol{\Xi_{12}} \\ \boldsymbol{\Xi_{21}} & \boldsymbol{\Xi_{22}} \end{bmatrix} \cdot \begin{bmatrix} c_{vc\mathbf{k}_1} \\ c_{vc\mathbf{k}_2} \end{bmatrix} = \begin{bmatrix} r_{vc\mathbf{k}_1} \\ r_{vc\mathbf{k}_2} \end{bmatrix}, \tag{A.2}$$

where $c_{vc\mathbf{k}_i} = \langle vc\mathbf{k}_i | V \rangle$ are the components of the Haydock vector $|V\rangle$ to be multiplied by the BSE kernel and $r_{vc\mathbf{k}_i}$ are, analogously, the coefficients of the resulting vector.

A.1.2 Double grid

We now add a fine $\boldsymbol{\kappa}$-grid to our calculation. For the sake of argument, let us say that $\mathbf{K_1}$ has one fine grid $\boldsymbol{\kappa}$-point associated to it ($\boldsymbol{\kappa}_{1_2}$), while $\mathbf{K_2}$ has two ($\boldsymbol{\kappa}_{2_2}$ and $\boldsymbol{\kappa}_{2_3}$) — we remind the reader that $\mathbf{K_1}$ and $\boldsymbol{\kappa}_{1_1}$ are the same $\mathbf{k}$-point. In this case, our e-h basis will grow from having 2 transitions, to 5 in total. This will lead to the BSE matrix

$$\begin{bmatrix} \boldsymbol{\Xi_{11}} & \Xi_{11_2} & \boldsymbol{\Xi_{12}} & \Xi_{12_2} & \Xi_{12_3} \\ \Xi_{1_2 1} & \Xi_{1_2 1_2} & \Xi_{1_2 2} & \Xi_{1_2 2_2} & \Xi_{1_2 2_3} \\ \boldsymbol{\Xi_{21}} & \Xi_{21_2} & \boldsymbol{\Xi_{22}} & \Xi_{22_2} & \Xi_{22_3} \\ \Xi_{2_2 1} & \Xi_{2_2 1_2} & \Xi_{2_2 2} & \Xi_{2_2 2_2} & \Xi_{2_2 2_3} \\ \Xi_{2_3 1} & \Xi_{2_3 1_2} & \Xi_{2_3 2} & \Xi_{2_3 2_2} & \Xi_{2_3 2_3} \end{bmatrix}. \tag{A.3}$$

Only the matrix elements in the coarse grid are explicitly calculated (those highlighted in bold), e.g., $\mathbf{\Xi_{11}}$. The matrix elements involving at least one transition in the fine grid, will be approximated to either zero or the corresponding matrix element in the coarse grid. This will depend on the element in question and the approach taken (DKE or FKE).

A.1.3 Diagonal Kernel Extension (DKE)

In this approximation, we set to zero some of the matrix elements according to Eq. 3.1. This implies, for instance, $\Xi_{11_2} = \Xi_{1_21} = 0$ while $\Xi_{1_21_2} = \mathbf{\Xi_{11}}$. This approximation leads to a matrix of the form

$$\begin{bmatrix} \mathbf{\Xi_{11}} & \Xi_{11_2} & \mathbf{\Xi_{12}} & \Xi_{12_2} & \Xi_{12_3} \\ \Xi_{1_21} & \Xi_{1_21_2} & \Xi_{1_22} & \Xi_{1_22_2} & \Xi_{1_22_3} \\ \mathbf{\Xi_{21}} & \Xi_{21_2} & \mathbf{\Xi_{22}} & \Xi_{22_2} & \Xi_{22_3} \\ \Xi_{2_21} & \Xi_{2_21_2} & \Xi_{2_22} & \Xi_{2_22_2} & \Xi_{2_22_3} \\ \Xi_{2_31} & \Xi_{2_31_2} & \Xi_{2_32} & \Xi_{2_32_2} & \Xi_{2_32_3} \end{bmatrix} \rightarrow \begin{bmatrix} \mathbf{\Xi_{11}} & 0 & \mathbf{\Xi_{12}} & 0 & 0 \\ 0 & \mathbf{\Xi_{11}} & 0 & \mathbf{\Xi_{12}} & 0 \\ \mathbf{\Xi_{21}} & 0 & \mathbf{\Xi_{22}} & 0 & 0 \\ 0 & \mathbf{\Xi_{21}} & 0 & \mathbf{\Xi_{22}} & 0 \\ 0 & 0 & 0 & 0 & \mathbf{\Xi_{22}} \end{bmatrix}. \tag{A.4}$$

The matrix-vector multiplication then leads to

$$\begin{bmatrix} \mathbf{\Xi_{11}} & 0 & \mathbf{\Xi_{12}} & 0 & 0 \\ 0 & \mathbf{\Xi_{11}} & 0 & \mathbf{\Xi_{12}} & 0 \\ \mathbf{\Xi_{21}} & 0 & \mathbf{\Xi_{22}} & 0 & 0 \\ 0 & \mathbf{\Xi_{21}} & 0 & \mathbf{\Xi_{22}} & 0 \\ 0 & 0 & 0 & 0 & \mathbf{\Xi_{22}} \end{bmatrix} \cdot \begin{bmatrix} c_{vc\mathbf{k}_1} \\ c_{vc\mathbf{k}_{1_2}} \\ c_{vc\mathbf{k}_2} \\ c_{vc\mathbf{k}_{2_2}} \\ c_{vc\mathbf{k}_{2_3}} \end{bmatrix} \approx \begin{bmatrix} r_{vc\mathbf{k}_1} \\ r_{vc\mathbf{k}_{1_2}} \\ r_{vc\mathbf{k}_2} \\ r_{vc\mathbf{k}_{2_2}} \\ r_{vc\mathbf{k}_{2_3}} \end{bmatrix}. \tag{A.5}$$

The output vector would then be composed as

$$\begin{bmatrix} r_{vc\mathbf{k}_1} \\ r_{vc\mathbf{k}_{1_2}} \\ r_{vc\mathbf{k}_2} \\ r_{vc\mathbf{k}_{2_2}} \\ r_{vc\mathbf{k}_{2_3}} \end{bmatrix} \approx \begin{bmatrix} \boldsymbol{\Xi_{11}} \cdot c_{vc\mathbf{k}_1} + \boldsymbol{\Xi_{12}} \cdot c_{vc\mathbf{k}_2} \\ \boldsymbol{\Xi_{11}} \cdot c_{vc\mathbf{k}_{1_2}} + \boldsymbol{\Xi_{12}} \cdot c_{vc\mathbf{k}_{2_2}} \\ \boldsymbol{\Xi_{21}} \cdot c_{vc\mathbf{k}_1} + \boldsymbol{\Xi_{22}} \cdot c_{vc\mathbf{k}_2} \\ \boldsymbol{\Xi_{21}} \cdot c_{vc\mathbf{k}_{1_2}} + \boldsymbol{\Xi_{22}} \cdot c_{vc\mathbf{k}_{2_2}} \\ \boldsymbol{\Xi_{22}} \cdot c_{vc\mathbf{k}_{2_3}} \end{bmatrix}. \tag{A.6}$$

Note that, in general (i.e., except in the very first Haydock iteration), $c_{vc\mathbf{k}_1} \neq c_{vc\mathbf{k}_{1_2}}$ due to the energy shifts coming from the diagonal part of the excitonic Hamiltonian.

This approximation then results in a very simple implementation, as it can be reformulated as

$$\begin{bmatrix} \boldsymbol{\Xi_{11}} & \boldsymbol{\Xi_{12}} \\ \boldsymbol{\Xi_{21}} & \boldsymbol{\Xi_{22}} \end{bmatrix} \cdot \begin{bmatrix} c_{vc\mathbf{k}_1} & c_{vc\mathbf{k}_{1_2}} & 0 \\ c_{vc\mathbf{k}_2} & c_{vc\mathbf{k}_{2_2}} & c_{vc\mathbf{k}_{2_3}} \end{bmatrix} = \begin{bmatrix} r_{vc\mathbf{k}_1} & r_{vc\mathbf{k}_{1_2}} & 0 \\ r_{vc\mathbf{k}_2} & r_{vc\mathbf{k}_{2_2}} & r_{vc\mathbf{k}_{2_3}} \end{bmatrix}. \tag{A.7}$$

This allows us to always work with the same BSE kernel matrix as in the coarse grid. Moreover, the structure of the Haydock subroutine can be somewhat maintained, as these double-grid extended Haydock vectors can be folded into "Haydock matrices". Then, what is a matrix-vector multiplication in single-grid Haydock, becomes a matrix-matrix multiplication in double-grid Haydock. The number 0 marked in red in Eq. A.7 has to be imposed in the code, i.e. preventing that matrix element from being calculated as the result would not be zero.

A noteworthy aspect of the DKE approximation is that the fine-grid index, e.g., $i = 2$, will not necessarily mean the same for $\mathbf{I} = 1$ and $\mathbf{I}' = 2$. In other words, the fine-grid point κ_{1_2} will not necessarily be at the same relative position from $\mathbf{k_1}$ as κ_{2_2} is from $\mathbf{k_2}$ (although the opposite will be true if $\mathbf{I} = \mathbf{I}'$ because they are essentially the same $\mathbf{k}$-points). Hence, the decision to couple κ_{1_2} with κ_{2_2} (instead of κ_{2_3}) is ultimately an arbitrary choice, but one maintains the approximated BSE kernel also sharply peaked at $\mathbf{q} = \mathbf{0}$. Let us analyse the case $\mathbf{I} = \mathbf{I}'$, in which the corresponding matrix elements belong to the diagonal (e.g.,

$\boldsymbol{\Xi_{22}}$). If we were to couple fine-grid indexes $i = 2$ with $i = 3$, we would have a $\mathbf{q} \neq \mathbf{0}$, off-diagonal matrix element ($\Xi_{2_2 2_3}$) with the same value as the corresponding diagonal $\mathbf{q} = \mathbf{0}$ matrix element ($\boldsymbol{\Xi_{22}}$), which would introduce artefacts in the optical response. This issue is more subtle when it comes to the $\mathbf{I} \neq \mathbf{I}'$ matrix elements, which are off-diagonal (e.g., $\boldsymbol{\Xi_{12}}$). In this case, there would be no obvious choice as to whether $i = 2$ should be coupled with $i = 2$ or $i = 3$. Any attempt to decide this based on the relative positions of those $\mathbf{k}$-points would make the method heavily dependent on the shape of the $\mathbf{k}$-grids used as input, and probably less robust. Ultimately, our double-grid method relies on these off diagonal elements being small compared to diagonal ones, as we are only interested in the latter. This is another way to see the limitations this method faces when the BSE kernel is not sharply peaked at $\mathbf{q} = \mathbf{0}$. Moreover, this is in line with the fact that this method cannot work for systems with strongly bound excitons, as these usually imply important contributions from $\mathbf{q} \neq \mathbf{0}$ matrix elements.

A.1.4 Full Kernel Extension (FKE)

In this approximation, we consider that all matrix elements involving transitions in the fine grid will be equal to the corresponding ones in the coarse grid, according to Eq. 3.5. This approximation leads to a matrix of the form,

$$\begin{bmatrix} \boldsymbol{\Xi_{11}} & \Xi_{11_2} & \boldsymbol{\Xi_{12}} & \Xi_{12_2} & \Xi_{12_3} \\ \Xi_{1_2 1} & \Xi_{1_2 1_2} & \Xi_{1_2 2} & \Xi_{1_2 2_2} & \Xi_{1_2 2_3} \\ \boldsymbol{\Xi_{21}} & \Xi_{21_2} & \boldsymbol{\Xi_{22}} & \Xi_{22_2} & \Xi_{22_3} \\ \Xi_{2_2 1} & \Xi_{2_2 1_2} & \Xi_{2_2 2} & \Xi_{2_2 2_2} & \Xi_{2_2 2_3} \\ \Xi_{2_3 1} & \Xi_{2_3 1_2} & \Xi_{2_3 2} & \Xi_{2_3 2_2} & \Xi_{2_3 2_3} \end{bmatrix} \rightarrow \begin{bmatrix} \boldsymbol{\Xi_{11}} & \boldsymbol{\Xi_{11}} & \boldsymbol{\Xi_{12}} & \boldsymbol{\Xi_{12}} & \boldsymbol{\Xi_{12}} \\ \boldsymbol{\Xi_{11}} & \boldsymbol{\Xi_{11}} & \boldsymbol{\Xi_{12}} & \boldsymbol{\Xi_{12}} & \boldsymbol{\Xi_{12}} \\ \boldsymbol{\Xi_{21}} & \boldsymbol{\Xi_{21}} & \boldsymbol{\Xi_{22}} & \boldsymbol{\Xi_{22}} & \boldsymbol{\Xi_{22}} \\ \boldsymbol{\Xi_{21}} & \boldsymbol{\Xi_{21}} & \boldsymbol{\Xi_{22}} & \boldsymbol{\Xi_{22}} & \boldsymbol{\Xi_{22}} \\ \boldsymbol{\Xi_{21}} & \boldsymbol{\Xi_{21}} & \boldsymbol{\Xi_{22}} & \boldsymbol{\Xi_{22}} & \boldsymbol{\Xi_{22}} \end{bmatrix}. \tag{A.8}$$

Consequently, the matrix vector multiplication would be

$$\begin{bmatrix} \boldsymbol{\Xi_{11}} & \boldsymbol{\Xi_{11}} & \boldsymbol{\Xi_{12}} & \boldsymbol{\Xi_{12}} & \boldsymbol{\Xi_{12}} \\ \boldsymbol{\Xi_{11}} & \boldsymbol{\Xi_{11}} & \boldsymbol{\Xi_{12}} & \boldsymbol{\Xi_{12}} & \boldsymbol{\Xi_{12}} \\ \boldsymbol{\Xi_{21}} & \boldsymbol{\Xi_{21}} & \boldsymbol{\Xi_{22}} & \boldsymbol{\Xi_{22}} & \boldsymbol{\Xi_{22}} \\ \boldsymbol{\Xi_{21}} & \boldsymbol{\Xi_{21}} & \boldsymbol{\Xi_{22}} & \boldsymbol{\Xi_{22}} & \boldsymbol{\Xi_{22}} \\ \boldsymbol{\Xi_{21}} & \boldsymbol{\Xi_{21}} & \boldsymbol{\Xi_{22}} & \boldsymbol{\Xi_{22}} & \boldsymbol{\Xi_{22}} \end{bmatrix} \cdot \begin{bmatrix} c_{vc\mathbf{k}_1} \\ c_{vc\mathbf{k}_{1_2}} \\ c_{vc\mathbf{k}_2} \\ c_{vc\mathbf{k}_{2_2}} \\ c_{vc\mathbf{k}_{2_3}} \end{bmatrix} \approx \begin{bmatrix} r_{vc\mathbf{k}_1} \\ r_{vc\mathbf{k}_{1_2}} \\ r_{vc\mathbf{k}_2} \\ r_{vc\mathbf{k}_{2_2}} \\ r_{vc\mathbf{k}_{2_3}} \end{bmatrix}. \tag{A.9}$$

The output vector would then be composed as

$$\begin{bmatrix} r_{vc\mathbf{k}_1} \\ r_{vc\mathbf{k}_{1_2}} \\ r_{vc\mathbf{k}_2} \\ r_{vc\mathbf{k}_{2_2}} \\ r_{vc\mathbf{k}_{2_3}} \end{bmatrix} \approx \begin{bmatrix} \boldsymbol{\Xi_{11}} \cdot (c_{vc\mathbf{k}_1} + c_{vc\mathbf{k}_{1_2}}) + \boldsymbol{\Xi_{12}} \cdot (c_{vc\mathbf{k}_2} + c_{vc\mathbf{k}_{2_2}} + c_{vc\mathbf{k}_{2_3}}) \\ \boldsymbol{\Xi_{11}} \cdot (c_{vc\mathbf{k}_1} + c_{vc\mathbf{k}_{1_2}}) + \boldsymbol{\Xi_{12}} \cdot (c_{vc\mathbf{k}_2} + c_{vc\mathbf{k}_{2_2}} + c_{vc\mathbf{k}_{2_3}}) \\ \boldsymbol{\Xi_{21}} \cdot (c_{vc\mathbf{k}_1} + c_{vc\mathbf{k}_{1_2}}) + \boldsymbol{\Xi_{22}} \cdot (c_{vc\mathbf{k}_2} + c_{vc\mathbf{k}_{2_2}} + c_{vc\mathbf{k}_{2_3}}) \\ \boldsymbol{\Xi_{21}} \cdot (c_{vc\mathbf{k}_1} + c_{vc\mathbf{k}_{1_2}}) + \boldsymbol{\Xi_{22}} \cdot (c_{vc\mathbf{k}_2} + c_{vc\mathbf{k}_{2_2}} + c_{vc\mathbf{k}_{2_3}}) \\ \boldsymbol{\Xi_{21}} \cdot (c_{vc\mathbf{k}_1} + c_{vc\mathbf{k}_{1_2}}) + \boldsymbol{\Xi_{22}} \cdot (c_{vc\mathbf{k}_2} + c_{vc\mathbf{k}_{2_2}} + c_{vc\mathbf{k}_{2_3}}) \end{bmatrix}. \tag{A.10}$$

It is important to note that $r_{vc\mathbf{k}_1} = r_{vc\mathbf{k}_{1_2}}$ and $r_{vc\mathbf{k}_2} = r_{vc\mathbf{k}_{2_2}} = r_{vc\mathbf{k}_{2_3}}$. Despite the computational advantage of not having to calculate all output vectors, this is essentially a drawback of the FKE approach (see below). Also, note that, unlike the DKE approach, FKE requires the kernel to be scaled down by a factor relative to the number of coarse-grid and fine-grid **k**-points.

A.1.5 Further analysis of kernel extension to the fine grid

In order to further explain the better performance of DKE over FKE, let us now consider a system with several **k**-points and only one pair of bands. In this case, the e-h space is composed directly by one vertical transition at each **K**- or κ-point, and the sharply peaked matrix elements correspond to those in the diagonal ($\mathbf{q} = \mathbf{0}$), while the rest of the matrix is considerably sparse. Nonetheless, this does not necessarily mean that the BSE kernel matrix meets the criteria for being strictly diagonally dominant (i.e., a matrix where all

elements $A_{i,j}$ satisfy $|A_{i,i}| > \sum_{j \neq i} |A_{i,j}|$ for all i). In fact, this is not the case. Even in the simple example of monolayer MoS_2 with only one pair of bands, the off-diagonal elements of the BSE kernel, albeit very small, add up to a value that is higher than the diagonal element in many rows of the matrix. Admittedly, the situation changes if one considers the two-particle Hamiltonian, where the energies are added to the diagonal. Indeed, the two-particle Hamiltonian is strictly diagonal dominant in the case of this two-band monolayer MoS_2 example. Alternatively, we can consider only a given *block* of the BSE kernel, determined by two *fragments* of the e-h basis set. We will consider the blocks in the diagonal, which are square by construction and contain the $\mathbf{q} = 0$ matrix elements we are discussing. Each of this blocks also satisfies the condition for being strictly diagonal dominant. The determination of the *fragments* is somewhat arbitrary and only relevant to Yambo, but it nonetheless helps us visualise the problem at hand. For instance, Fig. A.1 displays the real part of one block of the BSE kernel for two-band monolayer MoS_2. Fig. A.1A shows the coarse grid BSE kernel block (i.e., our starting point in the double grid approach) while Fig. A.1B and C display the fine grid BSE kernels approximated by DKE and FKE, respectively. Finally, Fig. A.1D illustrates the *full* BSE kernel as calculated with a $12 \times 12 \times 1$ **k**-grid. The term *full* here refers to the BSE kernel that is obtained if the **k**-grid that normally acts as a fine (double) grid, is actually used as the single **k**-grid in a BSE calculation with no double grid approach. In other words, Fig. A.1D is the matrix we are trying to approximate (which *can* be calculated in full in this case as only a $12 \times 12 \times 1$ **k**-grid is being used). Importantly, we see that both blocks in panels A and D are nearly diagonal. Now, it becomes apparent from panel B that the DKE approach respects the diagonally-dominant nature of the block in panel A, and thus represents a better approximation to the *full* block in panel D. At variance, the FKE approach prevents, by construction, any matrix from being diagonally dominant. Indeed, the FKE kernel approaches a block-diagonal matrix, which represents a greater deviation from the *full* block in panel D, and hence, a worse approximation to it.

We now consider a more realistic scenario where we include various conduction and valence bands in the BSE calculation in order to achieve convergence. In this case, the two-

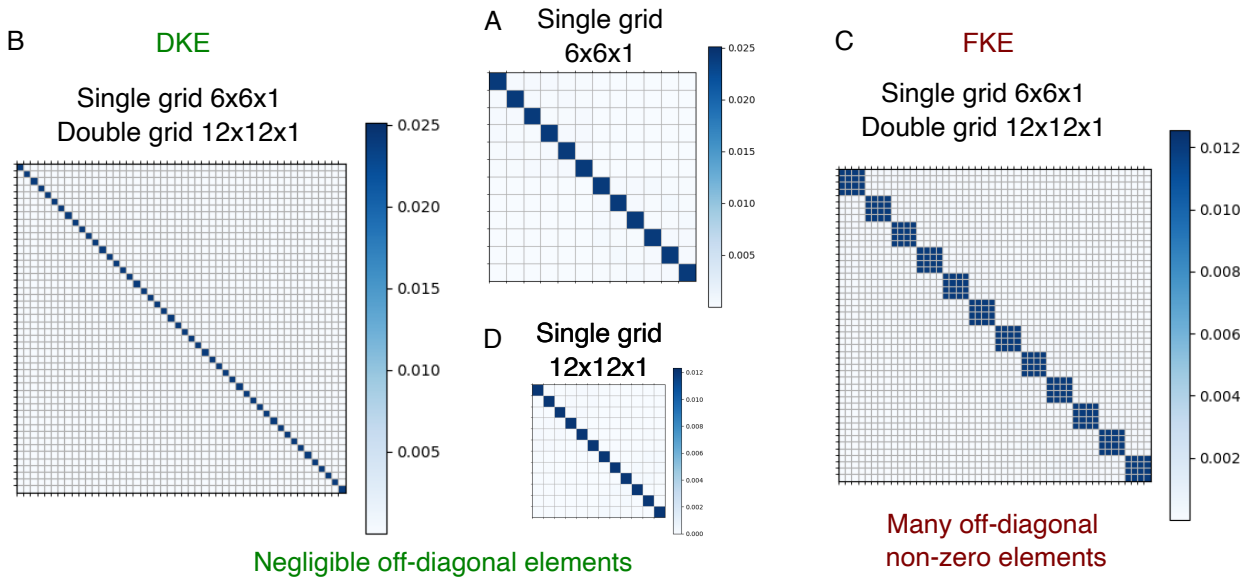

Figure A.1: Comparison of the BSE kernel matrices obtained via diagonal kernel extension (DKE) and full kernel extension (FKE). The data plotted here is the real part of one *block* of the BSE kernel in MoS_2 with only one pair of bands.

particle Hamiltonian is not diagonally dominant any more. This is because the e-h space grows considerably and so does the sum of non-diagonal elements in a given row, which ends up overtaking the value of the diagonal element. In other words, adding the transition energies to the diagonal of the BSE kernel is no longer enough to ensure the diagonally dominant character of the two-particle Hamiltonian when many bands are considered, unlike the two-band system described above. Nonetheless, we can still use arguments of this nature to address the comparison between DKE and FKE. Let us define the diagonal dominance per row i as $dd_i = \frac{\sum_{j \neq i} |H^{2p}_{i,j}|}{|H^{2p}_{i,i}|}$. Fig. A.2 shows dd_i of all rows for the case of MoS_2 with all the bands required for convergence. As in Fig. A.1, DKE and FKE represent the matrices calculated by extending a $6 \times 6 \times 1$ coarse $\mathbf{K}$-grid Hamiltonian into a $12 \times 12 \times 1$ double κ-grid one, while the fine grid data points correspond to the matrix we are trying to approximate, i.e, the Hamiltonian obtained with one single grid of $12 \times 12 \times 1$ $\mathbf{k}$-points. We can immediately confirm that none of these two-particle Hamiltonians are diagonally dominant any more, as they have rows with $dd_i > 1$. In addition, an average dd_i over

all rows for each case is shown with flat lines in Fig. A.2. It becomes apparent that the DKE and fine grid matrices have very similar average dd_i, while that of the FKE matrix is an order of magnitude higher. In other words, the DKE method is better than FKE at extending the coarse grid two-particle Hamiltonian into a matrix that closely resembles that of the fine grid Hamiltonian from the viewpoint of diagonal dominance.

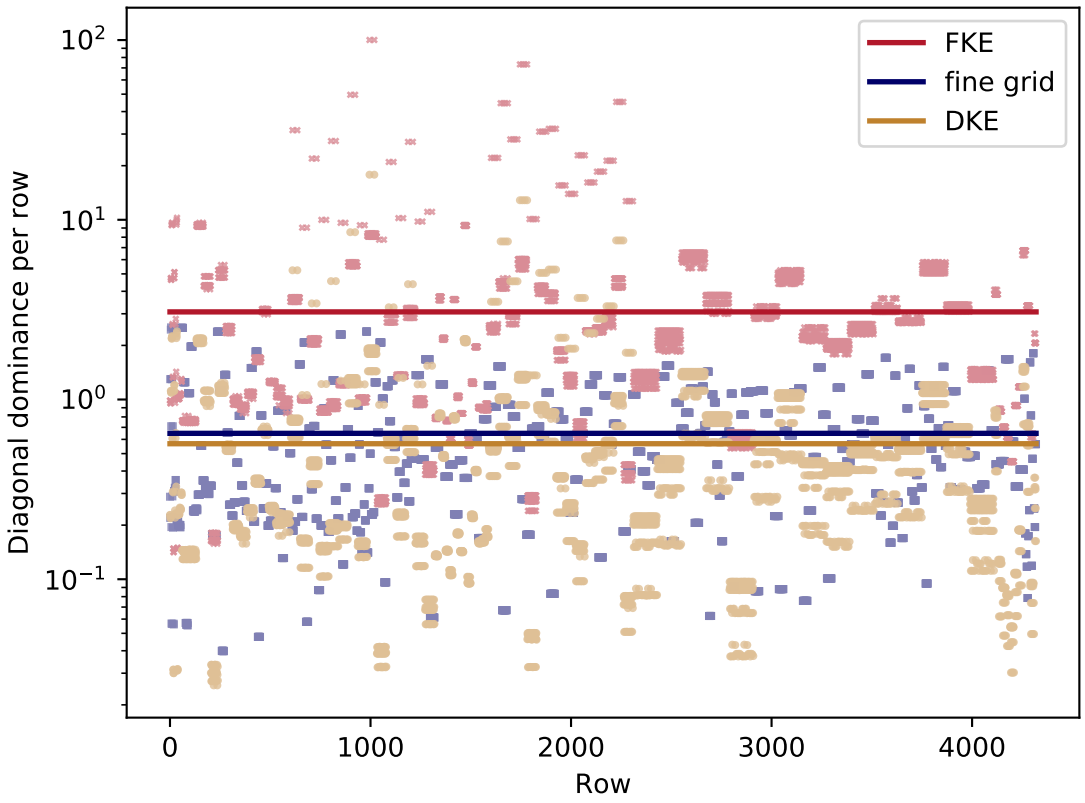

Figure A.2: Diagonal dominance of the two-particle Hamiltonian matrices obtained via diagonal kernel extension (DKE) and full kernel extension (FKE), compared with the case of . The data plotted here corresponds to MoS_2 with all the bands required for convergence. The DKE and FKE matrices are obtained from a $6 \times 6 \times 1$ coarse **K**-grid and a $12 \times 12 \times 1$ double κ-grid. The fine grid data is simply the matrix that DKE and FKE try to approximate, i.e., the two-particle Hamiltonian obtained with one single grid of $12 \times 12 \times 1$ **k**-points.

Finally, there is an algebraic argument against the FKE approach that can be derived from Eqs. A.9-A.10 (or Eq. 3.6), in comparison with their DKE analogues, Eqs. A.5-A.6

(or Eq. 3.4). First, it should be considered that these equations are embedded in a loop of Haydock iterations. As part of this loop, the Haydock vectors are multiplied by the two-particle Hamiltonian H^{2p}, which entails the multiplications in Eqs. A.6 or A.10 plus a shift due to the diagonal matrix of transition energies. Associated to this multiplication, there is a subtle point about the way in which the DKE or FKE approaches handle the benefits that the double grid brings. The impact of the double grid in the final spectrum depends crucially on the diagonal matrix of transition energies $E_{nm\mathbf{k}}\,\delta_{nn'}\delta_{mm'}\delta_{\mathbf{k}\mathbf{k}'}$. In other words, given that the kernel in the fine grid is approximated as equal to that of the coarse grid, the shift $E_{nm\mathbf{k}}\,\delta_{nn'}\delta_{mm'}\delta_{\mathbf{k}\mathbf{k}'}$ is what makes transitions inside a given domain $\mathbf{Dom}(\mathbf{K_I})$ different among themselves. Hence, this *differential shift* is why the double grid method gives a different spectrum than the coarse grid alone. As mentioned before, in the very first Haydock iteration, the components of the Haydock vector in the coarse and fine grid are the same, as they are equally initialised (see Eq. 3.2). However, in the second iteration and beyond, this vector will have picked up a shift coming from the diagonal matrix of transition energies, which will differ among components in the coarse and fine grid. **This** is the impact of the double grid in the Haydock method (since the fine grid kernel is approximated by the coarse grid). However, this impact is somewhat *lost* or *averaged out* in the FKE vector-matrix multiplication (Eq. 3.6 or A.9-A.10). This effect is exemplified in Eq. A.10, where $r_{vc\mathbf{k}_1} = r_{vc\mathbf{k}_{1_2}}$ and $r_{vc\mathbf{k}_2} = r_{vc\mathbf{k}_{2_2}} = r_{vc\mathbf{k}_{2_3}}$. In essence, Eq. 3.6 (or A.10) tells us that $r_{nm\kappa_{\mathbf{I}_i}}$ will be equal $\forall i \in \mathbf{Dom}(\mathbf{K_I})$, no matter how different $c_{n'm'\kappa_{\mathbf{I}'_{i'}}}$ may be across different values of I' and i'. Importantly, this difference among values of $c_{n'm'\kappa_{\mathbf{I}'_{i'}}}$ is a result of the differential shift *gained* in the previous Haydock iteration, so Eq. 3.6 (or A.10) effectively causes a *reset* of the Haydock vector that enters the loop at each iteration. Of course, these output components $r_{nm\kappa_{\mathbf{I}_i}}$ (equal among themselves) are different from ('better' than) the ones that would have been obtained if the input components $c_{n'm'\kappa_{\mathbf{I}'_{i'}}}$ had not been different at all. But overall, the FKE hinders the ability of the double grid to have an impact in the Haydock output vectors via the diagonal matrix of transition energies in the excitonic Hamiltonian. This detrimental *'homogenisation'* of the output vectors is not present in the

DKE approach, which lets the benefits of the double grid (the differential shifts) accumulate over successive iterations, leading to a greater impact of the fine grid overall, and a better final spectrum.

A.2 Impact of the coarse grid as a starting point

Fig. A.3 shows absorption spectra of monolayer MoS_2 with various coarse grids and a 24×24×1 fine grid. This also corresponds to some of the data points included in the computational cost comparison (see Fig. 3.7).

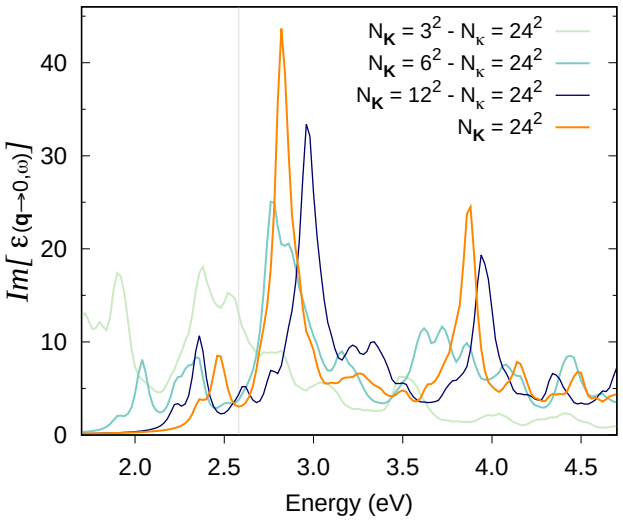

Figure A.3: Optical absorption spectra of monolayer MoS_2 at the BSE level *via* the double-grid approach using different coarse grids and a 24×24×1 fine grid.

A.3 Shifted grids

While Gamma-centred grids have been used throughout the study, our method can also be used with shifted grids, both with regular and random shifts. Taking the case of GaAs as an example, we present the results obtained with regular shifted grids in Fig. A.4. The $20 \times 20 \times 20$ shifted fine grid entails 36000 **k**-points, while the $10 \times 10 \times 10$ shifted grid, only 4000. Despite this difference, the two calculations in Fig. A.4 took essentially the same

time (relative difference less than 1%). This proves that the numerical advantages of the double-grid method are also present in the case of shifted grids.

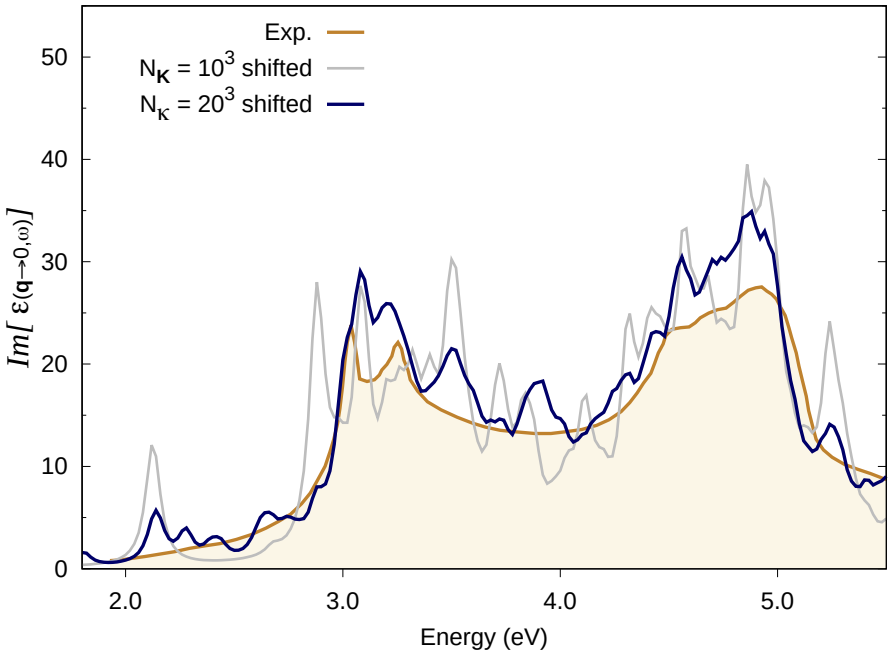

Figure A.4: Example of optical spectrum of bulk GaAs using shifted **k**-grids.

Regarding the result itself, Fig. A.4 shows that shifted grids converge faster, as reported elsewhere in the literature (see, e.g., Ref. [64]). In particular, the $10 \times 10 \times 10$ shifted grid result in Fig. A.4 looks better converged than the Gamma-centred one in Fig. 3.3. The same applies to the $20 \times 20 \times 20$ results. However, this is partly due to the fact that shifted grids represent many more non-equivalent **k**-points than Gamma-centred ones. For instance, Gamma-centred grids of the same dimensions contain 1000 and 4000 **k**-points, respectively. Moreover, there is a subtlety about what high symmetry **k**-points are included when using Gamma-centred or shifted grids, which has implications as to how well a given grid represents the physics of the material at hand. For example, the direct gap in GaAs (and Si) occurs at the Gamma point, which makes Gamma-centred grids a wise choice in this case.

Finally, the use of random shifted grids on their own right (rather than via a double grid approach) is a well-known method of improving **k**-points convergence. This usually offers

faster convergence than an equally dense Gamma-centred grid, while keeping the size of the BSE kernel unchanged. Despite this advantage, the number of **k**-points in the Irreducible Brillouin Zone increases, and so does the memory required to load the corresponding KS orbitals. These increased memory and disk storage requirements could become prohibitively large in materials for which very dense **k**-grids are needed. The random shift method does not address these problems, which are precisely what we intend to target with our method (as the fine-grid KS orbitals are not needed). Furthermore, **k**-grids with random shifts usually do not have the symmetries of the system, with the potential for breaking degeneracies and turning dark excitons into bright ones.

A.4 Code and data availability

A.4.1 Code availability

The double-grid method developed in this work for calculating optical absorption spectra via the Haydock solution of the BSE will be available in a future release of the Yambo code. A tutorial will be made available in due course through the tutorials section (`http://www.yambo-code.org/wiki/index.php?title=Tutorials`) of the official Yambo website (`http://www.yambo-code.org/`).

A.4.2 Data availability

Input and output files of the calculations presented in this study can be found in a GitHub repository (`https://github.com/aim137/double_grid_data_repository.git`)

Appendix B

Supplemental material for Floquet approach

The present Appendix provides supplemental material relative to the Floquet approach introduced in Chapter 4. This includes convergence tests and the full set of spectra computed with various **k**-grids, broadening values and electric-field intensities. We also present some supplementary figures relative to scaling tests and computational cost. Finally, we provide a statement regarding code and data availability.

B.1 Computational cost

In this section, we present the actual computational cost of each run, rather than the RT-to-FL ratio shown in Figs. 4.8 and 4.9. The format of these figures is the same as Fig. 7 and 8 for comparability.

B.2 Scaling with number of atoms

We present the scaling of the real-time and Floquet approaches with respect to the number of atoms. Tests were done for h-BN SHG spectra on a 6×6×1 **k**-grid. Various super-

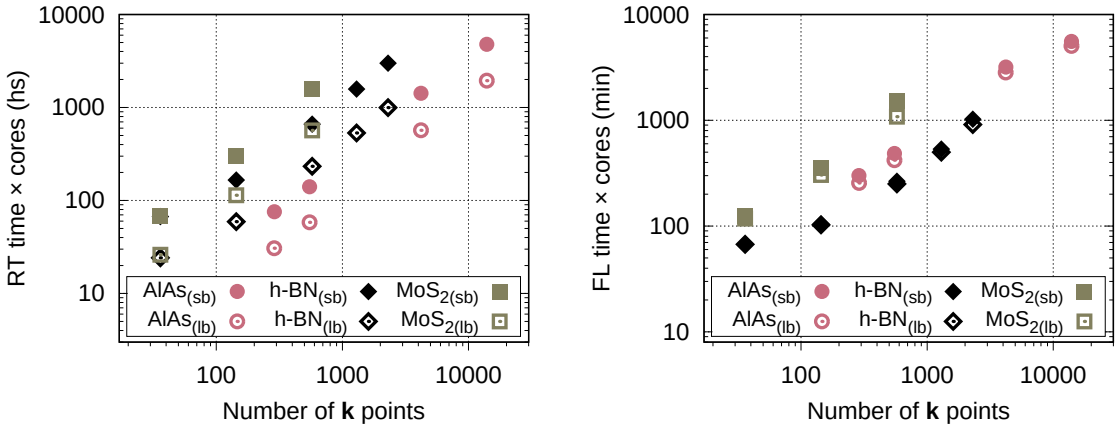

Figure B.1: Computational cost of SHG calculations in CPU time multiplied by the number of cores.

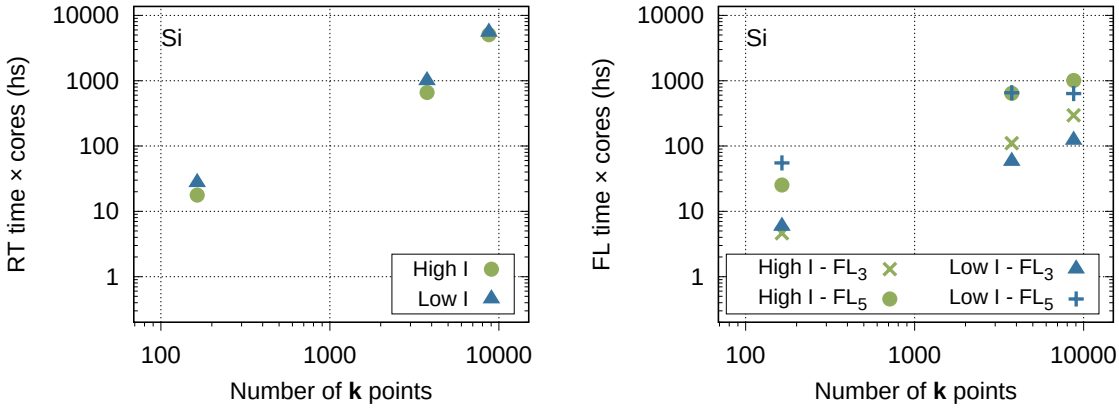

Figure B.2: Computational cost of THG calculations in CPU time multiplied by the number of cores.

cells (2×2×1 to 5×5×1) were used to obtain systems with large number of atoms and the number of bands included in each calculation was adjusted accordingly.

B.3 Scaling with number of Floquet modes

We present the scaling of the calculation time of our approach with respect to the number of Floquet modes. Bulk AlAs with a 20×20×20 **k**-grid was taken as an example. The data is produced *via* a first-order Floquet calculation with $\eta_{\max} = 1-6$, i.e., with $0-5$ extra Floquet modes. The data is presented as CPU time per iteration per frequency, so it is representative

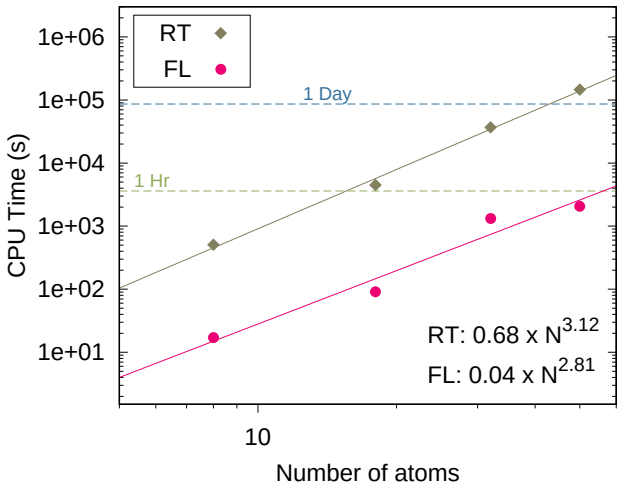

Figure B.3: Scaling with the number of atoms - CPU time per iteration per frequency.

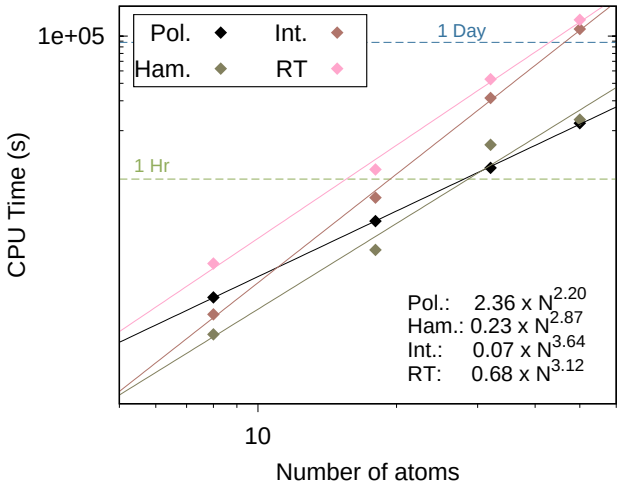

Figure B.4: Scaling with the number of atoms in the real-time method - CPU time per iteration per frequency. The abbreviations Ham., Int. and Pol. correspond to the tasks of building the Hamiltonian matrix, performing the numerical time integration and calculating the Berry-phase polarisation, respectively.

of calculating the Hamiltonian matrix, diagonalising it, calculating the polarisation and extracting the Fourier coefficients. The near-quadratic scaling reflects the diagonalisation time, since the size of the Hamiltonian at a given **k**-point is $N_{bands} \times (2\ \eta_{\max} + 1)$. This operation is performed using the QR-algorithm, i.e., what is usually referred to as full diagonalisation.

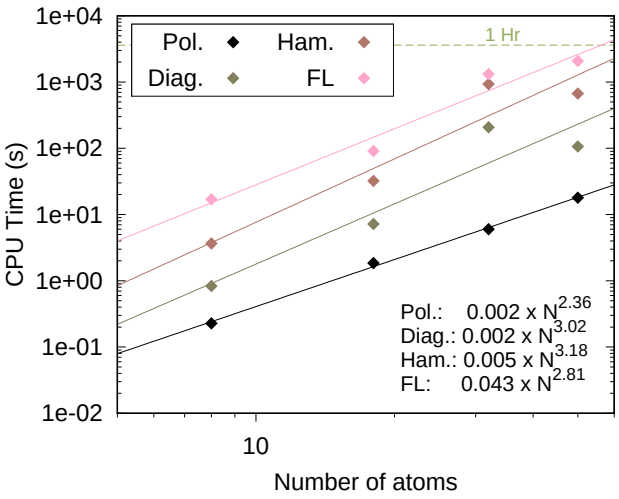

Figure B.5: Scaling with the number of atoms - CPU time per iteration per frequency. The abbreviation Diag. corresponds to the task of diagonalising the various quasi-energy matrices.

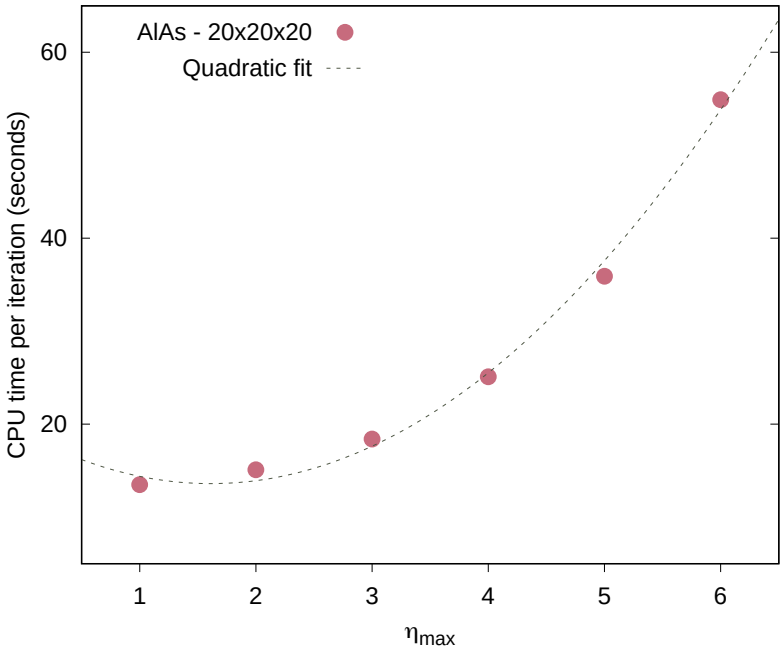

Figure B.6: Scaling with Floquet modes - CPU time per iteration per frequency.

B.4 Computational details

The DFT calculations were performed with Quantum Espresso (QE) 6.7. The real-time (RT) and Floquet calculations were done with a developer branch of Yambo 5.1 where we

	AlAs	h-BN	MoS_2
Calculated spectra	LR, SHG	LR, SHG	LR, SHG
k-grids (scf)	10×10×10	12×12×1	12×12×1
k-grids (nscf)	8×8×8,	6×6×1,	6×6×1,
	10×10×10,	12×12×1	12×12×1,
	20×20×20,	24×24×1	24×24×1,
	30×30×30	36×36×1	
		48×48×1	
Bands (full–empty)	3–6	4–4	5–5
Band-gap correction [eV]	0.9	3.3	0.72
Broadening [eV] (sb;lb)	0.04; 0.15	0.04; 0.15	0.04; 0.15
Total time [fs] (sb;lb)	118; 48	235; 83	230; 85
Time step [as]	10 (2.5)	2.5	10
Intensity [$\mathrm{W\,cm^{-2}}$]	1×10^6	1×10^6	1×10^6
Floquet modes $\eta_{\max}$	2	2	2

Table B.1: Computational details of the SHG data set. The acronyms sb and lb stand for small and large broadening, respectively.

incorporated our formalism. The details for these calculations are as show in Tables B.1 and B.2.

See next section for the determination of the real-time convergence parameters.

B.5 Convergence real-time

The real-time convergence parameters reported in the previous section were chosen on the basis of the following convergence tests. They are all performed on the coarse grid for each material. SHG convergence tests for the dephasing time are done with 0.04 eV (small broadening) and 0.15 eV (large broadening). SHG convergence tests for the time step are done only at small broadening. THG convergence tests are done only at large broadening, and also at two different intensities, namely 1×10^6 (low intensity) and 1×10^{10} (high intensity) $\mathrm{W\,cm^{-2}}$. These convergence tests allow us to determine the time step and dephasing time required for each calculation, as shown in Tables B.1 and B.2.

	Si
Calculated spectra	THG
k-grids (scf)	8×8×8
k-grids (nscf)	8×8×8
	24×24×24
	32×32×32
Bands (full–empty)	4–3
Band-gap correction [eV]	0.6
Broadening [eV]	0.15
Total time [fs]	74
Time step [as]	10
Intensity [W cm^{-2}] (lI;hI)	1×10^6; 1×10^{10}
Floquet modes $\eta_{\max}$ (lI;hI)	3; 5

Table B.2: Computational details of the THG data set. The acronyms lI and hI stand for low and high intensity, respectively.

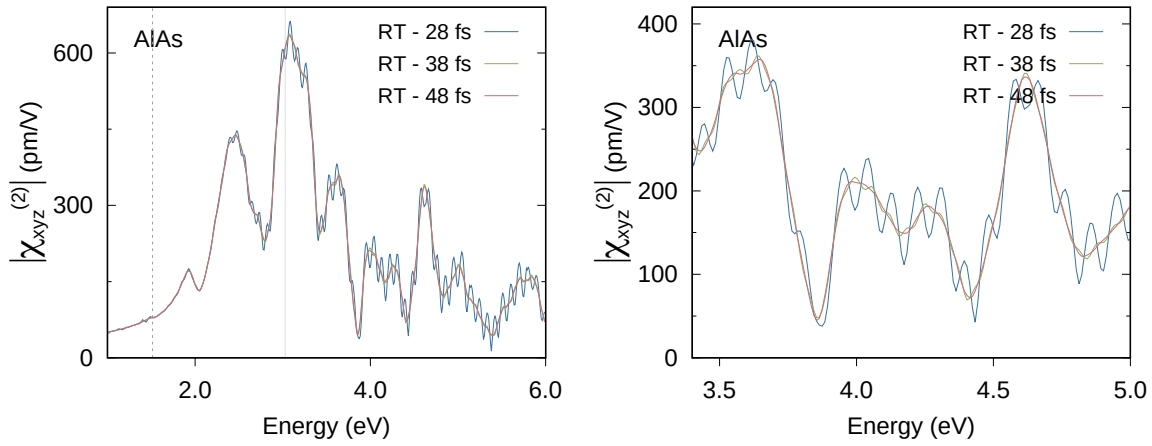

Figure B.7: Bulk AlAs - dephasing time - large broadening

B.6 Convergence Floquet

Convergence of our Floquet approach with respect to the number of Floquet modes is reported in this section. We present tests for AlAs, h-BN and MoS_2 with regards to their SHG spectra, which were all performed on the coarse grid for each material (convergence for THG spectra in bulk Si is covered in Section 4.2). We present data for $\eta_{\max} = 2$ (FL_2), $\eta_{\max} = 3$ (FL_3) and $\eta_{\max} = 4$ (FL_4). In addition to the electric-field intensity used to study SHG in Section 4.2 (i.e. 1×10^6 W cm^{-2}, labelled low intensity), we report convergence tests at a higher intensity, where higher-order contributions to the second order response

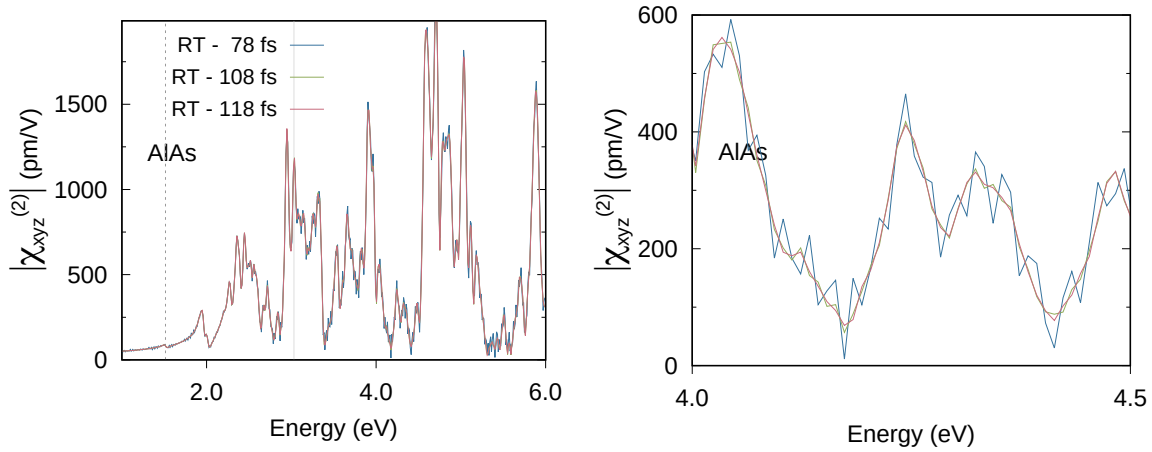

Figure B.8: Bulk AlAs - dephasing time - small broadening

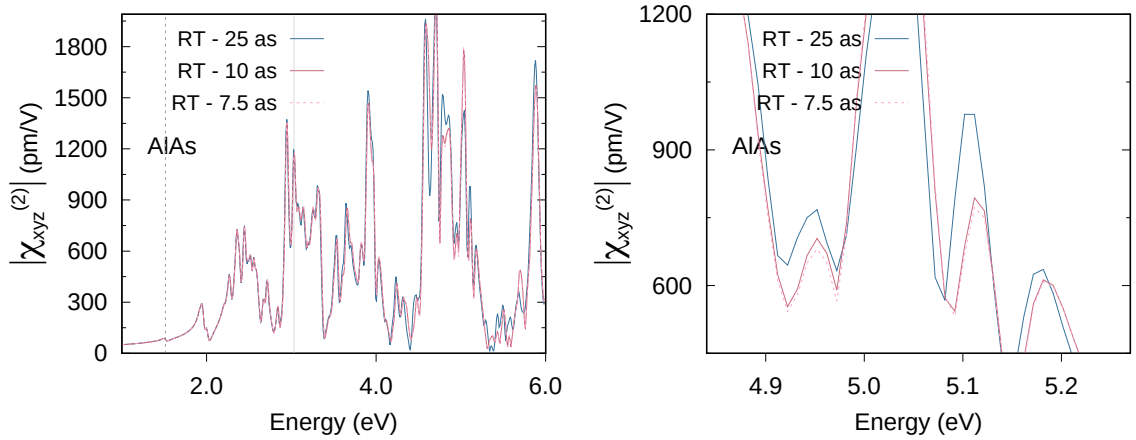

Figure B.9: Bulk AlAs - time step - small broadening

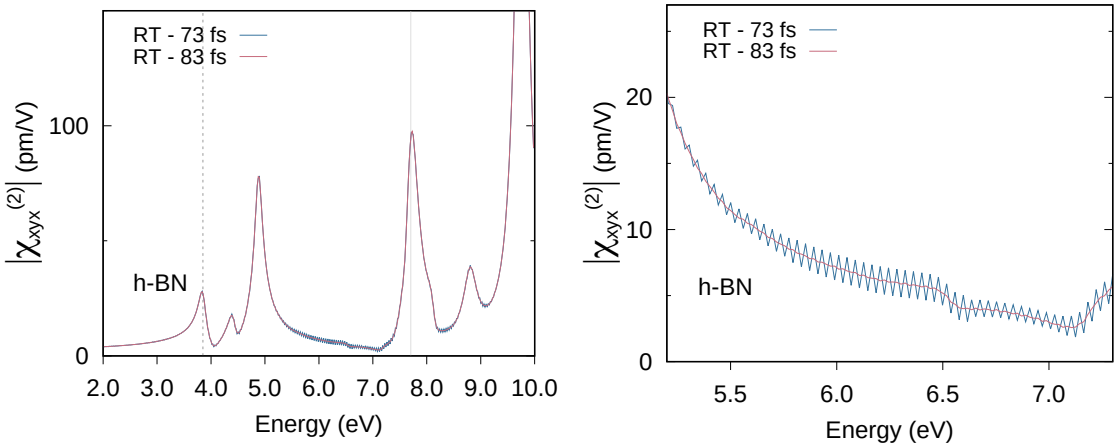

Figure B.10: h-BN 2D - dephasing time - large broadening

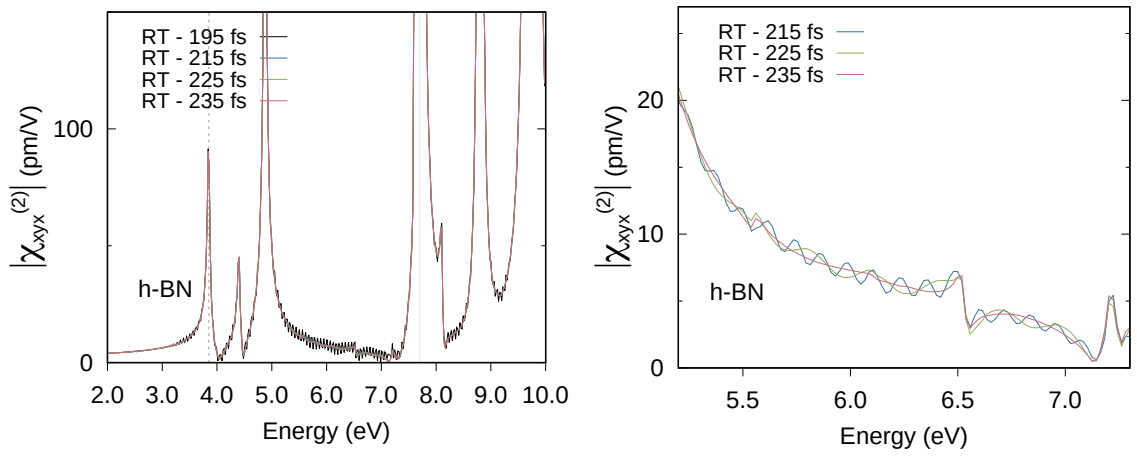

Figure B.11: h-BN 2D - dephasing time - small broadening

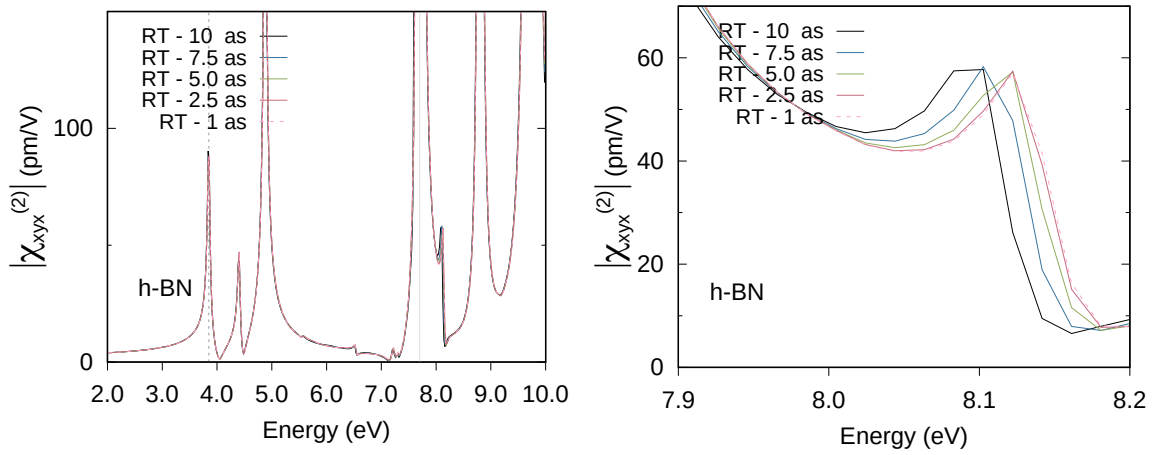

Figure B.12: h-BN 2D - time step - small broadening

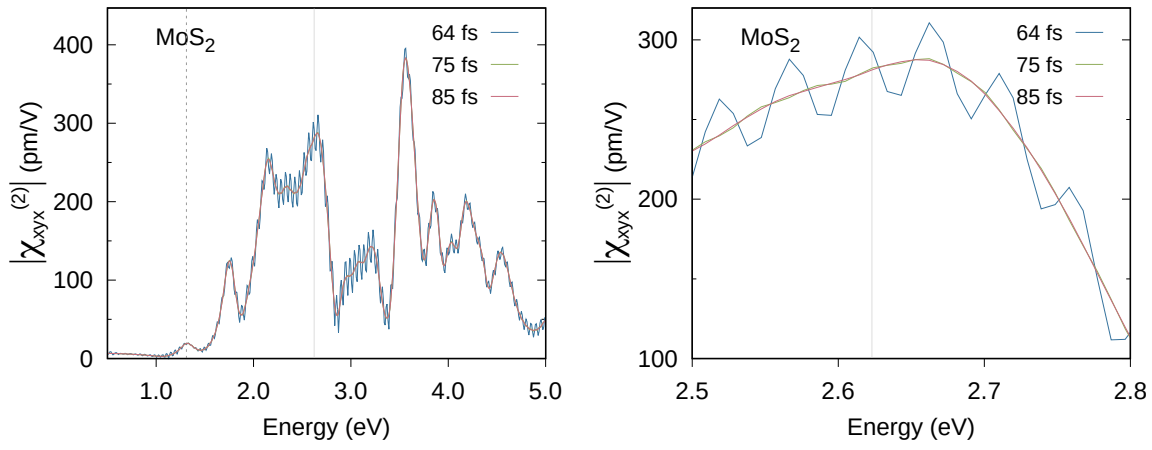

Figure B.13: MoS_2 2D - dephasing time - large broadening

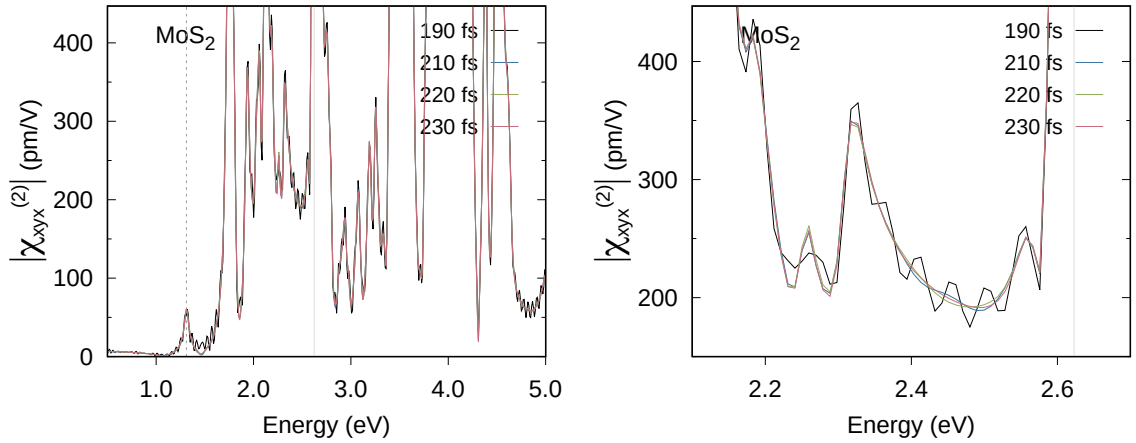

Figure B.14: MoS_2 2D - dephasing time - small broadening

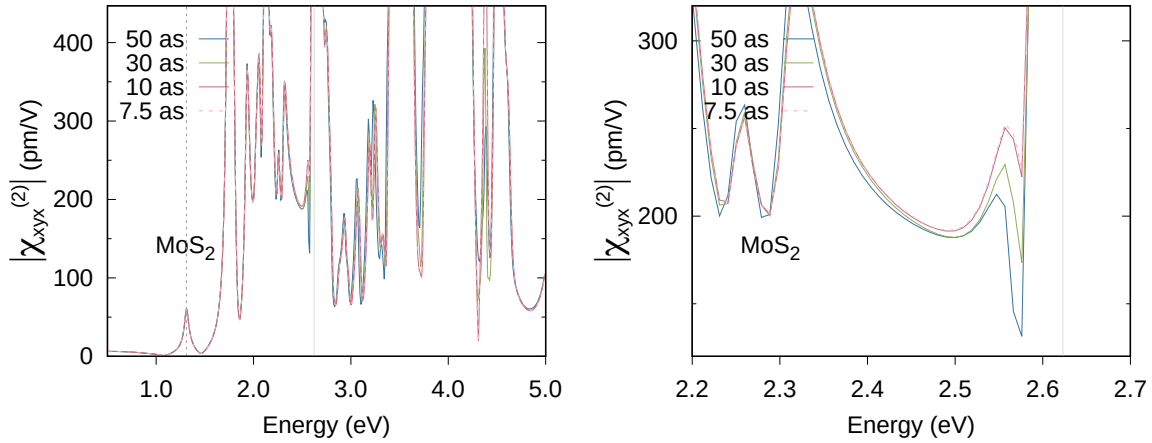

Figure B.15: MoS_2 2D - time step - small broadening

are expected to be important. This higher intensity is 1×10^{10} W cm^{-2} for AlAs and h-BN, and 1×10^{8} W cm^{-2} for MoS_2 since convergence issues appeared above this value. We did all our low intensity tests with a low broadening of 0.04 eV, however we had to raise it for some of the high intensity cases to improve convergence (mentioned in caption where applicable).

The results show that convergence with respect to the number of Floquet modes in the calculation of SHG spectra is very fast. Even at high intensities, higher-order contributions to SHG do not seem to have a big effect in the response and $\eta_{\max} = 2$ appears to be enough.

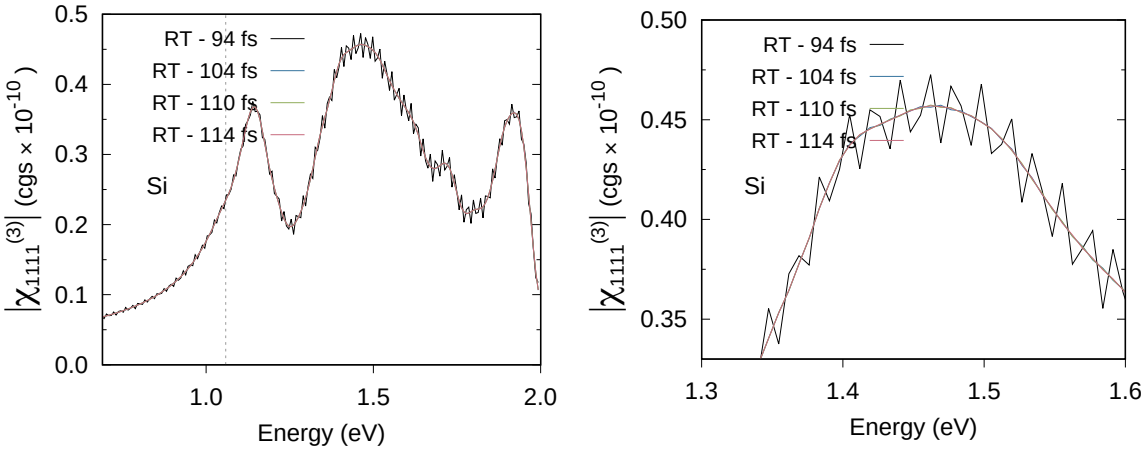

Figure B.16: Si bulk THG - dephasing time - low intensity

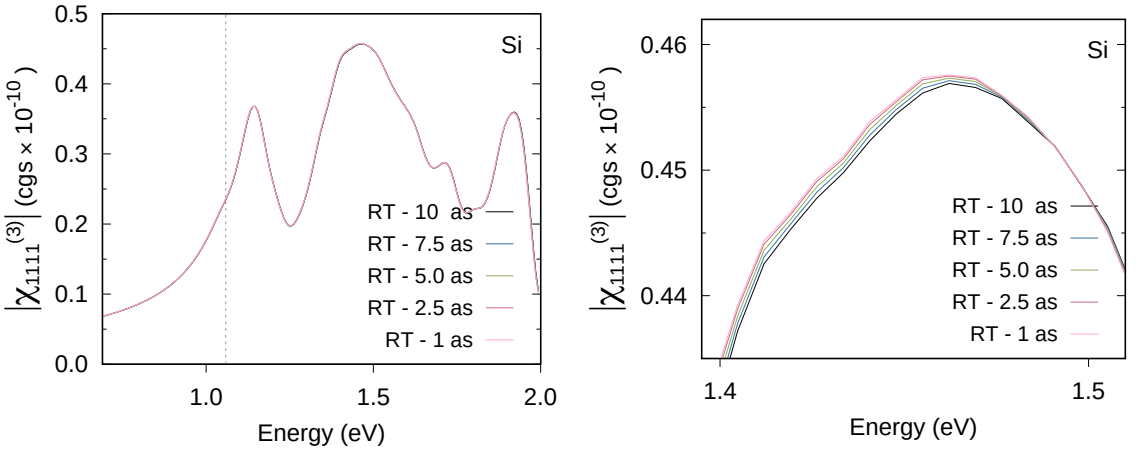

Figure B.17: Si bulk THG - time step - low intensity

B.7 Results

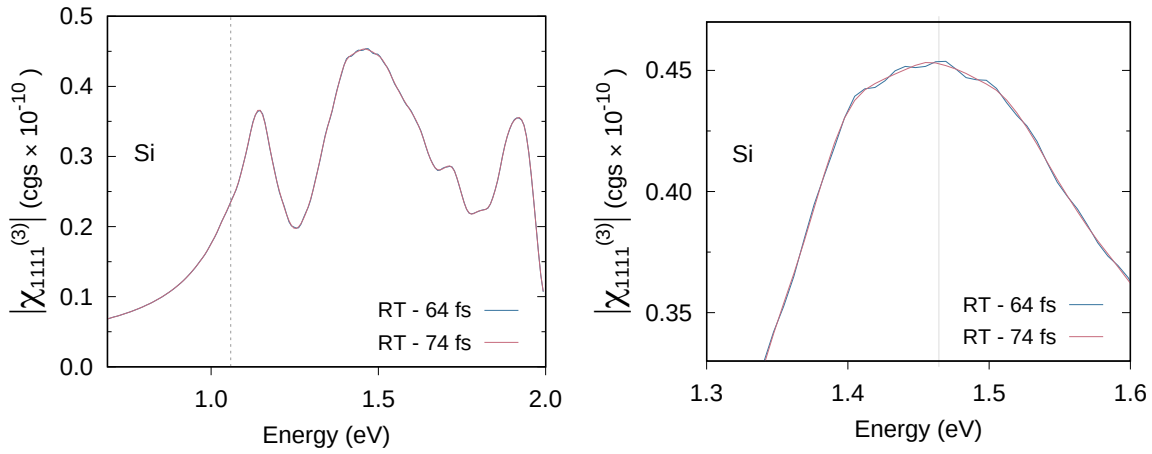

Figure B.18: Si bulk THG - dephasing time - high intensity

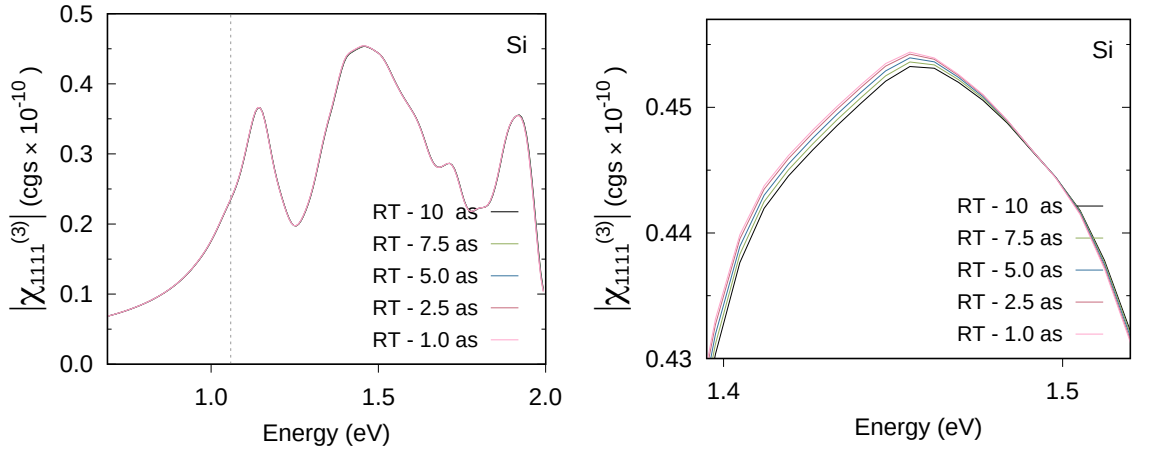

Figure B.19: Si bulk THG - time step - high intensity

B.8 Code and data availability

B.8.1 Code availability

The Floquet approach developed in this work for calculating non-linear optical properties will be available in a future release of the Yambo code. A tutorial will be made available in due course through the tutorials section (`http://www.yambo-code.org/wiki/index.php?title=Tutorials`) of the official Yambo website (`http://www.yambo-code.org/`).

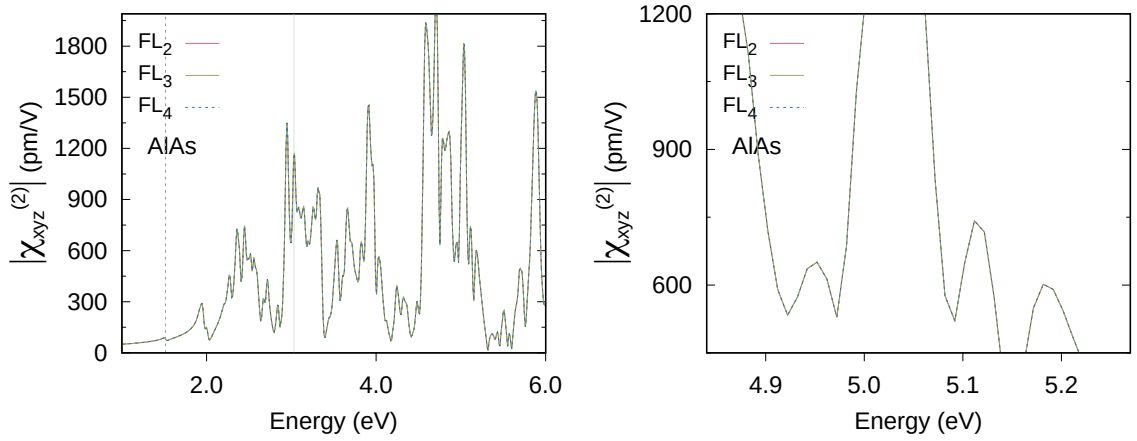

Figure B.20: AlAs bulk - Floquet modes - low intensity - 0.04 eV

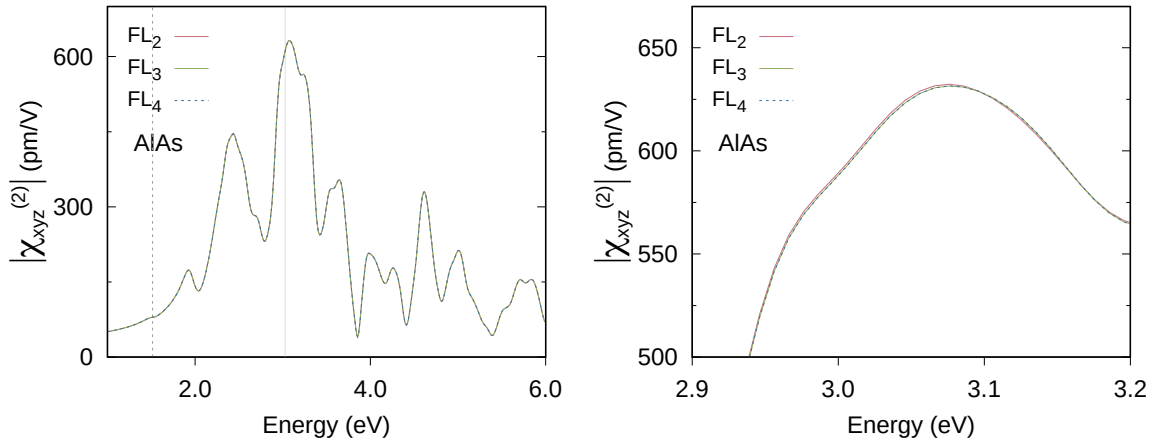

Figure B.21: AlAs bulk - Floquet modes - high intensity - 0.15 eV

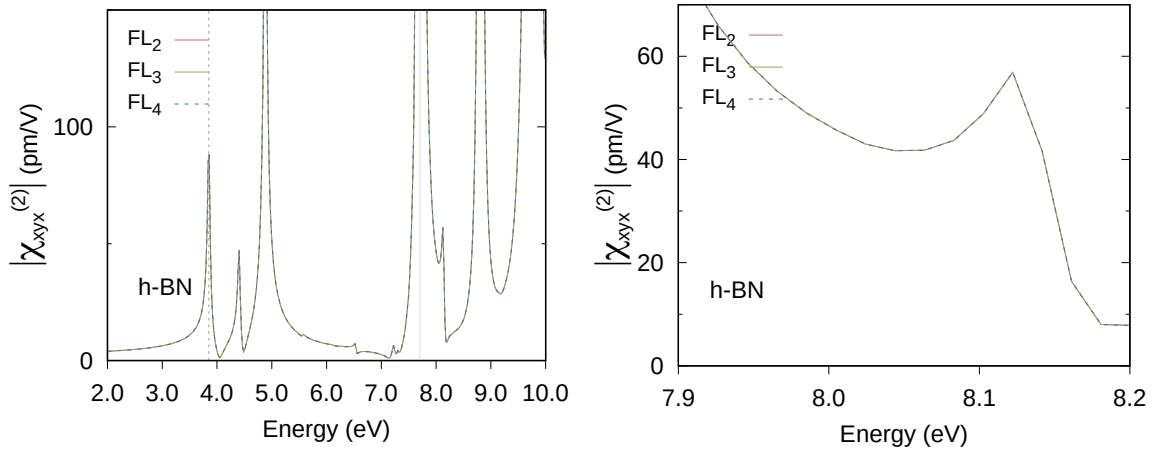

Figure B.22: h-BN 2D - Floquet modes - low intensity - 0.04 eV

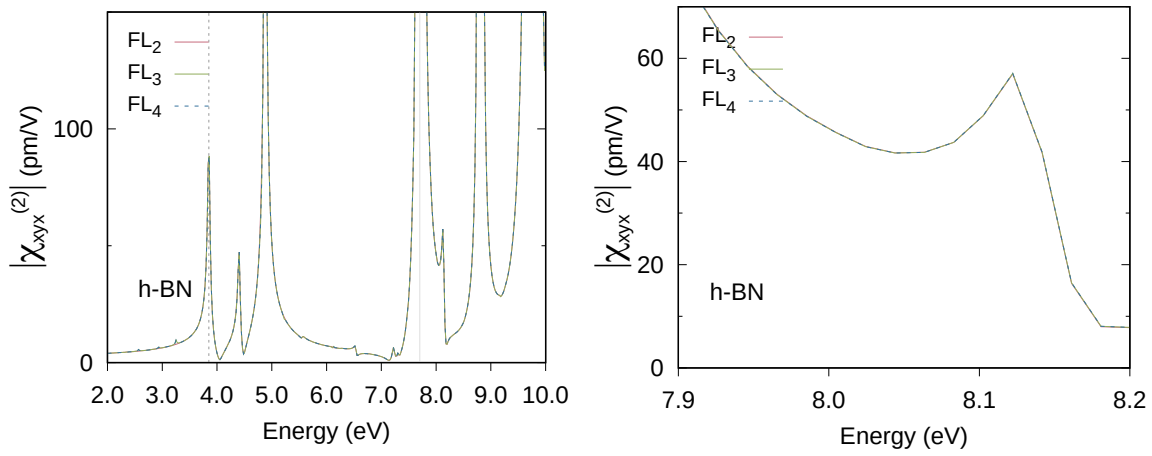

Figure B.23: h-BN 2D - Floquet modes - high intensity - 0.04 eV

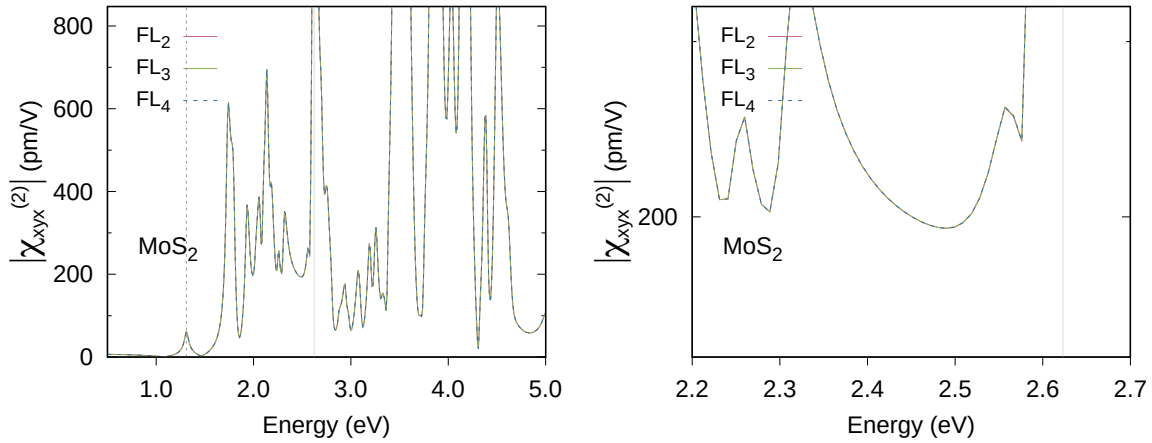

Figure B.24: MoS_2 2D - Floquet modes - low intensity - 0.04 eV

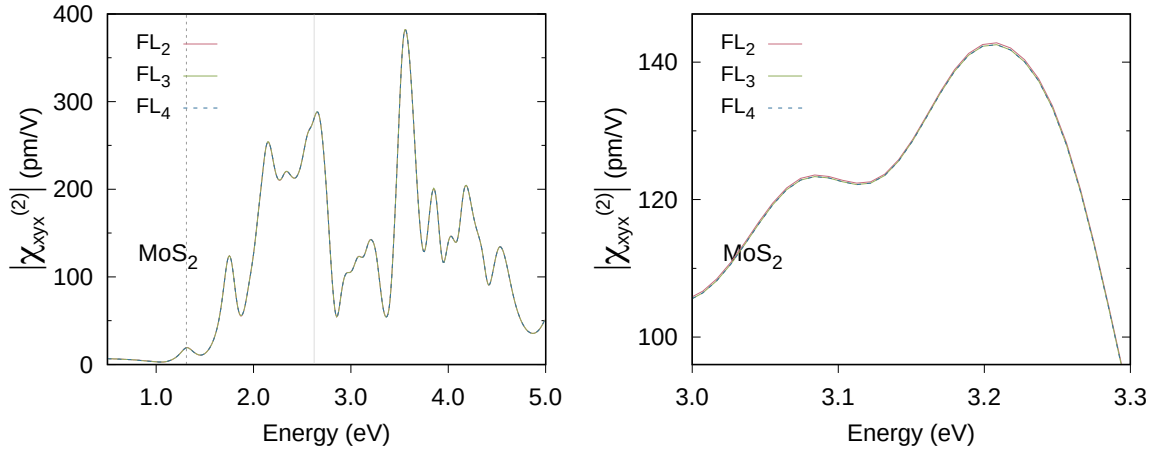

Figure B.25: MoS_2 2D - Floquet modes - high intensity - 0.15 eV

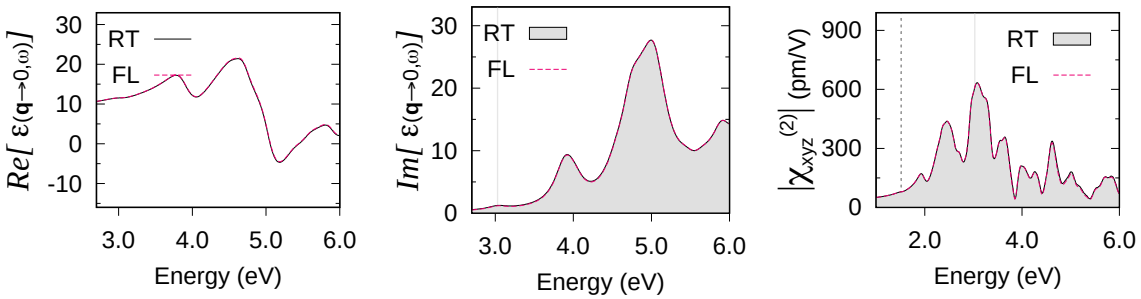

Figure B.26: Bulk AlAs - 8×8×8 - large broadening

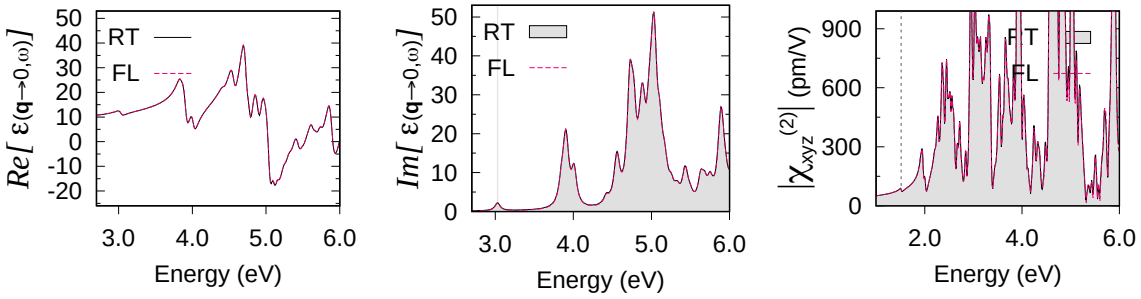

Figure B.27: Bulk AlAs - 8×8×8 - small broadening

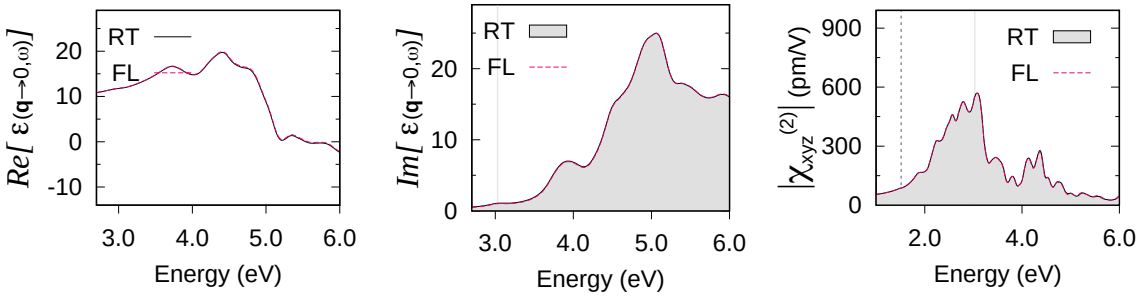

Figure B.28: Bulk AlAs - 10×10×10 - large broadening

B.8.2 Data availability

Input and output files of the calculations presented in this study can be found in a GitHub repository (`https://github.com/aim137/Floquet_IPA-data_repository.git`).

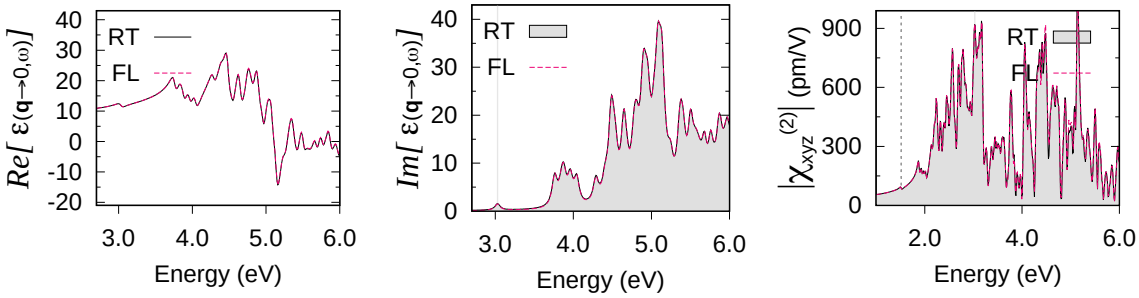

Figure B.29: Bulk AlAs - 10×10×10 - small broadening

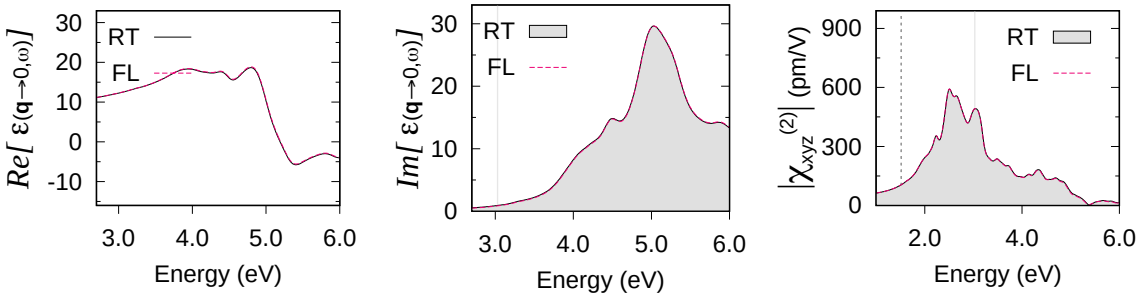

Figure B.30: Bulk AlAs - 20×20×20 - large broadening

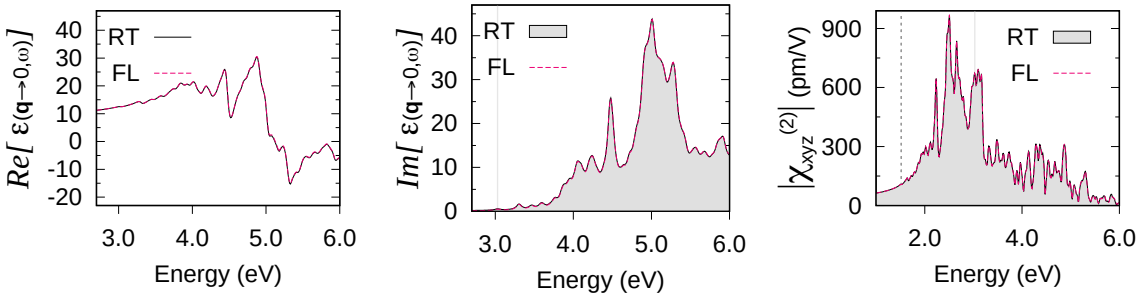

Figure B.31: Bulk AlAs - 20×20×20 - small broadening

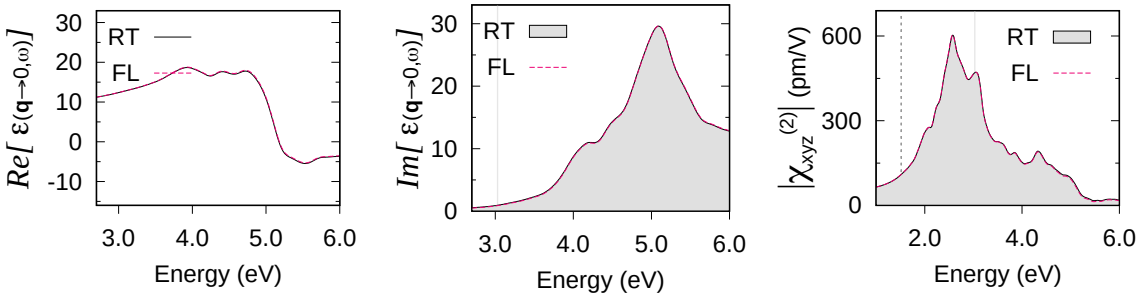

Figure B.32: Bulk AlAs - 30×30×30 - large broadening

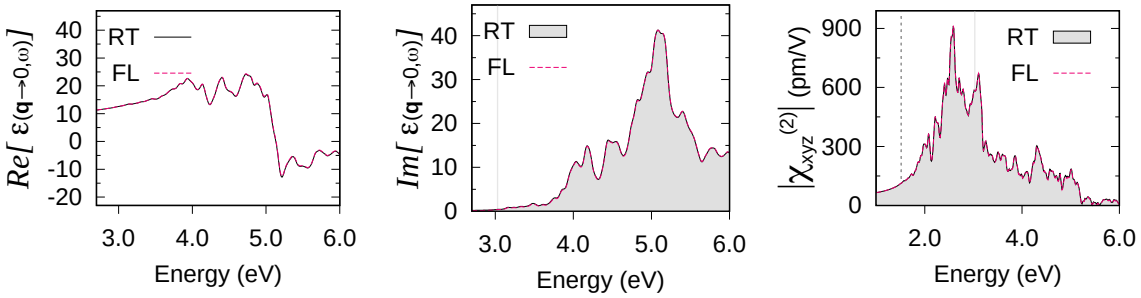

Figure B.33: Bulk AlAs - 30×30×30 - small broadening

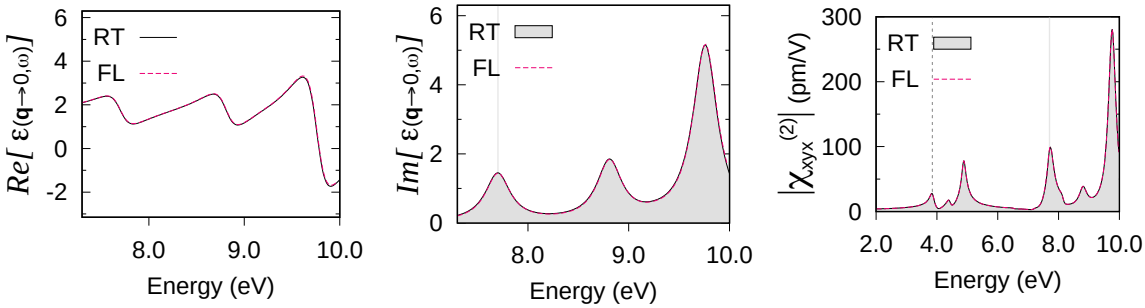

Figure B.34: h-BN 2D - 6×6×1 - large broadening

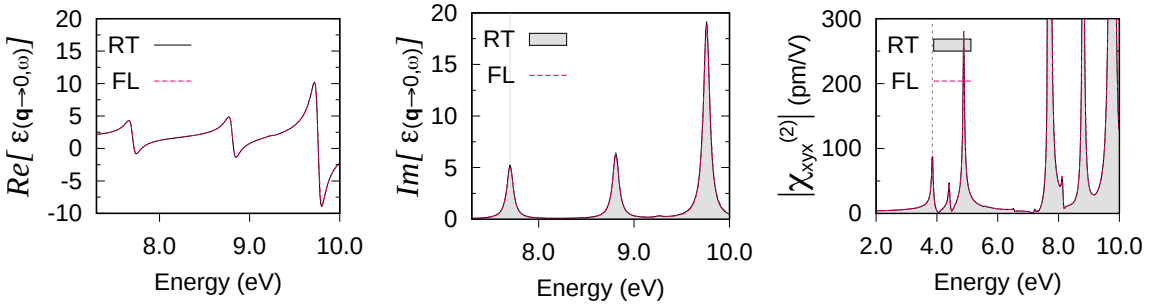

Figure B.35: h-BN 2D - 6×6×1 - small broadening

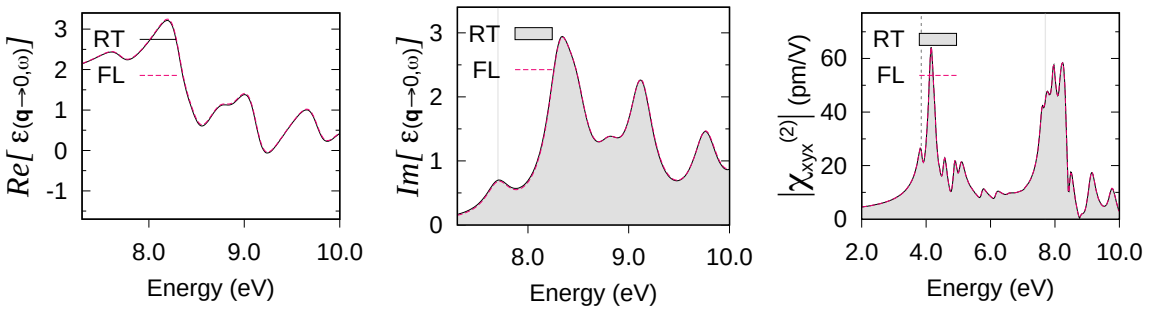

Figure B.36: h-BN 2D - 12×12×1 - large broadening

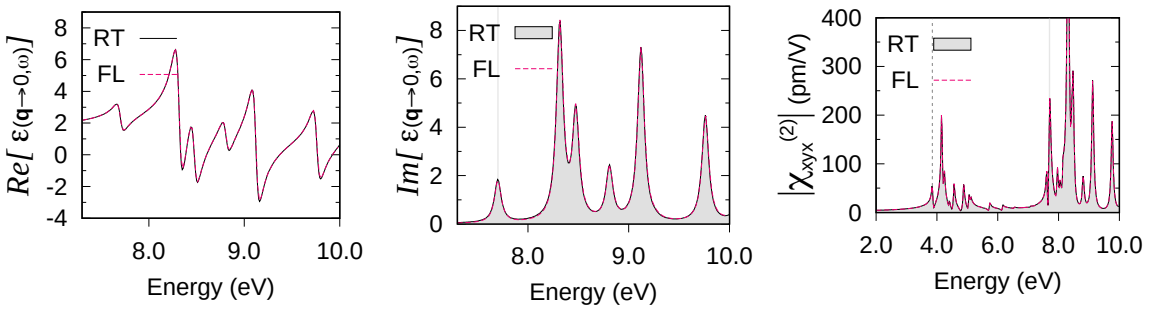

Figure B.37: h-BN 2D - 12×12×1 - small broadening

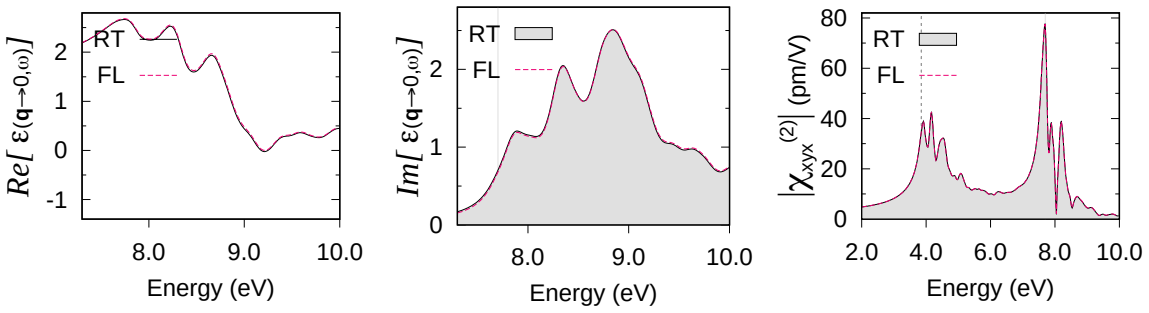

Figure B.38: h-BN 2D - 24×24×1 - large broadening

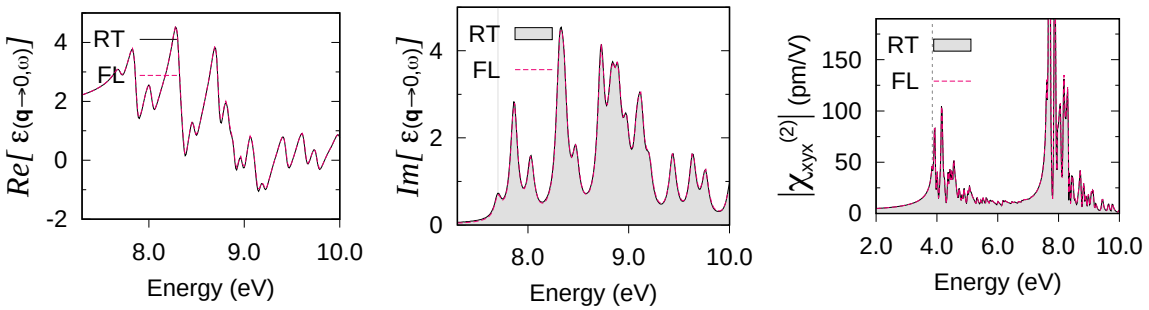

Figure B.39: h-BN 2D - 24×24×1 - small broadening

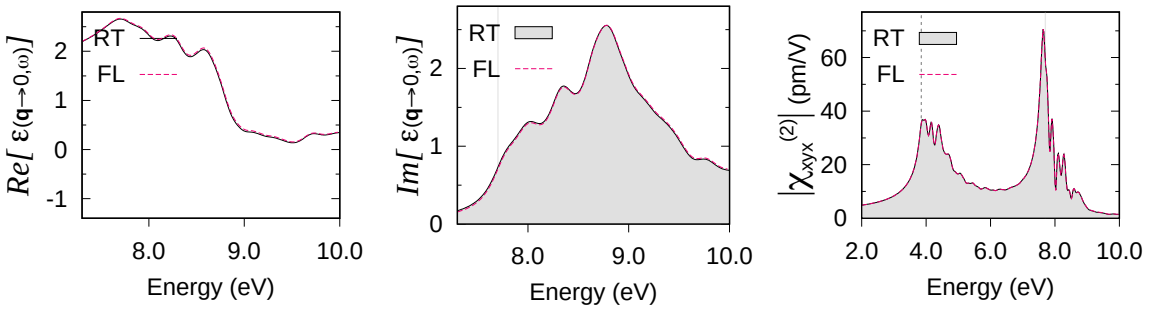

Figure B.40: h-BN 2D - 36×36×1 - large broadening

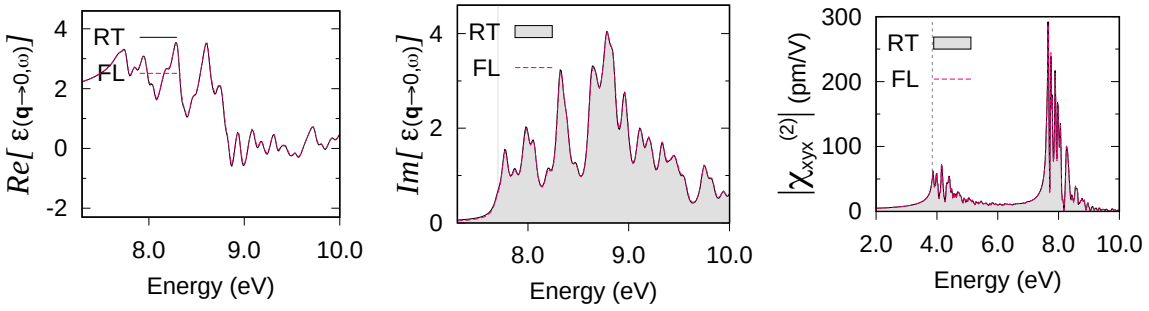

Figure B.41: h-BN 2D - 36×36×1 - small broadening

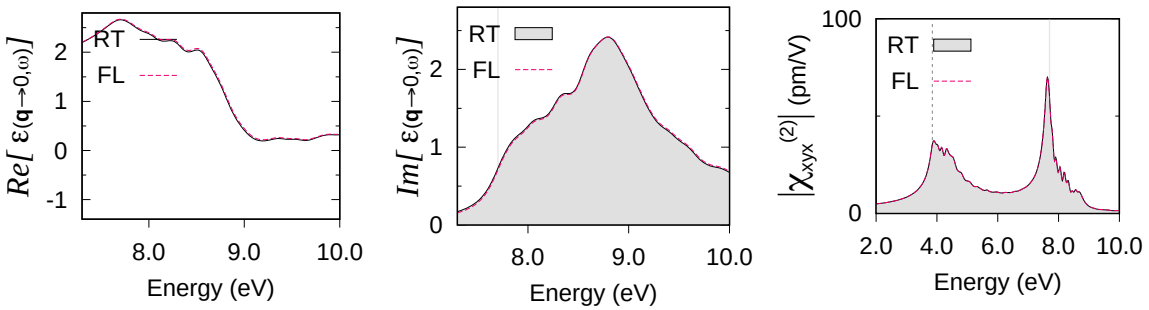

Figure B.42: h-BN 2D - 48×48×1 - large broadening

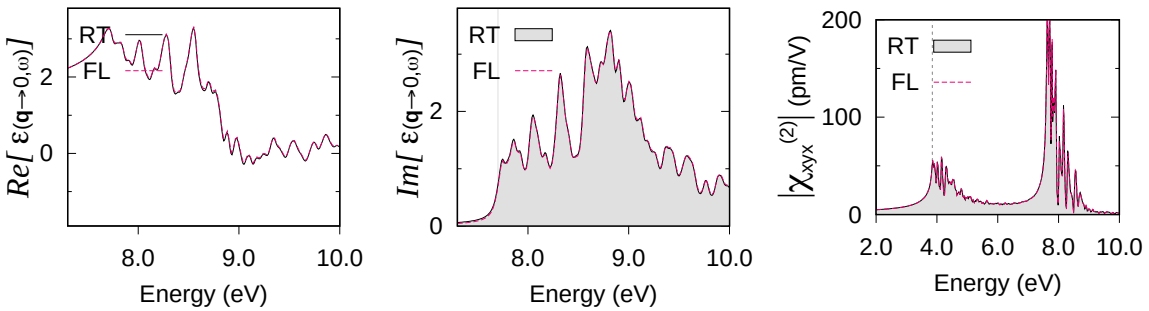

Figure B.43: h-BN 2D - 48×48×1 - small broadening

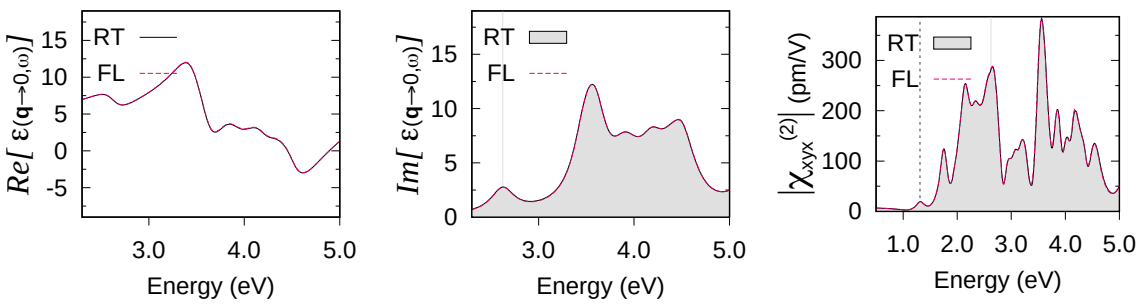

Figure B.44: MoS_2 2D - 6×6×1 - large broadening

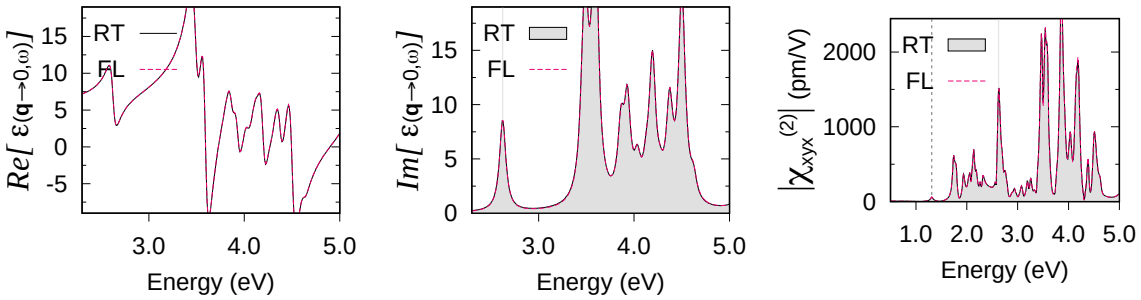

Figure B.45: MoS_2 2D - 6×6×1 - small broadening

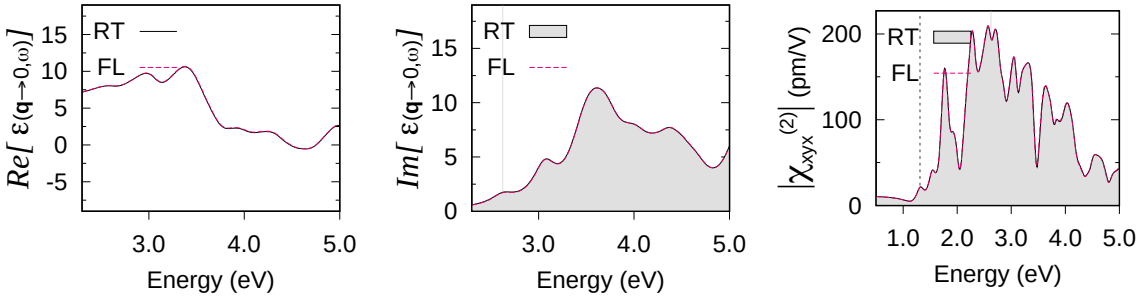

Figure B.46: MoS_2 2D - 12×12×1 - large broadening

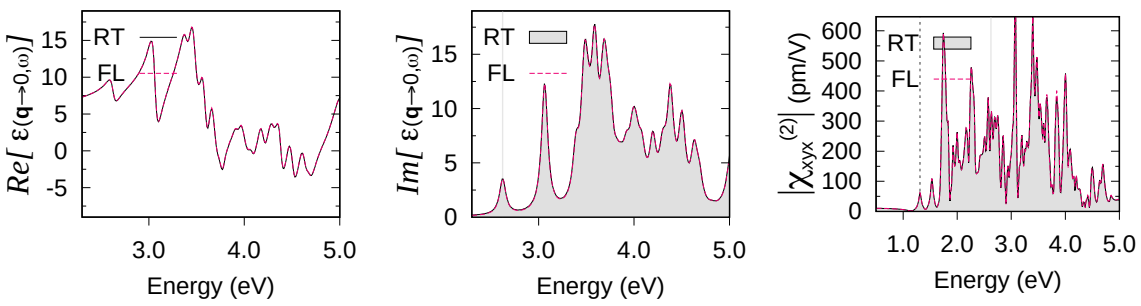

Figure B.47: MoS_2 2D - 12×12×1 - small broadening

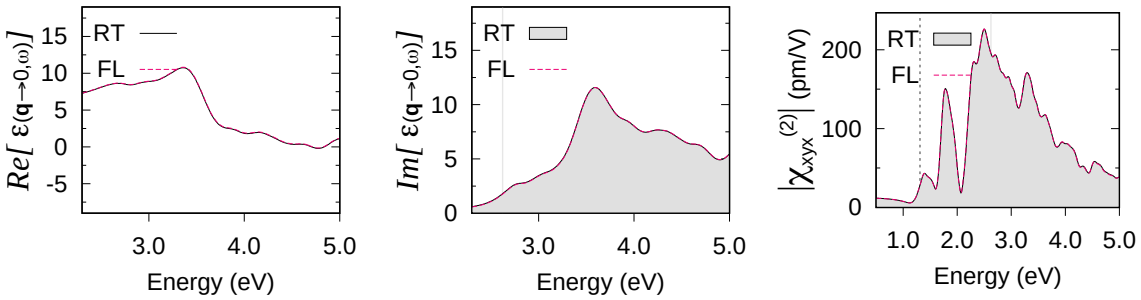

Figure B.48: MoS_2 2D - 24×24×1 - large broadening

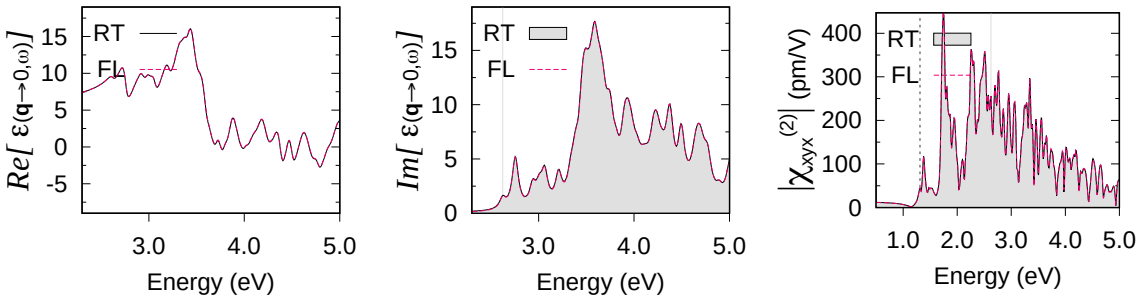

Figure B.49: MoS_2 2D - 24×24×1 - small broadening

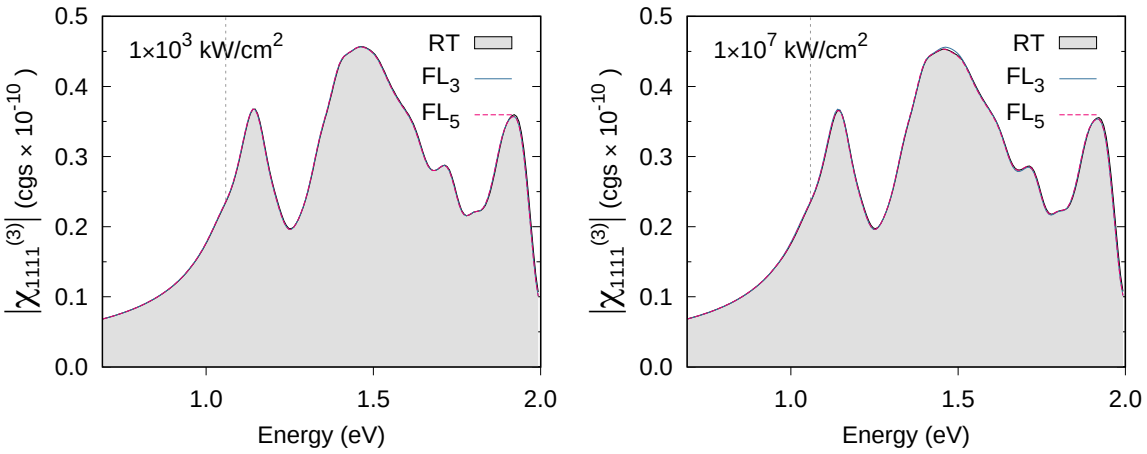

Figure B.50: Bulk Si THG - 8×8×8 - large broadening

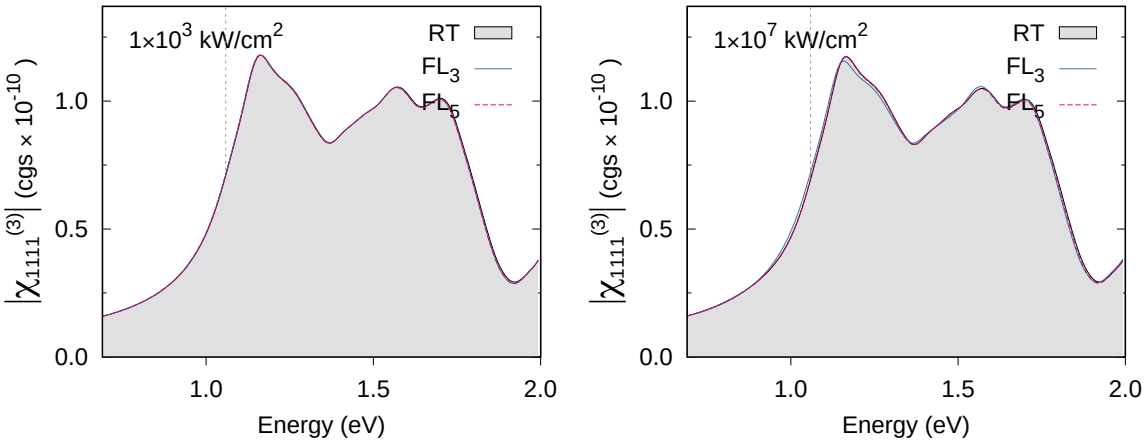

Figure B.51: Bulk Si THG - 24×24×24 - large broadening

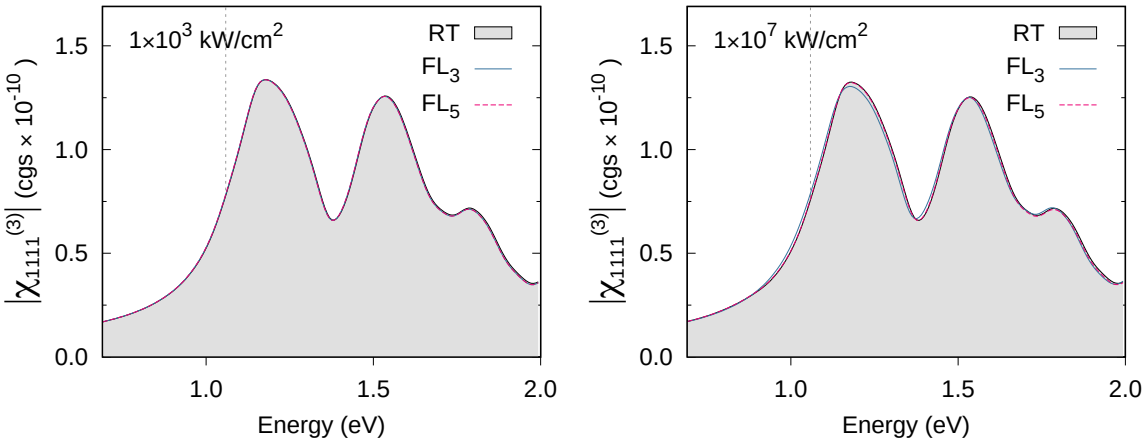

Figure B.52: Bulk Si THG - 32×32×32 - large broadening

Appendix C

Research output

Four publications were produced during the course of this PhD, namely:

- Cantos-Prieto, F. et al. Layer-Dependent Mechanical Properties and Enhanced Plasticity in the Van der Waals Chromium Trihalide Magnets. Nano Lett. 21, 3379–3385 (2021).
- Alliati, I. M., Evans, R. F. L., Novoselov, K. S. & Santos, E. J. G. Relativistic domain-wall dynamics in van der Waals antiferromagnet $MnPS_3$. npj Comput. Mater. 8, 1–9 (2022).
- Alliati, I. M., Sangalli, D. & Grüning, M. Double **k**-Grid Method for Solving the Bethe-Salpeter Equation via Lanczos Approaches. Front. Chem. 9, 1–11 (2022).
- Alliati, I. M. & Grüning, M. Floquet formulation of the dynamical Berry-phase approach to nonlinear optics in extended systems. Electron. Struct. 5, (2023).

The first two publications represent work done during this PhD under a different line of research and are not part of the present thesis.

Bibliography

[1] Griffiths, D. J. *Revolutions in Twentieth-Century Physics* (Cambridge University Press, 2012). URL https://www.cambridge.org/core/books/revolutions-in-twentiethcentury-physics/B0B2AD0F6445EC52784701A8C640D8EE.

[2] Giustino, F. *Materials Modelling Using Density Functional Theory: Properties and Predictions* (Oxford University Press, 2014). URL https://global.oup.com/academic/product/materials-modelling-using-density-functional-theory-9780199662432?lang=en&cc=gb.

[3] Marzari, N. *Handbook of Materials Modeling: Methods*, chap. Understand, Predict, and Design, 9–11 (Springer Netherlands, Dordrecht, 2005). URL https://link.springer.com/chapter/10.1007/978-1-4020-3286-8_2.

[4] Nakamura, S. Background story of the invention of efficient blue ingan light emitting diodes (nobel lecture). *Annalen der Physik* **527**, 335–349 (2015). URL https://onlinelibrary.wiley.com/doi/abs/10.1002/andp.201500801.

[5] Steranka, F. *et al.* High power leds – technology status and market applications. *Physica status solidi (a)* **194**, 380–388 (2002). URL https://onlinelibrary.wiley.com/doi/abs/10.1002/1521-396X%28200212%29194%3A2%3C380%3A%3AAID-PSSA380%3E3.0.CO%3B2-N.

[6] Nayak, P. K., Mahesh, S., Snaith, H. J. & Cahen, D. Photovoltaic solar cell technologies: Analysing the state of the art. *Nature Reviews Materials* **4**, 269 (2019). URL https://www.nature.com/articles/s41578-019-0097-0.

[7] Novoselov, K. S. & Neto, A. H. C. Two-dimensional crystals-based heterostructures: materials with tailored properties. *Physica Scripta* **2012**, 014006 (2012). URL https://dx.doi.org/10.1088/0031-8949/2012/T146/014006.

[8] Geim, A. K. & Grigorieva, I. V. Van der Waals heterostructures. *Nature* **499**, 419 (2013). URL https://www.nature.com/articles/nature12385.

[9] Novoselov, K. S., Mishchenko, A., Carvalho, A. & Neto, A. H. C. 2d materials and van der waals heterostructures. *Science* **353**, aac9439 (2016). URL https://www.science.org/doi/abs/10.1126/science.aac9439.

[10] Boyd, R. W. *Nonlinear Optics, Third Edition* (Academic Press, Inc., USA, 2008), 3rd edn. URL https://www.sciencedirect.com/book/9780128110027/nonlinear-optics.

[11] Franken, P. A., Hill, A. E., Peters, C. W. & Weinreich, G. Generation of optical harmonics. *Phys. Rev. Lett.* **7**, 118–119 (1961). URL https://link.aps.org/doi/10.1103/PhysRevLett.7.118.

[12] Hendrickson, S. M., Foster, A. C., Camacho, R. M. & Clader, B. D. Integrated nonlinear photonics: emerging applications and ongoing challenges. *J. Opt. Soc. Am. B* **31**, 3193–3203 (2014). URL https://opg.optica.org/josab/abstract.cfm?URI=josab-31-12-3193.

[13] Sirleto, L. & Righini, G. C. An introduction to nonlinear integrated photonics: Structures and devices. *Micromachines* **14** (2023). URL https://www.mdpi.com/2072-666X/14/3/614.

[14] Wegener, M. *Extreme Nonlinear Optics: An Introduction* (Springer Berlin Heidelberg, 2005). URL https://doi.org/10.1007/3-540-26688-7_1.

[15] Bloembergen, N., Chang, R. K., Jha, S. S. & Lee, C. H. Optical second-harmonic generation in reflection from media with inversion symmetry. *Phys. Rev.* **174**, 813–822 (1968). URL https://link.aps.org/doi/10.1103/PhysRev.174.813.

[16] Shen, Y. R. Surface second harmonic generation: A new technique for surface studies. *Annual Review of Materials Science* **16**, 69–86 (1986). URL https://doi.org/10.1146/annurev.ms.16.080186.000441.

[17] Shen, Y. R. Optical second harmonic generation at interfaces. *Annual Review of Physical Chemistry* **40**, 327–350 (1989). URL https://doi.org/10.1146/annurev.pc.40.100189.001551.

[18] Li, Y. *et al.* Probing symmetry properties of few-layer mos2 and h-bn by optical second-harmonic generation. *Nano Letters* **13**, 3329–3333 (2013). URL https://pubs.acs.org/doi/10.1021/nl401561r.

[19] Yin, X. *et al.* Edge nonlinear optics on a mos2 atomic monolayer. *Science* **344**, 488–490 (2014). URL https://www.science.org/doi/abs/10.1126/science.1250564.

[20] Hsu, W.-T. *et al.* Second harmonic generation from artificially stacked transition metal dichalcogenide twisted bilayers. *ACS Nano* **8**, 2951–2958 (2014). URL https://pubs.acs.org/doi/10.1021/nn500228r.

[21] Woodward, R. I. *et al.* Characterization of the second- and third-order nonlinear optical susceptibilities of monolayer mos_2 using multiphoton microscopy. *2D Materials* **4**, 011006 (2016). URL https://doi.org/10.1088/2053-1583/4/1/011006.

[22] Sun, Z. *et al.* Giant nonreciprocal second-harmonic generation from antiferromagnetic bilayer cri3. *Nature* **572**, 497–501 (2019). URL https://doi.org/10.1038/s41586-019-1445-3.

[23] Ni, Z., Huang, N., Haglund, A. V., Mandrus, D. G. & Wu, L. Observation of giant surface second-harmonic generation coupled to nematic orders in the van der waals antiferromagnet feps3. *Nano Letters* **22**, 3283–3288 (2022). URL https://doi.org/10.1021/acs.nanolett.2c00212.

[24] Chu, H. *et al.* Linear magnetoelectric phase in ultrathin $mnps_3$ probed by optical second harmonic generation. *Phys. Rev. Lett.* **124**, 027601 (2020). URL https://link.aps.org/doi/10.1103/PhysRevLett.124.027601.

[25] Chauleau, J.-Y., Haltz, E., Carrétéro, C., Fusil, S. & Viret, M. Multi-stimuli manipulation of antiferromagnetic domains assessed by second-harmonic imaging. *Nature Materials* **16**, 803–807 (2017). URL https://doi.org/10.1038/nmat4899.

[26] Xu, S. *et al.* Magnetoelectric coupling in multiferroics probed by optical second harmonic generation. *Nature Communications* **14**, 2274 (2023). URL https://www.nature.com/articles/s41467-023-38055-x.

[27] Huang, B. *et al.* Layer-dependent ferromagnetism in a van der Waals crystal down to the monolayer limit. *Nature* **546**, 270 (2017). URL https://www.nature.com/articles/nature22391.

[28] Regensburger, H., Vollmer, R. & Kirschner, J. Time-resolved magnetization-induced second-harmonic generation from the ni(110) surface. *Phys. Rev. B* **61**, 14716–14722 (2000). URL https://link.aps.org/doi/10.1103/PhysRevB.61.14716.

[29] Jang, H. *et al.* Transient shg imaging on ultrafast carrier dynamics of mos2 nanosheets. *Advanced Materials* **30**, 1705190 (2018). URL https://onlinelibrary.wiley.com/doi/abs/10.1002/adma.201705190.

[30] Hohenberg, P. & Kohn, W. Inhomogeneous electron gas. *Phys. Rev.* **136**, B864–B871 (1964). URL https://journals.aps.org/pr/abstract/10.1103/PhysRev.136.B864.

[31] Kohn, W. & Sham, L. J. Self-consistent equations including exchange and correlation effects. *Phys. Rev.* **140**, A1133–A1138 (1965). URL https://journals.aps.org/pr/abstract/10.1103/PhysRev.140.A1133.

[32] Jones, R. O. Density functional theory: Its origins, rise to prominence, and future. *Rev. Mod. Phys.* **87**, 897–923 (2015). URL https://journals.aps.org/rmp/abstract/10.1103/RevModPhys.87.897.

[33] Van Noorden, R., Maher, B. & Nuzzo, R. The top 100 papers. *Nature* **514**, 550–553 (2014). URL https://www.nature.com/news/the-top-100-papers-1.16224.

[34] Dumaz, M., Boucher, R., Marques, M. A. L. & Romero, A. H. Authorship and citation cultural nature in density functional theory from solid state computational packages. *Scientometrics* **126**, 6681 (2021). URL https://link.springer.com/article/10.1007/s11192-021-04057-z.

[35] Lejaeghere, K. *et al.* Reproducibility in density functional theory calculations of solids. *Science* **351**, aad3000 (2016). URL https://www.science.org/doi/10.1126/science.aad3000.

[36] Huber, S. P. *et al.* AiiDA 1.0, a scalable computational infrastructure for automated reproducible workflows and data provenance. *Scientific Data* **7**, 300 (2020). URL https://www.nature.com/articles/s41597-020-00638-4.

[37] Mathew, K. *et al.* Atomate: A high-level interface to generate, execute, and analyze computational materials science workflows. *Computational Materials Science* **139**, 140–152 (2017). URL https://www.sciencedirect.com/science/article/pii/S0927025617303919.

[38] Onida, G., Reining, L. & Rubio, A. Electronic excitations: density-functional versus many-body Green's-function approaches. *Rev. Mod. Phys.* **74**, 601–659 (2002). URL https://link.aps.org/doi/10.1103/RevModPhys.74.601.

[39] Martin, R. M., Reining, L. & Ceperley, D. M. *Interacting Electrons: Theory and Computational Approaches* (Cambridge University Press, 2016). URL https://www.cambridge.org/core/books/interacting-electrons/4317C43D0531C900920E83DD4632CFE9.

[40] Reining, L. The gw approximation: content, successes and limitations. *WIREs Computational Molecular Science* **8**, e1344 (2018). URL https://wires.onlinelibrary.wiley.com/doi/abs/10.1002/wcms.1344.

[41] Golze, D., Dvorak, M. & Rinke, P. The gw compendium: A practical guide to theoretical photoemission spectroscopy. *Frontiers in Chemistry* **7** (2019). URL https://www.frontiersin.org/articles/10.3389/fchem.2019.00377.

[42] Attaccalite, C. & Grüning, M. Nonlinear optics from an ab initio approach by means of the dynamical berry phase: Application to second- and third-harmonic generation in semiconductors. *Phys. Rev. B* **88**, 235113 (2013). URL https://link.aps.org/doi/10.1103/PhysRevB.88.235113.

[43] Grüning, M. & Attaccalite, C. Second harmonic generation in h-bn and mos_2 monolayers: Role of electron-hole interaction. *Phys. Rev. B* **89**, 081102 (2014). URL https://link.aps.org/doi/10.1103/PhysRevB.89.081102.

[44] Born, M. & Oppenheimer, R. Zur quantentheorie der molekeln. *Annalen der Physik* **389**, 457–484 (1927). URL https://onlinelibrary.wiley.com/doi/10.1002/andp.19273892002.

[45] Kaxiras, E. *Atomic and Electronic Structure of Solids* (Cambridge University Press, 2003). URL https://www.cambridge.org/core/books/atomic-and-electronic-structure-of-solids/1B7E5043BE2B6D12C749AB9A1E913295.

[46] Kohanoff, J. *Electronic Structure Calculations for Solids and Molecules: Theory and Computational Methods* (Cambridge University Press, 2006). URL https://www.cambridge.org/core/books/electronic-structure-calculations-for-solids-and-molecules/0C0AF2B01A380912FC13816A9A0C350F.

[47] Martin, R. M. *Electronic Structure: Basic Theory and Practical Methods* (Cambridge University Press, 2004). URL https://www.cambridge.org/core/books/electronic-structure/DDFE838DED61D7A402FDF20D735BC63A.

[48] Thomas, L. H. The calculation of atomic fields. *Mathematical Proceedings of the Cambridge Philosophical Society* **23**, 542–548 (1927). URL https://www.cambridge.org/core/journals/mathematical-proceedings-of-the-cambridge-philosophical-society/article/abs/calculation-of-atomic-fields/ADCA3D21D0FACD7077B5FDBB7F3B3F3A.

[49] Fermi, E. Eine statistische methode zur bestimmung einiger eigenschaften des atoms und ihre anwendung auf die theorie des periodischen systems der elemente. *Zeitschrift für Physik* **48**, 73 (1928). URL https://link.springer.com/article/10.1007/bf01351576.

[50] March, N. The thomas-fermi approximation in quantum mechanics. *Advances in Physics* **6**, 1–101 (1957). URL https://www.tandfonline.com/doi/abs/10.1080/00018735700101156.

[51] Perdew, J. P. & Zunger, A. Self-interaction correction to density-functional approximations for many-electron systems. *Phys. Rev. B* **23**, 5048–5079 (1981). URL https://link.aps.org/doi/10.1103/PhysRevB.23.5048.

[52] Perdew, J. P. & Wang, Y. Accurate and simple analytic representation of the electron-gas correlation energy. *Phys. Rev. B* **45**, 13244–13249 (1992). URL https://link.aps.org/doi/10.1103/PhysRevB.45.13244.

[53] Perdew, J. P., Burke, K. & Ernzerhof, M. Generalized gradient approximation made simple. *Phys. Rev. Lett.* **77**, 3865–3868 (1996). URL https://journals.aps.org/prl/abstract/10.1103/PhysRevLett.77.3865.

[54] Bloch, F. Über die quantenmechanik der elektronen in kristallgittern. *Zeitschrift für Physik* **52**, 555 (1929). URL https://link.springer.com/article/10.1007/BF01339455.

[55] Hamann, D. R., Schlüter, M. & Chiang, C. Norm-conserving pseudopotentials. *Phys. Rev. Lett.* **43**, 1494–1497 (1979). URL https://link.aps.org/doi/10.1103/PhysRevLett.43.1494.

[56] Vanderbilt, D. Soft self-consistent pseudopotentials in a generalized eigenvalue formalism. *Phys. Rev. B* **41**, 7892–7895 (1990). URL https://link.aps.org/doi/10.1103/PhysRevB.41.7892.

[57] Blöchl, P. E. Projector augmented-wave method. *Phys. Rev. B* **50**, 17953–17979 (1994). URL https://link.aps.org/doi/10.1103/PhysRevB.50.17953.

[58] Johnson, D. D. Modified broyden's method for accelerating convergence in self-consistent calculations. *Phys. Rev. B* **38**, 12807–12813 (1988). URL https://link.aps.org/doi/10.1103/PhysRevB.38.12807.

[59] Marzari, N., Vanderbilt, D., De Vita, A. & Payne, M. C. Thermal contraction and disordering of the al(110) surface. *Phys. Rev. Lett.* **82**, 3296–3299 (1999). URL https://link.aps.org/doi/10.1103/PhysRevLett.82.3296.

[60] Davidson, E. R. The iterative calculation of a few of the lowest eigenvalues and corresponding eigenvectors of large real-symmetric matrices. *Journal of Computational Physics* **17**, 87–94 (1975). URL https://www.sciencedirect.com/science/article/pii/0021999175900650.

[61] Kobe, D. H. Gauge transformations and the electric dipole approximation. *American Journal of Physics* **50**, 128–133 (1982). URL https://doi.org/10.1119/1.13029.

[62] Sangalli, D., Berger, J. A., Attaccalite, C., Grüning, M. & Romaniello, P. Optical properties of periodic systems within the current-current response framework: Pitfalls and remedies. *Phys. Rev. B* **95**, 155203 (2017). URL https://link.aps.org/doi/10.1103/PhysRevB.95.155203.

[63] Casida, M. E. Time-dependent density-functional theory for molecules and molecular solids. *Journal of Molecular Structure: THEOCHEM* **914**, 3–18 (2009). URL https://www.sciencedirect.com/science/article/pii/S0166128009005363.

[64] Albrecht, S., Reining, L., Del Sole, R. & Onida, G. Ab initio calculation of excitonic effects in the optical spectra of semiconductors. *Phys. Rev. Lett.* **80**, 4510–4513 (1998). URL https://link.aps.org/doi/10.1103/PhysRevLett.80.4510.

[65] Benedict, L. X., Shirley, E. L. & Bohn, R. B. Optical absorption of insulators and the electron-hole interaction: An ab initio calculation. *Phys. Rev. Lett.* **80**, 4514–4517 (1998). URL https://link.aps.org/doi/10.1103/PhysRevLett.80.4514.

[66] Rohlfing, M. & Louie, S. G. Electron-hole excitations in semiconductors and insulators. *Phys. Rev. Lett.* **81**, 2312–2315 (1998). URL https://link.aps.org/doi/10.1103/PhysRevLett.81.2312.

[67] Strinati, G. Application of the Green's functions method to the study of the optical properties of semiconductors. *La Rivista del Nuovo Cimento* **11**, 1 (1988). URL https://link.springer.com/article/10.1007/BF02725962.

[68] Bruus, H. & Flensberg, K. *Many-body quantum theory in condensed matter physics - an introduction* (Oxford University Press, 2004). URL https://global.oup.com/academic/product/many-body-quantum-theory-in-condensed-matter-physics-9780198566335?lang=en&cc=gb.

[69] Adler, S. L. Quantum theory of the dielectric constant in real solids. *Phys. Rev.* **126**, 413–420 (1962). URL https://link.aps.org/doi/10.1103/PhysRev.126.413.

[70] Wiser, N. Dielectric constant with local field effects included. *Phys. Rev.* **129**, 62–69 (1963). URL https://link.aps.org/doi/10.1103/PhysRev.129.62.

[71] Gross, E. K. U., Runge, E. & Heinonen, O. *Many-particle theory* (Verlag Adam Hilger, 1991).

[72] Hedin, L. New method for calculating the one-particle Green's function with application to the electron-gas problem. *Phys. Rev.* **139**, A796–A823 (1965). URL https://link.aps.org/doi/10.1103/PhysRev.139.A796.

[73] Petersilka, M., Gossmann, U. J. & Gross, E. K. U. Excitation energies from time-dependent density-functional theory. *Phys. Rev. Lett.* **76**, 1212–1215 (1996). URL https://link.aps.org/doi/10.1103/PhysRevLett.76.1212.

[74] Lanczos, C. An iteration method for the solution of the eigenvalue problem of linear differential and integral operators. *Journal of research of the National Bureau of Standards* **45**, 255–282 (1950). URL http://dx.doi.org/10.6028/jres.045.026.

[75] Cini, M. *Topics and Methods in Condensed Matter Theory: From Basic Quantum Mechanics to the Frontiers of Research* (Springer Berlin Heidelberg, Berlin, 2007). URL https://doi.org/10.1007/978-3-540-70727-1_14.

[76] Haydock, R. The recursive solution of the schrödinger equation. *Computer Physics Communications* **20**, 11–16 (1980). URL https://www.sciencedirect.com/science/article/pii/0010465580901010.

[77] Benedict, L. X. & Shirley, E. L. Ab initio calculation of $\epsilon_2(\omega)$ including the electron-hole interaction: Application to gan and caf_2. *Phys. Rev. B* **59**, 5441–5451 (1999). URL https://link.aps.org/doi/10.1103/PhysRevB.59.5441.

[78] Grüning, M., Marini, A. & Gonze, X. Implementation and testing of lanczos-based algorithms for random-phase approximation eigenproblems. *Computational Materials Science* **50**, 2148–2156 (2011). URL https://www.sciencedirect.com/science/article/pii/S092702561100111X.

[79] Rohlfing, M. & Louie, S. G. Electron-hole excitations and optical spectra from first principles. *Phys. Rev. B* **62**, 4927–4944 (2000). URL https://link.aps.org/doi/10.1103/PhysRevB.62.4927.

[80] Fuchs, F., Rödl, C., Schleife, A. & Bechstedt, F. Efficient $\mathcal{O}(N^2)$ approach to solve the bethe-salpeter equation for excitonic bound states. *Phys. Rev. B* **78**, 085103 (2008). URL https://link.aps.org/doi/10.1103/PhysRevB.78.085103.

[81] Kammerlander, D., Botti, S., Marques, M. A. L., Marini, A. & Attaccalite, C. Speeding up the solution of the bethe-salpeter equation by a double-grid method and wannier interpolation. *Phys. Rev. B* **86**, 125203 (2012). URL https://link.aps.org/doi/10.1103/PhysRevB.86.125203.

[82] Gillet, Y., Giantomassi, M. & Gonze, X. Efficient on-the-fly interpolation technique for bethe–salpeter calculations of optical spectra. *Computer Physics Communications* **203**, 83–93 (2016). URL https://www.sciencedirect.com/science/article/pii/S0010465516300236.

[83] Sipe, J. E. & Ghahramani, E. Nonlinear optical response of semiconductors in the independent-particle approximation. *Phys. Rev. B* **48**, 11705–11722 (1993). URL https://link.aps.org/doi/10.1103/PhysRevB.48.11705.

[84] Corso, A. D., Mauri, F. & Rubio, A. Density-functional theory of the nonlinear optical susceptibility: Application to cubic semiconductors. *Phys. Rev. B* **53**, 15638–15642 (1996). URL https://link.aps.org/doi/10.1103/PhysRevB.53.15638.

[85] Luppi, E., Hübener, H. & Véniard, V. Ab initio second-order nonlinear optics in solids: Second-harmonic generation spectroscopy from time-dependent density-functional theory. *Phys. Rev. B* **82**, 235201 (2010). URL https://link.aps.org/doi/10.1103/PhysRevB.82.235201.

[86] Leitsmann, R., Schmidt, W. G., Hahn, P. H. & Bechstedt, F. Second-harmonic polarizability including electron-hole attraction from band-structure theory. *Phys. Rev. B* **71**, 195209 (2005). URL https://link.aps.org/doi/10.1103/PhysRevB.71.195209.

[87] Chang, E. K., Shirley, E. L. & Levine, Z. H. Excitonic effects on optical second-harmonic polarizabilities of semiconductors. *Phys. Rev. B* **65**, 035205 (2001). URL https://link.aps.org/doi/10.1103/PhysRevB.65.035205.

[88] Yabana, K. & Bertsch, G. F. Time-dependent local-density approximation in real time. *Phys. Rev. B* **54**, 4484–4487 (1996). URL https://link.aps.org/doi/10.1103/PhysRevB.54.4484.

[89] Marques, M. & Gross, E. Time-dependent density functional theory. *Annual Review of Physical Chemistry* **55**, 427–455 (2004). URL https://doi.org/10.1146/annurev.physchem.55.091602.094449.

[90] Casida, M. & Huix-Rotllant, M. Progress in time-dependent density-functional theory. *Annual Review of Physical Chemistry* **63**, 287–323 (2012). URL https://doi.org/10.1146/annurev-physchem-032511-143803.

[91] Laurent, A. D. & Jacquemin, D. Td-dft benchmarks: A review. *International Journal of Quantum Chemistry* **113**, 2019–2039 (2013). URL https://onlinelibrary.wiley.com/doi/abs/10.1002/qua.24438.

[92] Kadanoff, L. & Baym, G. *Quantum Statistical Mechanics* (W.A. Benjamin Inc., New York, 1962). URL https://www.taylorfrancis.com/books/mono/10.1201/9780429493218/quantum-statistical-mechanics-leo-kadanoff.

[93] Attaccalite, C., Grüning, M. & Marini, A. Real-time approach to the optical properties of solids and nanostructures: Time-dependent bethe-salpeter equation. *Phys.*

Rev. B **84**, 245110 (2011). URL https://link.aps.org/doi/10.1103/PhysRevB.84.245110.

[94] King-Smith, R. D. & Vanderbilt, D. Theory of polarization of crystalline solids. *Phys. Rev. B* **47**, 1651–1654 (1993). URL https://link.aps.org/doi/10.1103/PhysRevB.47.1651.

[95] Vanderbilt, D. & King-Smith, R. D. Electric polarization as a bulk quantity and its relation to surface charge. *Phys. Rev. B* **48**, 4442–4455 (1993). URL https://link.aps.org/doi/10.1103/PhysRevB.48.4442.

[96] Resta, R. Macroscopic electric polarization as a geometric quantum phase. *Europhysics Letters* **22**, 133 (1993). URL https://dx.doi.org/10.1209/0295-5075/22/2/010.

[97] Souza, I., Íñiguez, J. & Vanderbilt, D. Dynamics of berry-phase polarization in time-dependent electric fields. *Phys. Rev. B* **69**, 085106 (2004). URL https://link.aps.org/doi/10.1103/PhysRevB.69.085106.

[98] Attaccalite, C., Nguer, A., Cannuccia, E. & Grüning, M. Strong second harmonic generation in sic, zno, gan two-dimensional hexagonal crystals from first-principles many-body calculations. *Phys. Chem. Chem. Phys.* **17**, 9533–9540 (2015). URL http://dx.doi.org/10.1039/C5CP00601E.

[99] Attaccalite, C., Cannuccia, E. & Grüning, M. Excitonic effects in third-harmonic generation: The case of carbon nanotubes and nanoribbons. *Phys. Rev. B* **95**, 125403 (2017). URL https://link.aps.org/doi/10.1103/PhysRevB.95.125403.

[100] Attaccalite, C., Grüning, M., Amara, H., Latil, S. & Ducastelle, F. m. c. Two-photon absorption in two-dimensional materials: The case of hexagonal boron nitride. *Phys. Rev. B* **98**, 165126 (2018). URL https://link.aps.org/doi/10.1103/PhysRevB.98.165126.

[101] Attaccalite, C., Palummo, M., Cannuccia, E. & Grüning, M. Second-harmonic generation in single-layer monochalcogenides: A response from first-principles real-time simulations. *Phys. Rev. Mater.* **3**, 074003 (2019). URL https://link.aps.org/doi/10.1103/PhysRevMaterials.3.074003.

[102] Wei, Y., Xu, X., Wang, S., Li, W. & Jiang, Y. Second harmonic generation in janus mosse a monolayer and stacked bulk with vertical asymmetry. *Phys. Chem. Chem. Phys.* **21**, 21022–21029 (2019). URL http://dx.doi.org/10.1039/C9CP03395E.

[103] Grüning, M., Sangalli, D. & Attaccalite, C. Dielectrics in a time-dependent electric field: A real-time approach based on density-polarization functional theory. *Phys. Rev. B* **94**, 035149 (2016). URL https://link.aps.org/doi/10.1103/PhysRevB.94.035149.

[104] Shirley, J. H. Solution of the schrödinger equation with a hamiltonian periodic in time. *Phys. Rev.* **138**, B979–B987 (1965). URL https://link.aps.org/doi/10.1103/PhysRev.138.B979.

[105] Sambe, H. Steady states and quasienergies of a quantum-mechanical system in an oscillating field. *Phys. Rev. A* **7**, 2203–2213 (1973). URL https://link.aps.org/doi/10.1103/PhysRevA.7.2203.

[106] Salzman, W. R. Quantum mechanics of systems periodic in time. *Phys. Rev. A* **10**, 461–465 (1974). URL https://link.aps.org/doi/10.1103/PhysRevA.10.461.

[107] Floquet, G. Sur les équations différentielles linéaires à coefficients périodiques. *Annales scientifiques de l'École Normale Supérieure* **2e série, 12**, 47–88 (1883). URL http://www.numdam.org/articles/10.24033/asens.220/.

[108] Tannor, D. J. *Introduction to quantum mechanics: a time-dependent perspective* (University science books, 2007). URL https://uscibooks.aip.org/books/introduction-to-quantum-mechanics-a-time-dependent-perspective/.

[109] Joachain, C. J., Kylstra, N. J. & Potvliege, R. M. *Atoms in Intense Laser Fields* (Cambridge University Press, 2011). URL https://www.cambridge.org/core/books/atoms-in-intense-laser-fields/D651A1E67661E3F76E44748FB1DB82B0.

[110] Maquet, A., Chu, S.-I. & Reinhardt, W. P. Stark ionization in dc and ac fields: An L^2 complex-coordinate approach. *Phys. Rev. A* **27**, 2946–2970 (1983). URL https://link.aps.org/doi/10.1103/PhysRevA.27.2946.

[111] Potvliege, R. M. & Shakeshaft, R. Nonperturbative calculation of partial differential rates for multiphoton ionization of a hydrogen atom in a strong laser field. *Phys. Rev. A* **38**, 1098–1100 (1988). URL https://link.aps.org/doi/10.1103/PhysRevA.38.1098.

[112] Burke, P. G., Francken, P. & Joachain, C. J. R-matrix-floquet theory of multiphoton processes. *Europhysics Letters* **13**, 617 (1990). URL https://dx.doi.org/10.1209/0295-5075/13/7/008.

[113] Burke, P. G., Francken, P. & Joachain, C. J. R-matrix-floquet theory of multiphoton processes. *Journal of Physics B: Atomic, Molecular and Optical Physics* **24**, 761 (1991). URL https://dx.doi.org/10.1088/0953-4075/24/4/005.

[114] Chu, S.-I. Recent developments in semiclassical floquet theories for intense-field multiphoton processes. vol. 21 of *Advances in Atomic and Molecular Physics*, 197–253 (Academic Press, 1985). URL https://www.sciencedirect.com/science/article/pii/S0065219908601438.

[115] Joachain, C., Dörr, M. & Kylstra, N. High-intensity laser-atom physics. vol. 42 of *Advances In Atomic, Molecular, and Optical Physics*, 225–286 (Academic Press, 2000). URL https://www.sciencedirect.com/science/article/pii/S1049250X08601883.

[116] Ho, T.-S., Wang, K. & Chu, S.-I. Floquet-liouville supermatrix approach: Time development of density-matrix operator and multiphoton resonance fluorescence spectra in intense laser fields. *Phys. Rev. A* **33**, 1798–1816 (1986). URL https://link.aps.org/doi/10.1103/PhysRevA.33.1798.

[117] Chu, S.-I. Generalized Floquet Theoretical Approaches to Intense-Field Multiphoton and Nonlinear Optical Processes. In Hirschfelder, J. O., Wyatt, R. E., Coalson, R. D., Prigogine, I. & Rice, S. A. (eds.) *Lasers, Molecules, and Methods*, vol. 73 of *Advances in Chemical Physics*, 739–799 (John Wiley & Sons, Inc, 1989). URL https://www.wiley.com/en-us/Lasers%2C+Molecules%2C+and+Methods%2C+Volume+73-p-9780470141830.

[118] Telnov, D. A. & Chu, S.-I. Floquet formulation of time-dependent density functional theory. *Chemical Physics Letters* **264**, 466–476 (1997). URL https://www.sciencedirect.com/science/article/pii/S000926149601370X.

[119] Chu, S.-I. & Telnov, D. A. Beyond the floquet theorem: generalized floquet formalisms and quasienergy methods for atomic and molecular multiphoton processes in intense laser fields. *Physics Reports* **390**, 1–131 (2004). URL https://www.sciencedirect.com/science/article/pii/S0370157303003946.

[120] Salek, P., Helgaker, T. & Saue, T. Linear response at the 4-component relativistic density-functional level: application to the frequency-dependent dipole polarizability of hg, auh and pth2. *Chemical Physics* **311**, 187–201 (2005). URL https://www.sciencedirect.com/science/article/pii/S0301010404005749.

[121] Kapoor, V., Ruggenthaler, M. & Bauer, D. Periodicity of the time-dependent kohn-sham equation and the floquet theorem. *Phys. Rev. A* **87**, 042521 (2013). URL https://link.aps.org/doi/10.1103/PhysRevA.87.042521.

[122] Hone, D. W., Ketzmerick, R. & Kohn, W. Time-dependent floquet theory and absence of an adiabatic limit. *Phys. Rev. A* **56**, 4045–4054 (1997). URL https://link.aps.org/doi/10.1103/PhysRevA.56.4045.

[123] Maitra, N. T. & Burke, K. On the floquet formulation of time-dependent density functional theory. *Chemical Physics Letters* **359**, 237–240 (2002). URL https://www.sciencedirect.com/science/article/pii/S0009261402005869.

[124] Maitra, N. T. & Burke, K. Comment on "analysis of floquet formulation of time-dependent density-functional theory"[chem. phys. lett. 433 (2006) 204]. *Chemical Physics Letters* **441**, 167–169 (2007). URL https://www.sciencedirect.com/science/article/pii/S0009261407005519.

[125] Le, C. M., Akashi, R. & Tsuneyuki, S. Defining a well-ordered floquet basis by the average energy. *Phys. Rev. A* **102**, 042212 (2020). URL https://link.aps.org/doi/10.1103/PhysRevA.102.042212.

[126] Le, C. M., Akashi, R. & Tsuneyuki, S. Missing quantum number of floquet states. *Phys. Rev. A* **105**, 052213 (2022). URL https://link.aps.org/doi/10.1103/PhysRevA.105.052213.

[127] Krüger, N. Variational principle for time-periodic quantum systems. *Zeitschrift für Naturforschung A* **75**, 855–861 (2020). URL https://doi.org/10.1515/zna-2020-0209.

[128] Marini, A., Hogan, C., Grüning, M. & Varsano, D. yambo: An ab initio tool for excited state calculations. *Computer Physics Communications* **180**, 1392–1403 (2009). URL https://www.sciencedirect.com/science/article/pii/S0010465509000472.

[129] Sangalli, D. *et al.* Many-body perturbation theory calculations using the yambo code. *Journal of Physics: Condensed Matter* **31**, 325902 (2019). URL https://dx.doi.org/10.1088/1361-648X/ab15d0.

[130] Giannozzi, P. *et al.* Advanced capabilities for materials modelling with quantum espresso. *Journal of Physics: Condensed Matter* **29**, 465901 (2017). URL https://dx.doi.org/10.1088/1361-648X/aa8f79.

[131] Jellison, G. E. & Modine, F. A. Optical functions of silicon between 1.7 and 4.7 ev at elevated temperatures. *Phys. Rev. B* **27**, 7466–7472 (1983). URL https://link.aps.org/doi/10.1103/PhysRevB.27.7466.

[132] Sottile, F., Olevano, V. & Reining, L. Parameter-free calculation of response functions in time-dependent density-functional theory. *Phys. Rev. Lett.* **91**, 056402 (2003). URL https://link.aps.org/doi/10.1103/PhysRevLett.91.056402.

[133] Marini, A. Ab initio finite-temperature excitons. *Phys. Rev. Lett.* **101**, 106405 (2008). URL https://link.aps.org/doi/10.1103/PhysRevLett.101.106405.

[134] Lautenschlager, P., Garriga, M., Logothetidis, S. & Cardona, M. Interband critical points of gaas and their temperature dependence. *Phys. Rev. B* **35**, 9174–9189 (1987). URL https://link.aps.org/doi/10.1103/PhysRevB.35.9174.

[135] Molina-Sánchez, A., Sangalli, D., Hummer, K., Marini, A. & Wirtz, L. Effect of spin-orbit interaction on the optical spectra of single-layer, double-layer, and bulk mos_2. *Phys. Rev. B* **88**, 045412 (2013). URL https://link.aps.org/doi/10.1103/PhysRevB.88.045412.

[136] Qiu, D. Y., da Jornada, F. H. & Louie, S. G. Optical spectrum of mos_2: Many-body effects and diversity of exciton states. *Phys. Rev. Lett.* **111**, 216805 (2013). URL https://link.aps.org/doi/10.1103/PhysRevLett.111.216805.

[137] Tran, V., Soklaski, R., Liang, Y. & Yang, L. Layer-controlled band gap and anisotropic excitons in few-layer black phosphorus. *Phys. Rev. B* **89**, 235319 (2014). URL https://link.aps.org/doi/10.1103/PhysRevB.89.235319.

[138] Duffin, R. J. The Reciprocal of a Fourier Series. *Proceedings of the American Mathematical Society* **13**, 965–970 (1962). URL https://www.ams.org/journals/proc/1962-013-06/S0002-9939-1962-0145259-X/.

[139] Margulis, V. A., Muryumin, E. E. & Gaiduk, E. A. Optical second-harmonic generation from two-dimensional hexagonal crystals with broken space inversion symmetry. *Journal of Physics: Condensed Matter* **25**, 195302 (2013). URL https://dx.doi.org/10.1088/0953-8984/25/19/195302.

[140] Trolle, M. L., Seifert, G. & Pedersen, T. G. Theory of excitonic second-harmonic generation in monolayer mos_2. *Phys. Rev. B* **89**, 235410 (2014). URL https://link.aps.org/doi/10.1103/PhysRevB.89.235410.

[141] Galvani, T. *et al.* Excitons in boron nitride single layer. *Phys. Rev. B* **94**, 125303 (2016). URL https://link.aps.org/doi/10.1103/PhysRevB.94.125303.

[142] Hernandez, V., Roman, J. E. & Vidal, V. Slepc: A scalable and flexible toolkit for the solution of eigenvalue problems. *ACM Trans. Math. Softw.* **31**, 351–362 (2005). URL https://doi.org/10.1145/1089014.1089019.

[143] Saad, Y. *Numerical Methods for Large Eigenvalue Problems* (Society for Industrial and Applied Mathematics, 2011). URL https://epubs.siam.org/doi/abs/10.1137/1.9781611970739.

[144] Kerker, G. P. Efficient iteration scheme for self-consistent pseudopotential calculations. *Phys. Rev. B* **23**, 3082–3084 (1981). URL https://link.aps.org/doi/10.1103/PhysRevB.23.3082.

[145] Baker, G. A. *Essentials of Pade Approximants* (Academic Press, 1975). URL https://www.elsevier.com/books/essentials-of-pade-approximants/baker/978-0-12-074855-6.

[146] Vidberg, H. J. & Serene, J. W. Solving the Eliashberg equations by means of n-point Padé approximants. *Journal of Low Temperature Physics* **29**, 179 (1977). URL https://link.springer.com/article/10.1007/BF00655090.

[147] Giustino, F., Cohen, M. L. & Louie, S. G. Gw method with the self-consistent sternheimer equation. *Phys. Rev. B* **81**, 115105 (2010). URL https://link.aps.org/doi/10.1103/PhysRevB.81.115105.

[148] Hübener, H. & Giustino, F. Time-dependent density functional theory using atomic orbitals and the self-consistent sternheimer equation. *Phys. Rev. B* **89**, 085129 (2014). URL https://link.aps.org/doi/10.1103/PhysRevB.89.085129.

[149] Shirley, E. L. Optimal basis sets for detailed brillouin-zone integrations. *Phys. Rev. B* **54**, 16464–16469 (1996). URL https://link.aps.org/doi/10.1103/PhysRevB.54.16464.

[150] Prandini, G., Galante, M., Marzari, N. & Umari, P. Simple code: Optical properties with optimal basis functions. *Computer Physics Communications* **240**, 106–119 (2019). URL https://www.sciencedirect.com/science/article/pii/S0010465519300682.

[151] Ljungberg, M. P., Koval, P., Ferrari, F., Foerster, D. & Sánchez-Portal, D. Cubic-scaling iterative solution of the bethe-salpeter equation for finite systems. *Phys. Rev. B* **92**, 075422 (2015). URL https://link.aps.org/doi/10.1103/PhysRevB.92.075422.

[152] Castro, A., De Giovannini, U., Sato, S. A., Hübener, H. & Rubio, A. Floquet engineering the band structure of materials with optimal control theory. *Phys. Rev. Res.* **4**, 033213 (2022). URL https://link.aps.org/doi/10.1103/PhysRevResearch.4.033213.

[153] Alliati, I. M., Evans, R. F. L., Novoselov, K. S. & Santos, E. J. G. Relativistic domain-wall dynamics in van der Waals antiferromagnet MnPS3. *npj Computational Materials* **8**, 3 (2022). URL https://www.nature.com/articles/s41524-021-00683-6.

[154] Chittari, B. L. *et al.* Electronic and magnetic properties of single-layer $m\mathrm{P}X_3$ metal phosphorous trichalcogenides. *Phys. Rev. B* **94**, 184428 (2016). URL https://link.aps.org/doi/10.1103/PhysRevB.94.184428.